

STOCHASTIC MODELING OF THE TURBULENT BOUNDARY LAYER

Von der Fakultät für Maschinenbau, Elektro- und Energiesysteme der
Brandenburgischen Technischen Universität Cottbus-Senftenberg zur Erlangung
des akademischen Grades eines

**Doktors der Ingenieurwissenschaften
(Dr.-Ing.)**

genehmigte Dissertation vorgelegt von

**Master of Technology
Rakhi**

geboren am 05.06.1992 in Asaudha, India

Vorsitzender	Apl. Prof. Dr. rer. nat. habil. Uwe Harlander	BTU Cottbus-Senftenberg
Gutachter	Prof. Dr.-Ing. Heiko Schmidt	BTU Cottbus-Senftenberg
Gutachter	Prof. Michael Oevermann	BTU Cottbus-Senftenberg
Gutachter	Prof. Philipp Schlatter	KTH Sweden

Tag der mündlichen Prüfung: 23.01.2023

STOCHASTIC MODELING OF THE TURBULENT BOUNDARY LAYER

M.Tech. Rakhi

University:

Brandenburg University of Technology Cottbus-Senftenberg

Faculty:

Mechanical Engineering, Electrical and Energy Systems

Chair:

Numerical Fluid and Gas Dynamics

M.Tech. Rakhi:
Stochastic Modeling of the Turbulent Boundary Layer,

CHAIR OF EVALUATION COMMITTEE:
Apl. Prof. Dr. rer. nat. habil. Uwe Harlander

SUPERVISOR:
Prof. Dr.-Ing. Heiko Schmidt

REVIEWERS:
Prof. Dr.-Ing. Heiko Schmidt
Prof. Michael Oevermann
Prof. Philipp Schlatter

LOCATION:
Cottbus

SUBMISSION DATE:
June 2021

“Success is a science; if you have the conditions, you get the result.”

Oscar Wilde

Abstract

The incompressible temporally developing turbulent boundary layer (TBL) and spatially developing turbulent boundary layer (SBL) with and without blowing is analyzed using the map-based stochastic one-dimensional turbulence (ODT) model. An understanding of these idealized flows is of fundamental relevance for boundary layer-type problems, which are frequently encountered in several applications, from atmospheric sciences to engineering. In the ODT model, the flow variables are resolved on all scales along a wall-normal, 1-D domain. These variables are evolved by a deterministic process representing molecular diffusion and by a stochastic process modeling the effect of turbulent advection and pressure fluctuations. Due to the reduction in dimensionality, the model is particularly appropriate for high Reynolds number flow. It is shown that the ODT model is able to capture salient features of the turbulent boundary layer-type flows by comparing the results with various available reference direct numerical simulation (DNS), large eddy simulation (LES) and experimental results. The comparison is presented for the mean velocity profiles, turbulent velocity fluctuation profiles (up to fourth order), the skin friction coefficient and shape factor for different bulk (Re_b) and momentum Reynolds numbers (Re_θ) using fixed model parameters. The influence of the model parameters is also discussed for various momentum Reynolds numbers for each investigated flow configuration. The results discussed in this thesis suggest that the ODT model is an economical and reasonably accurate approach for the simulation of turbulent boundary layer flows.

Kurzfassung

Die inkompressible sich zeitlich entwickelnde turbulente Grenzschicht (TBL) und die sich räumlich entwickelnde turbulente Grenzschicht (SBL) ohne Ausblasen und mit gleichmäßigem Ausblasen werden mit dem abbildungsbasierten stochastischen eindimensionalen Turbulenzmodell (ODT) analysiert. Das Verständnis dieser idealisierten Strömung ist von grundlegender Bedeutung für turbulente Grenzschichtströmungen, die in verschiedenen Anwendungen, von den Atmosphärenwissenschaften bis hin zu den Ingenieurwissenschaften, häufig anzutreffen sind. Die Strömungsvariablen werden in den vorliegenden ODT-Simulationen auf allen Skalen entlang eines wandnormalen 1-D-Rechengebietes aufgelöst. Diese Variablen werden durch einen deterministischen Prozess, der die molekulare Diffusion repräsentiert, und einen stochastischen Prozess entwickelt, der die Wirkung von turbulenten Advektions- und Druckschwankungen modelliert. Das Modell eignet sich aufgrund der reduzierten Dimensionalität besonders für hohe Reynoldszahlen. Es wird gezeigt, dass das ODT-Modell in der Lage ist, die wesentlichen Merkmale der turbulenten Grenzschichtströmungen zu erfassen, indem es die mittleren Geschwindigkeitsprofile, die turbulenten Geschwindigkeitsschwankungsprofile (bis zur vierten Ordnung), den Mantelreibungskoeffizienten und den Formfaktor mit verschiedenen verfügbaren direkten numerischen Referenzsimulationen (DNS) und Grobstruktursimulationen (LES) vergleicht, die Ergebnisse für verschiedene Bulk- (Re_b) und Momentum-Reynoldszahlen (Re_θ) unter Verwendung fester Modellparameter. Der Einfluss der Modellparameter wird ebenfalls für die betrachteten Momentum-Reynoldszahlen und für die untersuchten Strömungskonfigurationen diskutiert. Die in dieser Arbeit gezeigten Ergebnisse deuten darauf hin, dass das ODT-Modell ein wirtschaftlicher und akkurater Ansatz für die Simulation von turbulenten Grenzschichtströmungen ist.

Acknowledgements

Seeing this manuscript in its final form has made me realize how much I have grown as a scholar. The work put up during this thesis has not only made me a better researcher, but also a more dedicated person overall. It is, however, impossible to come so far without the support of people around you. The support I received from the following people throughout the duration of my thesis is the reason that I am in a position to complete this manuscript.

First and foremost, I would like to thank Prof. Dr.-Ing. Heiko Schmidt, my thesis supervisor, for offering me an opportunity to work on this exciting subject. His constructive criticism always motivated me to out-perform my own capabilities.

Secondly, I want to express my gratitude to David O. Lignell for always being available for discussions regarding ODT and for his valuable comments on blowing formulation of the ODT model. Moreover, his support and supervision during our BYU visit is highly appreciated.

Next, I would like to thank Prof. Dr. Moritz M. Fagner. He helped me with his valuable comments and discussions for concept-building during the inception of my thesis. His experience and deep understanding of the subject provided insights that helped me formulate this thesis.

I also take this opportunity to acknowledge the Graduate Research School (GRS) of the BTU Cottbus-Senftenberg for the financial support provided for this thesis in the framework of the Cluster StochMethod SP7, 'Stochastic Modeling of Turbulent Flow'.

I cannot thank enough the members of the jury for accepting to be a part of the jury for the thesis defense. I thank Prof. Heiko Schmidt, Prof. Michael Oevermann and Prof. Philipp Schlatter for reviewing this thesis and Prof. Uwe Harlander for becoming the commission head for my defense.

I would also like to extend my gratitude to Marten Klein for his contribution in writing the responses in my first publication and for providing constant motivation and feedback throughout the thesis. This made sure that various stages of the thesis were going in the right direction and in the right time to meet the deadlines. I am also thankful to Juan Medina for his suggestions regarding spectra calculations and his feedback during the review process.

Special mention goes to Silke Kaschwich from BTU and Robert Rode from GRS for taking care of all my administrative requirements. I would also like to thank Mark Simon for his discussions regarding numerics, and computational advancements. I also thank Andreas Krebs for helping me with Heraklit related issues. Further, thanks go to my colleague Tommy Starrick for being there for any discussions and helping me out in translating several German

documents.

A shout-out to all the wonderful friends I made here in Cottbus, Samah, Nisha, Samarth, Aishwarya, Nikita, Abhishek, Harry, Neha, Pedro, Amir, Arun, who kept my social life alive and did not let me feel home sick. My friends back in India, Sushma, Rachita, Anjali, Lav, supported me throughout this journey.

Special shout-out to my husband Lokesh, who kept encouraging me, not letting me lose hope during my low times. Thank you, Lokesh, for being by my side through thick and thin.

There is no force backing us more than the blessings of our parents and elders. Thank you Mumma, Bua and Savita aunty for bestowing upon me your blessings and love that made me keep going. My elder brother, Vivek has been a real support system, not only during this thesis, but at every stage of my life. Thank you for your love.

Last but not at all the least, I thank God for giving me the strength and will to keep going during tough times. There were so many times that I doubted myself, but my faith in God always got me back on my feet.

Rakhi

Contents

Abstract	v
Kurzfassung	vii
Acknowledgements	ix
List of Figures	xv
List of Tables	xix
List of Abbreviations	xxi
List of Symbols	xxiii
Publications	1
1 General Introduction	3
1.1 Introduction to Turbulent Flow	3
1.2 The Governing Equations	4
1.2.1 Continuity Equation	5
1.2.2 Momentum Equation	6
1.3 Modeling and Simulation	6
1.4 Boundary Layer Theory	9
1.5 State of the Art	15
1.6 Organisation of the Manuscript	18
1.7 In Closing	20
2 ODT Model Formulation	21
2.1 Introduction to the ODT Model	21
2.2 Governing Equations for ODT	23
2.2.1 Temporal ODT Evolution Equations	23
Eulerian Temporal Form	23
Lagrangian Temporal Form	24
2.2.2 Spatially Evolving ODT Equations	25
Eulerian Spatial Form	25
Lagrangian Spatial Form	26
2.3 Formulation of the Eddy Events	28
2.4 Eddy Event Selection	31
2.5 Numerical Basics	34
2.6 Statistical Quantities in ODT Realizations	35
2.7 In Closing	37

3	ODT Simulation Set-Up	39
3.1	Characterization of the TBL and ODT Simulation Set-Up	39
3.1.1	Characterization of the TBL	39
3.1.2	ODT Simulation Set-Up for the TBL	41
3.2	Simulation Set-Up for the SBL	46
3.3	Simulation Set-Up for Uniform Blowing in the SBL	48
3.4	In Closing	51
4	Temporally Developing Turbulent Boundary Layer	53
4.1	Velocity Boundary Layer for the TBL Case	53
4.2	First and Second Order Velocity Statistics	56
4.3	Higher Order Velocity Statistics	65
4.4	Energy Spectra and Isotropy Indicator	70
4.5	Temporal Behavior and its Influence on Structural Properties	75
4.6	Coefficients in the Transient and Asymptotic State	83
4.7	In Closing	86
5	Spatially Developing Turbulent Boundary Layer	87
5.1	Influence of Domain	87
5.2	Variation of Bulk Reynolds Numbers	88
5.2.1	First and Second Order Velocity Statistics	94
5.2.2	Higher Order Velocity Statistics	101
5.3	Variation of the Structural Properties with Re_θ	108
5.4	Comparison between TBL and SBL	113
5.5	In Closing	126
6	SBL with Uniform Blowing	127
6.1	Velocity Statistics for Uniform Blowing Configuration	127
6.1.1	First and Second Order Velocity Statistics	127
6.1.2	Higher Order Velocity Statistics	133
6.2	Variation of the Global Properties with Re_θ	139
6.3	In Closing	143
7	Comparison with Experiments	145
7.1	The Logarithmic Law of the Wall	145
7.2	Second Order Velocity Statistics	146
7.3	Higher Order Velocity Statistics	148
7.4	In Closing	151
8	Conclusions & Outlook	153
8.1	Conclusions	153
8.2	Outlook	155
A	Turbulent Kinetic Energy	159
B	ODT Model Details	161
B.1	Eddy Sampling	161
B.2	Eddy Sampling: the smart way	161

C	Model Parameter Sensitivity for TBL	163
C.1	Variation of the Model Parameter α	164
C.2	Variation of the Model Parameter C	167
C.3	Variation of the Model Parameter Z	175
C.4	Influence of the LS Mechanism	178
D	Influence of Initial Conditions	183
E	Generation of Energy Spectra in ODT	185
E.1	Generation of Time-Dependent Energy Spectra	185
E.2	Generation of Position-Dependent Energy Spectra	187
F	TBL Results for High Bulk Reynolds Number	189
G	Model Parameter Sensitivity for SBL	201
G.1	Variation of the Model Parameter C	202
G.2	Variation of the Model Parameter Z	207
H	Model Parameter Sensitivity for Uniform Blowing in SBL	211
H.1	Variation of the Model Parameter C	212
H.2	Variation of the Model Parameter Z	214
H.3	Influence of the LS Mechanism	217
H.4	Variation of the Model Parameter α	222
	Bibliography	223

List of Figures

1.1	A schematic for different prediction methods	8
1.2	A schematic for different prediction methods in spectral space	9
1.3	Boundary layer over a flat plate	10
1.4	Velocity profile for laminar and turbulent boundary layer	12
1.5	The normalized mean velocity profile	13
2.1	Schematic of an eddy turnover	29
2.2	Schematic of 1D representation of the map	29
2.3	Algorithm for the eddy selection and implementation.	33
3.1	Schematics of the SBL and TBL configuration	42
3.2	Streamwise velocity profile at $t = 0$ and $t > 0$	44
3.3	Comparison between ODT and Blasius laminar solution	48
3.4	Schematic of SBL with uniform blowing	49
4.1	Snapshots of Velocity field for TBL	55
4.2	Temporal development of the velocity boundary layer	56
4.3	Mean streamwise velocity profile for TBL	57
4.4	Indicator function for TBL	59
4.5	The rms velocity profiles for TBL	61
4.6	The probability density functions	63
4.7	Contour of constant rms values	64
4.8	Profiles of the Reynolds shear stresses for TBL	65
4.9	Turbulent kinetic energy production for TBL	66
4.10	Profiles of the skewness of the streamwise velocity for TBL	68
4.11	Profiles of the flatness of the streamwise velocity for TBL	69
4.12	Isotropy indicator for TBL	71
4.13	Streamwise energy spectra for TBL	73
4.14	Wall-normal position dependent ODT energy spectra	74
4.15	The global properties with Re_θ for TBL	76
4.16	The quantity Re_δ with Re_x	78
4.17	The global properties with time for TBL	79
4.18	Other quantities with time	80
4.19	H with time	81
4.20	C_f variation for TBL	82
4.21	Integral coefficients for TBL	84
5.1	The velocity statistics for various domain size at $Re_\theta \approx 2000$	89
5.2	The velocity statistics for various domain size at $Re_\theta \approx 4000$	90
5.3	The velocity statistics for various domain size at $Re_\theta \approx 8000$	91

5.4	Velocity field for SBL	92
5.5	Velocity boundary layer development with Re_θ	93
5.6	Velocity boundary layer development with x	94
5.7	The mean velocity profile at $Re_\theta \approx 2000$ and 4000 for SBL	96
5.8	The mean streamwise velocity profile at $Re_\theta \approx 8000$ for SBL	97
5.9	Indicator function at $Re_\theta \approx 2000$ and $Re_\theta \approx 4000$ for SBL	98
5.10	Indicator function at $Re_\theta \approx 8000$ for SBL	99
5.11	The rms velocity profile at $Re_\theta \approx 2000$ and $Re_\theta \approx 4000$ for SBL	100
5.12	The rms velocity profile at $Re_\theta \approx 8000$ for SBL	101
5.13	The Reynolds shear stresses at $Re_\theta \approx 2000$ and $Re_\theta \approx 4000$ for SBL	102
5.14	The Reynolds shear stresses at $Re_\theta \approx 8000$ for SBL	103
5.15	Production at $Re_\theta \approx 2000$ and $Re_\theta \approx 4000$ for SBL	104
5.16	Production at $Re_\theta \approx 8000$ for SBL	105
5.17	The skewness at $Re_\theta \approx 2000$ and $Re_\theta \approx 4000$ for SBL	107
5.18	The skewness at $Re_\theta \approx 8000$ for SBL	108
5.19	The flatness at $Re_\theta \approx 2000$ $Re_\theta \approx 4000$ for SBL	109
5.20	The flatness at $Re_\theta \approx 8000$ for SBL	111
5.21	Re_τ with Re_θ for SBL	112
5.22	H with Re_θ for SBL	112
5.23	C_f with Re_θ for SBL	113
5.24	C_f variation for SBL	114
5.25	Re_δ with Re_θ for SBL	115
5.26	H variation for SBL	116
5.27	The mean streamwise velocity for SBL and TBL	117
5.28	Indicator function for SBL and TBL	118
5.29	The rms of the streamwise velocity for SBL and TBL	119
5.30	Production for SBL and TBL	120
5.31	The skewness and flatness for SBL and TBL	122
5.32	C_f for SBL and TBL	123
5.33	C_f and H for SBL and TBL	124
5.34	Re_δ with Re_θ for SBL and TBL	125
5.35	Re_τ with Re_θ for SBL and TBL	125
6.1	The mean streamwise velocity profile for blowing	129
6.2	The indicator function for blowing	131
6.3	The rms velocity profile for blowing	132
6.4	The Reynolds shear stresses for blowing	134
6.5	Production for blowing	135
6.6	The skewness for blowing	137
6.7	The flatness for blowing	138
6.8	Re_τ with Re_θ for blowing	141
6.9	H with Re_θ for blowing	142
6.10	C_f with Re_θ for blowing	142
7.1	The mean streamwise velocity profile	146
7.2	The indicator function	147
7.3	The rms velocity profile	147

7.4	The Reynolds shear stresses	148
7.5	Turbulent kinetic energy production	149
7.6	The skewness profile	150
7.7	The flatness profile	150
C.1	The mean streamwise velocity for various α	165
C.2	The rms streamwise velocity for various α	166
C.3	The mean streamwise velocity for various C	168
C.4	The rms streamwise velocity for various C	169
C.5	The cross stresses for various C	170
C.6	The skewness of the streamwise velocity for various C	172
C.7	The global properties for various C	173
C.8	C_f for various C	174
C.9	The mean streamwise velocity for various Z	176
C.10	The rms streamwise velocity for various Z	177
C.11	The mean streamwise velocity for various LS methods	179
C.12	The rms streamwise velocity for various LS methods	180
C.13	Indicator function for various LS methods	180
D.1	Production to analyse the influence of initial conditions	184
F.1	Mean streamwise velocity profile for high Re_b	190
F.2	Indicator function for high Re_b	191
F.3	The rms velocity profiles for high Re_b	192
F.4	Profiles of the cross stresses for high Re_b	192
F.5	Turbulent kinetic energy production for high Re_b	193
F.6	Profiles of the skewness for high Re_b	193
F.7	Profiles of the flatness for high Re_b	194
F.8	Isotropy indicator for high Re_b	195
F.9	The global properties for high Re_b	196
F.10	Other quantities for high Re_b	196
F.11	Re_δ with Re_θ for high Re_b	197
F.12	The quantity Re_X for high Re_b	197
F.13	C_f variation for high Re_b	198
F.14	Integral coefficients for high Re_b	199
G.1	The velocity statistics for various C at $Re_\theta \approx 2000$	204
G.2	The velocity statistics for various C at $Re_\theta \approx 4000$	206
G.3	The velocity statistics for various C at $Re_\theta \approx 8000$	207
G.4	The velocity statistics for various Z at $Re_\theta \approx 2000$	208
G.5	The velocity statistics for various Z at $Re_\theta \approx 4000$	209
G.6	The velocity statistics for various Z at $Re_\theta \approx 8000$	210
H.1	The mean streamwise velocity for various C	213
H.2	The mean streamwise velocity with outer units for various C	213
H.3	The rms velocity profiles for various C	214
H.4	H with Re_θ for various C	215
H.5	C_f with Re_θ for various C	215
H.6	The mean streamwise velocity for various Z	216

H.7	The mean streamwise velocity with outer units for various Z	217
H.8	The rms velocity profiles for various Z	218
H.9	C_f with Re_θ for various Z	218
H.10	The mean streamwise velocity for various LS methods	219
H.11	The mean velocity with outer units for various LS methods	220
H.12	The rms velocity profiles for various LS methods	220
H.13	H with Re_θ for various LS methods	221
H.14	C_f with Re_θ for various LS methods	221
H.15	The mean streamwise velocity for various α	222

List of Tables

3.1	Summary of the cases and model parameters for TBL	45
3.2	Summary of the cases and model parameters for SBL	47
3.3	Summary of the cases and model parameters for blowing	50
4.1	ODT simulation results for TBL	77
4.2	Contributions to the semi-empirical equation	85
5.1	The simulations results for SBL	110
6.1	The simulations results for blowing	140

List of Abbreviations

1-D	one- d imensional
2-D	two- d imensional
3-D	three- d imensional
BL	B oundary L ayer
CFD	C omputational F luid D ynamics
DNS	D irect N umerical S imulation
EE	E ddy E vents
LES	L arge E ddy S imulation
NC-LES	N o C ontrol LES
NC-ODT	N o C ontrol ODT
ODT	O ne D imensional T urbulence
ODTLES	ODT with a 3-D LES coupling
PDE	P artial D ifferential E quation
PDF	P robability D ensity F unction
RANS	R eynolds A veraged N avier- S tokes
RE	R elative E rror
rms	root m ean s quare
RTT	R eynolds T ransport T heorem
SBL	S patially developing turbulent B oundary L ayer
S-DNS	S patial DNS
S-LES	S patial LES
S-ODT	S patial ODT
sgn	sign function
TBL	T emporally developing turbulent B oundary L ayer
TKE	T urbulent K inetic E nergy
T-DNS	T emporal DNS
T-ODT	T emporal ODT
ZPG	Z ero P ressure G radient

List of Symbols

Dimensionless parameters

Re	Reynolds number
Re_b	bulk Reynolds number
Re_δ	displacement Reynolds number
Re_t	turbulent Reynolds number
Re_τ	friction Reynolds number
Re_θ	momentum thickness Reynolds number

Physical model parameters

α	energy redistribution parameter
C	turbulence intensity parameter
LS	large-eddy suppression mechanism
Z	viscous damping parameter

Numerical model parameters

Δy_{max}	maximum allowed grid cell size	[m]
Δy_{min}	smallest allowed grid cell size	[m]
$gDens$	grid density factor	[m ⁻¹]
L_{max}	maximum eddy size	[m]
L_{min}	minimum eddy size	[m]
L_p	most probable eddy size	[m]

Nomenclature

A	log-layer offset	[-]
c	coefficient vector	[s ⁻¹]
C_f	skin friction coefficient	[-]
d	trip wire diameter	[m]
dt	time step	[s]
D	domain size	[m]
δ	displacement thickness	[m]

δ_{99}	boundary layer thickness	[m]
ΔE_i	change of the kinetic energy	[J]
ϵ	dissipation of TKE	[m ² s ⁻³]
η	Kolmogorov length scale	[m]
\mathbf{g}	gravitational acceleration vector	[m s ⁻²]
H	shape factor	[-]
\mathbf{l}	unit tensor	[-]
k	von Kármán constant	[-]
K	ODT kernel function	[m]
\mathcal{K}	turbulent kinetic energy	[m ² s ⁻²]
l	eddy size	[m]
L	characteristic length scale	[m]
λ	eddy rate distribution	[m ⁻² s ⁻¹]
m	mass	[kg]
μ	dynamic viscosity	[kg m ⁻¹ s ⁻¹]
\mathbf{n}	unit normal vector	[-]
N	number of ensemble members	[-]
ν	kinematic viscosity	[m ² s ⁻¹]
$v_\psi(t)$	control volume moving with the local velocity of ψ	[m ³]
p	pressure	[Pa]
\mathcal{P}	production of TKE	[m ² s ⁻³]
P_a	acceptance probability	[-]
ϕ	generic symbol for variable	[unit]
Π	wake strength	[-]
ψ	generic symbol for an intensive property	[unit kg ⁻¹]
Ψ	generic symbol for an extensive property	[unit]
Q_i	maximum extractable energy	[J]
ρ	density	[kg m ⁻³]
$R(t)$	eddy event rate	[s ⁻¹]
R_t	trial event rate	[s ⁻¹]
S	arbitrary surface	[m ²]
$S(t)$	surface change in time	[m ²]
$S_\psi(t)$	surface moving with the local velocity of ψ	[m ²]
t	time	[s]
\mathcal{T}	turbulent transport of TKE	[m ³ s ⁻³]
τ	eddy turnover time	[s]
τ_s	mean sampling time scale	[s]
τ_w	wall shear stress	[kg m ⁻¹ s ⁻²]
$\underline{\boldsymbol{\tau}}$	stress tensor	[Pa]
θ	momentum thickness	[m]
u	streamwise velocity	[m s ⁻¹]
\mathbf{u}	velocity vector field	[m s ⁻¹]
\bar{u}	streamwise ensemble-averaged velocity	[m s ⁻¹]
u'	fluctuating velocity in streamwise direction	[m s ⁻¹]
u^+	the dimensionless velocity	[-]
u_t	turbulent fluctuation velocity	[m s ⁻¹]
u_τ	friction velocity	[m s ⁻¹]

u_∞	free-stream velocity	$[\text{m s}^{-1}]$
U	characteristic velocity of the flow	$[\text{m s}^{-1}]$
U_b	bulk velocity	$[\text{m s}^{-1}]$
Y_i	mass fraction of species i	$[-]$
v	velocity component in the crosswise direction	$[\text{m s}^{-1}]$
\bar{v}	mean velocity in crosswise direction	$[\text{m s}^{-1}]$
v'	fluctuating velocity in crosswise direction	$[\text{m s}^{-1}]$
\mathbf{v}_i	velocity of species i	$[\text{m s}^{-1}]$
\mathbf{v}_ψ	local velocity of ψ	$[\text{m s}^{-1}]$
\mathbf{v}_ψ^D	diffusion velocity	$[\text{m s}^{-1}]$
V	control volume	$[\text{m}^3]$
$V(t)$	control volume changing in time	$[\text{m}^3]$
\tilde{v}_ϵ	Favre averaged velocity	$[\text{m s}^{-1}]$
w	velocity component in the spanwise direction	$[\text{m s}^{-1}]$
\bar{w}	mean velocity in spanwise direction	$[\text{m s}^{-1}]$
w'	fluctuating velocity in spanwise direction	$[\text{m s}^{-1}]$
W	Coles' wake function	$[-]$
x	cartesian streamwise position coordinate	$[\text{m}]$
ξ	eddy streamwise increment	$[\text{m}]$
y	cartesian crosswise position coordinate	$[\text{m}]$
y^+	the wall normal coordinate	$[-]$
y_τ	viscous length scale	$[\text{m}]$
y_0	eddy event position	$[\text{m}]$
z	cartesian spanwise position coordinate	$[\text{m}]$

Dedicated to my father, Late Shri Om Parkash

List of publications

[1] **Rakhi**, and H. Schmidt, One-dimensional turbulence: application to incompressible spatially developing turbulent boundary layers, *International Journal of Heat and Fluid Flow*, **85**, 108626, (2020). doi:<https://doi.org/10.1016/j.ijheatfluidflow.2020.108626>.

[2] **Rakhi**, M. Klein, J. A. Medina M. and H. Schmidt, One-dimensional turbulence modeling of incompressible temporally developing turbulent boundary layers with comparison to DNS, *Journal of Turbulence*, **20:8**, 506-543, (2019). doi:[10.1080/14685248.2019.1674859](https://doi.org/10.1080/14685248.2019.1674859).

[3] **Rakhi**, and H. Schmidt, Using a Stochastic One-Dimensional Turbulence model to study Incompressible Spatially Developing Turbulent Boundary Layers. *In Proceedings of TSFP-11*, July 30–August 2, (2019). Southampton, UK.

[4] **Rakhi**, and H. Schmidt, A stochastic approach to investigate the incompressible temporally developing turbulent boundary layer. *In Proceedings of CMFF'18*, September 4–7, (2018). Budapest, Hungary.

[5] **Rakhi**, and H. Schmidt, Investigating incompressible temporally developing turbulent boundary layers using One-Dimensional Turbulence, *Proceedings of Applied Mathematics and Mechanics*, **18** e201800214, (2018). doi:[10.1002/pamm.201800214](https://doi.org/10.1002/pamm.201800214).

Chapter 1

General Introduction

The main focus of this chapter is to describe the problem of turbulent flows along with some of the examples. The Navier-Stokes equations, which represents the set of governing equations will also be discussed along with the different simulation and modeling approaches, for example, DNS, LES and RANS with their merits and demerits. Next, the theory related to the boundary layer (BL) and various important parameters are summarized. The chapter is closed with the state of the art and organisation of the thesis.

1.1 Introduction to Turbulent Flow

We are surrounded by numerous examples to observe the turbulent flows in our everyday life and some of these include smoke from a chimney, water in a river or waterfall, or the buffeting of a strong wind [1]. These examples demonstrates that the flow is unsteady, irregular, seemingly random and chaotic, and surely the motion of every eddy or droplet is unpredictable. Also, the turbulent motions of many scales can be observed in such flows. These features mentioned above are common to all turbulent flows. Careful observations and more details can be analyzed in laboratory experiments. For a detailed explanation, the reader is referred to [2, 3, 4, 5, 6].

Turbulent flows are prevalent in engineering applications, as in the processing of liquids or gases with pipe lines, pumps, compressors, etc. and also the flows around vehicles - e.g., airplanes, automobiles, ships, and submarines.

The above discussion implies that an essential feature of turbulent flows is the fluid velocity field which varies significantly and irregularly in both position and time. The velocity field (which is used in the upcoming chapters of the thesis) is denoted by $\mathbf{u}(\mathbf{x}, t)$ where \mathbf{x} is the position, t is the time and u (or u_1), v (or u_2) and w (or u_3) are the components of \mathbf{u} in x , y and z direction, respectively. (Note that all the bold symbols are used to represent the vector quantities.)

The turbulent flow shows the ability to transport and mix fluid much more effectively as compared to the laminar flow. This is an important characteristic

of turbulence and was demonstrated by an experiment first reported by Osborne Reynolds in 1883 where a dye was steadily injected on the centerline of a long pipe in which water was flowing. Later, in 1894, Reynolds established that the flow can be characterized by a single non-dimensional parameter which is known as the Reynolds number Re , defined as the ratio of Inertial force to Viscous force (Reynolds number is discussed in much more detail in upcoming sections of this chapter). It is defined as $Re = UL/\nu$, where U is the characteristic velocity, L is the length scales and ν is the kinematic viscosity of the fluid. In this experiment, when $Re < 2,300$, the flow is laminar and for $Re > 4,000$, the flow is turbulent. In between the laminar and turbulent region, the flow is in transition.

1.2 The Governing Equations

Due to the highly non-linear nature of the turbulent flow, their research is a challenge for theoretical and computational analysis. During the 19th century, several non-successful attempts were made in order to find analytical solutions to the Navier-Stokes equations. The Navier-Stokes equations represents the set of equations for conservation of mass, momentum and energy in the fluid flow. Originally, the postulates for mass, momentum and energy conservation were stated for point systems in classical mechanics however, with the arrival of the concept of fields to physics, the Lagrangian perspective of a point system tracked in space and time had an Eulerian counterpart for the change of the field in time. The Euler equations (named after Leonhard Euler) were among the first partial differential equations which appeared in 1757 [7] representing a set of quasilinear hyperbolic equations governing adiabatic and inviscid flow. For more details, the reader is referred to [8, 9, 10]. The Navier-Stokes equations in Lagrangian as well as Eulerian framework (same notations have been used as in [11]) are obtained by the application of the Reynolds Transport Theorem (RTT) [8] and are given below.

The RTT in its integral form may be written for an intensive property ψ moving with velocity \mathbf{v}_ψ as,

$$\frac{d}{dt} \int_{v_\psi(t)} \rho \psi dV = \int_{V(t)} \frac{\partial \rho \psi}{\partial t} dV + \int_{S(t)} \rho \psi \mathbf{v}_\psi \cdot \mathbf{n} dS, \quad (1.1)$$

where S is the surface enclosing the control volume V which may change in time, i.e., $V(t)$ and $S(t)$. $v_\psi(t)$ is a control volume with corresponding surface $S_\psi(t)$ which is defined such that it moves with the local velocity of the property ψ , \mathbf{v}_ψ . \mathbf{n} is the unit normal vector [11].

If we want to use the same volume $v(t)$ for all ψ then it needs to be accounted that $v(t)$ may not define a closed system for Ψ [11]. $v(t)$ is defined for convenience as a Lagrangian control volume that moves with the local mass-averaged velocity, \mathbf{v} . With this, the Lagrangian volume associated with $v_\psi(t)$ can be related to the one associated with the mass averaged velocity,

$v(t)$. The Lagrangian conservation equation for ψ using a Lagrangian control volume moving at \mathbf{v} is,

$$\frac{d}{dt} \int_{v(t)} \rho \psi dV = - \int_{S(t)} \Phi_{\psi} \cdot \mathbf{n} dS + \int_{v(t)} \sigma_{\psi} dV, \quad (1.2)$$

here Φ_{ψ} is the flux of ψ apart from the flux associated with the mass-averaged velocity, σ_{ψ} is the net rate of production of $\rho\psi$.

Using RTT, the Eulerian conservation equation for ψ is written as,

$$\int_{V(t)} \frac{\partial \rho \psi}{\partial t} dV + \int_{S(t)} \rho \psi \mathbf{v} \cdot \mathbf{n} dS = - \int_{S(t)} \Phi_{\psi} \cdot \mathbf{n} dS + \int_{V(t)} \sigma_{\psi} dV, \quad (1.3)$$

here $\rho\psi\mathbf{v}$ is the net rate of production of $\rho\psi$.

Using Gauss' integral theorem, the differential forms of equations 1.2 and 1.3 in the Lagrangian and Eulerian frames, respectively can be written as,

$$\rho \frac{d\psi}{dt} = -\nabla \cdot \Phi_{\psi} + \sigma_{\psi}, \quad (1.4)$$

$$\frac{\partial \rho \psi}{\partial t} + \nabla \cdot \rho \psi \mathbf{v} = -\nabla \cdot \Phi_{\psi} + \sigma_{\psi}. \quad (1.5)$$

The details of the definition of ψ , Φ_{ψ} and σ_{ψ} for various governing equations are discussed in the following subsections.

1.2.1 Continuity Equation

For the continuity equation, $\psi = \partial \Psi / \partial m = 1$, $\mathbf{v}_{\psi=1} = \mathbf{v}$ (the velocity advecting the density is the mass-averaged velocity) which leads to $v_{\psi=1}(t) = v(t)$. Since the mass is conserved for a closed system, we get,

$$\frac{d}{dt} \int_{v(t)} \rho dV = 0, \quad (1.6)$$

$$\int_{V(t)} \frac{\partial \rho}{\partial t} dV + \int_{S(t)} \rho \mathbf{v} \cdot \mathbf{n} dS = 0. \quad (1.7)$$

When the above equations are compared with equations 1.2 and 1.3, we get,

$$\Phi_{\psi=1} = 0, \quad (1.8)$$

$$\sigma_{\psi=1} = 0. \quad (1.9)$$

1.2.2 Momentum Equation

For the momentum equation, $\psi = \mathbf{v}$, $\Psi = m\mathbf{v}_{\psi=\mathbf{v}} = m\mathbf{v}\mathbf{v}$ ($\mathbf{v}\mathbf{v} = \mathbf{v}$, i.e., the mass-averaged velocity is the one that advects momentum in a closed system). So equation 1.1 becomes,

$$\frac{d}{dt} \int_{v(t)} \rho \mathbf{v} dV = \int_{V(t)} \frac{\partial \rho \mathbf{v}}{\partial t} dV + \int_{S(t)} \rho \mathbf{v} \otimes \mathbf{v} \cdot \mathbf{n} dS, \quad (1.10)$$

with \otimes as the tensor product. Further, using Newton's second law of motion we get,

$$\frac{d}{dt} \int_{v(t)} \rho \mathbf{v} dV = \int_{S(t)} (p \mathbf{l} + \underline{\boldsymbol{\tau}}) \cdot \mathbf{n} dS + \int_{v(t)} \rho \mathbf{g} dV, \quad (1.11)$$

where p is the pressure, \mathbf{l} is the unit tensor, $\underline{\boldsymbol{\tau}}$ is the stress tensor, and \mathbf{g} is the gravitational acceleration vector. Using equation 1.2, we get,

$$\Phi_{\mathbf{v}} = p \mathbf{l} + \underline{\boldsymbol{\tau}}, \quad (1.12)$$

$$\sigma_{\mathbf{v}} = \rho \mathbf{g}. \quad (1.13)$$

As discussed above, the symbols, ψ , Φ_{ψ} and σ_{ψ} are 1, 0, 0, respectively for the continuity equation and \mathbf{v} , $p \mathbf{l} + \underline{\boldsymbol{\tau}}$ and $\rho \mathbf{g}$ for the momentum equation.

1.3 Modeling and Simulation

As discussed in the previous section, for fluid flows, either laminar or turbulent, the conservation laws are embodied in the Navier-Stokes equations. Taking into account the diversity and complexity of fluid flows, it is pretty phenomenal that the Navier-Stokes equations describe them accurately and in complete detail. In the context of turbulent flows, the equations describe the turbulent velocity field starting from the largest to the smallest length as well as the time scales.

A complete description for the various numerical methods to solve the Navier-Stokes equations is omitted, instead only an overview is given here. The growing need of numerical simulations to study the behaviour of systems whose mathematical models are too complex to provide analytical solutions, as in most nonlinear systems, leads to the direct numerical simulation (DNS). DNS in computational fluid dynamics (CFD) is the direct approach of solving the Navier-Stokes equations (without any assumption) for turbulent flows. In DNS, the Navier-Stokes equations are solved by resolving all the scales of motion (i.e., the whole range of spatial and temporal scales) with initial and boundary conditions appropriate to the flow problem (shown in Figure 1.1 and in Figure 1.2 in spectral space). However, DNS is intractable for the high Reynolds number flows of practical interest in engineering applications, it is nonetheless a powerful research tool for investigating turbulent flows at low

to moderate Reynolds numbers. A detailed description of DNS is given in [12, 13], among others.

For a DNS, the required resolution can be estimated from the turbulent Reynolds number $Re_t = u_t L \nu^{-1} \approx (L \eta^{-1})^{4/3}$, where u_t is the turbulent fluctuation velocity, L is a characteristic large length scale or integral scale, η represents the Kolmogorov scale and ν is the kinematic viscosity. The requirement for this resolution for industrial flows can possibly reach up to 10^{15} or more grid cells. Hence, the memory storage requirement grows with the Reynolds number and is very large. Therefore, DNS is currently restricted to simulation problems at small to moderate Reynolds numbers. For practical high Reynolds number calculations, other simulation or modeling techniques are required.

As the high Reynolds number flows are prevalent in numerous applications, the alternative is to pursue a filtering approach where the turbulent flow is described in terms of statistics, the simplest being the mean velocity field $\bar{\mathbf{u}}$ instead of the velocity $\mathbf{u}(\mathbf{x}, t)$. A tractable set of equations can be deduced from a model based on such statistics. The statistical model, large eddy simulations (LES), is explained next which can be used to calculate the properties of turbulent flows [1].

In LES, the effects of the smaller scale motions are modeled and the dynamics of the larger 3-D unsteady turbulent motions are represented explicitly [1]. Here, a spatial low-pass filter is applied to the equations and the velocity is decomposed into the sum of a filtered or resolved component and a residual/ subgrid-scale component. The momentum equations contain the residual stress tensor (which are modeled to obtain the closure) arising from the residual motions and the equations for the evolution of the filtered velocity field (solved numerically) are derived from the Navier-Stokes equations.

LES was initially proposed in 1963, detailed in [14], and later explored in [15]. Currently, this method is applied to a wide variety of engineering problems [16, 17, 18]. The computational cost in LES is reduced as compared to the DNS by modeling the smallest length scales. However, in some problems, for example, [19, 20, 21], the small-scales plays an important role. In that sense, LES is more accurate and reliable where large-scale unsteadiness is significant as the large-scale unsteady motions are represented explicitly. A detailed description of LES is provided in [22].

Next, the Reynolds-averaged Navier–Stokes (RANS) equations played an important role. The RANS equations are time-averaged equations of motion for fluid flow and the idea behind RANS is based on the separation of the flow field into a mean value and fluctuations (Reynolds decomposition) [23], for example, the $\mathcal{K} - \epsilon$ model (see Appendix A). The RANS equations can be used with approximations to provide approximate time-averaged solutions to the Navier-Stokes equations, however, these equations were primarily used to describe the turbulent flows [1]. As discussed in [24, 25], information is lost in case of RANS simulations due to averaging on the integral scale.

A schematic for comparison between different prediction methods discussed above is given in Figure 1.1 (depicting various scales) indicating that in case of DNS, the full range of length scale is resolved and no modeling

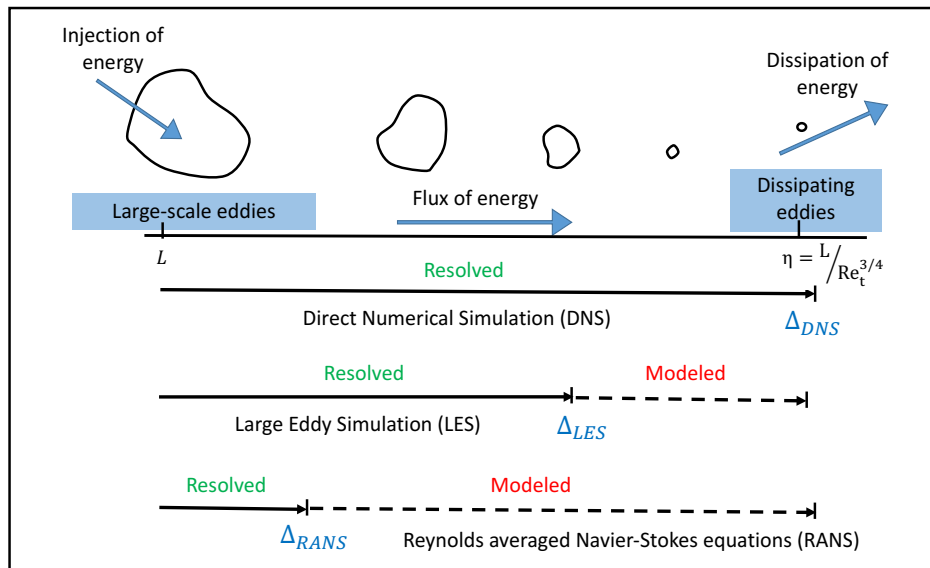


FIGURE 1.1: A schematic for comparison between different prediction methods [26].

tool is required, whereas, for LES and RANS, the complete range of length scale is not resolved. Some modeling methods are needed in LES as well as RANS. LES is a compromise between DNS and RANS. It is capable of providing more information than RANS at a lesser cost than DNS. A corresponding schematic in spectral space for DNS, LES and RANS is presented in Figure 1.2.

To summarize, industrial applications typically exhibit extremely large values of the dimensionless parameters, such as, the Reynolds number (Re) which leads to a very broad range of scales in the turbulence field. A very high spatial resolution is required to resolve the full range of scales. Therefore, the DNS of a high-Reynolds-number turbulent flow or turbulent boundary layer quickly becomes prohibitively expensive. To compensate for this, small scales may be modeled, as it is done in RANS and LES, which bear the problem that the spatio-temporal development of the turbulent flows cannot be captured very well. To overcome such limitations, a lower-order, stochastic turbulence model, such as the one-dimensional turbulence (ODT) [28, 29], can be useful since in ODT the flow variables are resolved only on a statistically representative, one-dimensional flow domain.

The main idea behind ODT is to model the effects of Navier–Stokes turbulence on a 1-D computational domain (i.e., the ODT line) which is essential to make the resolution of small-scale processes feasible. In the ODT model, to mimic the 3-D nature of turbulence in one spatial dimension, a stochastic process is adopted whereby motions accelerating mixing are modeled through a series of stochastic rearrangement events interpreted as the model analogue of individual turbulent eddies [28, 29]. The deterministic part is given by diffusion equation. The stochastic part is formulated with the aid of discrete mappings, so-called eddy events, and these events displace fluid parcels instantaneously on a given length scale and, thus, model the effects of an eddy

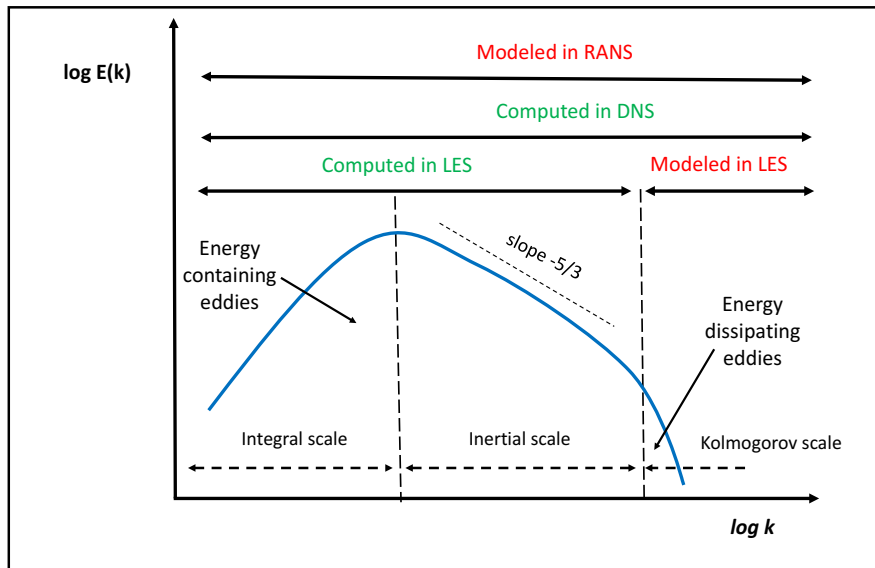


FIGURE 1.2: A schematic for comparison between different prediction methods in spectral space [27]. The wavenumber, $k = 2\pi/\text{eddy size}$.

turnover. A stochastic sequence of eddy events aims to capture the statistical properties of the turbulent flow by encompassing a range of scales.

In this thesis, ODT is used as a stand-alone tool for the simulation of the full range of scales found in the different simulation configurations for turbulent boundary layer. Since it is difficult to capture all the aspects of a full 3-D DNS with a lower-order model, this requires some compromises for the results to be obtained using the ODT model. Nevertheless, it is of fundamental interest to see how far one can get with the simplest possible set-up used in the study. As the ODT model is utilized to investigate turbulent boundary layer, the boundary layer theory is discussed next before moving to the formulation of the model.

1.4 Boundary Layer Theory

Boundary layer theory and its applications are discussed in this section and for detailed discussion, the reader is referred to [30]. The important objectives are external flows, laminar and turbulent boundary layer and the BL over a flat plate.

The boundary layer is one of the most important subjects in fluid mechanics. The flow can be classified into external flows and internal flows. Most of the times, the fluid is passing through a pipe or duct (internal flows) or it is moving over a plate (external flows). In both the cases, the fluid is in contact with at least one solid boundary.

Consider a car moving and passing through air. If the flow passing over the car is analyzed, the different phenomenon occur, such as initially creation of a boundary layer and the transformation of the flow from laminar/transition to turbulent. Another example can be considered the fluid passing over an

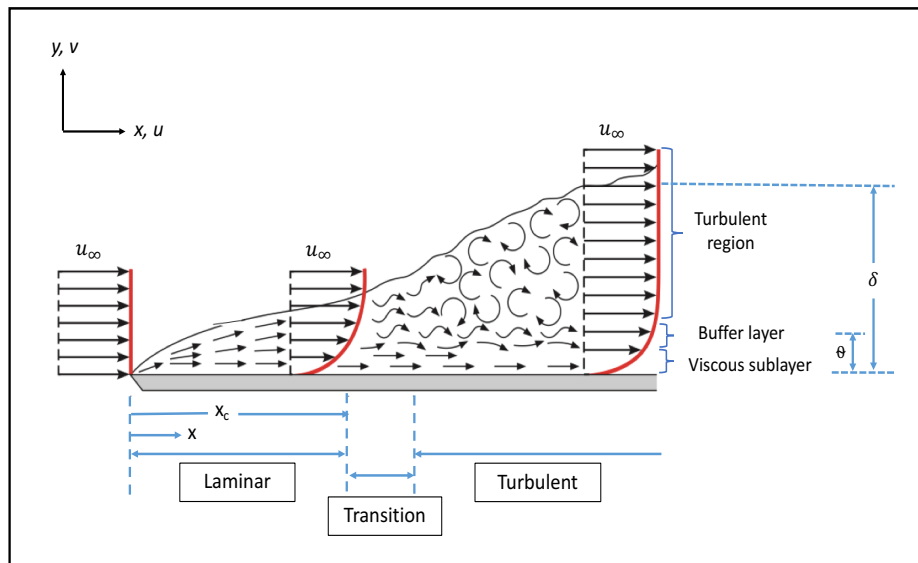


FIGURE 1.3: Velocity boundary layer development over a flat plate. The differences in velocity of the fluid particles between the objects and the fluid surface is confined to a region called 'Boundary Layer'. u_{∞} is the free stream velocity, δ is the boundary layer thickness and θ is the momentum thickness [31].

immersed circular cylinder or a sphere which is at rest. Assuming that at a solid boundary, the fluid will have zero velocity relative to the boundary or termed as no slip condition due to the viscous forces. Along with these external flows, other examples can be a bird flying surrounded by the fluid, the fluid flow surrounding an airplane or a space shuttle or submarine, flow past vehicles, buildings, etc. In these cases the solid or the body is surrounded by the fluid.

Like this, there is always a boundary layer created in most of the external flow problems. When the fluid flow is analyzed, it is required to deal with this layer and the remaining fluid flow. Sometimes, the flow is considered as a potential or ideal which is outside the BL. (For the internal flows as well, the velocity change takes place and there is also a boundary layer created. However, here our prime focus is on external flows.) This boundary layer is the major area which needs to be studied in detail. For example, how the boundary layer is behaving, whether it is laminar or turbulent and how the velocity changes, how the pressure and other parameters change. First, the concept of BL is discussed followed by some of the equations related to it.

If the flow is considered viscous, there is a no slip condition at the boundary where the fluid has a velocity same as that of the boundary. Hence, due to this condition and the viscous effect, a thin layer near to the boundary layer is generated and this is called the 'boundary layer' (shown in Figure 1.3 for a flat plate).

Whenever the viscous flows are dealt, this boundary layer generated due to the no slip condition needs to be considered and hence, the theory of the boundary layer forms the backbone of the modern fluid dynamics. Due to

its importance, the boundary layer theory was proposed in 1904 by Ludwig Prandtl [32] and then many related theories were developed.

Prandtl considered the boundary layer as a surface dividing between the rotational (within the boundary layer) and irrotational (beyond the boundary layer) flow (as in the case of a flow over a flat plate discussed below and shown in Figure 1.3). He also tried to establish certain relationship (discussed below), so that, various parameters like velocity and the pressure can be calculated, with respect to the boundary layer.

Figure 1.3 shows that a free stream flow with velocity u_∞ , is coming and depicts the boundary layer growth over a flat plate. The difference in velocity of the fluid particles between the object and the fluid surface is confined to a layer (boundary layer). In this region, the shear stresses are dominant. Depending upon the case, remaining fluid flow can be considered as a potential or ideal fluid flow, simplifying the problem by considering the boundary layer and the flow beyond the boundary layer.

In Figure 1.3, x is equal to zero and the length of the flat plate is l . u_∞ is the free stream velocity coming and touching the flat plate placed. The flat plate is not moving and due to the no slip condition, the velocity of the fluid touching the surface of the flat plate should be zero. Initially it is the laminar boundary layer tending towards the turbulent region through a transition zone. Due to the shear stresses, flow in the boundary layer is rotational and flow outside boundary layer is irrotational and also the boundary layer thickness is increasing as the fluid passes over the flat plate.

The velocity profile for the laminar boundary layer and the turbulent boundary layer is shown in Figure 1.4. Initially for some distance (say up to x_c in streamwise direction x as shown in Figure 1.3), the flow in the boundary layer is totally laminar in nature and after sometime, a mixing starts and transition takes place, finally, the flow becomes turbulent after a certain distance.

In the case of laminar boundary layer, within the boundary layer, the flow takes place in layers with each layer gliding over the adjacent layer as shown in Figure 1.4. Here, the exchange of mass or momentum takes place only between the adjacent layers and the dynamic viscosity of co-efficient is used to predict the shear stress within the layer. It is found only where the flow is taking place with a small Reynolds number ($Re_x = \frac{u_\infty x}{\nu}$ where Re_x is the Reynolds number at a particular location x). As the distance from the leading edge increases, the Reynolds number goes on increasing. Initially, in some region, up to x_c , the Reynolds number will be low and the flow will be laminar. As the Reynolds number increases, say above Re_{x_c} (critical Reynolds number which is 5×10^5 for flat plate) the flow becomes turbulent in nature with erratic motion of fluid particles with a violent transverse interchange of momentum.

Now going back to Figure 1.3, again in the turbulent boundary layer, if the boundary or the wall is very smooth, the turbulent boundary layer has a very narrow zone (shown in the figure), very close to the boundary in which the flow is still laminar, this narrow region is known as laminar or viscous sublayer.

The various regions formed in the turbulent boundary layer are shown in Figure 1.5 depicting the logarithmic law of the wall first published in 1930 by Theodore Von Kármán [34]. The logarithmic law of the wall is a self similar

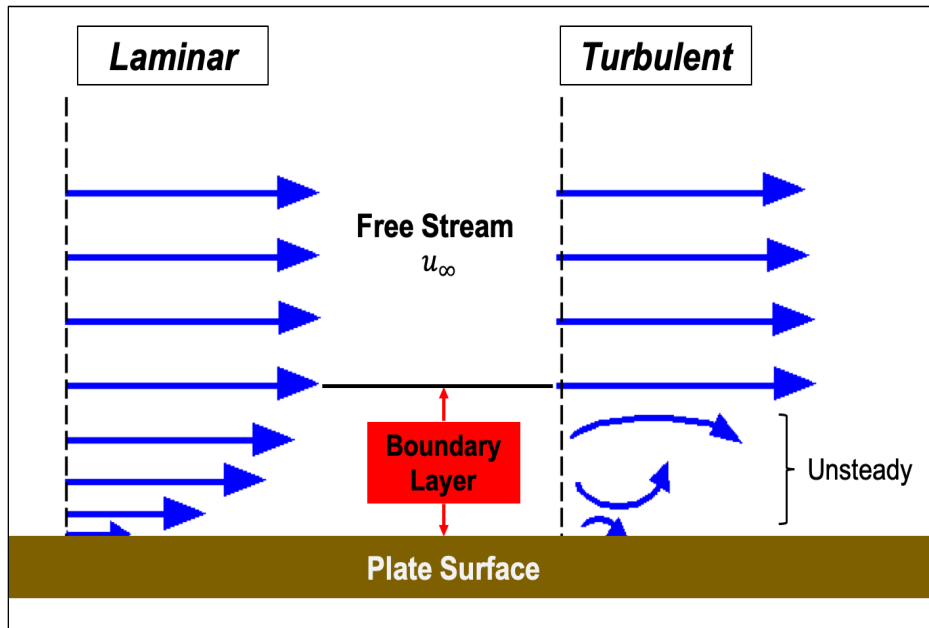


FIGURE 1.4: The velocity profile for laminar and turbulent boundary layers. Velocity is zero at the surface, i.e., no-slip condition [33].

solution for the mean velocity parallel to the wall and is valid for flows at high Reynolds numbers. Figure 1.5 represents the variation of u^+ with y^+ , where y^+ is the wall normal coordinate dimensionized with the friction velocity u_τ and kinematic viscosity ν as $y^+ = \frac{y u_\tau}{\nu}$ and u^+ is the dimensionless velocity as $u^+ = \frac{u}{u_\tau}$, where $u_\tau = \sqrt{\frac{\tau_w}{\rho}}$. In the viscous sublayer region, i.e., $y^+ < 5$, the velocity varies linearly with the wall normal coordinate as $u^+ = y^+$. In the buffer region, i.e., $5 < y^+ < 30$, the variation is $u^+ \neq y^+$ and $u^+ \neq \frac{1}{k} \ln y^+ + C^+$ and in the turbulent region, i.e., $30 < y^+ < 300$, $u^+ = \frac{1}{k} \ln y^+ + C^+$. Here, k is the Von Kármán constant, C^+ is a constant and τ_w is the wall shear stress.

The Prandtl's boundary layer equations are presented next. Prandtl showed that Navier-Stokes equations can be simplified to get approximate solution of boundary layer. According to Prandtl, flow can be divided into two regions, i.e., (i) region of boundary layer which lies in immediate neighborhood of solid boundary and within which about 99% of the velocity changes takes place and velocity gradient normal to the solid boundary is very large and in this region Navier-Stokes equations are valid and (ii) region outside boundary layer which constitutes the main body of flowing fluid with velocities of the order of free stream velocity, u_∞ and the flow in this zone is governed by potential flow (ideal fluid) theory.

For the analysis of the flow in the boundary layer, we present the boundary layer equation only, i.e., in region (i). Using scale analysis (or an order of magnitude analysis), it can be shown that the Navier-Stokes equations inside

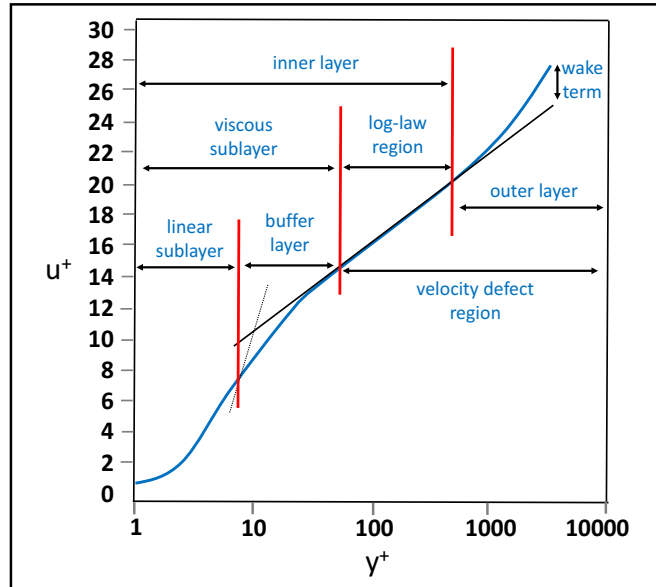


FIGURE 1.5: The normalized mean velocity profile in a turbulent boundary layer in semi-log coordinates which illustrates the various layers that make up the boundary layer [35].

a boundary layer reduce to,

$$\frac{\partial u}{\partial t} + u \frac{\partial u}{\partial x} + v \frac{\partial u}{\partial y} = -\frac{1}{\rho} \frac{\partial p}{\partial x} + \nu \frac{\partial^2 u}{\partial y^2}, \quad (1.14)$$

$$\frac{\partial p}{\partial y} = 0. \quad (1.15)$$

The continuity equation in 2-D steady flow is,

$$\frac{\partial u}{\partial x} + \frac{\partial v}{\partial y} = 0. \quad (1.16)$$

The above equations are known as Prandtl's Boundary Layer equations. In 1908, H. Blasius derived simplified solution by considering 2-D steady incompressible flow over a flat plate at zero angle of incidence with uniform flow u_∞ . According to Blasius, since the plate is flat and has negligible thickness and is uniform, $\partial p / \partial x$ must vanish. Hence, Prandtl's boundary layer equations becomes,

$$u \frac{\partial u}{\partial x} + v \frac{\partial u}{\partial y} = \nu \frac{\partial^2 u}{\partial y^2}, \quad (1.17)$$

along with equation 1.16.

Further, the boundary layer flow analysis based on momentum equation was derived by Von Kármán [36] by integrating the Prandtl's boundary layer equations. The momentum equation can be derived from the equation of motion by integration over the boundary layer thickness known as 'Momentum

Integral Equation' for boundary flow or 'Von Kármán Integral Equation'. The reader is referred to [1, 30, 36, 37] for more details.

Based on the boundary layer theory developed by Prandtl, various fundamental definitions related to the boundary layer are discussed below such as, the boundary layer thickness, displacement thickness, momentum thickness and the energy thickness.

The boundary layer thickness, δ is defined as the small distance from the boundary where velocity achieves a value which is very close ($\approx 99\%$) to the free stream velocity, u_∞ (This differentiates whether the fluid flow is within the boundary layer or it is beyond the boundary layer). δ depends upon Reynolds number (boundary layer thickness is much smaller for very high Reynolds numbers). The boundary layer thickness is sometimes called the velocity thickness or the velocity boundary layer thickness as it is defined depending upon the velocity distribution.

Blasius has given an expression for boundary layer thickness (δ) for laminar flow case, for incompressible fluid flow over flat plate (see Figure 1.3) as [30],

$$\frac{\delta}{x} = \frac{5.0}{\sqrt{Re_x}}, \quad (1.18)$$

The next important definition in boundary layer is called 'displacement thickness' as δ^* . The displacement thickness is defined as a distance measured perpendicular to the boundary by which the free stream is displaced to yield the same flow rate outside the boundary layer as the boundary layer equations yield and the expression for the displacement thickness is,

$$\delta^* = \int_0^\delta \left(1 - \frac{u}{u_\infty}\right) dy. \quad (1.19)$$

This expression connects the free stream velocity and the velocity in the boundary layer and the displacement thickness. When a fluid flow is considered, there is a need to deal with the momentum and the energy. There will also be a change in momentum due to the formation of the boundary layer and the expression called momentum thickness (θ) is defined as,

$$\theta = \int_0^\delta \frac{u}{u_\infty} \left(1 - \frac{u}{u_\infty}\right) dy. \quad (1.20)$$

The momentum thickness can be defined as the distance from actual boundary such that momentum flux through that distance at a velocity is same as the momentum deficit due to boundary layer formation. Experimentally, the boundary layer thickness (δ) is approximately three times the displacement thickness (δ^*) which is equal to 7.5 times the momentum thickness (θ) [30] for a flow past flat plate,

$$\delta \approx 3\delta^* \approx 7.5\theta. \quad (1.21)$$

The term called 'energy thickness' (δ_e) is defined as the thickness of a layer of fluid moving with velocity u_∞ that represent the loss of energy transport rate

as,

$$\delta_e = \int_0^\delta \frac{u}{u_\infty} \left(1 - \frac{u^2}{u_\infty^2}\right) dy. \quad (1.22)$$

Another important quantity in case of boundary layer is called shape factor (H) which is define as the ratio of the displacement thickness to the momentum thickness,

$$H = \frac{\delta^*}{\theta}, \quad (1.23)$$

and the skin friction coefficient, C_f , is calculated as the ratio of the wall shear stress to the dynamic pressure,

$$C_f = \frac{\tau_w}{\frac{1}{2}\rho u^2}. \quad (1.24)$$

1.5 State of the Art

Over the last decades, the role of turbulent boundary layers in numerous applications in the fields of atmospheric sciences, engineering and industry, have attracted the interest of researchers. Two fundamental approaches, spatial and temporal, have been used to analyze the incompressible as well as the compressible boundary layers. The spatially developing boundary layer (SBL) is characterized by inhomogeneity in the streamwise and wall-normal directions. This results in large computational requirements (e.g. [38, 39, 40, 41, 42, 43]), particularly in the case of three-dimensional direct numerical simulations (3-D DNS), where the full information of the flow is required. The spatial approach has been further considered in [40, 41, 44] to evaluate zero pressure gradient (ZPG) turbulent boundary layers from moderate Reynolds numbers up to computationally high Reynolds numbers. Under the presence of scalars, such as temperature, water vapor or chemical species, the resource requirements increase dramatically (e.g. [45]). Nevertheless, DNS seems to be inevitable whenever one is interested in details of the dynamics and very accurate global measures, like the skin-friction drag (e.g. [46]).

The simulations of the turbulent boundary layers at various discrete Reynolds numbers were carried out in [38] using a special coordinate transformation of the governing equations. Later, some studies were conducted in [47] using a temporal approach. This temporal approach has been used to investigate the compressible turbulent boundary layer in [48] revealing that for quasi-steady flows, the streamwise periodic boundary conditions were valid. DNS of the incompressible temporally developing turbulent boundary layer using no-slip and impermeable boundary conditions has been described in [49] and [50]. Their study demonstrate that the temporally and spatially developing boundary layers are similar in many aspects.

[51] modified the method given in [38] for generating the inflow data for 3-D simulation of the complex spatially developing boundary layers. Their approach was to extract instantaneous planes of the velocity data from an

auxiliary simulation of a zero pressure gradient boundary layer for a large eddy simulation (LES). The approach was further exhibited and used in [52] for producing inflow conditions for DNS. The authors introduced a set of additional steps that involved imposing at the inlet plane an appropriate spectrum for the turbulent kinetic energy and a condition for insuring that the statistical correction retains a non-vanishing magnitude. [42] presented the effects of the outer intermittent region of the boundary layer on the structures of the large scales of the flow by considering a long domain for their simulations. Microbubble-laden spatially developing turbulent boundary layers have been studied in [46]. In their study, bubble concentration gradient creates local positive velocity divergence which displaces the vertical structure to study the effect of Reynolds number on drag reduction. Temporal boundary layer have also been investigated using spatial approach in [43].

All these points make simulations of the spatially developing turbulent boundary layer both dynamically complex and numerically costly. Hence, to cut computational costs without simplifying the dynamics too much, the temporally developing boundary layer (TBL) has been suggested in several studies, like [47, 48, 49, 50, 53], where the streamwise inhomogeneity is removed by imposing periodic boundary conditions in both lateral directions (x and z). For DNS, the 3-D computational domain comprises a 'tower', i.e., the streamwise and spanwise extents are comparable to the maximum attainable boundary layer thickness. The 3-D temporal simulations have been proved to be cost effective and provide a reasonably accurate simplification of the spatially developing flow [49, 50, 53]. The temporal approach has been further used to analyze the incompressible turbulent boundary layer in [50] and the compressible turbulent boundary layer in [48]. The crucial aspect is the generation of the initial conditions (e.g. [51, 52, 44]).

Spatially developing turbulent boundary layers have been studied in [40] for the Reynolds number up to $Re_\theta = 2500$ based on momentum thickness and free-shear velocity presenting the statistics for the skin friction, mean velocity and turbulent fluctuations. Around the same time, [39] triggered the transition by intermittent localized disturbance arising from patches of isotropic turbulence introduced periodically from the free stream and investigated incompressible boundary layers with ZPG over a flat plate. Organization of hairpin vortex in the outer region of the turbulent boundary layer has been studied in [54]. Since these hairpin vortices can auto-generate and populate a significant fraction of the boundary layer, a detailed description of their transport mechanism is presented in the study. [55] have discussed an idealized assessment of Townsend's outer-layer similarity hypothesis for wall turbulence by performing DNS of turbulent channel flow to compare the effects of no-slip and shear-stress boundary condition. The simulations of fully turbulent channel with passive scalars has been done in [56] and [57, 58] provides velocity statistics in turbulent channel flow for high Reynolds numbers. [59] have carried out DNS of fully developed turbulent and oscillatory pipe flows. DNS for turbulent boundary layers under ZPG have been done in [41]. On comparing their results with experiments, they found that there was a large difference in skin friction coefficients, shape factor, mean profiles and fluctuation profiles

far into the sublayer and further analyzed tripping effects in their later study [44].

DNS of unbounded and unsteady turbulent convection for free convection over a smooth and heated plate have been done in [53]. The author has performed simulations for four different boundary conditions for temporally evolving free convection and reported interesting results. [45] studied the statistical behavior of the scalars in the outer region of the boundary layer by solving the governing equations using a fully spectral method. They also focused on DNS of spatially developing boundary layer over a flat plate under ZPG and computed the evolution of the passive scalars. Simulation performed using DNS to capture evolution inside a vertical plane was presented in [60] and the smoke cloud simulated using LES in [61].

Another important application is to control the flow for turbulent wall-bound flows. This is done by the mechanism of adding or removing mass through a porous surface, and has led to extensive studies of such kind of flows over the last decades. In case of adding mass, i.e., blowing, skin friction drag is reduced and removing mass, by suction, results in drag enhancement [62, 63, 64]. The fluid viscosity on the surface of vehicles causes skin friction drag on solid surfaces which is drastically increased by turbulent transition of the flow and has a large economical and ecological impact from the fuel consumption point of view. For reducing fuel consumption in major transportation systems, like aircrafts, trains and ships, the reduction of skin friction drag in turbulent flows is of great importance. Additionally, drag reduction for aerial vehicle has positive ramifications such as larger operational range, greater endurance and higher achievable speeds.

A variety of techniques have been devised for skin friction drag reduction and to control other flow properties. Various passive and active flow control techniques have been used. The passive control methods have been examined in several studies which include [65, 66, 67, 68]. However, the active control methods were found to be more attractive due to higher control performances and have been the focus in the studies from [69, 70, 71, 72, 73, 74]. A majority of the studies focus on internal flows, however, due to practical importance, external flows are investigated via blowing and suction.

The spatially developing turbulent boundary layer (SBL) with blowing or suction from a spanwise localized slot have been performed in [75] by DNS. The study by means of LES is done in [76]. In [77] drag reduction effects of blowing generated by a microblowing plate have been reported. An identity equation decomposing the skin friction drag into a laminar component and a turbulent component for canonical internal flows was introduced in [78]. This equation was latter used in several studies related to external flows and it shows a direct connection between the reduction of the Reynolds shear stress and friction drag reduction. A DNS of the spatially evolving turbulent boundary layer with uniform blowing and suction was performed in [63] and experimentally in [77, 79]. However, the DNS [63] was performed at a low Reynolds number which was only up to $Re_\theta = 300$. Recently the effect of uniform blowing and suction with the finite streamwise length of the uniform blowing or suction region have been studied in [64] reaching up to $Re_\theta = 2500$.

However, further investigations are still required for the effective and practical drag reduction in external flows. Additionally, a large computational domain is required due to the inhomogeneity in the streamwise and wall-normal directions in SBL canonical flow [38, 39, 40, 41, 42, 43] and hence, limited to small and moderate momentum Reynolds numbers. However, the Reynolds number needed in engineering applications is much higher [80, 81]. To achieve moderate Reynolds numbers, LES have been performed in [82] for $Re_\theta = 8300$ in case of SBL and in [64] for blowing and suction up to $Re_\theta = 2500$.

Even with the different methods available, there is a steady need for improving the simulation methods. For high Reynolds number flows, a very high grid resolution is required, which is computationally limited. To remove such limitations, a new development in this field, which is not based on the RANS or LES, is the one-dimensional turbulence (ODT) model.

In this thesis, the lower order simulation approach, ODT, is used as a stand-alone model, to investigate the incompressible temporally and spatially developing turbulent boundary layer. The study is further extended to investigate the effects of uniform blowing in spatially developing turbulent boundary layer. A good reason for validating the ODT temporal formulation is that there is ample comparison data. The reason for validating the ODT spatial formulation is because it is physically more relevant. ODT achieves major cost reduction, while covering the large Reynolds number regime as compared to the full 3-D simulations. The ODT model is based on two primary ingredients. Firstly, the governing equations are written in terms of two independent variables, i.e., temporal ODT formulations or spatial ODT formulation. Secondly, the non linear term is replaced by discrete “eddy events” that occur at various points in temporal and spatial ODT formulations. This distinctive feature of ODT is represented by a stochastic process modeling eddy motions via discrete mappings [28]. The diffusion effects are fully and deterministically resolved along a 1-D domain. The eddy size, the time, and the location of its occurrence are chosen as a function of the local energy. Further details for the formulation of the ODT model are discussed in the next chapter.

1.6 Organisation of the Manuscript

In order to present the relevant information in a continuous manner, this manuscript is structured into eight main chapters. The first two chapters aim to present a theory related to turbulent flow including turbulent boundary layer and the methodology adopted in the ODT model. The simulation set-up used for all the cases is discussed in Chapter 3 and the findings obtained from the numerical analyses carried out using ODT are presented in Chapter 4, 5, 6 and 7. The last chapter of the thesis summarises the major conclusions for all the different configurations and also presents an outlook. The organization of this thesis in the form of different chapters is as follows:

Chapter 1 provides an overview of the theory related to turbulent flows and turbulent boundary layer along with NS equations and various strategies to solve NS equations. A literature review is also given in order to provide a context to the physics related to the subject. It gathers essential study for a good understanding of the work done during this thesis.

Chapter 2 presents the methodology adopted for the development of the ODT model. This chapter discusses the various physical phenomena implemented in the model and describes in detail the mathematical and numerical aspects of these physical phenomena. The verification tests are presented for the credibility of the ODT model to carry out further studies.

Chapter 3 provides the simulation set-up for all the three configurations used in this thesis. These configurations are, temporally developing turbulent boundary layer (TBL), spatially developing turbulent boundary layer (SBL) and uniform blowing in SBL.

Chapter 4 aims to present the simulation results produced from the first configuration, i.e., the TBL configuration. This chapter includes the simulation results for four bulk Reynolds numbers at three momentum Reynolds numbers. The comparison of these results with the DNS data is also presented.

Chapter 5 presents the simulation results for the SBL configuration in comparison with the reference DNS and LES data. This chapter is divided into sections discussing about domain size sensitivity towards the statistics and simulation results for two bulk velocities. This chapter also shows the comparison between TBL and SBL configurations obtained from the ODT model, as well as the reference data.

Chapter 6 aims to extend the well validated spatial ODT formulation by applying uniform blowing on the bottom wall. The various velocity statistics as functions of wall-normal coordinate and several global properties for boundary layer varied with Re_θ are presented in this chapter in comparison with the reference LES data.

Chapter 7 provides the comparison between ODT results with the experiments conducted at BTU (chair of Prof. Egbers) in collaboration with the University of Lille, CNRS, France.

Lastly, Chapter 8 presents the conclusions and perspectives of the thesis. This chapter summarises all the key findings from the three ODT configurations used to carry out the simulations. Also, an outlook is given in this chapter.

Some details of the ODT model and analysis of the influence of the ODT

physical model parameters on various statistics produced by using the different configurations is given in Appendices in the end of the thesis.

1.7 In Closing

The description of the problem in case of turbulent flows with examples is discussed in this chapter. The Navier-Stokes equations obtained from RTT are presented along with simulation and modeling approaches, for example, DNS, LES and RANS. Further, theory related to boundary layer and various important parameters are summarized along with the state of the art. Finally, organisation of the thesis is given.

Chapter 2

ODT Model Formulation

In this chapter, we start with the general Navier-Stokes equations and finally reach to the ODT equations for spatial and temporal formulation. Next, the main features of the one-dimensional turbulence model are summarized. This includes the map-based formulation of eddy events, their selection, description of the model parameters and an overview. Further details of the ODT model are provided in Appendix B.

2.1 Introduction to the ODT Model

The One Dimensional Turbulence (ODT) model conceptually represents a line of sight through a turbulent flow field. The ODT model is a stand-alone model applicable in a situation where there is a direction of predominant large-scale gradient such as shear-driven flow (channel flow), buoyancy-driven flow (plumes) etc. Although the model has been implemented as sub-grid scale model in LES and RANS, much of its application has been stand-alone model and in this thesis also, the stand-alone ODT model has been utilized for investigating turbulent boundary layer.

There are many other applications which involve the inclusion of additional properties of the flow such as the temperature and the transport of species or impurities. Since ODT is a 1D domain model, so this is the major restriction of ODT. Although this restriction provides an opportunity for high grid resolution, so that, each scale can be resolved. As ODT can simulate every scale, it shows similar characteristic as DNS and can therefore be used for fundamental simulations of turbulence, providing the information needed to improve the model used by LES and RANS. The literature related to the ODT model and some of its applications are discussed next.

As explained in introduction, the ODT model enables affordable simulation of high Reynolds number turbulence over the full range of dynamically relevant length scales. This allows physically sound representation of interactions between turbulent advection and microphysical processes and the first formulation of the model was given in [29]. Another advantage of the model is the demonstration of a degree of commonality among turbulent flow

phenomena. This might not otherwise be readily apparent, by capturing diverse flow behaviors within a concise modeling framework based on broadly applicable empirical principles [28, 29]. The lack of a unique, kinematically and dynamically consistent analogy between the 1-D model formulation and the 3-D turbulent flow under consideration is however, an inherent limitation of the model [28].

The original formulation of ODT was given in [28] which was later extended to include pressure scrambling effects in [29]. The model was gradually extended for the simulation of variety of flows [29, 83, 84, 85, 86, 87, 88, 89, 90, 91, 92, 93, 94, 95, 96]. These are channel [90, 89, 95, 97], pipe [98, 99], multi-physics and reactive flows [92, 100, 93, 88, 101, 94, 102, 91] among others.

Further elaborating these studies, in [29] the approach is extended by treating the velocity as a three-component vector. A subgrid implementation of ODT is formulated in [83] which also discussed the potential advantages and limitation of the model. Based on the revised form of ODT, near-wall LES model was developed in [84] and was tested with turbulent channel flow for a wide range of Reynolds number. In [85], the model was generalized to incorporate variable-density effects where the model was used to analyze the planar mixing layers and compared the results with DNS data. The model was applied to turbulent convection over a wide range of physical parameter values and is found to be in good agreement with available experimental data in [86]. [87] also applied the model to simulate the stably stratified atmosphere boundary layer. The model was later on used to study the fluxes of heat and salt across unshered and shered double-diffusive interfaces in [88].

In a later study, mesh adaption was implemented to further enhance the performance of the model [89]. The computationally accessible scale range in spatial domain was increased and in the time domain, it enabled Lagrangian implementation of dilatation. ODT has been applied to study channel flow in [89, 90] and has also been applied to investigate multi-physics and reacting flows with complex chemical reactions on small scales in [91, 92, 93, 90]. ODT was used to study the radiatively induced entrainment in stratiform clouds driven by cloud-top cooling in [94]. The one-dimensional model is extended to investigate complex flow by embedding ODT line in a coarse 3D LES mesh and this multi-scale model is referred as ODTLES [103]. ODTLES is applied to wall-bounded flows in [104] and to turbulent flows through heated channels and ducts in [95]. Recently, ODT was used to analyse the suction boundary layers in [96, 105, 106, 107]. These studies have demonstrated that the model has the capability to produce results comparable with DNS in various fields.

Moreover, with these detailed applications, some important references which are, in general, important for boundary layer-type flows are highlighted here. In [89], a limited validation of a case involving forcing of a boundary layer flow is presented and [87] discusses stably-stratified boundary layers and in [84, 103, 102, 104, 108, 98] more complex cases were discussed. [96] presented an asymptotic suction boundary layer exhibiting a temporal evolution running into a statistical steady state. The work presented in [96] further motivated to investigate the effects of uniform blowing in SBL which inspired to

first validate the reduced order model for simple canonical TBL [109, 110, 111] and SBL [112] and then extent the investigation to the uniform blowing in SBL.

The main focus of the ODT model in this thesis is to investigate the idealized constant-property non-buoyant configuration of an incompressible temporally and spatially developing turbulent boundary layer for the first time which is further extended for uniform blowing in SBL. These presents important validation cases for the model.

The ODT model consists of two primary ingredients. Firstly, the governing equations are written in terms of two independent variables i.e. temporal ODT (T-ODT) formulations (t, y) and spatial ODT (S-ODT) formulation (x, y) . (In this thesis, the ODT aligned coordinate is referred as y and the streamwise coordinate as x .) Secondly, the discrete eddy events that occur at various points in (t, y) or (x, y) . A detailed discussion has been carried out for both the ingredients in further sections of this chapter.

2.2 Governing Equations for ODT

The bases for the development of numerical simulations are the conservation of the mass and momentum. For this purpose, it is useful to write the equations governing the flow for a fluid [1, 113].

Before discussing the key modeling concept, i.e., the triplet map and kernel transformation, several forms of governing equations are summarised first in Lagrangian and Eulerian frame of reference for T- and S-ODT. The equation and explanation in this section is taken from [11] and hence, for details, the reader is referred to [11].

ODT formulation can be broadly classified into two categories. Firstly, the temporal developing flows (T-flow), where (t, y) are chosen as the independent variable. Secondly, the spatial developing flows (S-flow), where (x, y) are chosen as the independent variables. We have Eulerian and Lagrangian variants of ODT for both the categories [11]. Earlier ODT was described with reference to T-flow which was later formulated to S-flow due to its extended applications. As both the formulations are used in this thesis, the governing equations for the two categories are discussed next.

2.2.1 Temporal ODT Evolution Equations

In this section the Eulerian and the Lagrangian forms of governing equations are presented. As mentioned above, the ODT equations will describe evolution of various quantities on a line oriented on the y -direction and evolution in time i.e. (t, y) [11].

Eulerian Temporal Form

Retaining only (t, y) as independent variables, we get from equation 1.5,

$$\frac{\partial \rho \psi}{\partial t} = -\frac{\partial \rho \psi v}{\partial y} - \frac{\partial \Phi_{\psi,y}}{\partial y} + \sigma_{\psi}, \quad (2.1)$$

where v is the local mass-averaged fluid velocity in y -direction and $\Phi_{\psi,y} = \Phi_{\psi} \cdot \vec{y}$ represent the component of Φ_{ψ} in y -direction. The equation can be solved for ρ , streamwise momentum ρu and lateral momentum ρv (relevant for this thesis) by using $\psi = 1$, u and v , respectively [11].

Lagrangian Temporal Form

Retaining only (t, y) as independent variables, we get from equation 1.4,

$$\rho \frac{d\psi}{dt} = -\frac{\partial \Phi_{\psi,y}}{\partial y} + \sigma_{\psi}, \quad (2.2)$$

and the equation can be written in integral form as,

$$\frac{d}{dt} \int_{y_1(t)}^{y_2(t)} \rho \psi dy = \int_{y_1(t)}^{y_2(t)} \left(-\frac{\partial \Phi_{\psi,y}}{\partial y} + \sigma_{\psi} \right) dy. \quad (2.3)$$

These are the most often used forms for temporally evolving ODT simulations (also for this thesis). (The quantities are evaluated at y_1 and y_2 respectively.) In this frame of reference $v(t)$ (the volume of a finite material element), $S(t)$ (its associated surface) changes with time according to the v (the local mass-averaged velocity). Ordinary differential equations (ODEs) may be solved to determine the locations of the cell centroids (and faces) for position of cell centroids or faces by [11],

$$\frac{dy}{dt} = v, \quad (2.4)$$

here v is the y -component of velocity. To get v i.e., the lateral velocity component which is required in equation 2.4, we can solve equation 2.2 for $\psi = v$. If we put $\psi = 1$ (enforcing continuity) in equation 2.3, we get [11],

$$\frac{d}{dt} \int \rho dy = \frac{dm}{dt} = 0. \quad (2.5)$$

The right hand side term in above equation states that mass is constant. Thus, solving equation 2.4 evolves the size of the control volume that enforces continuity. However, the y and z components of velocity are used as repositories of kinetic energy rather than advective velocities. Hence, even if v is solved, rather than solving equation 2.4 to determine the limits for the integrals in equation 2.3, equation 2.5 is utilized to describe the change in cell size and is discretized using a first-order time approximation as [11],

$$(\Delta y)^{n+1} = \frac{\rho^n (\Delta y)^n}{\rho^{n+1}}. \quad (2.6)$$

Note that the time coordinate is transformed to an equivalent spatial coordinate by solving an ODT in one of two ways,

$$\frac{dx}{dt} = \bar{u}, \quad (2.7)$$

$$\frac{dx}{dt} = u, \quad (2.8)$$

here u is the x (streamwise) component of the velocity. The downstream position for the ODT domain is determined by choosing average velocity \bar{u} from equation 2.7 and equation 2.8 uses the local velocity at each point on the ODT line to solve a position equation for each point [11].

2.2.2 Spatially Evolving ODT Equations

It is advantageous in some situations to formulate governing equations by considering (x, y) as independent variables because of the ambiguity in determining a downstream location (x) in the temporally evolving approach. The spatial approach has been used for this thesis as well. In this section, Eulerian and Lagrangian equations sets have been presented that uses (x, y) as independent variables [11].

Eulerian Spatial Form

Retaining the independent variables, (x, y) in equation 1.5, we get the spatially evolving governing equations as,

$$\frac{\partial \rho \psi u}{\partial x} = -\frac{\partial \rho \psi v}{\partial y} - \frac{\partial \Phi_{\psi, x}}{\partial x} - \frac{\partial \Phi_{\psi, y}}{\partial y} + \sigma_{\psi}. \quad (2.9)$$

The above equation is an elliptic equation and an elliptic flow is governed by a second order PDE in which there is no time-dependence, only steady state spatial flow, and requires boundary conditions, for example, 2D Poisson equation. However, in case of S-ODT, there are no boundary conditions which can be enforced on streamwise direction, only an initial condition. So the flow is parabolic, which also explains why we can not have negative velocities. It is only possible to start from an initial condition and backward advancement in streamwise direction is not possible. Hence, by neglecting the second derivative term in above equation (second term on right hand side), gives a convection-diffusion equation given below which can be solved using the method of lines for the streamwise fluxes, $\rho \psi u$,

$$\frac{\partial \rho \psi u}{\partial x} = -\frac{\partial \rho \psi v}{\partial y} - \frac{\partial \Phi_{\psi, y}}{\partial y} + \sigma_{\psi}. \quad (2.10)$$

By putting $\psi = 1$, we get continuity equation [11],

$$\frac{\partial \rho u}{\partial x} + \frac{\partial \rho v}{\partial y} = 0. \quad (2.11)$$

The complete set of equations will be equations 2.11 and 2.10 with $\psi = u$ and v (used in this thesis). Alternately equation 2.10 can be solved,

$$\frac{\partial \psi}{\partial x} = -\frac{1}{\rho u} \left[\rho v \frac{\partial \psi}{\partial y} + \frac{\partial \Phi_{\psi,y}}{\partial y} - \sigma_{\psi} \right], \quad (2.12)$$

along with an alternate form of equation 2.11,

$$\frac{\partial \rho}{\partial x} = -\frac{1}{u} \left[\rho \frac{\partial u}{\partial x} + \frac{\partial \rho v}{\partial y} \right]. \quad (2.13)$$

If we substitute $\psi = u$ in equation 2.12, we get the term $\partial u / \partial x$. The complete set of equations are 2.13 and 2.12 with different definitions of ψ along with an equation of state [11] (not discussed here because it is not used for this thesis).

Lagrangian Spatial Form

Taking (x, y) as independent variables, we can write,

$$\frac{d}{dx} = \frac{\partial}{\partial x} + \frac{dy}{dx} \frac{\partial}{\partial y} = \frac{\partial}{\partial x} + \frac{v}{u} \frac{\partial}{\partial y}. \quad (2.14)$$

Equation 2.12 can be rewritten in Lagrangian form by using equation 2.14 as,

$$\frac{d\psi}{dx} = -\frac{1}{\rho u} \left[\frac{\partial \Phi_{\psi,y}}{\partial y} - \sigma_{\psi} \right]. \quad (2.15)$$

This equation is applicable to all definitions of ψ except continuity equation, $\psi = 1$. Therefore we can get the Lagrangian form of the continuity equation by putting (ρu) in equation 2.14 and using equation 2.11 [11],

$$\frac{d\rho u}{dx} = \frac{v}{u} \frac{\partial \rho u}{\partial y} - \frac{\partial \rho v}{\partial y}. \quad (2.16)$$

The integral form of equation 2.15 can be written as,

$$\frac{d}{dx} \int_{y_1(x)}^{y_2(x)} \rho \psi u dy = \int_{y_1(x)}^{y_2(x)} \left(-\frac{\partial \Phi_{\psi,y}}{\partial y} + \sigma_{\psi} \right) dy. \quad (2.17)$$

If Leibniz' rule is applied to equation 2.17, then we get (equation 2.19 is used for the transformation in equation 2.18),

$$\begin{aligned}
\frac{d}{dx} \int_{y_1(x)}^{y_2(x)} \rho \psi u dy &= \rho_2 \psi_2 u_2 \frac{dy_2}{dx} - \rho_1 \psi_1 u_1 \frac{dy_1}{dx} + \int_{y_1(x)}^{y_2(x)} \frac{\partial \rho \psi u}{\partial x} dy \\
&= \rho_2 \psi_2 v_2 - \rho_1 \psi_1 v_1 + \int_{y_1(x)}^{y_2(x)} \frac{\partial \rho \psi u}{\partial x} dy \\
&= \int_{y_1(x)}^{y_2(x)} \left(\frac{\partial \rho \psi u}{\partial x} + \frac{\partial \rho \psi v}{\partial y} \right) dy, \tag{2.18}
\end{aligned}$$

where subscripts 1 and 2 indicate that the quantities are evaluated at y_1 and y_2 respectively. Equation 2.18 shows that equation 2.10 and 2.17 are equivalent and also equation 2.15 and 2.17 are equivalent. An equation for y is required to solve equation 2.15 in order to determine the position of the Lagrangian system as [11],

$$\frac{dy}{dx} = \frac{v}{u}, \tag{2.19}$$

with u and v as the local fluid velocities in the x and y directions, respectively. The position is required to determine the limits on the integral in equation 2.17 for each discrete volume element, if solving the integral form of the Lagrangian evolution equations whereas, to solve the differential form of the equations, via, e.g. a finite difference method, the position is required to evaluate the fluxes and their divergences. The role of the velocity in both the cases is to maintain the proper definition of the Lagrangian control volume. Equation 2.15 and 2.19 forms a complete set of equations together with an equation of state. The Lagrangian position (y) is obtained via equation 2.17 with $\psi = 1$ (instead of solving equation 2.19) as [11],

$$\frac{d}{dx} \int \rho u dy = 0. \tag{2.20}$$

A first-order time discretization of the above equation results,

$$(\Delta y)^{n+1} = \frac{(\rho u \Delta y)^n}{(\rho u)^{n+1}}, \tag{2.21}$$

with n as the solution at the streamwise position x_n and $n + 1$ at x_{n+1} . Note that to determine a residence time in spatially developing formulation (e.g., in order to advance a chemical-kinetic mechanism), we need to solve one of the below equations [11],

$$\frac{dt}{dx} = u^{-1}, \tag{2.22}$$

$$\frac{dt}{dx} = \bar{u}^{-1}. \tag{2.23}$$

Equation 2.22 accounts for the variation of residence time due to variation in u . Whereas, equation 2.23 obtains a characteristic residence time for the domain with the assumption that it moves with some characteristic velocity u .

2.3 Formulation of the Eddy Events

The distinctive feature of the ODT model is coupling of a stochastic implementation of 1-D eddy events (EE) to the deterministic solution of 1-D diffusion evolution equation. The effects of turbulent transport due to eddies on the 1-D property profile of the flow are modeled by the eddy events. The deterministic diffusion process catches up to the implemented eddy events.

These events occur through the instantaneous displacement of the fluid elements to represent a turbulent stirring motion and this process modifies any property profile over the ODT line interval $[y_0, y_0 + l]$, with y_0 as the lower edge of a notional eddy and l its size. The eddy events are implemented by using the triplet map which induces fluid displacement and fulfills two other fundamental requirements: (i) the mapping is measure preserving, (ii) it does not introduce spatial discontinuities.

The triplet map essentially takes a property profile in an eddy region and replaces it with three copies of the original in which each copy is compressed by a factor of three and the middle copy is inverted in order to avoid discontinuities shown in Figures 2.1 and 2.2. This correlate with a physical mapping, that is, an advective, transport of fluid from a given location $f(y)$ to a new location y and the mapping function $f(y)$ is given as [28],

$$f(y) = y_0 + \begin{cases} 3(y - y_0), & y_0 \leq y \leq y_0 + l/3 \\ 2l - 3(y - y_0), & y_0 + l/3 \leq y \leq y_0 + 2l/3 \\ 3(y - y_0) - 2l, & y_0 + 2l/3 \leq y \leq y_0 + l \\ (y - y_0), & \text{otherwise.} \end{cases} \quad (2.24)$$

To represent the effects of fluctuating pressure gradient forces, the mapped velocity field, $\mathbf{u}(f(y), t)$ is accomplished with the aid of a kernel function and a coefficient vector $\mathbf{c} = (c_1, c_2, c_3)^T$ [29]. The mapped velocity for S-ODT is $\mathbf{u}(f(y), x)$, however, here the equation are only presented for T-ODT to avoid redundancy. The kernel function is defined as $K(y) = y - f(y)$,

$$EE: \quad \mathbf{u}(y, t) \rightarrow \mathbf{u}(f(y), t) + \mathbf{c}K(y) \quad (2.25)$$

There is no uniquely preferable functional form noted for the kernel function $K(y)$. It is convenient to relate it to the fluid displacement induced by the mapping $f(y)$, that is, $K(y) = y - f(y)$ [28]. An important physical constraints is satisfies by this choice which makes the kernel function nonzero only in the eddy-size interval $[y_0, y_0 + l]$ and it integrates to zero which ensures that there are no artificial momentum sources regardless of the selection of the (Cartesian) components c_i , where $i \in \{1, 2, 3\}$. However, care has to be

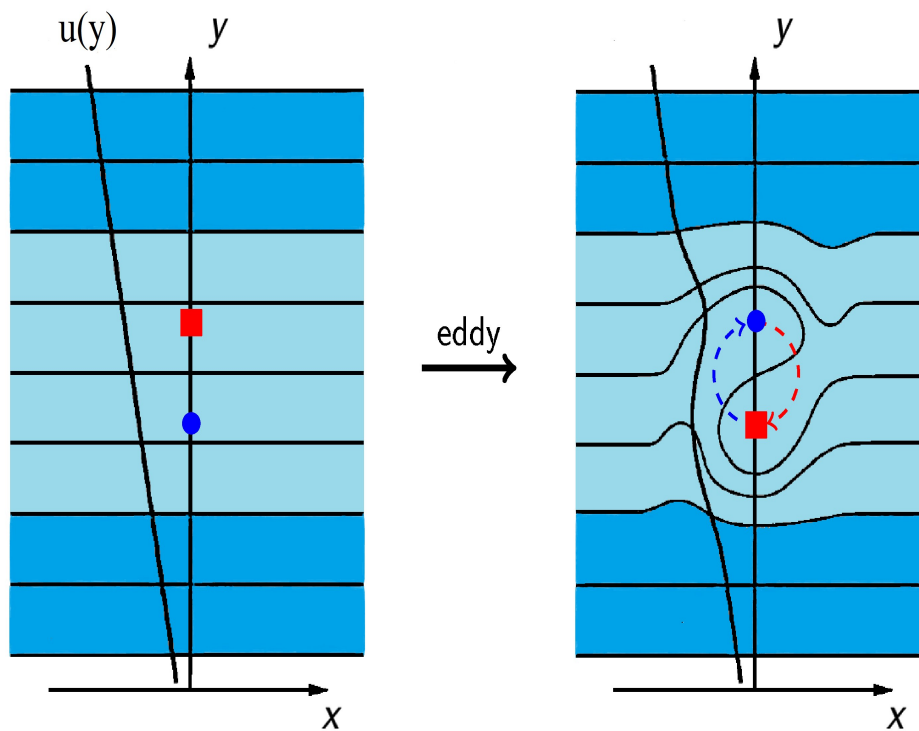


FIGURE 2.1: Schematic of an eddy turnover by displacement of the fluid elements (shown with red square and blue circle) to represent turbulent stirring motion [114].

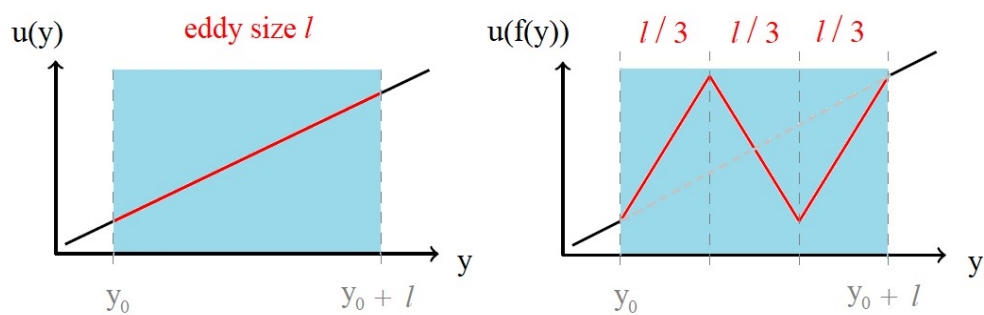


FIGURE 2.2: Schematic of 1-D representation of a scalar profile before and after implementing the triplet map [114].

taken in the selection of c_i to ensure that the kinetic energy is not artificially generated but only redistributed among the velocity components.

To determine the coefficients c_i , the change of the kinetic energy ΔE_i in the i th velocity component due to the application of Eq. 2.25 is considered [29] next. This change of the kinetic energy is given as,

$$\Delta E_i = \frac{\rho}{2} \int_{y_0}^{y_0+l} \left(\left[u_i(f(y), t) + c_i K(y) \right]^2 - u_i^2(y, t) \right) dy \quad (2.26)$$

When the sum of the individual contributions ΔE_i vanishes, i.e., $\Delta E_1 + \Delta E_2 + \Delta E_3 = 0$ then Energy is conserved and it constrains the selection of c_i because each velocity component has a finite amount of energy that can be added and removed to the other two components.

The extractable kinetic energies ($-\Delta E_i$) are maximized with respect to the c_i to find an appropriate energy scale which yields the maximum extractable energy, Q_i , for component i as,

$$Q_i = \frac{1}{2\hat{K}} \rho l u_{i,K}^2, \quad (2.27)$$

where the two kernel-weighted quantities $u_{i,K}$ and \hat{K} are,

$$u_{i,K} = \frac{1}{l^2} \int_{y_0}^{y_0+l} u_i(f(y), t) K(y) dy \quad (2.28)$$

and,

$$\hat{K} = \frac{1}{l^3} \int_{y_0}^{y_0+l} K^2(y) dy. \quad (2.29)$$

The model parameter α has been introduced considering that the pressure fluctuations may not be universal. The pressure fluctuations do not necessarily imply a maximization of the inter-component kinetic energy transfer. α controls the fraction of each of the extractable (available) kinetic energies that is actually used for the redistribution. This yields,

$$\Delta E_i = -\alpha Q_i + \frac{\alpha}{2} Q_j + \frac{\alpha}{2} Q_k, \quad (2.30)$$

where (ijk) represents cyclic permutations of (123) . The model parameter α varies in the range $[0, 1]$ with $\alpha = 0$ means there is no transfer of the kinetic energy, $\alpha = 2/3$ means equipartition of the energies and $\alpha = 1$ represents maximal transfer of the kinetic energy.

Equations 2.27 and 2.30 are inserted in Eq. 2.26 to obtain the coefficients c_i encountered in Eq. 2.25 and which gives,

$$c_i = \frac{1}{\hat{K}l} \left(-u_{i,K} + \text{sgn}(u_{i,K}) \sqrt{(1-\alpha)u_{i,K}^2 + \frac{\alpha}{2}u_{j,K}^2 + \frac{\alpha}{2}u_{k,K}^2} \right), \quad (2.31)$$

where sgn represents the sign function which is needed for consistency of the original single-velocity formulation [28] with the ODT vector formulation [29].

2.4 Eddy Event Selection

For the above formulated eddy events, it is essential to determine the location y_0 , size l , and time of occurrence t for T-ODT and streamwise position of occurrence x for S-ODT. These stochastic variables are governed by an 'eddy rate distribution' $\lambda(y_0, l, t)$ or $\lambda(y_0, l, x)$ [28] and $\lambda(y_0, l, t) dy_0 dl dt$ specifies the number of eddies in the size range $[l, l + dl]$, position range $[y_0, y_0 + dy_0]$ and during a time interval $[t, t + dt]$. Note that the time interval for S-ODT is replaced by a space interval $[x, x + dx]$. Constructing λ is not hard, sampling the eddy PDF, which is defined in terms of λ is hard. The actual implementation constructs λ directly for each eddy event, but we do not know whether those eddy events make sense because we do not construct the actual eddy PDF, which is based on λ . The eddy PDF is λ/Λ , where Λ is the total rate of all eddies. But to get that would require evaluating λ for all sizes and locations, and that is expensive to do considering that it changes as soon as an eddy event or diffusive advancement occurs. The form for λ is given by,

$$\lambda(l, y_0, t) = \frac{C}{l^2 \tau(l, y_0, t)}. \quad (2.32)$$

In this equation, τ represents the eddy turnover time. It is related to the instantaneous flow state. C is a model parameter which is related to the overall rate of eddy events in the flow and it needs to be estimated for a given flow configuration as the turbulence intensity in general depends on the prescribed forcing mechanism.

The spatial analogue of eddy rate distribution explained above, λ can be rewritten as [28, 85, 98],

$$\lambda(l, y_0, x) = \frac{C \tilde{v}_\epsilon}{l^2 \bar{\xi}(l, y_0, x)}. \quad (2.33)$$

In this equation, $\bar{\xi}$ is the eddy streamwise increment related to the instantaneous flow state and \tilde{v}_ϵ is the Favre averaged velocity in the eddy region.

To calculate τ in Eq. 2.32, the kinetic energy per unit mass l^2/τ^2 contained in the eddy motion is considered in T-ODT and for S-ODT it becomes $l^2 \tilde{v}_\epsilon^2 / \bar{\xi}^2$. This energy should be similar to the extractable kinetic energy given in Eqs. 2.26 and 2.27. Therefore, maintaining consistency of the formulation it yields,

$$\frac{l^2}{\tau^2} \sim \sum_{i=1}^3 u_{i,K}^2 - Z \frac{v^2}{l^2}, \quad (2.34)$$

$$\frac{l^2 \tilde{v}_\epsilon^2}{\bar{\xi}^2} \sim \sum_{i=1}^3 u_{i,K}^2 - Z \frac{v^2}{l^2}, \quad (2.35)$$

for T-ODT and S-ODT, respectively. Summation of $u_{i,K}^2$ in the above equation (instead of ΔE_i) indicates the fact that the total extractable kinetic energy does not depend on model parameter α representing the inter-component energy transfer. The last term on right hand side of Eq. 2.34 represents the damping

effects of the viscosity, and Z is a model parameter which takes values larger or equal to zero. When $Z = 1$, the eddy events below the Kolmogorov scale are suppressed effectively [28] since such small eddy events do not contribute to the turbulent transport, neglecting them improves the numerical efficiency.

Once the location y_0 and size l of an eddy event have been selected, the eddy time scale τ for T-ODT and eddy streamwise increment ξ for S-ODT, respectively, is computed from the instantaneous velocity profiles $u_i(y, t)$ ($u_i(y, x)$) as,

$$\frac{1}{\tau} = \sqrt{\frac{1}{l^2} \sum_{i=1}^3 u_{i,K}^2 - Z \frac{v^2}{l^4}}, \quad (2.36)$$

$$\frac{1}{\xi} = \frac{1}{\bar{v}_\epsilon} \sqrt{\frac{1}{l^2} \sum_{i=1}^3 u_{i,K}^2 - Z \frac{v^2}{l^4}}. \quad (2.37)$$

The eddy time scale τ and the mean sampling time scale τ_s are compared to obtain the acceptance probability $p_a = (\tau/\tau_s)^{-1} < 1$ for T-ODT and $(= \xi/\xi_s)^{-1} < 1$ for S-ODT of a physically plausible eddy event. For this purpose, τ and ξ needs to be computed at a specific instant or streamwise position, respectively, that is sampled with the aid of a marked Poisson process. Eddy events are assumed to be independent of each other in this process, such that time or streamwise increment between two such events can be sampled economically from an exponential distribution but the rejection process introduces a dependence as eddy acceptance depends on property profiles that are affected by previous eddy events. See [28] for more details.

The eddy selection process is schematised in Figure 2.3. This algorithm includes an exception for the case the time-step dt becomes too large before a viable eddy is found, where the governing equations of the flow will be advanced without implementing an eddy. Further details of the eddy selection process are provided in Appendix B.

Sometimes it is important to suppress the unphysically large eddy events which may occur seldomly in the sampling procedure. To suppress these eddies, a large-eddy suppression (LS) is often used. A simple suppression based on the fraction of the domain length [89, 98] may be sufficient for confined flows, like channel or pipe flows and this suppression is termed as frac domain. The elapsed-time LS mechanism [100, 92] is preferred for free shear flows, such as jets, in which only eddy events satisfying $\tau \leq \beta_{LS} t$ are allowed, ($l \leq \beta_{LS} x$ for S-ODT) where t is the current simulation time and β_{LS} a model parameter [100, 115]. For boundary layer type flows, the shear can be highly concentrated in a thin layer close to the wall, although the associated shear in an eddy is nearly zero in almost all parts of its size range, such unphysical eddy event may be accepted and can be suppressed with the two-thirds LS mechanism [85]. In the two-thirds mechanism, the eddy interval is subdivided into three equidistant subsections with the purpose of verifying that the eddy is energetically feasible in at least two of these subsections.

2.5 Numerical Basics

This section presents a short overview of the numerical basics used in the ODT code. The code is based on the finite volumes method. A finite volume method uses the integral form of the conservation equations where the calculation of the solution (the simulation domain) is divided into arbitrary control volumes. The finite volume method integrates the solution within these control volumes. Whereas, in the finite difference method, the unknown continuous solution of the variable is approximated by the conservation laws at specific grid points. For more detailed discretization, the reader is referred to [116, 117].

The starting point is the Lagrangian transport equations derived from the Reynolds transport theorem as explained in [89] and also in previous chapter of the thesis. To be consistent, the same terminology is followed as done in [89]. The Reynolds transport theorem (RTT) in terms of an intensive variable (equation 1.1 from previous chapter), i.e., some quantity per unit mass, ψ , is written as,

$$\frac{d}{dt} \int_{v_\psi(t)} \rho \psi dV = \int_{V(t)} \frac{\partial \rho \psi}{\partial t} dV + \int_{S(t)} \rho \psi \mathbf{v}_\psi \cdot \mathbf{n} dS. \quad (2.38)$$

Here, the equations are presented for individual control volumes on the computational grid with quantities evaluated at the cell center. The quantities evaluated on cell faces are denoted with subscript e and w representing the right and left cell faces, respectively. The spatial derivatives appearing in the governing equations are evaluated at cell faces using first-order central differences such that, for cell i ,

$$\left(\frac{d\phi}{dy} \right)_{i,e} = \frac{(\phi_{i+1} - \phi_i)}{\frac{1}{2}(\Delta y_{i+1} + \Delta y_i)}, \quad (2.39)$$

for some variable ϕ . Now, for the continuity equation, using $\psi = 1$ in Equation 2.38, so that the system encloses the mixture mass and the system boundary moves with the mass average velocity and $\mathbf{v}_\psi = 0$. As there is no mass source term, Eq. 2.38 becomes,

$$\frac{d}{dt} \int_{v(t)} \rho dV = 0. \quad (2.40)$$

The equation for uniform properties inside control volumes and in 1D is,

$$\frac{d}{dt} (\rho \Delta y) = 0 \Rightarrow \rho \Delta y = C. \quad (2.41)$$

For momentum equation, $\psi = \mathbf{v}$ is taken. The system and control volume velocities are the same and $\mathbf{v}_\psi = 0$. Hence, equation 2.38 becomes,

$$\frac{d}{dt} \int_{v(t)} \rho \mathbf{v} dV = \frac{d}{dt} \int_{V(t)} \rho \mathbf{v} dV. \quad (2.42)$$

The Lagrangian conservation law is,

$$\frac{d}{dt} \int_{v(t)} \rho \mathbf{v} dV = \int_{S(t)} \mathbf{F}_{ext} dS = - \int_{S(t)} (p \mathbf{l} + \underline{\boldsymbol{\tau}}) \cdot \mathbf{n} dS. \quad (2.43)$$

Substituting above equation in Eq.2.42 and integrating over the control volume gives the u , v and w momentum equations. The u – momentum equation is given below and v – and w – momentum equations can be written following similar analogy,

$$\frac{du}{dt} = -\frac{1}{\rho \Delta y} (\tau_{yy,e} - \tau_{yy,w}), \quad (2.44)$$

where, the stress tensor is modeled as,

$$\tau_{yy} = -\mu \frac{du}{dy}. \quad (2.45)$$

Now, Equation2.44 can be written as,

$$\frac{du}{dt} = \frac{1}{\rho \Delta y} \left[\left(\mu \frac{du}{dy} \right)_e - \left(\mu \frac{du}{dy} \right)_w \right]. \quad (2.46)$$

Equation2.39 can be used in Eq.2.46 for further simplification. Time integration is performed explicitly using either the first-order Euler method, or a second-order trapezoid method also known as modified Euler method [118]. These methods are in the class of Runge-Kutta methods. So, Equation2.46 is solved as,

$$\frac{u^{n+1} - u^n}{\Delta t} = \frac{1}{\rho \Delta y} \left[\left(\mu \frac{du}{dy} \right)_e - \left(\mu \frac{du}{dy} \right)_w \right]^n, \quad (2.47)$$

where superscript n denoted the time advancement which is from t_n to t_{n+1} . Above equation can be written as,

$$u^{n+1} = u^n + \frac{\Delta t}{\rho \Delta y} \left[\left(\mu \frac{du}{dy} \right)_e - \left(\mu \frac{du}{dy} \right)_w \right]^n, \quad (2.48)$$

$$u^{n+1} = u^n + \frac{\Delta t}{\rho \Delta y} \left[\mu \frac{u_{i+1} - u_i}{y_{i+1} - y_i} - \mu \frac{u_i - u_{i-1}}{y_i - y_{i-1}} \right]^n. \quad (2.49)$$

2.6 Statistical Quantities in ODT Realizations

A detailed description between DNS and ODT statistical quantities is given in [29]. For this purpose, the mean ODT and Reynolds-Averaged Navier-Stokes (RANS) momentum equations are compared. This section presents the Reynolds stresses and Turbulent Kinetic Energy (TKE) budgets for T-ODT. A similar analogue is followed for S-ODT.

As detailed above, a mathematical representation of the generalized T-ODT momentum evolution equation is,

$$\frac{\partial u}{\partial t} = -\frac{1}{\rho} \frac{\partial \bar{p}}{\partial x} + \nu \frac{\partial^2 u}{\partial y^2} + M_1 + T_1 + S_1. \quad (2.50)$$

M_1 represented the effect of the triplet map, S_1 for pressure scrambling and T_1 for turbulent transport contribution in the ODT velocity component u . For convenience, $S_1 = 0$ due to absence of pressure scrambling effects in the mean Navier-Stokes momentum equation. The steady state channel flow RANS momentum equation is,

$$0 = -\frac{1}{\rho} \frac{\partial \bar{p}}{\partial x} + \nu \frac{\partial^2 \bar{u}}{\partial y^2} - \frac{\partial \overline{u'v'}}{\partial y}, \quad (2.51)$$

and the mean T-ODT momentum evolution equation is,

$$\frac{\partial \bar{u}}{\partial t} = -\frac{1}{\rho} \frac{\partial \bar{p}}{\partial x} + \nu \frac{\partial^2 \bar{u}}{\partial y^2} + \overline{M_1} + \overline{T_1}. \quad (2.52)$$

Comparing the above two equations gives Reynolds stress component $\overline{u'v'}$ in the T-ODT case as,

$$-\overline{u'v'} = \int_{y^*}^{\infty} (\overline{M_1} + \overline{T_1}) dy. \quad (2.53)$$

$\overline{u'v'} = 0$ at $y = \infty$, y^* refers to the position of the wall and $\overline{M_1} + \overline{T_1}$ is defined by changes in the velocity profiles due to eddies which can be constructed based on the cumulative sum of changes in the u velocity profiles due to eddies. This can be represented by considering the stochastic interaction in Eq.2.50 only, within a given interval of time Δt in which an eddy is deemed to occur as,

$$\frac{\Delta u}{\Delta t} = M_1 + T_1. \quad (2.54)$$

The Reynolds stress component $\overline{u'v'}$ for S-ODT is also given by Eq.2.53, however, in S-ODT, $\overline{M_1} + \overline{T_1}$ is calculated accounting for the changes in the u^2 velocity profile as,

$$\frac{\Delta u^2}{\Delta x} = M_1 + T_1. \quad (2.55)$$

Now, Equation2.50 is multiplied by the u velocity component representing the kinetic energy of this component. This is done to evaluate the TKE Budgets and it gives,

$$\frac{1}{2} \frac{\partial u^2}{\partial t} = -\frac{u}{\rho} \frac{\partial \bar{p}}{\partial x} + \nu u \frac{\partial^2 u}{\partial y^2} + M_{11} + T_{11} + S_{11}, \quad (2.56)$$

which is further simplified as,

$$\frac{\partial u^2}{\partial t} = -\frac{2u}{\rho} \frac{\partial \bar{p}}{\partial x} + \nu \frac{\partial^2 u^2}{\partial y^2} - 2\nu \left(\frac{\partial u}{\partial y} \right)^2 + M_{11} + T_{11} + S_{11}, \quad (2.57)$$

where M_{11} , T_{11} and S_{11} are the effect of mapping, transport and pressure scrambling, respectively to the kinetic energy of the u velocity component. Further, Equation 2.52 is multiplied with $2\bar{u}$ and Equation 2.57 is averaged to get an equation for the average of the square of the fluctuation velocity u' as,

$$\frac{\partial \overline{u'^2}}{\partial t} = \nu \frac{\partial^2 \overline{u'^2}}{\partial y^2} - 2\nu \overline{\left(\frac{\partial u'}{\partial y} \right)^2} + \left[\frac{\partial}{\partial y} (I_{11} - 2\bar{u}I_1) + \overline{S_{11}} \right] + 2I_1 \frac{\partial \bar{u}}{\partial y}, \quad (2.58)$$

with $I_1 = \int (\overline{M_1} + \overline{T_1}) dy$, $I_{11} = \int (\overline{M_{11}} + \overline{T_{11}}) dy$ and $\overline{u^2} - \bar{u}^2 = \overline{u'^2}$.

The equations for $\overline{v'^2}$ and $\overline{w'^2}$ are similar to Eq. 2.58. Eq. 2.58 is then compared to the generalized TKE equation (see Appendix A) in a Cartesian Coordinate system to give the TKE budgets for production \mathcal{P} and dissipation ϵ as,

$$\mathcal{P} = \sum_k I_k \frac{\partial \bar{u}_k}{\partial y}, \quad (2.59)$$

$$\epsilon = \sum_k \nu \overline{\left(\frac{\partial u'_k}{\partial y} \right)^2}. \quad (2.60)$$

It is possible to deduce an accurate representation of the flow by summing up the contributions by $\overline{u'^2}$, $\overline{v'^2}$ and $\overline{w'^2}$ such that $\text{TKE} = (1/2)(\overline{u'^2} + \overline{v'^2} + \overline{w'^2})$. Here, in the ODT model $\alpha \neq 0$ and the most reasonable choice is $\alpha = 2/3$ indicating equal available energy redistribution after an eddy event. Following the similar analogue, the production and dissipation budgets for S-ODT are calculated as,

$$\mathcal{P} = I_1 \frac{\partial \bar{u}}{\partial y}, \quad (2.61)$$

$$\epsilon = \nu \overline{\left(\frac{\partial u'}{\partial y} \right)^2}. \quad (2.62)$$

2.7 In Closing

The main features of the one-dimensional turbulence model are summarized in this chapter which includes the governing equations for spatial and temporal ODT, the map-based formulation of eddy events, their selection and description of the model parameters.

Chapter 3

ODT Simulation Set-Up

In this chapter, simulation set-up used for temporally developing turbulent boundary layer (TBL), spatially developing turbulent boundary layer (SBL) and uniform blowing in SBL is explained in detail. These set-ups are used for the simulations and their results are presented in Chapter 4, 5, 6 and 7.

3.1 Characterization of the TBL and ODT Simulation Set-Up

The TBL is characterized by statistically homogeneous fields in the streamwise and spanwise directions, thus, only the wall-normal direction remains, which makes this problem statistically one-dimensional. This makes TBL feasible to investigate with ODT as stand-alone tool. In the following, first the relevant bulk quantities that characterize the TBL are discussed and afterwards, the ODT simulation set-up, given that it references some of the characterizing quantities.

3.1.1 Characterization of the TBL

This section summarises the definition of the relevant bulk quantities that are useful for a characterization and quantitative understanding of the TBL.

The starting point is the ensemble-averaged velocity field $\bar{u}_i(y, t)$. This velocity field only has a nonzero streamwise component $\bar{u}(y, t)$ due to symmetry of the configuration. For large enough ensemble sizes, $\bar{u}(y, t)$ is smooth. Here, it can be used directly to define the boundary layer thickness. For example by thresholding a fraction of the bulk velocity U_b . The 99% rule [119] is used to yield,

$$\delta_{99}(t) = y \quad \text{for} \quad \frac{\bar{u}(y, t)}{U_b} = 0.99. \quad (3.1)$$

The thickness δ_{99} carries the dilemma that non-monotonic and instantaneous velocity profiles cannot be adequately characterized. This problem is addressed by the displacement and momentum thicknesses. These are

integrals of the first and second order moments of the velocity field. The displacement thickness and the momentum thickness are given as,

$$\delta(t) = \int_0^\infty \frac{\bar{u}}{U_b} dy, \quad (3.2)$$

$$\theta(t) = \int_0^\infty \frac{\bar{u}}{U_b} \left(1 - \frac{\bar{u}}{U_b}\right) dy. \quad (3.3)$$

Both $\delta(t)$ and $\theta(t)$ are well-defined even for instantaneous profiles of the streamwise velocity $u(y, t)$ and will be used below for conditional computations of the turbulence spectra.

The wall-shear stress $\tau_w(t) = \rho\nu |\partial\bar{u}/\partial y| (y = 0, t)$ is another important quantity used to characterize turbulent boundary layers. This quantity quantifies the average momentum transfer from the fluid to the rigid surface or *vice versa*. The related kinematic quantity is the friction velocity $u_\tau = \sqrt{\tau_w/\rho}$. It provides an inner scale of the wall-bounded flow and is therefore, frequently used for the analysis of the similarity properties and the comparison of results from different sources. The inner velocity and length scales are u_τ and $y_\tau = \nu/u_\tau$. Whereas the outer ones are U_b and δ_{99} . The usual convention is followed and the variables rescaled to the inner units are denoted with the superscript '+', for example, $u^+ = u/u_\tau$ and $y^+ = y/y_\tau$.

For future reference, the friction, bulk and displacement or momentum Reynolds numbers for the TBL are defined as follows,

$$Re_\tau = \frac{u_\tau \delta_{99}}{\nu}, \quad Re_b = \frac{U_b d}{\nu}, \quad Re_\xi = \frac{U_b \xi}{\nu}. \quad (3.4)$$

In the first equation, the thickness δ_{99} serves as outer length scale of the solution and in the second equation, the length scale d is prescribed by the initial condition and it is constant similarly to laboratory experiments, where d would be the trip-wire diameter explained below. In the last equation, ξ is a placeholder for the thicknesses δ and θ or the streamwise length scale X , respectively and it matches the TBL solution at time t to the local SBL solution at position X via the Galilean transformation,

$$X = U_b t. \quad (3.5)$$

For the TBL ODT simulations, the main control parameter is Re_b . This is modified by adjusting the bulk velocity, U_b , prescribed at the bottom wall.

The boundary layer flow profiles can be characterized by a few well-defined coefficients. These coefficients are frequently encountered in the literature. For the TBL, the coefficients are considered as,

$$C_1 = \frac{\delta}{\delta_{99}}, \quad C_2 = \frac{\theta}{\delta_{99}}, \quad H = \frac{\delta}{\theta} = \frac{C_1}{C_2}. \quad (3.6)$$

The ensemble-averaged velocity profile together with the quantities defined above are combined in Coles' empirical law [120], which is given as,

$$\frac{U_b - \bar{u}}{u_\tau} = \frac{1}{K} \log\left(\frac{u_\tau y}{\nu}\right) + A + \frac{\Pi}{K} W\left(\frac{y}{\delta_{99}}\right). \quad (3.7)$$

In this equation, K is the von Kármán constant and A the log-layer offset, $W(y/\delta_{99})$ Coles' wake function and Π the corresponding wake strength. The wake quantities are not discussed further as they are merely constant for the TBL [49, 50] and [119] is followed. An outer-layer similarity is assumed for TBL configuration. Inserting the definitions of the displacement and momentum thicknesses, as well as the coefficients C_1 and C_2 gives the balance equation [119, 120],

$$\frac{\theta}{\delta_{99}} = \frac{C_1}{U_b^+} - \frac{C_2}{(U_b^+)^2}. \quad (3.8)$$

The contributions to this equations are due to the boundary layer thickness θ and δ_{99} , the normalized bulk velocity $U_b^+ = U_b/u_\tau$ (or the friction velocity u_τ since U_b is constant here), and the coefficients C_1 and C_2 and these quantities are addressed in the upcoming chapters by comparing the ODT solutions to available reference DNS. To the best of our knowledge, the balance of this equation has not been presented so far in the relevant literature. The balance equation is addressed numerically in Chapter 4.

3.1.2 ODT Simulation Set-Up for the TBL

The ODT simulation set-up used for the present study follows from Kozul et al. [50]. The two fundamental configurations for SBL (used in Chapter 5 and 6) and TBL (utilized in Chapter 4) are sketched in Figure 3.1 (A) and (B), respectively. The ODT computational domain is a line of size (height) D and this line is here approximately taken as a closed system for each instant in time. The TBL is realized on this line by prescribing Dirichlet boundary conditions at the top as well as bottom walls and the shear is initially concentrated at the lower wall in order to mimic a trip-wire configuration. The lower wall is taken as moving and the free stream at rest for practical reasons, i.e., $u = U_b$ and $v = w = 0$ for $y = 0$ and $u = v = w = 0$ for $y = D$, respectively. One has to make sure that the TBL remains confined to a region sufficiently smaller than the domain height for the given set-up.

Conventional statistics, like mean velocity profiles, are obtained on an ensemble basis using at least $N = 1000$ members and these members are individual ODT realizations that are run in parallel on a large computing cluster. All members are autonomous so that communication is not a limiting factor and an ensemble of different turbulent solutions is obtained from the same initial conditions by varying the seed of the underlying random number generator.

The initial conditions used for the ODT simulations are precisely those of the reference DNS [50] and only the streamwise component u is initially non-zero and exhibits a smooth, monotonic profile,

$$u_0(y) = \frac{U_b}{2} + \frac{U_b}{2} \tanh \left[\frac{d}{2\theta_{sl}} \left(1 - \frac{y}{d} \right) \right], \quad (3.9)$$

where $\theta_{sl} = 54\nu/U_b$, the scale length, depends on the prescribed kinematic viscosity ν and bulk velocity U_b which implies that the shape factor depends

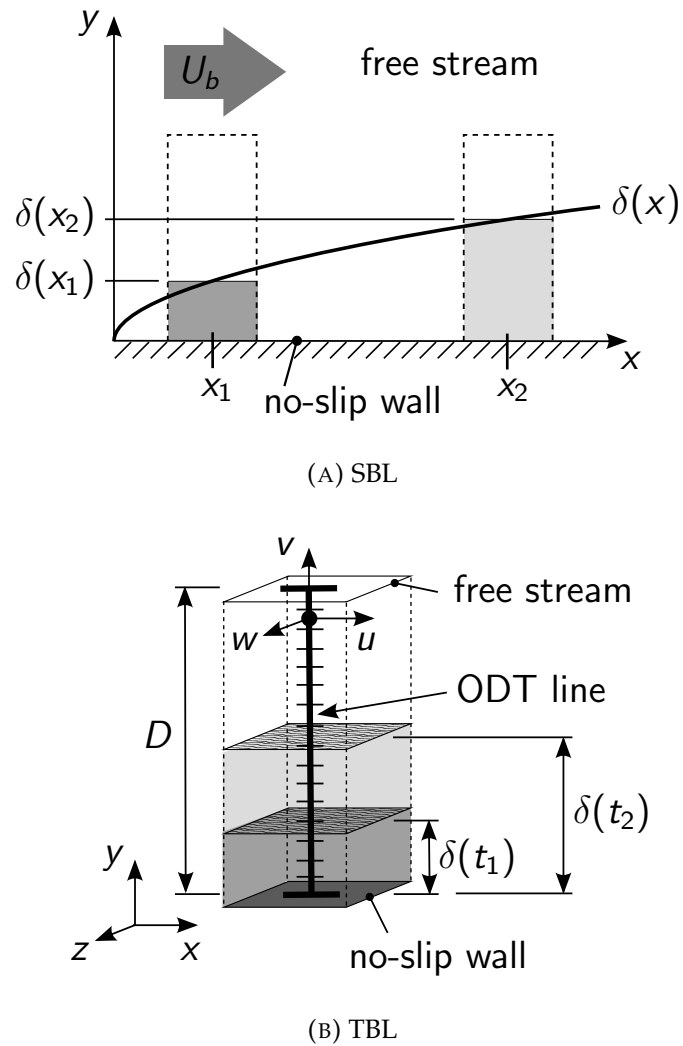


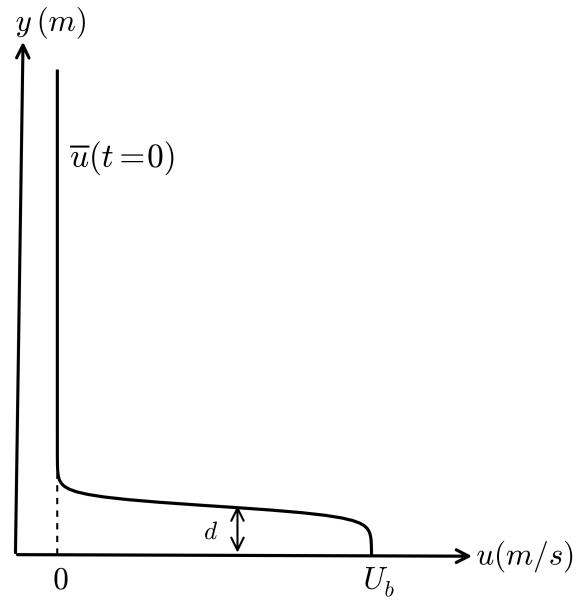
FIGURE 3.1: Schematics of the (A) spatially developing boundary layer (SBL) and (B) temporally developing boundary layer (TBL). The correspondence between the two configurations is indicated by broken domain boundaries in panel (A). The SBL solution at locations x_1 and x_2 (with thickness $\delta(x_1)$ and $\delta(x_2)$) corresponds roughly to the TBL solution at times t_1 and t_2 . In this study, stochastic ODT simulations are conducted only for the TBL using the 1-D wall-normal domain of height D (ODT line).

on the bulk Reynolds number, that is, $d/(2\theta_{sl}) = Re_b/108$. The other velocity components (v, w) are initialized to zero. All the constants used in the equation are taken from [50] to make a better comparison of the results. d is an external length scale which is here imposed through the bulk Reynolds number $Re_b = U_b d/\nu$, whereas, in laboratory experiments, d would be the trip-wire diameter. The streamwise velocity profile at $t = 0$ i.e. the initial profile used to set the fluid at rest into motion and at $t > 0$ is depicted in Figure 3.2.

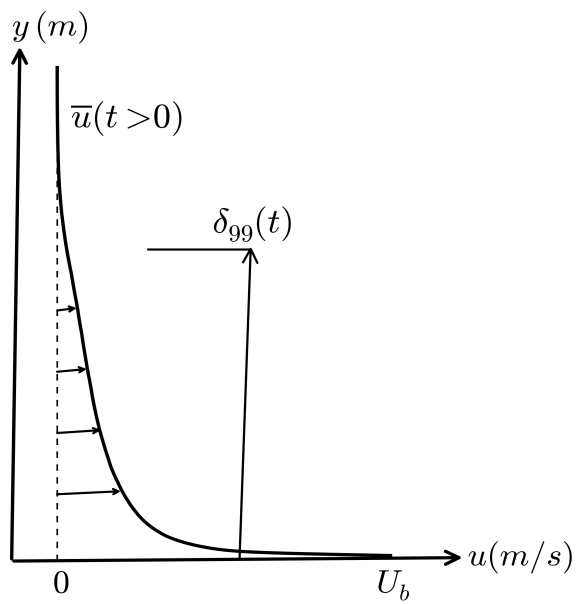
An overview of the simulated cases and the relevant model parameters is given in Table 3.1. Five bulk Reynolds numbers from the range $250 \leq Re_b \leq 2000$ are considered as shown in Table 3.1. The initial length scale d and the kinematic viscosity ν of the working fluid are fixed. $d = 10^{-3}$ m and $\nu = 1.5 \times 10^{-5}$ m²/s (air) are used for TBL simulations. The domain size D has been selected such that it is constant in bulk units ν/U_b . D for the simulations is used as $D U_b/\nu = 43,200$. The physical model parameters α , C , and Z , as well as the large-eddy suppression (LS), have been described in Chapter 2 and a few more numerical ones are addressed below.

Eddy events are efficiently sampled from empirical distributions and the specific choice does not change the results as long as the physically relevant range-of-scales is permitted [28]. In the present implementation, i.e., TBL, three numerical parameters are needed and these are the maximum (L_{max}), minimum (L_{min}), and most probable (L_p) eddy size [89] (see Table 3.1). It is unnecessary to sample very large eddy events as these are unphysical and instantly rejected by the large-eddy-suppression mechanism because the TBL thickness must remain sufficiently smaller than the domain size, The maximum eddy size has been selected as $L_{max} U_b/\nu = 25,920$, which corresponds to 60% of the domain size and this aids the numerical efficiency. The minimum eddy size, L_{min} , is estimated as the Kolmogorov length scale, L_K , with the aid of pre-simulations and the most probable eddy size has been selected as $L_p = 3L_{min}$. The value for L_p is motivated by the triplet map and the presence of a direct turbulence cascade. Due to the former the eddy events of size $l = 3L_K \simeq 3L_{min}$ and larger will remain unaffected by viscosity and due to the latter the most frequent eddy events have sizes just above L_K .

A dynamic adaptive mesh [89] is used to carry out the simulations which demands the specification of several more numerical parameters. The default values for most of them is used for TBL configuration. The most important adaptivity parameters control the size range of the cells and the frequency of mesh adaptations and it is important that the minimum and maximum allowed grid cell sizes must be spaced sufficiently from each other for the dynamic mesh adaption procedure [89]. The minimum and maximum grid cell sizes of the reference DNS [50] are used to carry out the TBL simulations and their values are given in Table 3.1). This range of values is sufficient for the dynamic grid adaption procedure and the grid is adapted whenever an eddy event has been accepted but at least every ten viscous time units. The latter is not limiting, however, used to minimize the numerical transport for less turbulent regions.



(A)



(B)

FIGURE 3.2: Streamwise velocity (in m/s) profile along the domain y (in m) at (A) $t = 0$ and (B) $t > 0$ (U_b , in m/s is the uniform velocity provided at the bottom of the wall).

TABLE 3.1: Summary of the cases and model parameters. Re_b is the bulk Reynolds number. The asterisk (*) represents the 1-D laminar solution for a given Re_b . The physical model parameters are α , C , Z , and β_{LS} from the large-eddy suppression (LS). The relevant numerical parameters are the minimum allowed eddy size L_{min} , most probable eddy size L_p , smallest allowed grid cell size Δy_{min}^+ , and maximum allowed grid cell Δy_{max}^+ . Note that L_{min} and L_p are in bulk units (ν/U_b), whereas Δy_{min}^+ and Δy_{max}^+ are in viscous units (ν/u_τ , where u_τ is the friction velocity).

Case	Re_b	L_{min}	L_p	Δy_{min}^+	Δy_{max}^+	C	Z	α	LS
R1000C1	1000	10	30	0.140	9.79	6	400	2/3	2/3
R1000C2	1000	10	30	0.140	9.79	12	400	2/3	2/3
R1000Z1	1000	10	30	0.140	9.79	9	200	2/3	2/3
R1000Z2	1000	10	30	0.140	9.79	9	600	2/3	2/3
R1000A1	1000	10	30	0.140	9.79	9	400	0	2/3
R1000A2	1000	10	30	0.140	9.79	9	400	1	2/3
R1000L1	1000	10	30	0.140	9.79	9	400	2/3	none
R1000L2	1000	10	30	0.140	9.79	9	400	2/3	frac. domain
R1000L3	1000	10	30	0.140	9.79	9	400	2/3	elapsed time
R250*	250*	104	312	0.126	8.81	9	400	2/3	2/3
R500	500	33	99	0.141	9.88	9	400	2/3	2/3
R1000	1000	10	30	0.140	9.79	9	400	2/3	2/3
R1500	1500	5	15	0.126	8.79	9	400	2/3	2/3
R2000	2000	3	9	0.065	7.91	9	400	2/3	2/3

3.2 Simulation Set-Up for the SBL

The simulation set-up which was used for TBL [109] configuration as explained above is utilized for SBL as well by slightly modifying the boundary and initial conditions which are discussed below for the present case (see Figure 3.1 (A)). Some of the physical as well as numerical parameters are also adjusted according to the problem and are given in Table 3.2. The spatial formulation of ODT allows simulations of flows that are statistically 2-D. The time dimension is replaced by evolution in a direction orthogonal to the ODT line [89]. A dynamic adaptive mesh is utilized to carry out the simulations with the default values for the numerical parameters associated with mesh adaption [89] for SBL as well and results are presented in Chapter 5. The minimum and maximum allowed grid cell sizes must be sufficiently spaced from each other to allow the dynamic mesh adaption procedure [89] and for SBL configuration the maximum grid cell sizes of the reference DNS in [41] is used and minimum cell size allowed by the mesh adaption process is calculated using the Kolmogorov length scale as $\Delta y_{min} = \eta/3$ and are summarised in Table 3.2 along with the physical and numerical parameters used to carry out the simulations for SBL configuration.

The ODT computational domain is a line of size D on which the SBL is realized by prescribing Dirichlet boundary condition at the bottom wall with bulk velocity, U_b and Neumann condition at the open domain and the lower wall is taken as moving and the free stream at rest. The velocity statistics are obtained on an ensemble basis using at least $N = 4000$ members which is very high as compared to the TBL simulations. This is because in TBL simulations, velocity statistics is averaged over number of realizations as well as time window, however, in case of SBL averaging is only over number of realization. These members are individual ODT realizations and are run in parallel on a large computing cluster similar to TBL case explained above.

For the SBL configuration, the streamwise velocity component u has been initialized using a laminar profile generated by solving the diffusion part using the ODT model. The other velocity components (v, w) are initialized to zero. Figure 3.3 shows that the ODT laminar solution is similar to the Blasius laminar solution from [1] which is generally used to initiate the DNS results and a good degree of agreement between the ODT laminar solution and the Blasius laminar solution from [1] is noted.

The simulations are carried out for different momentum Reynolds numbers, $Re_\theta = \theta U_b / \nu$, where θ is the momentum layer thickness and the kinematic viscosity ν of the working fluid air is $\nu = 1.5 \times 10^{-5} \text{ m}^2/\text{s}$ (same as TBL case). The analyses is presented at $Re_\theta \approx 2000, 4000$, and 8000 . The domain size D has been selected such that it is constant in bulk units ν/U_b as $D U_b / \nu = 45,000$ (or 100 in terms of δ^* , which is displacement thickness).

The friction Reynolds number is defined above and the thickness and displacement Reynolds numbers for future reference for SBL are defined as,

$$Re_{\delta_{99}} = \frac{U_b \delta_{99}}{\nu}, \quad Re_X = \frac{U_b X}{\nu}. \quad (3.10)$$

TABLE 3.2: Summary of the cases and model parameters. U_b is the bulk velocity in m/s. The relevant numerical parameters are the minimum allowed eddy size L_{min} , smallest allowed grid cell size Δy_{min}^+ and maximum allowed grid cell Δy_{max}^+ . C and Z are the physical model parameters. L_{min} is in bulk units (ν/U_b), and Δy_{min}^+ and Δy_{max}^+ are in viscous units (ν/u_τ , where u_τ is the friction velocity).

Case	U_b	L_{min}	Δy_{min}^+	Δy_{max}^+	C	Z
U1C1	12	17	0.14	8.6	3	600
U1C2	12	17	0.14	8.6	9	600
U1Z1	12	17	0.14	8.6	6	400
U1Z2	12	17	0.14	8.6	6	800
U1	12	17	0.14	8.6	6	600
U2	24	8	0.12	8.8	6	600

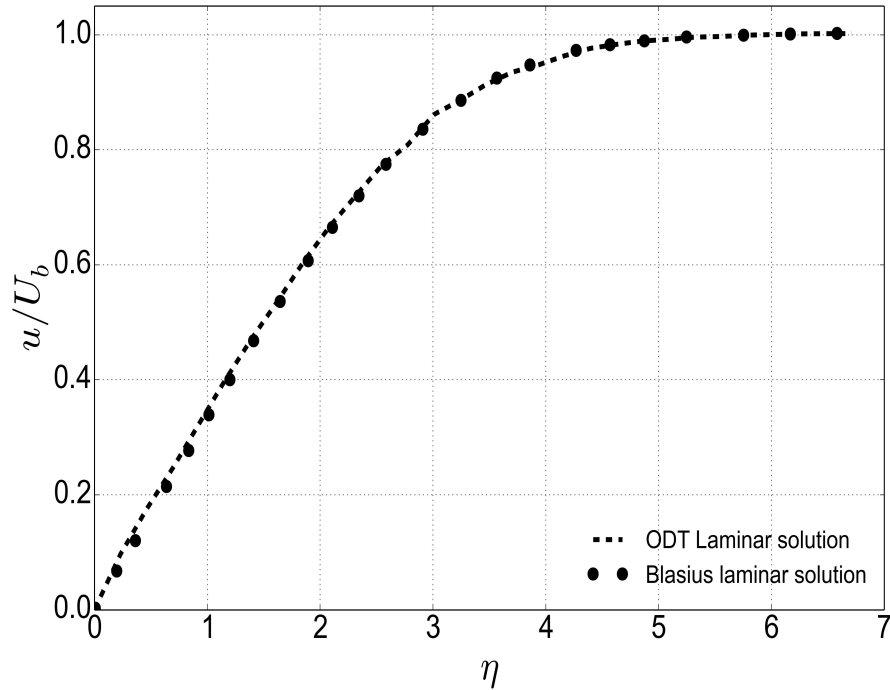


FIGURE 3.3: A comparison between the ODT laminar solution and the Blasius laminar solution from [1]. The ODT solution is used to initialize the streamwise velocity component for the SBL configuration.

Here the thickness δ_{99} serves as outer length scale of the solution and X is the streamwise length scale.

The maximum eddy size has been selected as $L_{max} U_b/\nu = 27,000$, which corresponds to 60% of the domain size to improve the numerical efficiency. The minimum eddy size, L_{min} , is estimated from the Kolmogorov length scale and for the most probable eddy size we have used $L_p = 3L_{min}$ to capture the initial transient stage. The physical and numerical model parameters are given in Table 3.2. Note that the usual convention is followed for the SBL configuration as explained above for the TBL configuration.

3.3 Simulation Set-Up for Uniform Blowing in the SBL

For the uniform blowing configuration, a similar simulation set-up is used which is used for LES in [64]. Figure 3.4 presents the schematic for ODT simulation set-up used for blowing in SBL. The present configuration is realized on the computational domain of the ODT model by prescribing no-slip conditions at the bottom wall and Neumann conditions at the open domain with $u = u_\infty$, $\frac{\partial v}{\partial y} = \frac{\partial w}{\partial y} = 0$. The streamwise velocity component u has been initialized with

a laminar profile similar to the SBL configuration explained above and shown in Figure 3.3. The other two velocity components (v, w) are initialized to zero.

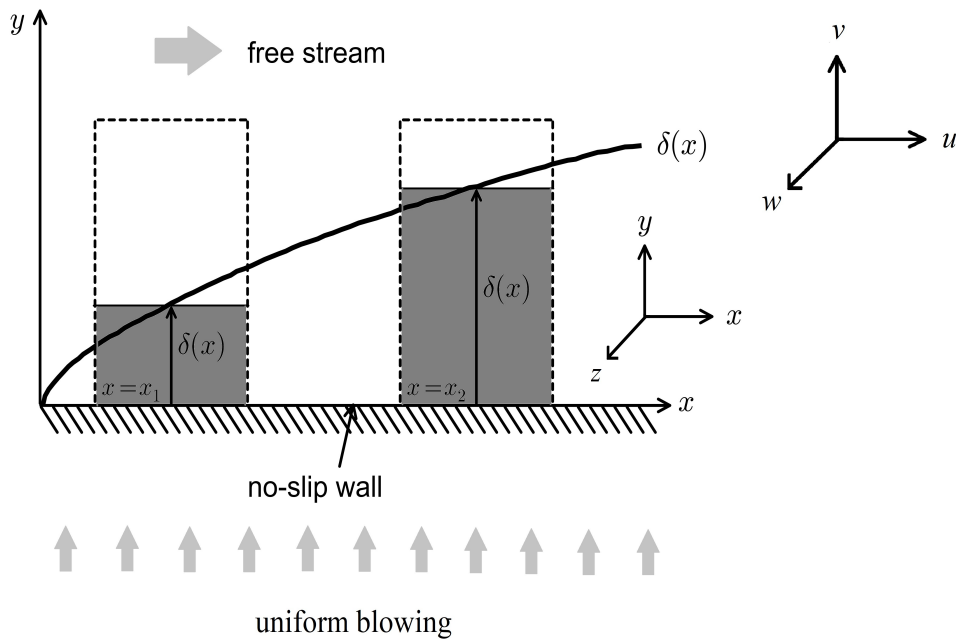


FIGURE 3.4: Schematics of the spatially developing boundary layer with uniform blowing.

Blowing is achieved by the constant wall-normal velocity (in the cross-stream direction) on the bottom wall, v_0 as shown in Figure 3.4. A Lagrangian method is used to establish blowing. In this method the mesh is evolved by marching the ODT domain upwards [89] and hence, no extra source term is required for this case. The amplitude of uniform blowing is set to be 0.1% of the free-stream velocity, i.e, $v_0 = 1.0 \times 10^{-3}$ m/s. A dynamic C++ adaptive code is utilized to carry out the simulations [89]. The important numerical parameters associated with the mesh adaptations are the minimum and maximum allowed grid size (dx_{min}, dx_{max}). Another important numerical parameter is the grid density factor (gDens) which controls the approximate number of cells generated after the adaption process [98]. dx_{min} and dx_{max} are spaced sufficiently from each other for the dynamic mesh adaption procedure and these values are used from the reference paper [64] for uniform blowing configuration. Table 3.3 gives all the physical model parameters used to carry out the simulations..

The data was gathered until the statistical convergence of the desired quantities was achieved. This was done on an ensemble basis using at least $N = 1000$ members representing individual ODT realizations running in parallel on a large computing cluster and are autonomous so that communication is not a limiting factor.

Other numerical parameters, L_{max} , L_{min} and L_p are explained in previous sections. The simulations, for uniform blowing configuration, are carried out

TABLE 3.3: Summary of the cases and model parameters. These are the physical model parameters.

Case	C	Z	α	LS
U1C1	5	100	2/3	thirds
U1C2	7	100	2/3	thirds
U1Z1	6	50	2/3	thirds
U1Z2	6	150	2/3	thirds
U1L1	6	100	2/3	elapsed time
U1L2	6	100	2/3	frac. domain
U1	6	100	2/3	thirds

for momentum Reynolds number, $Re_\theta = \theta u_\infty / \nu$ up to 2500, where θ is the momentum layer thickness, ν is the kinematic viscosity of the fluid and u_∞ is the free stream velocity. ν is fixed as $1.5 \times 10^{-5} \text{ m}^2/\text{s}$. The velocity statistics is compared with the reference data for $Re_\theta \approx 1407, 2082$, and 2395 in Chapter 6. The friction, thickness and displacement Reynolds numbers for future reference are defined in previous section for the SBL configuration and remain fixed for uniform blowing configuration. The usual convention is also same as TBL and SBL case.

3.4 In Closing

This chapter describes the simulation set-up used for SBL, TBL and uniform blowing in SBL. The simulation results produced using these set-ups are discussed next in Chapter 4, 5, 6 and 7.

Chapter 4

Temporally Developing Turbulent Boundary Layer

In this chapter we focus on the application of temporal ODT (T-ODT) formulation to investigate the temporally developing turbulent boundary layer (TBL). The various statistics for higher Reynolds numbers are also given in Appendix F for this validated flow configuration which can be used in future. Some of the results discussed in this chapter have been published in [109, 110, 111]

In the following, the predictive capabilities of ODT are addressed. This is done by varying the bulk Reynolds number in the range $250 \leq Re_b \leq 2000$ for TBL configuration. However, the physical model parameters remain fixed for this purpose and are used as $\alpha = 2/3$, $C = 9$, $Z = 400$, and the two-thirds large-eddy suppression (further detailed for selecting physical model parameters is given in Appendix C). The set-up used for TBL is summarized in Chapter 3. The numerical model parameters like the minimum eddy event size or the minimum allowed grid cell size need to be adjusted accordingly as these parameters are dependent on the Reynolds number.

In this section, ODT simulation results are discussed and compared to available reference DNS results of [50]. Various statistical quantities are presented for different instants in time, or normalized for different Re_θ . The velocity statistics presented here are averaged within time windows encompassing several eddy events per realization in addition to the conventional ensemble-averaging procedure. Smoother statistics are obtained by using larger time windows in case of DNS as well [50]. This issue is discussed later in detail, as it is specifically important for larger bulk Reynolds numbers. Same domain length and grid points are used for all the simulation cases with the same initial condition as used for DNS [50].

4.1 Velocity Boundary Layer for the TBL Case

Figure 4.1(A-D) illustrate the simulation set-up for four bulk Reynolds number, i.e., $Re_b = [500, 1000, 1500, 2000]$, respectively. The velocity U_b at the bottom wall initiate transitions and propagation of turbulence is observed at several instances. Velocity field is shown on a ODT domain on y -axis which is same

for all Re_b and on x -axis, is the time window. Note that x -axis does not represent complete domain, instead, the time window represent only a screenshot for a particular window. Since time is represented by Re_θ so different Re_θ corresponding to the time window are provided in the figure. Figure 4.1(A) depicts the snapshots for $Re_b = 500$ at $Re_\theta = [109, 581, 1076, 1843, 2606]$ (representing different time window on the x -axis) and corresponding Re_τ are $[7, 232, 497, 887, 1245]$ and we also show Re_δ as $[514, 900, 1506, 2449, 3390]$ from (i-v), respectively. It can be seen from the snapshots that for $Re_\theta = 109$, i.e. in the initial stage (Figure 4.1(A)(i)), the fluctuations are less than higher Re_θ . However, the turbulence is propagated away from the wall with time and is increased for higher Re_θ . The general observation for Figure 4.1(A) remains consistent with Figure 4.1(B), (C) and (D) as well. On comparing these visualizations with the different cases, i.e. Figure 4.1(A-D), it is found that the transition also depends on Re_b . It is observed that for $Re_b = 2000$, the transition to turbulence is started earlier and is further enhanced with time showing the dependence on Re_θ as well as Re_b . Nevertheless, the details of the transitions to turbulence are captured by ODT. The snapshots for all the Re_b are at the same instant and the values for several quantities are highly influenced showing their dependency on Re_b .

The temporally developing turbulent velocity boundary layer is shown in Figure 4.2 (A-D) for all bulk Reynolds numbers, $Re_b = [500, 1000, 1500, 2000]$, respectively. The velocity boundary layer is represented on the ODT domain on y -axis (similar to the figure discussed above) and growing with time on x -axis. The time on the axis is represented by the Re_θ corresponding to some instant and shown in figure for all Re_b considered for TBL configuration. This figure also demonstrates the dependence of propagation of transitions to turbulence on time as well as on Re_b . The variations are weaker for lower Re_b and stronger for higher Re_b and are maximum for $Re_b = 2000$. Note that the Re_θ mentioned in Figure 4.2 for various Re_b is corresponding to same instants for all cases, however, the Re_θ is increasing with Re_b . For $Re_b = 500$, the value for Re_θ is 109 and for corresponding instant this value is 251, 474 and 613 for $Re_b = 1000, 1500$ and 2000, respectively. Hence, this Figure demonstrates the capability of ODT to capture the behavior of the velocity boundary layer with time and Re_b , provided the model is one-dimensional.

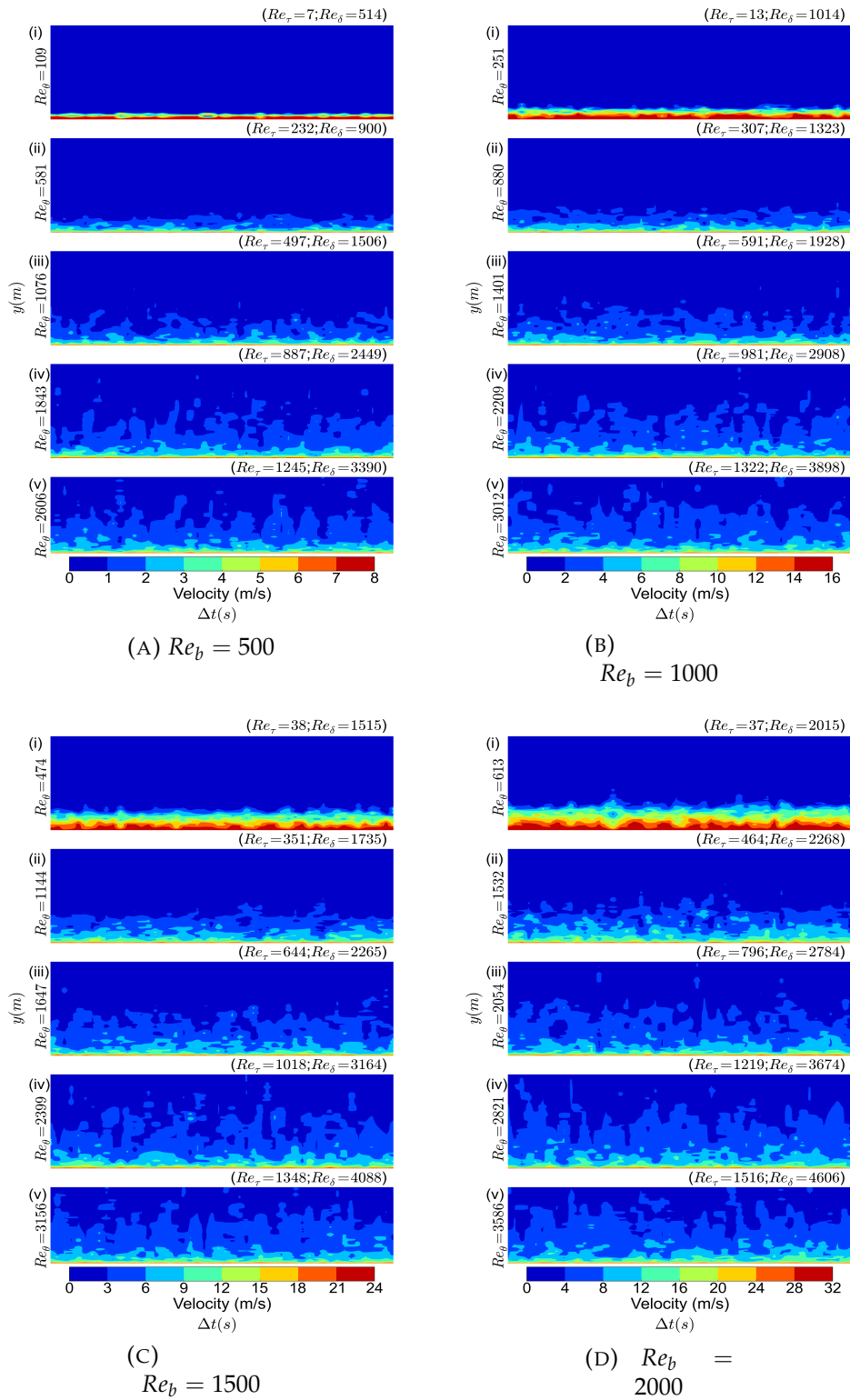


FIGURE 4.1: Velocity field with domain on y-axis (in m) and time window on x-axis (in s) which is represented by Re_θ at (A-D) $Re_b = [500, 1000, 1500, 2000]$. These snapshots represent velocity fields at small time windows corresponding to particular Re_θ (single value) mentioned in the figure above.

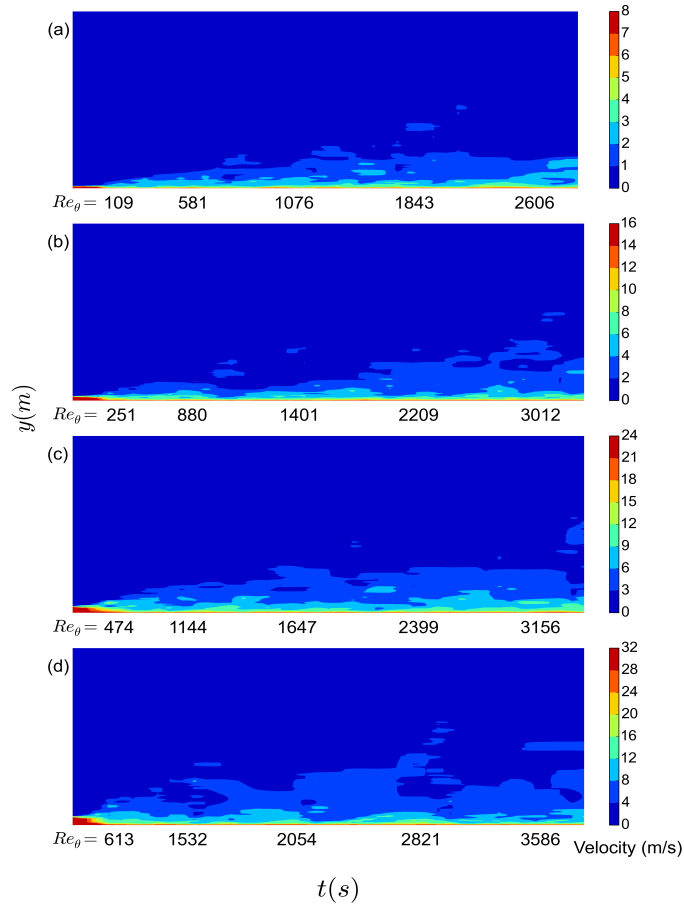


FIGURE 4.2: Temporal development of the velocity boundary layer with domain on y -axis (in m) and time on x -axis (in s) represented by Re_θ for bulk Reynolds number (A-D) $Re_b = [500, 1000, 1500, 2000]$. The figure illustrate the influence of Re_b on the velocity boundary layer.

4.2 First and Second Order Velocity Statistics

Figure 4.3 displays the mean streamwise velocity profile as a function of the wall-normal coordinate at (A) $Re_\theta \sim 1100$, (B) $Re_\theta \sim 1968$ and (C) $Re_\theta \sim 2500$ for $Re_b \in \{500, 1000, 1500, 2000\}$. The DNS reference data (dashed line) is available only for $Re_\theta \sim 1100$ and $Re_\theta \sim 1968$. The lower Re_θ , i.e., $Re_\theta \sim 1100$ represents transitions to turbulence and the higher Re_θ , i.e., $Re_\theta \sim 2500$ shows fully turbulent state. The influence of the initial conditions on the velocity profile is depicted in Figure 4.3 (A) particularly in the outer log-region.

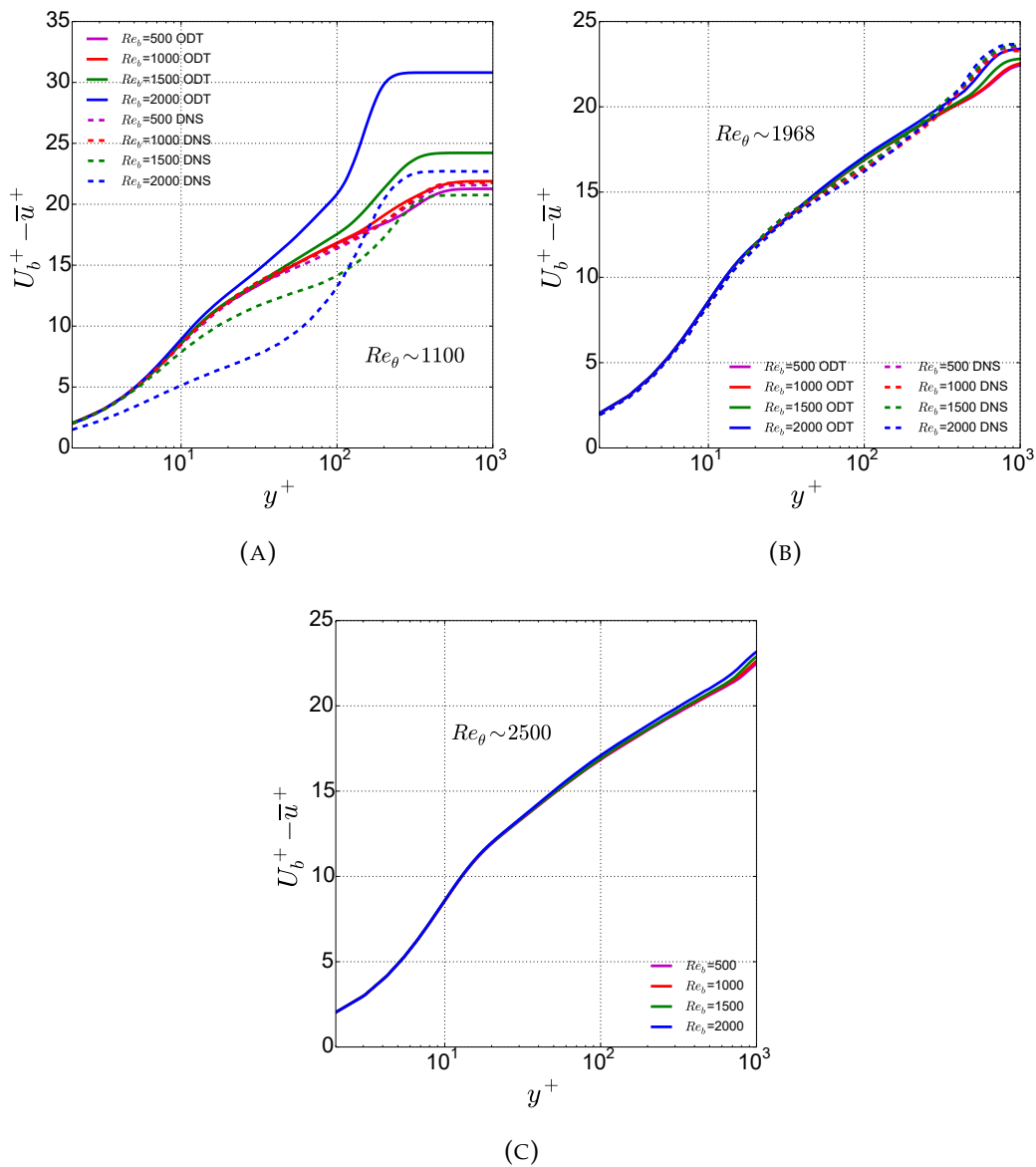


FIGURE 4.3: Mean streamwise velocity profile as a function of the wall-normal coordinate (in viscous units) at (A) $Re_\theta \sim 1100$, (B) $Re_\theta \sim 1968$ and (C) $Re_\theta \sim 2500$. For comparison, the available reference DNS data from [50] are shown at $Re_\theta \sim 1100$ and $Re_\theta \sim 1968$.

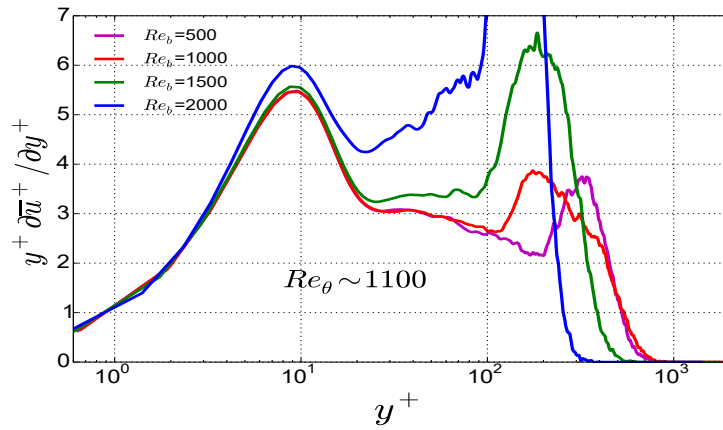
The profiles show agreement with the DNS data for low Re_b , i.e., for $Re_b = 500$ and 1000 (Figure 4.3 (A)). However, there are deviations for the other two cases, i.e., $Re_b \geq 1500$. For the case at $Re_\theta \sim 1968$, displayed in Figure 4.3 (B), all the curves are collapsing on top of each other. For this Re_θ , a slight variation is observed in the bulk, i.e., the outer log-region and the profiles increases with increasing bulk Reynolds number. In the inner layer, i.e., $y^+ < 10$, the velocity profile is independent of Re_b . The mean velocity profile for $Re_\theta \sim 2500$ shown in Figure 4.3 (C) behaves similar to $Re_\theta \sim 1968$, with better collapse between profiles for all Re_b for higher Re_θ . ODT shows very good agreement with the DNS data at both low and high momentum Reynolds

numbers ($Re_\theta \sim 1100$ and 1968), with deviations only in the outer-log region. This shows the ability of the model to capture transitions from the inner to the buffer layer, and further into the log-region.

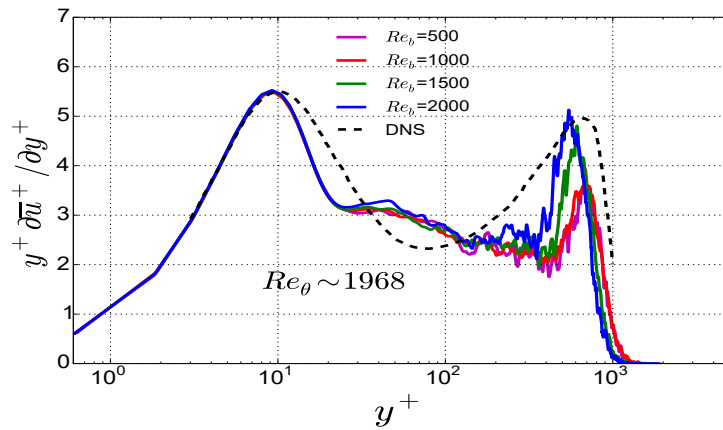
The indicator function, $y^+ (\partial \bar{u}^+ / \partial y^+)$, as a function of wall-normal coordinate in viscous units is presented in Figure 4.4 at (A) $Re_\theta \sim 1100$, (B) $Re_\theta \sim 1968$ and (C) $Re_\theta \sim 2500$ for $Re_b \in \{500, 1000, 1500, 2000\}$. This function aids in assessing whether there is a logarithmic region in the mean velocity profile or not. The DNS data of a fully turbulent zero pressure gradient SBL from [44] is plotted as a black dashed line at $Re_\theta \sim 2000$ for reference. The evaluated Re_b are not sufficiently large in order to reach an asymptotic logarithmic region. Hence, it is difficult to deduce an accurate value for the log-law constants [44]. The log-region in the velocity profile is identified by a constant region in the plot. However, this log-region starts appearing only at fairly large Reynolds numbers regimes and it is not discerned at the evaluated Reynolds number for DNS as well as ODT.

The curves show dependence on Re_b at $Re_\theta \sim 1100$ as shown in Figure 4.4 (A). The indicator profiles at this Re_θ are increasing with increasing Re_b from 500 to 2000 in outer log-region starting from $y^+ > 4$ depicting the transitions to turbulence. The lower momentum thickness Reynolds number also capture initial transients similar to the mean velocity. Nevertheless, the profiles remain unaffected in the inner log-region ($y^+ < 4$) for all Re_b .

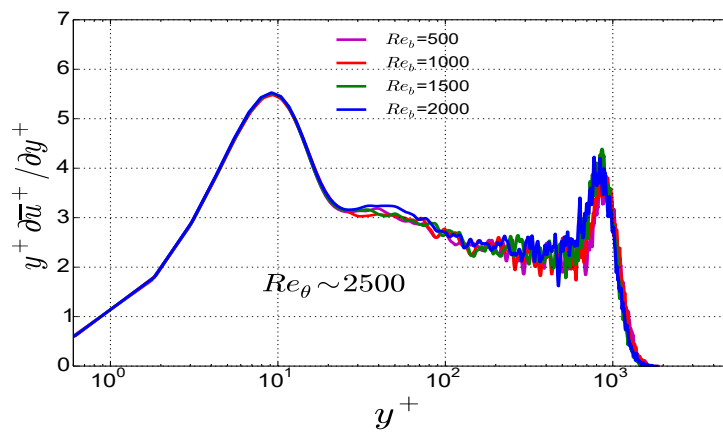
For $Re_\theta \sim 1968$ illustrated in Figure 4.4 (B), the curves are independent of Re_b in the inner and buffer regions up to $y^+ < 200$ and are found to be dependent on it in the outer-log region after $y^+ > 200$. A relatively large noise component further away from the wall is noted which can be improved by using very large ensemble sizes to achieve the statistical convergence. This would not notably change the results and the qualitative trend would remain same. The noise component occur due to the larger but less frequently occurring eddy events. Interestingly, for $Re_\theta \sim 2500$ displayed in Figure 4.4 (C), the curves for all Re_b collapses onto each other. This represents the fully turbulent state for the TBL configuration for higher Re_θ .



(A)



(B)



(C)

FIGURE 4.4: Indicator function versus wall-normal coordinate (in viscous units) at (A) $Re_\theta \sim 1100$, (B) $Re_\theta \sim 1968$ and (C) $Re_\theta \sim 2500$. For comparison, the reference DNS data for the SBL from [44] at $Re_\theta \sim 2000$ is given by a black dashed line.

Next the similarity properties are addressed by considering the von Kármán constant K of the law of the wall. The constant K is defined as the inverse

of the indicator function in the logarithmic region. Since there is no clear logarithmic region discerned either for ODT or the DNS, for ODT methodology, K was obtained by averaging this function over $40 \leq y^+ \leq 300$. The value obtained is close to $K \sim 0.4$ and it is in very good agreement with the reference value [50] given that it is an empirical idealization. The qualitative trends from the DNS [44], and the value of K are confirmed with ODT, despite the disagreement in the outer-log region (see Figure 4.4 (B)). ODT can reproduce but not confirm the value of K as the ODT parameters were tuned to match the mean profile.

The root mean square (rms) of the normalized streamwise velocity component ($u_{rms}^+ = \sqrt{u'^2}/u_\tau$) as a function of the normalized wall-normal coordinate in viscous units is shown in Figures 4.5 at (A) $Re_\theta \sim 1100$, (B) $Re_\theta \sim 1968$ and (C) $Re_\theta \sim 2500$ for $Re_\theta \in \{500, 1000, 1500, 2000\}$. At $Re_\theta \sim 1100$, shown in Figure 4.5(A), the profiles are in transition to turbulence and do not show collapse. However, these profiles achieve collapse at higher Re_θ as can be seen in Figure 4.5 (B) and (C). The rms peaks are under-predicted compared to the DNS data in both cases, i.e., at $Re_\theta \sim 1100$ and 1968. The reference data is not available for $Re_\theta \sim 2500$ case. This case is shown only to illustrate fully turbulent state achieved for the flow dynamics. The ODT modeling artifact for under-predicting rms peak has already been reported in the literature [84], and it can be avoided by retaining some 3-D information of the flow.

The weak double peak discerned in the vicinity of the wall at $10 < y^+ < 40$ might be due to the similarity of the mapping when the triplet map is applied frequently close to a wall. This is explained in detail in [89]. This weak near-wall double peak tends to disappear for low values of the α parameter shown in Figures C.2 (A) at $Re_\theta \sim 1100$ which might be due to the transient effects because for $Re_\theta \sim 1968$ in Figures C.2 (B), this peak exist for low α as well. It was also not present in the single-velocity ODT Couette flow simulations of [28]. This suggests that the specific choice of the mapping kernel, $K(y) = y - f(y)$, may contribute to this artifact. The eddy-event-based energy extraction on the scale l from the driving mean shear in the u velocity component has a spatial structure similar to $K(y)$. On the same scale l , the mean shear is in addition manipulated by application of the triplet map $f(y)$. The other velocity components, v and w receive the extracted energy on the selected scale but, on average, do not provide energy back to u on that scale as they possess no mean shear.

Further, note that the rms profiles in Figures 4.5 for all three Re_θ values exhibit an additional peak in the outer log-region. This additional peak is attributed to the transient flow, or the effect of the initial conditions. This peak is sensitive to the LS method used (see Figure C.12). It is also sensitive to the time window used for averaging. For example, the time window to get the profiles at $Re_\theta \sim 1968$ is $1940 \leq Re_\theta \leq 2003$. If this window is increased, and selected as $1819 \leq Re_\theta \leq 2126$, then the extra peak in the outer region is resolved and we can obtain smoother statistics. For higher order statistics, this window size is specially important [50]. Interestingly, the reference DNS results in Figure 4.5 (A) also exhibit a similar outer peak around $y^+ \sim 100$ for

higher bulk Reynolds numbers, i.e., $Re_b = 1500$ and 2000 . The peak is decreased after the initial transient has passed (see Figures 4.5 (B)). A ‘shoulder’ remains in the reference DNS data for all Re_b investigated. Therefore, the outer peak seems to be a general property of the outer layer dynamics of the asymptotic TBL. To investigate this outer peak, the inner-outer interaction have been considered in [121, 122] and [123] illustrated that the larger outer-scaled contributions are peaking in the log region.

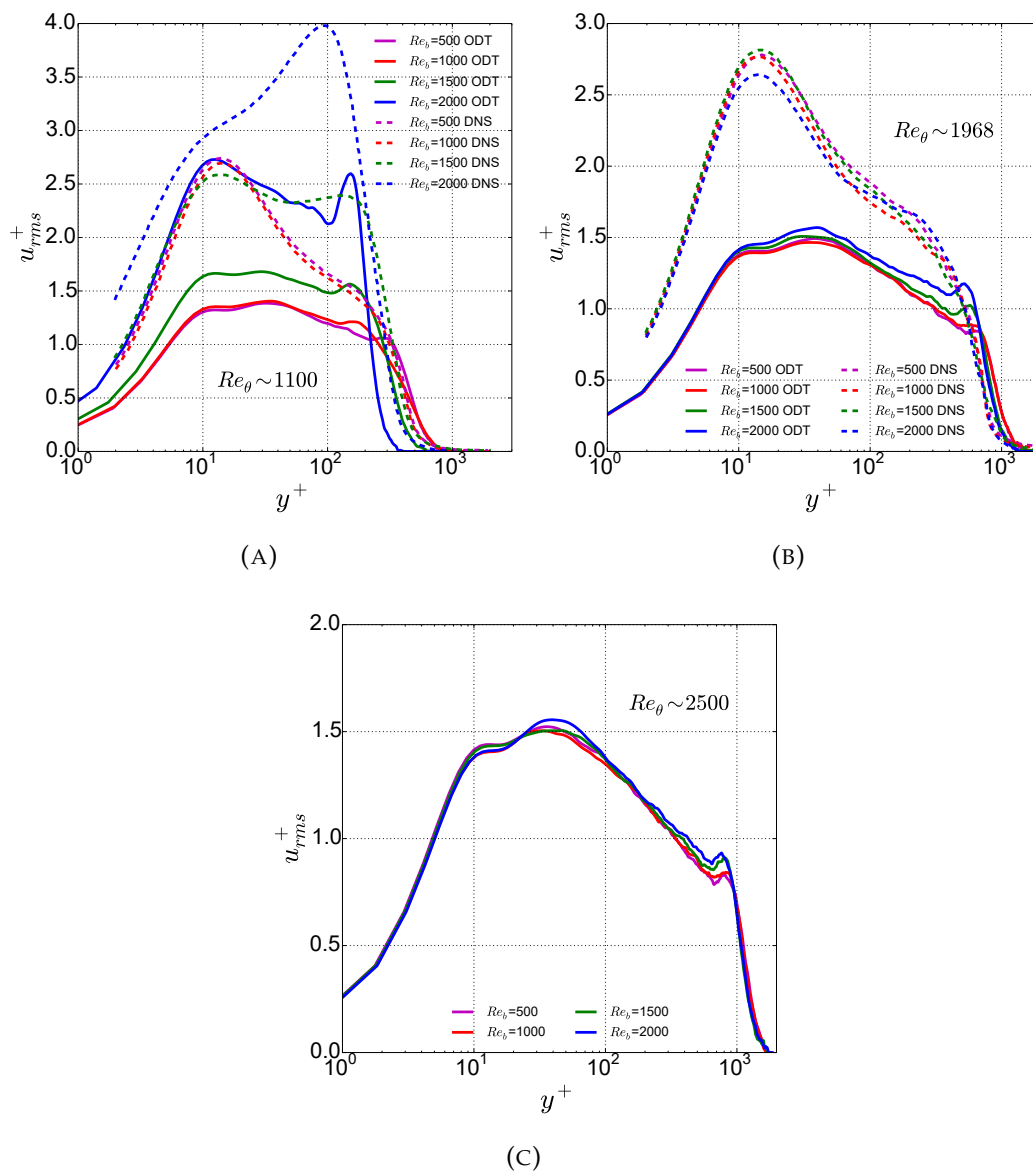


FIGURE 4.5: Streamwise root-mean-square velocity profiles at (A) $Re_\theta \sim 1100$, (B) $Re_\theta \sim 1968$ and (C) $Re_\theta \sim 2500$. All quantities are functions of the wall-normal coordinate (in viscous units). For comparison, the reference DNS data from [50] is shown at $Re_\theta \sim 1100$ and $Re_\theta \sim 1968$.

The reference DNS data reveals that the locations of the rms maxima shown in Figure 4.5 (A) coincide approximately with the locations of inflection

points of the mean profiles in Figure 4.3 (A). Moreover, the rms peak heights are correlated with the mean velocity gradients at the nearby inflection points. The ODT results presented here are in qualitative agreement with these DNS results, which is seen best for the profiles at $Re_b = 1500$ and 2000 . The outer layer dynamics exhibit strong random wall-normal fluid displacements by which the upper edge of the boundary layer progresses into the bulk of the fluid in case of DNS. In case of ODT, these displacements are represented by large stochastic mapping events that are constrained by the scale locality property of the triplet map and the LS mechanism. We note in this respect that the velocity profiles at higher Re_θ (later time) shown in Figures 4.3 (B) and 4.5 (B) exhibit weaker mean gradients in the outer layer suggesting that the boundary layer growth is more vigorous during the initial transient stage since the maximum permitted eddy sizes are small and thus frequent. At the same time, they are relatively large in comparison to the thickness of the boundary layer. The larger eddies become permissible as the boundary layer grows but these occur less often and more probable ones only cover a fraction of the boundary layer. The mean gradient as well as the rms fluctuations reduce as the wall-normal fluid motions are relatively weaker. Finally, a developing but asymptotic turbulent boundary layer flow is established and it has ‘forgotten’ its initial conditions.

In the following, we discuss additional Figure 4.6 giving the probability density functions (PDFs) of the eddy event locations in normalized wall-normal coordinates for the $1/3$ and $2/3$ positions of these eddies at (A) $Re_\theta \sim 1100$ and (B) $Re_\theta \sim 1968$. This type of PDF was used in [89] to explain the double bump in the rms velocity profiles occurring in channel-type flows. This can be adopted directly for other wall-bounded flows, for example the temporal boundary layer considered here.

At the low momentum Reynolds number, we can see how the low bulk Reynolds number flow exhibits already an approximately exponential tail of the eddy event location PDFs far away from the wall. For the large bulk Reynolds number flow, these PDFs are almost constant or even non-monotonic at large distances from the wall. In the latter case the events are spread with more or less equal probability throughout the whole boundary layer thus signaling the pronounced transient effect in the flow. For the large momentum Reynolds numbers, we see that both low and large bulk Reynolds number flows have collapsed on overlapping PDFs of the eddy locations, signaling the end of the transient and the achievement of a fully-developed condition (absence of the influence of the initial conditions).

This PDF is also interesting to analyze, since, as in [89] the position of the peaks for the $1/3$ and $2/3$ positions coincides with the double peak of the rms profiles close to the wall (for the low bulk Reynolds number flow at the low and high momentum Reynolds number, and for the large bulk Reynolds number flow at the high momentum Reynolds number). There is no peak of the PDF in the outer region, signaling that there is nothing particularly special (other than the influence of the initial conditions) in the large bulk Reynolds number case at the low momentum Reynolds number.

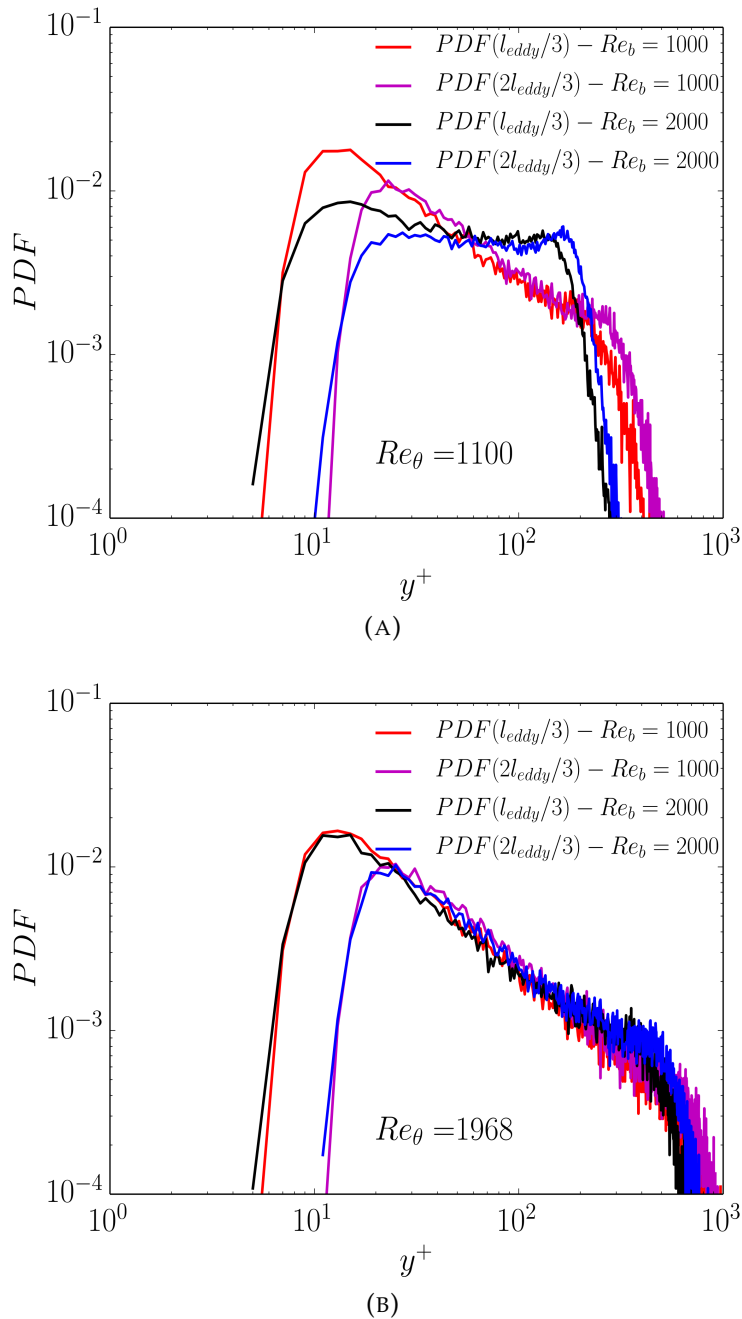


FIGURE 4.6: The probability density functions (PDFs) of the eddy event locations in normalized wall-normal coordinates for the 1/3 and 2/3 positions of these eddies at (A) $Re_\theta \sim 1100$ and (B) $Re_\theta \sim 1968$.

The contour of constant root-mean-squared values of the streamwise velocity fluctuations (u_{rms}^+) as a function of Re_θ is plotted in Figure 4.7 to quantify the extent to which the initial conditions hasten or delay the collapse for the profiles discussed for TBL flow configuration. As expected, we find collapse of the profiles for all Re_b investigated at high momentum Reynolds numbers for the ODT model.

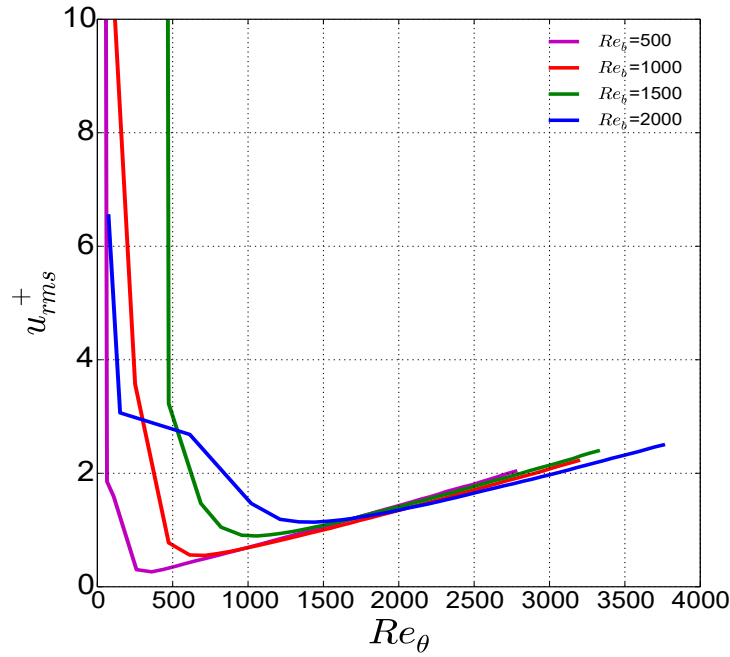


FIGURE 4.7: Contour of constant root-mean-squared values of the streamwise velocity fluctuations (u_{rms}^+) in steps of $\Delta u_{rms}^+ = 0.5$ as a function of Re_θ .

Figures 4.8 show the normalized Reynolds shear stresses as a function of the wall-normal coordinate in viscous units, $(\overline{u'v'}/u_\tau^2)$ at (A) $Re_\theta \sim 1100$, (B) $Re_\theta \sim 1968$ and (C) $Re_\theta \sim 2500$ for $Re_b \in \{500, 1000, 1500, 2000\}$. The calculation of the Reynolds shear stresses are based on the changes of the velocity profiles due to eddies (see [28] Appendix C). The Reynolds shear stresses obtained using ODT matches well with the DNS data.

The profiles at $Re_\theta \sim 1100$ (Figures 4.8 (A)) are still in transition to turbulence for the ODT model as well as DNS. These profiles collapse at $Re_\theta \sim 1968$ (Figures 4.8 (B)) for $Re_b \leq 1500$ and shows an additional peak for $Re_b = 2000$ in the outer region, indicating the sensitivity of Reynolds shear stresses to the large eddy suppression mechanism discussed earlier. In order to discard possible numerical artifacts and confirm the effects of the transient flow, we also show the Reynolds shear stresses at high Re_θ , that is, at $Re_\theta \sim 2500$, in Figure 4.8 (C) for which we do not have DNS data for comparison. The additional peak is found sensitive to the instabilities and disappears at the large Re_θ and for this case all the profiles track each other. For the given initial conditions ODT takes slightly longer to transition to a fully turbulent state as compared to DNS. In [96], the Reynolds shear stresses for the suction boundary layer were reported to be over-predicted compared to DNS data. But for the present analysis for temporally developing turbulent boundary layer, the Reynolds shear stresses are in very good agreement with the reference DNS results from [50]. This adds yet another sign of confidence in the predictive capabilities of ODT for the TBL configuration.

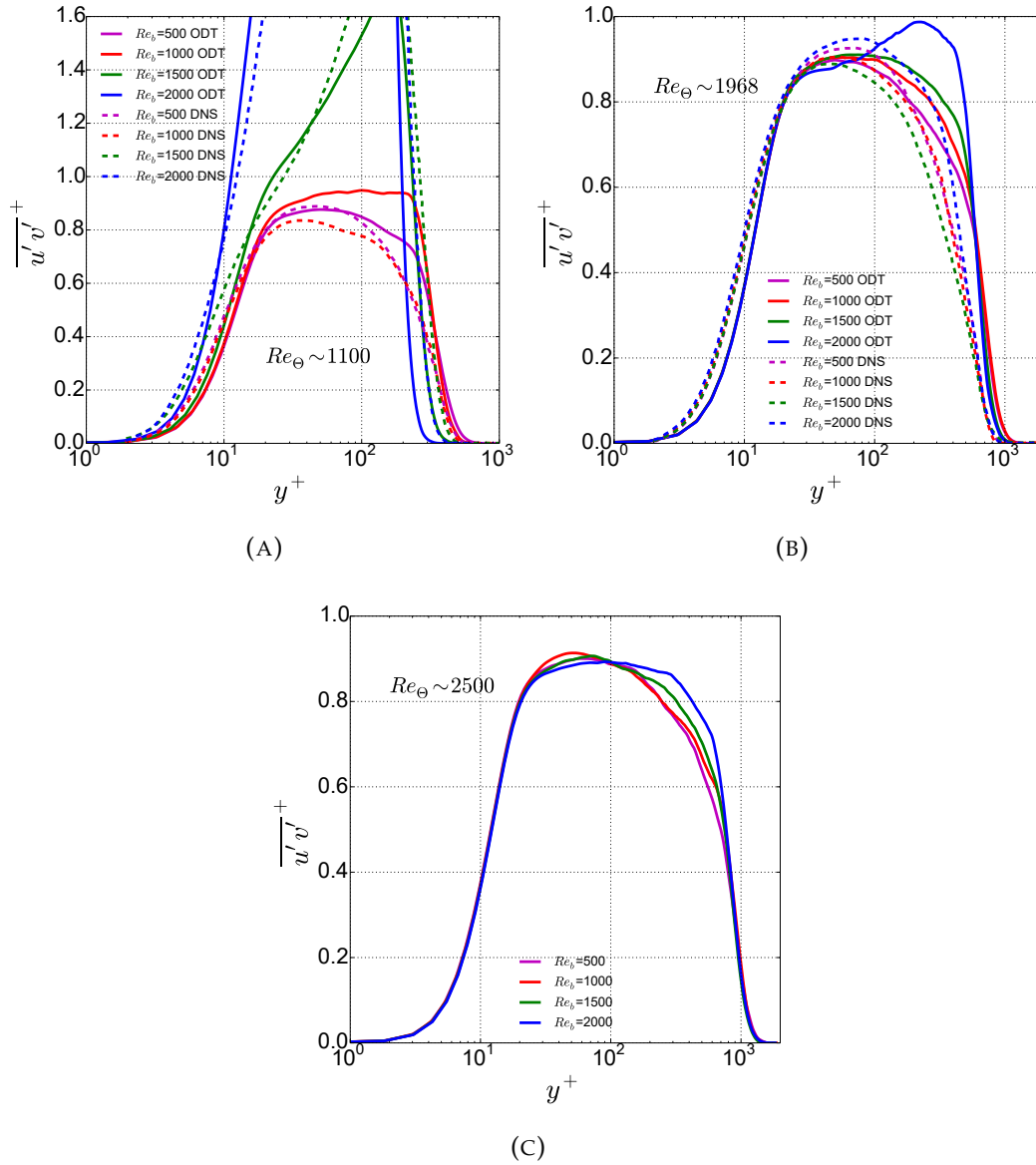


FIGURE 4.8: Profiles of the Reynolds shear stresses at (A) $Re_\theta \sim 1100$, (B) $Re_\theta \sim 1968$ and (C) $Re_\theta \sim 2500$. All quantities are functions of the wall-normal coordinate (in viscous units). For comparison, the reference DNS data from [50] is shown at $Re_\theta \sim 1100$ and $Re_\theta \sim 1968$ s.

4.3 Higher Order Velocity Statistics

The turbulent production in the flow is calculated as $-\overline{u'v'}^+ \frac{\partial \overline{u}^+}{\partial y^+}$. The turbulent production as a function of the wall-normal coordinate in viscous units (normalized with u_τ^4/ν) at (A) $Re_\theta \sim 1100$, (B) $Re_\theta \sim 1968$ and (C) $Re_\theta \sim 2500$ for $Re_b \in \{500, 1000, 1500, 2000\}$ is shown in Figure 4.9.

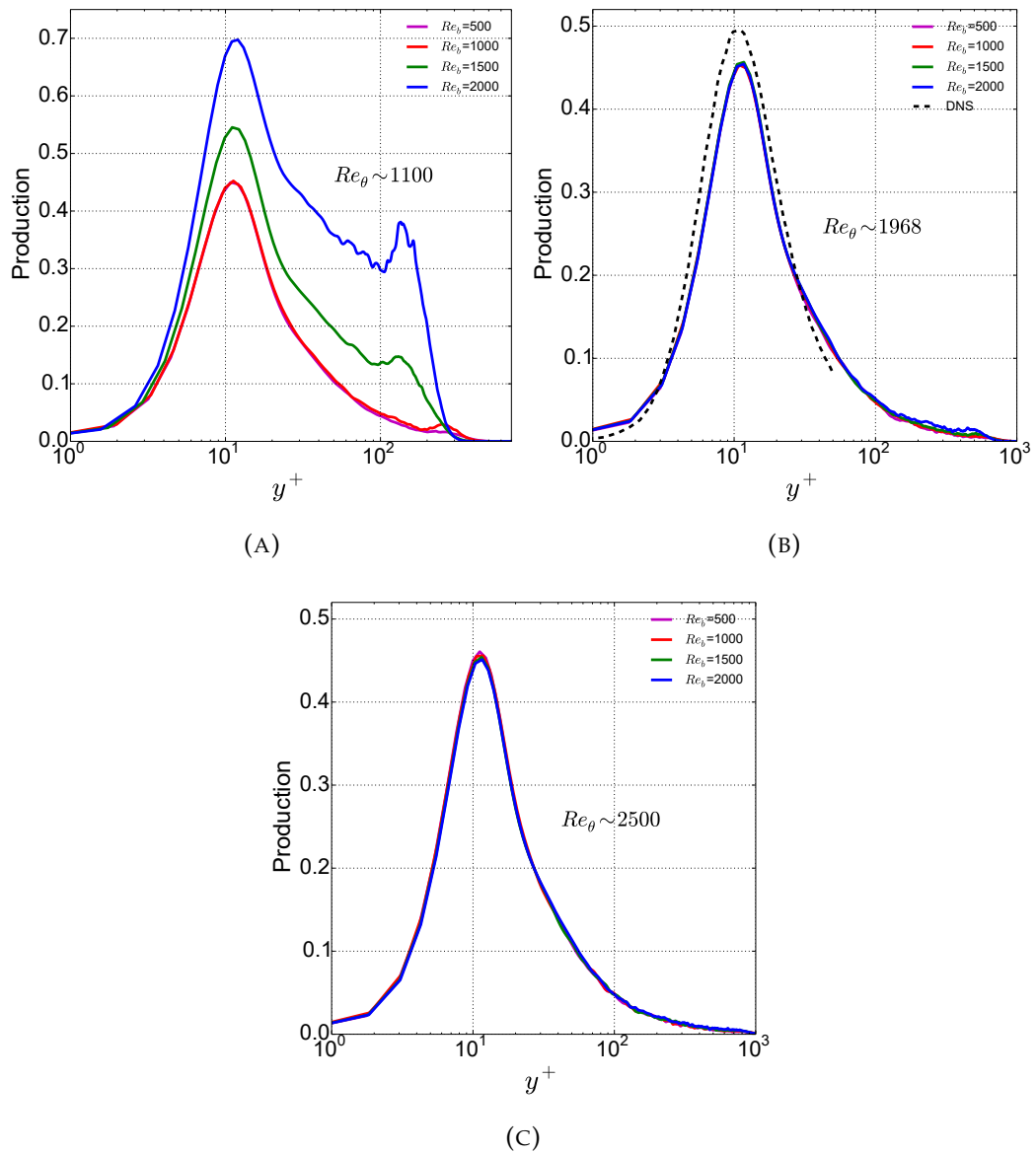


FIGURE 4.9: Turbulent kinetic energy production as a function of the wall-normal coordinate (in viscous units) for (A) $Re_\theta \sim 1100$, (B) $Re_\theta \sim 1968$ and (C) $Re_\theta \sim 2500$. For comparison, the reference DNS data from [38] is given by a black dashed line

For $Re_\theta \sim 1100$, the DNS data is not available and the curves for $Re_b \leq 1000$ collapse well onto each other for ODT simulation. The profile is smooth with a small peak in outer log-region for $Re_b = 1500$ but has not yet collapsed with low Re_b . Whereas, for $Re_b = 2000$, this extra peak in the outer region similar to the rms velocity profile and Reynolds shear stresses is discerned for the production mechanism as well. This is exclusively due to the transient effects in the flow and have been addressed in Appendix D by displaying production mechanism for several Re_θ starting from very low to high values. As the DNS production results for $Re_\theta \sim 1100$ is not available, we note that we would also expect a peak in the outer region in the DNS data due to the

transient effects. This is expected based on the shape of the DNS mean velocity profiles and Reynolds shear stresses. This transient effect is removed for statistics at higher Re_θ shown Figure 4.9 (C) at $Re_\theta \sim 2500$ and also shown in Appendix D. The production profiles for all Re_b cases at $Re_\theta \sim 1968$ and 2500 collapse to a good degree. The ODT profiles at $Re_\theta \sim 1968$ show fair agreement with the DNS data from [38]. Therefore, an overall good estimation of the turbulent production in ODT is expected.

The skewness of the streamwise velocity component, $-\overline{u'^3}/u_{rms}^3$, as a function of the wall-normal coordinate y^+ (in viscous units), is shown in Figure 4.10 at (A) $Re_\theta \sim 1100$, (B) $Re_\theta \sim 1968$ and (C) $Re_\theta \sim 2500$ for all four Re_b . The ODT results are qualitatively consistent with the DNS data for $Re_\theta \sim 1100$ and $Re_\theta \sim 1968$. The DNS data for TBL is not available at $Re_\theta \sim 2500$. With the increase of Re_b , the skewness increases slightly in the buffer region, $20 < y^+ < 100$ and decreases in the inner ($20 < y^+$) and outer log-region, ($y^+ > 100$) at lower Re_θ , i.e., $Re_\theta \sim 1100$ shown in Figure 4.10 (A), This trend is consistent with the reference DNS. However, for the other two cases presented in Figure 4.10 (B) and (C), the ODT skewness profiles are collapsing onto each other representing a fully developed turbulent flow. Although, the skewness was reported over-predicted for both, inner as well as outer regions in case of a suction boundary layer [96]. The profiles for all three Re_θ show similar behavior as reported for rms and Reynolds shear stresses, however, the ODT profiles are sensitive towards C and α model parameters.

The figure also shows that the ODT model tends to under-predict the positive skewness near the wall for $y^+ < 10$ which is similar to the suction boundary layer [96]. A qualitatively different behavior in comparison to DNS can be discerned in Figure 4.10 (A) and (B) for the buffer region, $10 < y^+ < 40$, where ODT yields positive instead of negative skewness and the magnitude is over-predicted in comparison to the DNS results. This behaviour is attributed to some unrepresented features of the buffer layer dynamics analogous to the argumentation for u_{rms} above. For the outermost region, $y^+ > 900$, where u_{rms} is positive but close to zero as discussed above shows the largest disagreement for skewness profiles.

The skewness values of the order one or larger are likely caused by the small values of $|\overline{u'^3}|$ that result from occasional penetration of fluid from the turbulent region into the free stream. In ODT, the skewness remains negative whereas it recovers to positive values in the DNS. This indicates at qualitatively different dynamics at the edge of the boundary layer. The weakly positive deviations u' (negative u) presumably dominate the negative skewness observed for ODT as the mean, $U_b - \bar{u}$, is very close to U_b . These positive values in ODT are because of the inter-component energy redistribution, but neither the triplet map nor the viscous diffusion causes positive skewness. The viscous diffusion and the triplet map would retain the streamwise velocity in its initial range $0 \leq u \leq U_b$. Hence, the ODT model is not fully representative of the 3-D outer layer dynamics as these exhibit more degrees of freedom and close to the upper edge of the boundary layer both positive and negative u' are generated.

Note that the above argumentation does not apply in the interior of the

boundary layer. The mean streamwise velocity profile, \bar{u} , is monotonic across the log-region, for $40 < y^+ < 600$ and both $\bar{u} > 0$ and $(U_b - \bar{u}) > 0$, whereas the gradient $d\bar{u}/dy < 0$ and $d(U_b - \bar{u})/dy > 0$. This suggests that the instantaneous u velocity is not required to become negative to generate the observed negative skewness under the action of the triplet map. The structure of the triplet map together with the monotonicity of the driving mean streamwise velocity can explain the positive skewness towards the wall for $y^+ < 40$ by positive u departures (negative u') and this is consistent with the above interpretation. Nevertheless, this figure illustrates the potential of ODT to calculate third order velocity statistics.

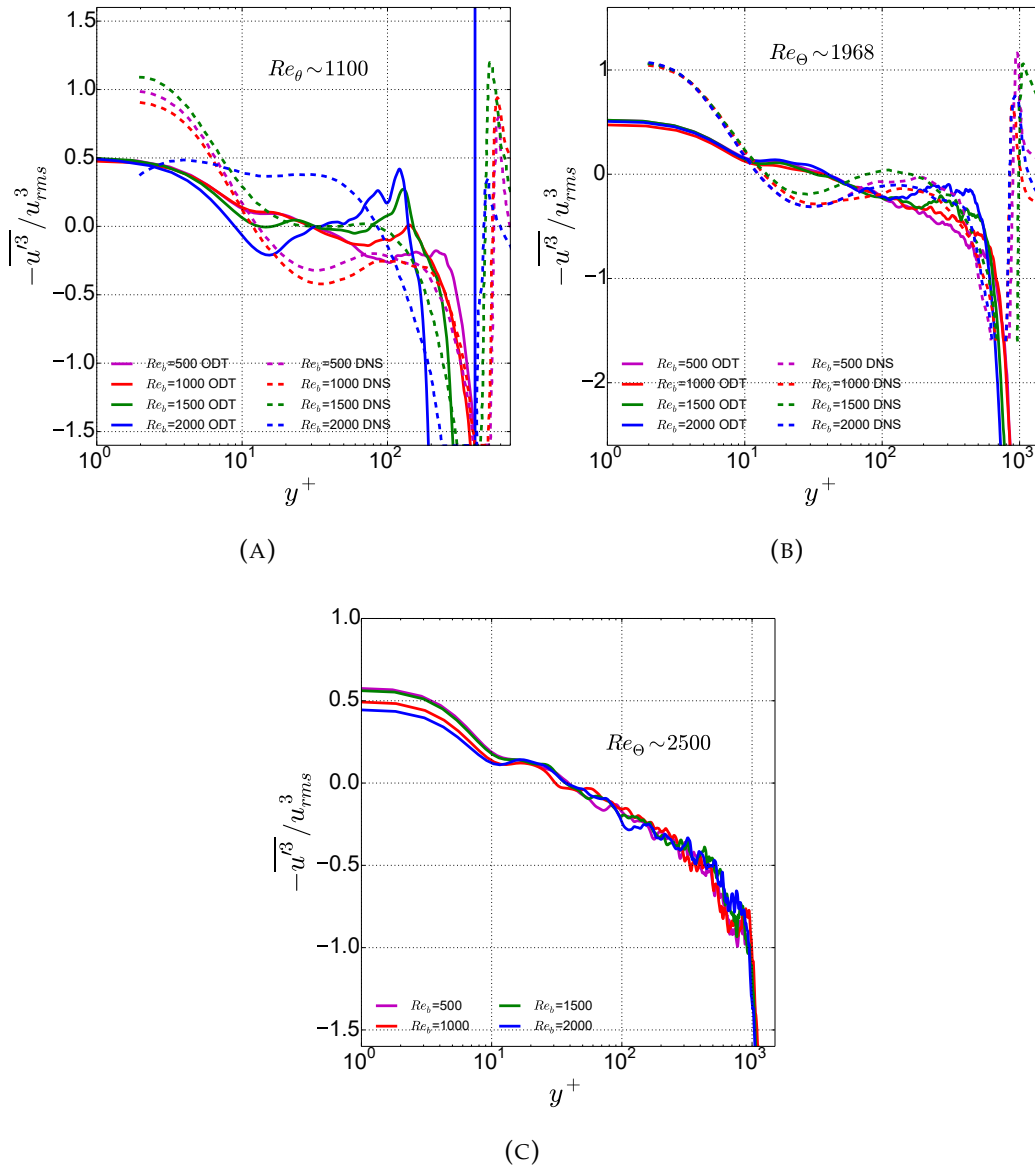


FIGURE 4.10: Profiles of the skewness of the streamwise velocity fluctuations as a function of the wall-normal coordinate (in viscous units) at (A) $Re_\theta \sim 1100$, (B) $Re_\theta \sim 1968$ and (C) $Re_\theta \sim 2500$. For comparison, the reference DNS data from [50] is shown at $Re_\theta \sim 1100$ and $Re_\theta \sim 1968$ s.

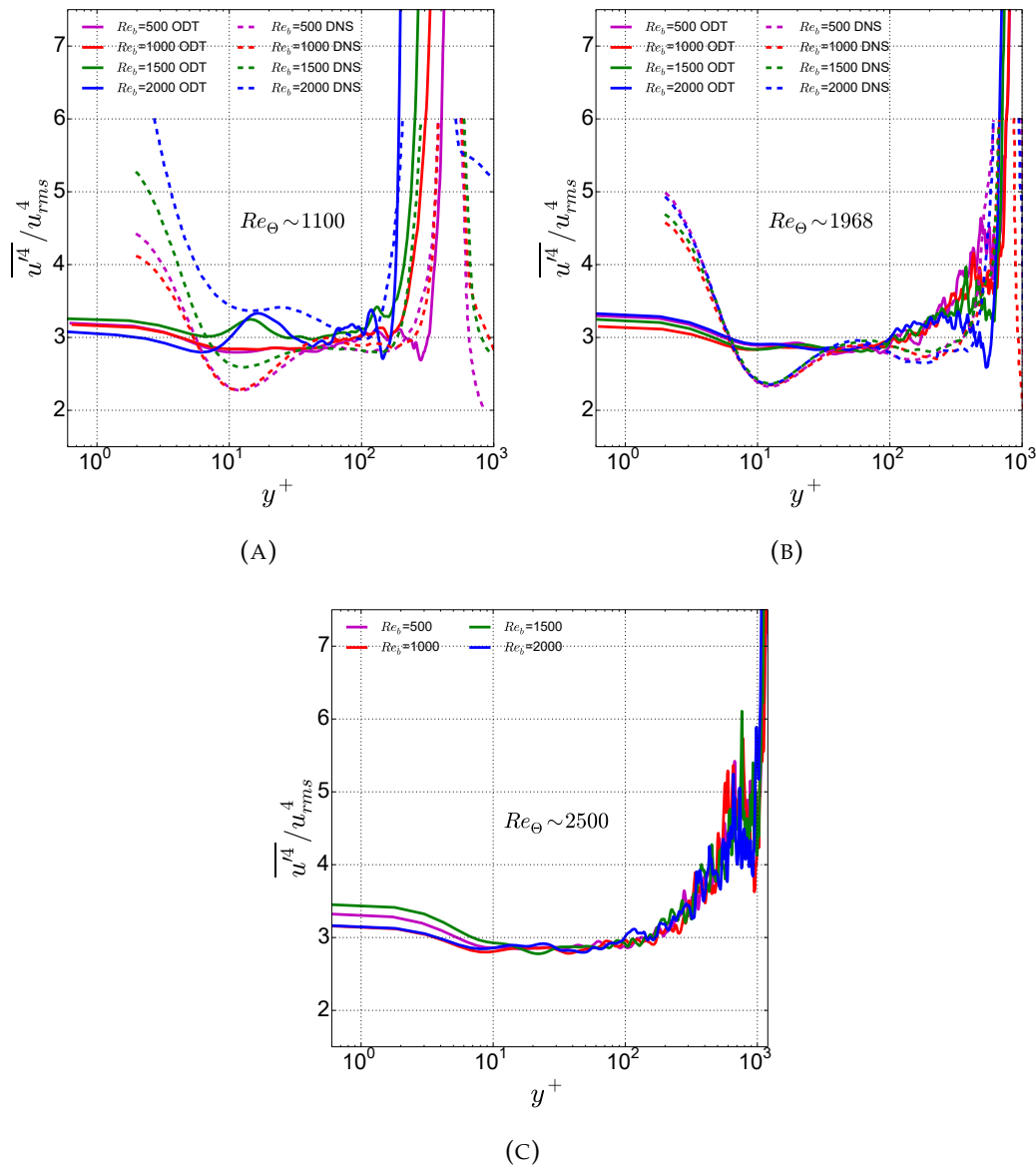


FIGURE 4.11: Profiles of the flatness of the streamwise velocity fluctuations as a function of the wall-normal coordinate (in viscous units) at (A) $Re_\theta \sim 1100$, (B) $Re_\theta \sim 1968$ and (C) $Re_\theta \sim 2500$. For comparison, the reference DNS data from [50] is shown at $Re_\theta \sim 1100$ and $Re_\theta \sim 1968$ s.

Further, the tendency of the ODT model is checked towards the flatness of the streamwise velocity component, $\overline{u'^4}/u_{rms}^4$, as a function of the wall-normal coordinate y^+ (in viscous units) and demonstrated in Figure 4.11 at (A) $Re_\theta \sim 1100$, (B) $Re_\theta \sim 1968$ and (C) $Re_\theta \sim 2500$ for $Re_b \geq 500$. ODT highly under-predicts the fourth-order velocity statistics in the inner region near the wall i.e. $y^+ < 10$ and over-predicts it in the region $10 < y^+ < 80$ for $Re_\theta \sim 1100$ as well as 1968. The profiles for ODT collapses onto each other for $Re_\theta \sim 1968$ and 2500 but do not collapse for $Re_\theta \sim 1100$ due to transitions to turbulence and these profiles do not show good agreement with the DNS data. Unlike the skewness, the kurtosis is relatively well captured by ODT for moderate

to large distances from the wall. Here the sign of u has no influence on the flatness, which is different from the skewness.

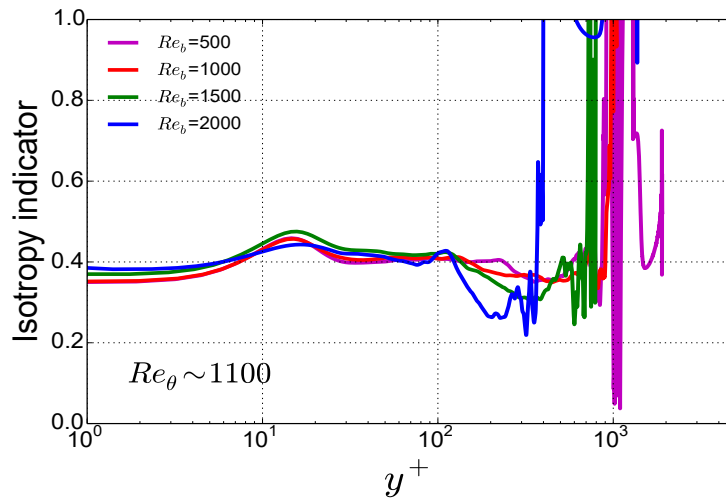
In general, ODT is more Gaussian than the DNS and close to the wall, we observe approximately a Gaussian flatness with a value close to three. This is attributed to the eddy motions and vortex stretching that remains unresolved in ODT but leads to inhomogeneity. The DNS may exhibit full 3-D instabilities and coherent structures that are completely absent in the stochastic picture of ODT. We might need to retain some 3D information to reproduce fourth-order velocity statistics and the model might overcome this limitation if finely resolved ODT lines are coupled with a coarse 3D LES mesh referred as OTLES [103]. OTLES allows simulations of much more complex flows by removing the restriction to one dimension.

4.4 Energy Spectra and Isotropy Indicator

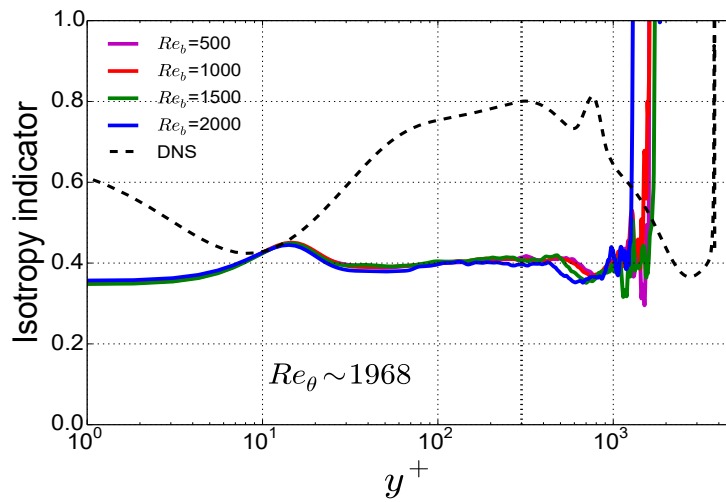
Figure 4.12 shows the isotropy indicator as a function of the wall-normal coordinate in viscous units at (A) $Re_\theta \sim 1100$, (B) $Re_\theta \sim 1968$ and (C) $Re_\theta \sim 2500$ for $Re_b \geq 500$. For reference, the DNS data from [41] is shown with black dashed line for $Re_\theta \sim 2000$ in Figure 4.12(B). The ratio of the wall-normal and streamwise rms velocity fluctuations, that is, v_{rms}^+/u_{rms}^+ is defined as the isotropy indicator. It is noted that in the present ODT set-up by construction $w_{rms} = v_{rms}$. The condition for isotropic turbulence is $v_{rms}/u_{rms} = 1$. This condition is not met for the present formulation as shown in Figure 4.12. Hence the turbulence dominated by u fluctuations across the boundary layer is not isotropic.

The initial conditions have influence on lower Re_θ , i.e., at $Re_\theta \sim 1100$ as shown in Figure 4.12 (A). The profiles for this particular Re_θ captures transitions to turbulence. Whereas, for higher Re_θ in Figure 4.12 (B) and (C) the flow is in fully turbulent state and the profiles for all Re_b overlap each other. The isotropy indicator in ODT depends very weakly on Re_b in the inner and buffer regions for the considered cases.

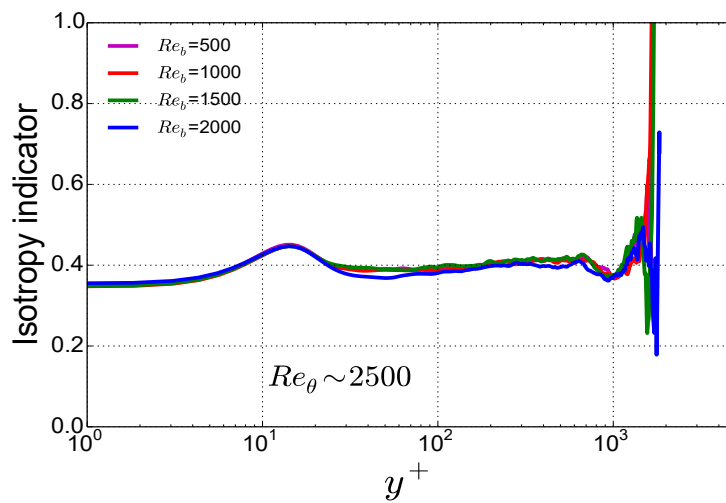
For all three Re_θ considered here, the isotropy indicator in the inner region is found to be slightly increasing for ODT and decreasing for DNS. ODT yields more anisotropic state for the turbulent boundary layer in comparison to DNS in the region $y^+ > 20$. The transfer coefficient α can be modified to achieve a much better match to the DNS isotropy indicator profile in the outer layer [96]. For the TBL flow configuration, the isotropy indicator is taken as a diagnostic model result in order to estimate 1-D turbulence spectra as discussed below.



(A)



(B)



(C)

FIGURE 4.12: Isotropy indicator v_{rms}^+/u_{rms}^+ as a function of the wall-normal coordinate (in viscous units) at (A) $Re_\theta \sim 1100$, (B) $Re_\theta \sim 1968$ and (C) $Re_\theta \sim 2500$. For comparison, the reference DNS data from [41] at $Re_\theta \sim 2000$ is given by a black dashed line.

Figures 4.13(A, B) show the energy spectra of the streamwise velocity at two different momentum Reynolds numbers, (A) $Re_\theta \sim 1100$ and (B) $Re_\theta \sim 1968$, respectively. The energy spectra in case of DNS can be calculated at different wall-normal positions due to the availability of both streamwise and spanwise statistics along with different Re_θ . But for the ODT model, the energy spectra are not dependent on wall-normal position while calculating for a particular Re_θ . In Figures 4.13(C,D), we try to calculate energy spectra at a different wall-normal position for the same Re_θ considered above and it was found that the energy spectra are same as Figures 4.13(A, B), hence, confirming that they are not dependent on wall-normal position while calculating for Re_θ .

The streamwise wavenumber in DNS is associated to the Fourier transformation of the streamwise profile of the fluctuating velocity field at a given wall-normal position y , or rather y^+ , while the spanwise direction can be used for ensemble averaging purposes. However, in ODT it is not possible to obtain a direct expression for the velocity field as a function of the streamwise position x due to the reduced dimensionality. Alternatives are available and could be considered. For example, by displacing solutions in time by means of a temporal-to-spatial correlation with a local advecting velocity. However, this alternative (displacing solutions from time-to-space) turns out to be counter-productive in this case, due to the developing character of the boundary layer in time. Hence, no temporal-to-spatial transformation can be used if the purpose of the study is to analyse energy spectra at a certain Re_θ , directly associated to a given instant of time.

To resort to the calculation of the spectra of velocity fluctuations along the line could be another possible alternative. In this case, for a certain Re_θ , the dependence on y^+ of the spectra is eliminated. The ODT and DNS fluctuating velocity spectra are compared based on the above reasoning. This is done by assuming equivalent isotropic turbulence energy spectra in ODT, i.e., a spatial Fourier transformation of the fluctuating velocity field along the line and a dependence on a k_{ODT} wavenumber. This represent the 1-D analog of the 3-D k -shell. However, the isotropic turbulence consideration here is clearly not the case in a boundary layer flow. This comparison nevertheless, allows us to assess the dependence of the turbulence spectra between DNS and ODT for the given Re_θ .

This approach is justified with the isotropy indicator shown above. The isotropy indicator exhibits a y^+ range with approximately uniform anisotropy. This range, $0 < y^+ < 300$ (for $Re_b = 500$ case at a $Re_\theta \sim 2000$), is used to generate the corresponding spectra. This range varies heavily with Re_b at the low $Re_\theta \sim 1100$ and more modestly at the high $Re_\theta \sim 2000$. The ODT spectra obtained using this methodology agrees qualitatively with DNS in the inertial range, although there is more large scale variability in ODT. This is also consistent with the outer peak observed for the Reynolds stress and the rms velocity profiles discussed above.

It is noted that the spectra for the lower Re_θ , i.e., $Re_\theta \sim 1100$ exhibit a clearer inertial range than those for the larger Re_θ ($Re_\theta \sim 1968$) in both DNS and ODT. The reason for this feature could be that the non-asymptotic state

($Re_\theta \sim 1100$) is more imbalanced than the asymptotic one ($Re_\theta \sim 2000$). The former is governed by a developing direct cascade that is closer to Kolmogorov's picture than the latter, in which the small-scale dissipation and multi-scale dynamics have saturated.

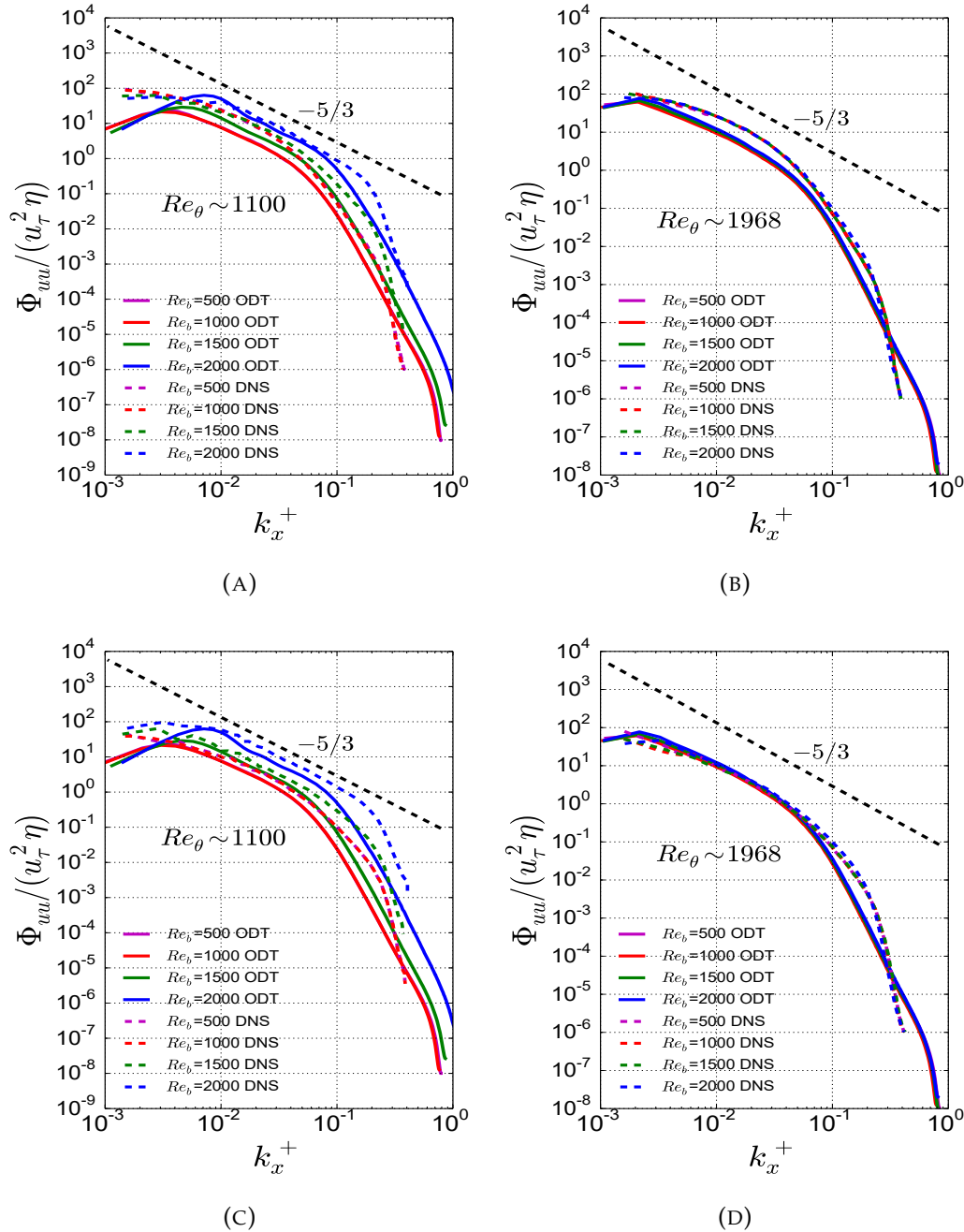
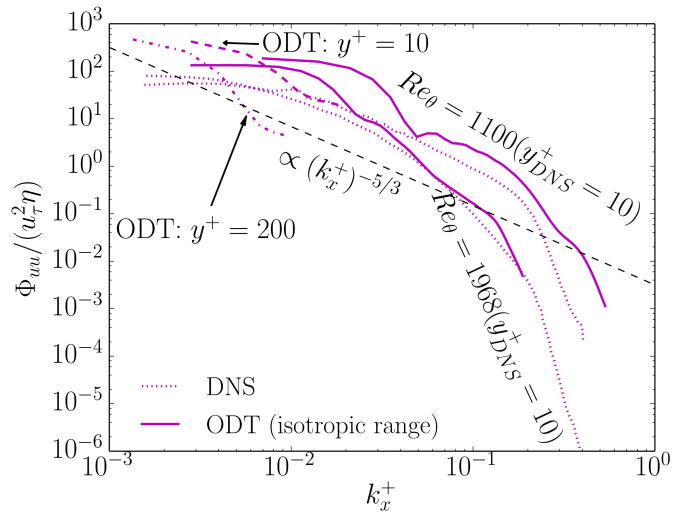
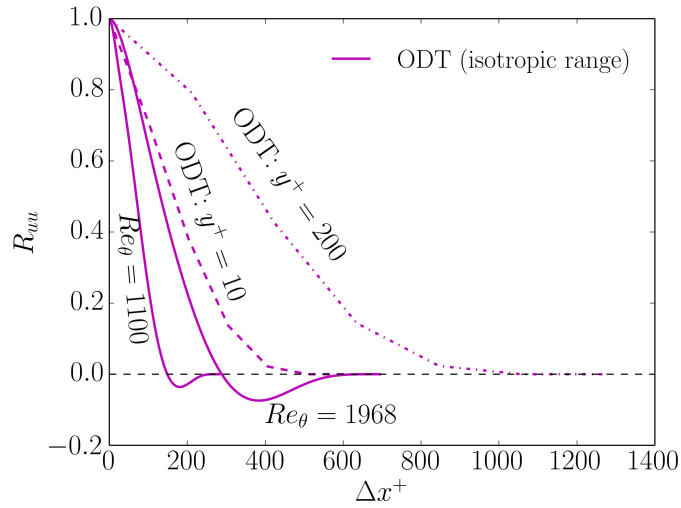


FIGURE 4.13: Streamwise energy spectra as a function of normalized wavenumber at (A) $Re_\theta \sim 1100$ and (B) $Re_\theta \sim 1968$. ODT has no dependence on y^+ in this case. For comparison, the DNS data from [50] at $y^+ = 10$ is shown.



(A)



(B)

FIGURE 4.14: (A) Wall-normal position dependent ODT energy spectra for the case $Re_b = 2000$. For comparison, the reference DNS data from [50] at $Re_{\theta} \sim 1100$ and $Re_{\theta} \sim 1968$ are shown. ODT results obtained for the time dependent spectra (in the uniform anisotropy range) are shown as well. The position dependent spectrum has no dependence on Re_{θ} in this case, while the time dependent spectrum has no dependence on the wall normal position. (B) Autocorrelation of the streamwise velocity fluctuations as a function of the normalized streamwise distance. Time dependent generated ODT spectra (in the uniform anisotropy range) are shown along the position dependent ODT spectra.

The alternative method to obtain spectra could be a transformation of a time series into a streamwise profile by means of Taylor's frozen-turbulence hypothesis, as in [124]. These spectra are just a modest comparison to show both the y^+ and θ dependence of the spectra and are considered next. Both

the effects are isolated from each other. In case of the DNS, the calculated spectra are certainly more detailed and faithful as compared to the reduced order formulation to the flow dynamics. Details for the calculation of the spectra along an alternative method proposed for the generation of the energy spectra is explained Appendix E.

Next, the alternative method to calculate spectra (for $Re_b = 2000$) is shown in Figure 4.14. The energy spectra is generated from a transformation of the time-series into a streamwise-series by means of Taylor's frozen-turbulence hypothesis, as in [124]. The comparison of spectra using this method is more direct in terms of the streamwise wavenumber k_x , however, as in [124], the fidelity of the magnitude of the energy is lost up to some extent due to the temporal-to-spatial transformation. Note that in this second alternative, there is no possible Re_θ dependency to calculate due to which we simultaneously plot both DNS spectra at different Re_θ for the comparison. The assumed window for time-averaging of the results is another drawback from these latter spectra. In this approach large amounts of simulation data (instantaneous flow profiles) have to be stored and processed afterwards and a serious drawback. As done in a more practical application, the output is limited and that is why we are not able to capture all temporal (and subsequently, streamwise) wavenumbers in this approach. This is seen in the shape of the autocorrelation function in Figure 4.14, which is only approximated in a very coarse time grid.

4.5 Temporal Behavior and its Influence on Structural Properties

The comparison of ODT structural properties with DNS i.e., (A) Re_τ , (B) H , (C) Re_δ and (D) Re_X with Re_θ , is plotted in Figure 4.15 for the five bulk Reynolds numbers $Re_b \in \{250, 500, 1000, 1500, 2000\}$ investigated. Note that the subfigure in all the plots represents the 1-D laminar profile obtained with the ODT solver ($Re_b = 250^*$) and $Re_b = 250$ the corresponding case for DNS. The DNS flow for this case is considered as laminar, however, for ODT, there is no prior guarantee that the transition to turbulence happens for the same values of diagnostic quantities as in the DNS. For the laminar profile, no eddy is implemented in the flow and only the diffusion term is solved. Additionally, we have also plotted the solution of $Re_b = 250$ case when both stochastic and deterministic terms are solved using the ODT methodology.

Figure 4.15 (A) shows the Re_τ variation with Re_θ and it is calculated using δ_{99} . The comparisons are made with the DNS data and the profiles are generally in good agreement. Although no convergence of the values with increased Re_θ is observed, unlike in the DNS data. At higher Re_θ , the Re_τ seems to converge for lower Re_b and it is expected that for higher Re_b , these profiles might converge for very high Re_θ . The value of Re_τ in case of DNS converges for $Re_\theta \sim 2000$, whereas for ODT in case of lower bulk Reynolds number it converges at $Re_\theta \sim 3000$. Table 4.1 summarises the values of Re_τ achieved at the last sampled Re_θ .

The shape factor (H) is the ratio of displacement thickness and momentum thickness, i.e., $H = \delta/\theta$, and is plotted with Re_θ in Figure 4.15 (B). The asymptotic H value reaches ~ 2.41 for the laminar flow, whereas for the other cases, the value converges to ~ 1.3 . In case of DNS, the value for H is ~ 1.4 . Like Re_τ variation explained above, H variation also confirms that the DNS results converges for $Re_\theta \sim 2000$ and the ODT results converges at $Re_\theta \sim 3000$. The figure presents that the shape factor for ODT is in relatively good agreement with DNS.

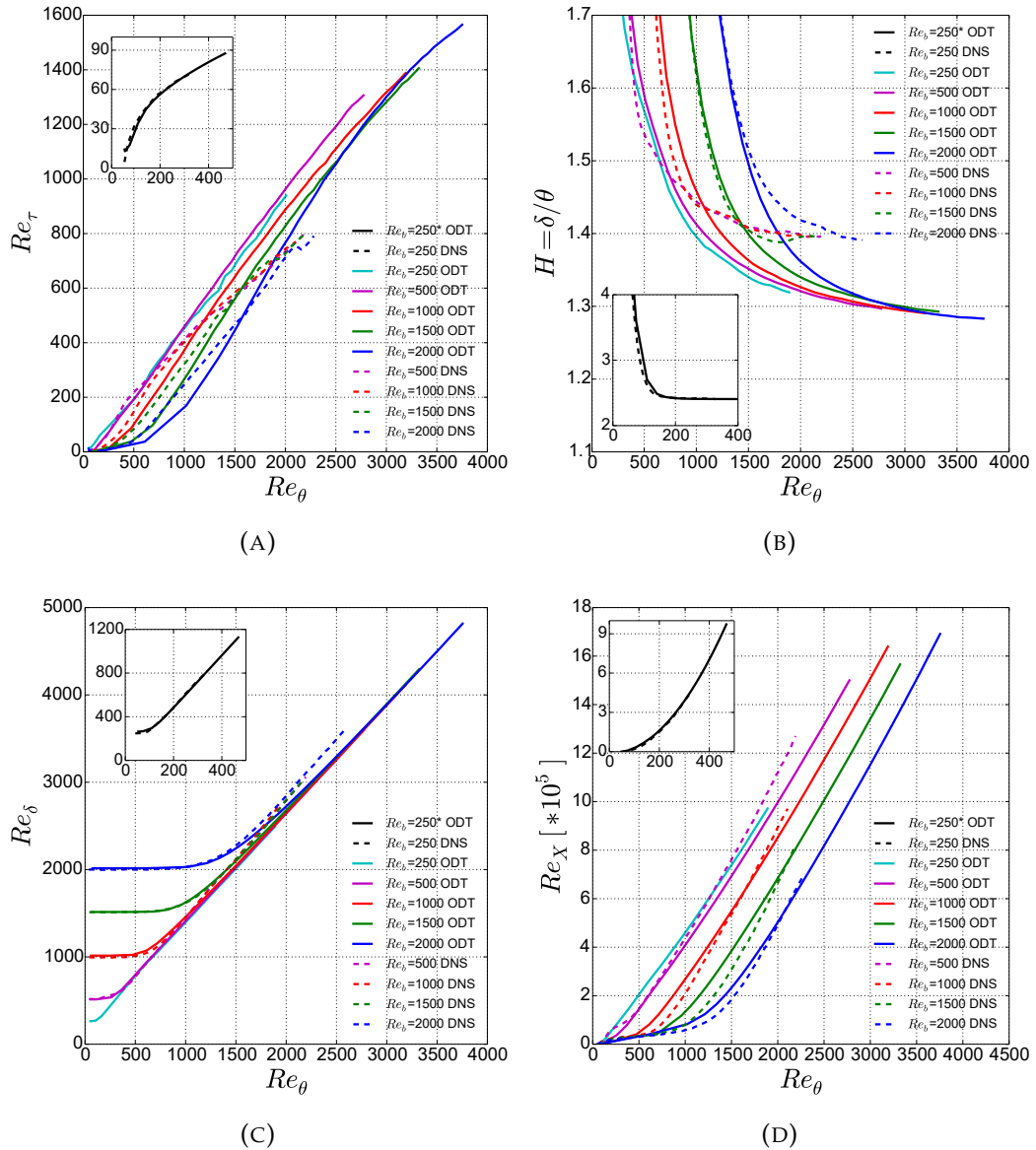


FIGURE 4.15: The quantities (A) Re_τ , (B) H , (C) Re_δ and (D) Re_x as a function of Re_θ . For comparison, the reference DNS data from [50] is shown. The sub-figure in all the plots shows the laminar profile for ODT ($Re_b = 250^*$) and the corresponding DNS [50].

The variation of the displacement Reynolds number Re_δ with momentum

TABLE 4.1: ODT simulation results for friction Reynolds number Re_{τ} , displacement Reynolds number $Re_{\delta_{99}}$, momentum Reynolds number Re_{θ} (f for final value of the quantities), skin friction C_f , displacement thickness δ_{99} (relative to d here), von Kármán's constant K and shape factor H .

Case	$Re_{\tau,f}$	$Re_{\delta_{99},f}$	$Re_{\theta,f}$	$Re_{\delta,f}$	$Re_{X,f} [10^5]$	$C_f [10^{-3}]$	δ_{99}/d	K	H
R1000C1	1388	32,900	2779	3691	16.4	3.67	32.9	0.33	1.33
R1000C2	1388	32,900	3519	4463	16.4	4.72	32.9	0.46	1.27
R1000Z1	1388	32,900	3357	4346	16.4	4.62	32.9	0.40	1.29
R1000Z2	1388	32,900	3070	3956	16.4	4.02	32.9	0.39	1.29
R1000A1	1388	32,900	3353	4281	16.4	4.45	32.9	0.44	1.28
R1000A2	1388	32,900	2887	3811	16.4	3.86	32.9	0.35	1.28
R1000L1	1388	32,900	3578	4557	16.4	5.16	32.9	0.43	1.27
R1000L2	1388	32,900	3546	4551	16.4	5.17	32.9	0.42	1.28
R1000L3	1388	32,900	3308	4301	16.4	4.57	32.9	0.40	1.30
R250*	88	3675	468	1127	9.72	3.48	1.47	—	2.41
R500	1306	28,900	2774	3598	15.0	5.05	57.8	0.40	1.30
R1000	1388	32,900	3190	4118	16.4	4.24	32.9	0.40	1.29
R1500	1406	33,600	3322	4294	15.7	3.91	22.4	0.39	1.29
R2000	1565	38,000	3754	4816	16.9	4.09	19.0	0.37	1.28

Reynolds number Re_θ is shown in Figure 4.15 (C) for all the bulk Reynolds numbers, i.e., $Re_b \in \{250^*, 500, 1000, 1500, 2000\}$. The final values for all bulk Reynolds numbers achieved are $Re_\delta \in \{1127, 3598, 4118, 4294, 4816\}$, respectively. All the profiles show good agreement with DNS for all Re_b cases. As $Re_\delta/Re_\theta = H$, therefore, the collapse of the profiles into the very same slope signalize the consistency with the results for the asymptotic H value.

The streamwise Reynolds number Re_X as a function of the momentum Reynolds number Re_θ is shown in Figure 4.15(D) for the considered cases. This quantity is directly proportional to the elapsed simulation time ($X = U_b t$). The ODT results show a slight shift for low Re_b numbers in comparison with the DNS results. However, the shift is reduced for higher Re_b . This can be expected as the assumptions for ODT are more applicable to fully developed turbulent flows at higher Reynolds numbers. For $Re_b \in \{250^*, 500, 1000, 1500, 2000\}$, the $Re_X/10^5$ achieves 9.7, 15.0, 16.4, 15.7, 16.9, respectively as its final values and are given in Table 4.1. All the profiles show very good agreement with the DNS profiles, considering the reduced dimensionality of the ODT model.

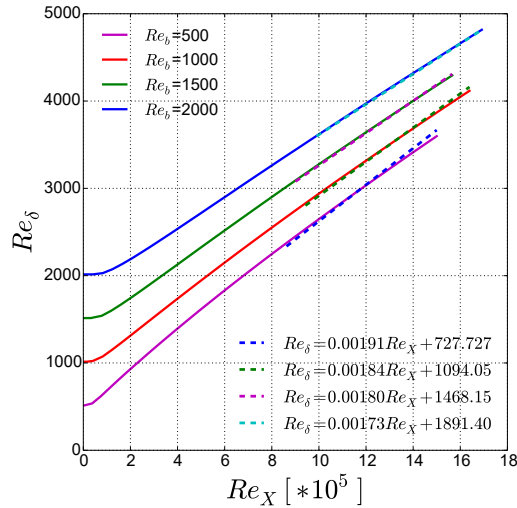


FIGURE 4.16: The quantity Re_δ as a function of Re_X . Dashed line represent linear fit between Re_X and Re_δ for the considered bulk Reynolds numbers.

The far-field asymptote of the boundary layer growth law, i.e., the dependence of Re_δ on Re_X is the most basic global boundary layer property and is shown in Figure 4.16. This connects the boundary layer growth in terms of $\delta(t)$ with the notional spatial displacement $X(t)$ and emphasizes the correlation between the TBL and the SBL cases. Now that ODT has been calibrated and validated for the TBL, it is a unique tool for exploration of global TBL properties at large Re_X . The Figure shows linear behaviour of the quantities and the equation for empirical linear fits, $Re_\delta = m Re_X + n$, are given together with the ODT data in Figure 4.16. These equations relates Re_δ with Re_X and can be used to convert between the two Reynolds numbers. The slope m does not depend on Re_b and it reduces only weakly for increasing Re_b , whereas, the constant offset, n , depends strongly on Re_b . The slope is obtained as

$m = (1.82 \pm 0.08) \times 10^{-3}$ for $500 \leq Re_b \leq 2000$. Here the confidence level is estimated with the standard deviation.

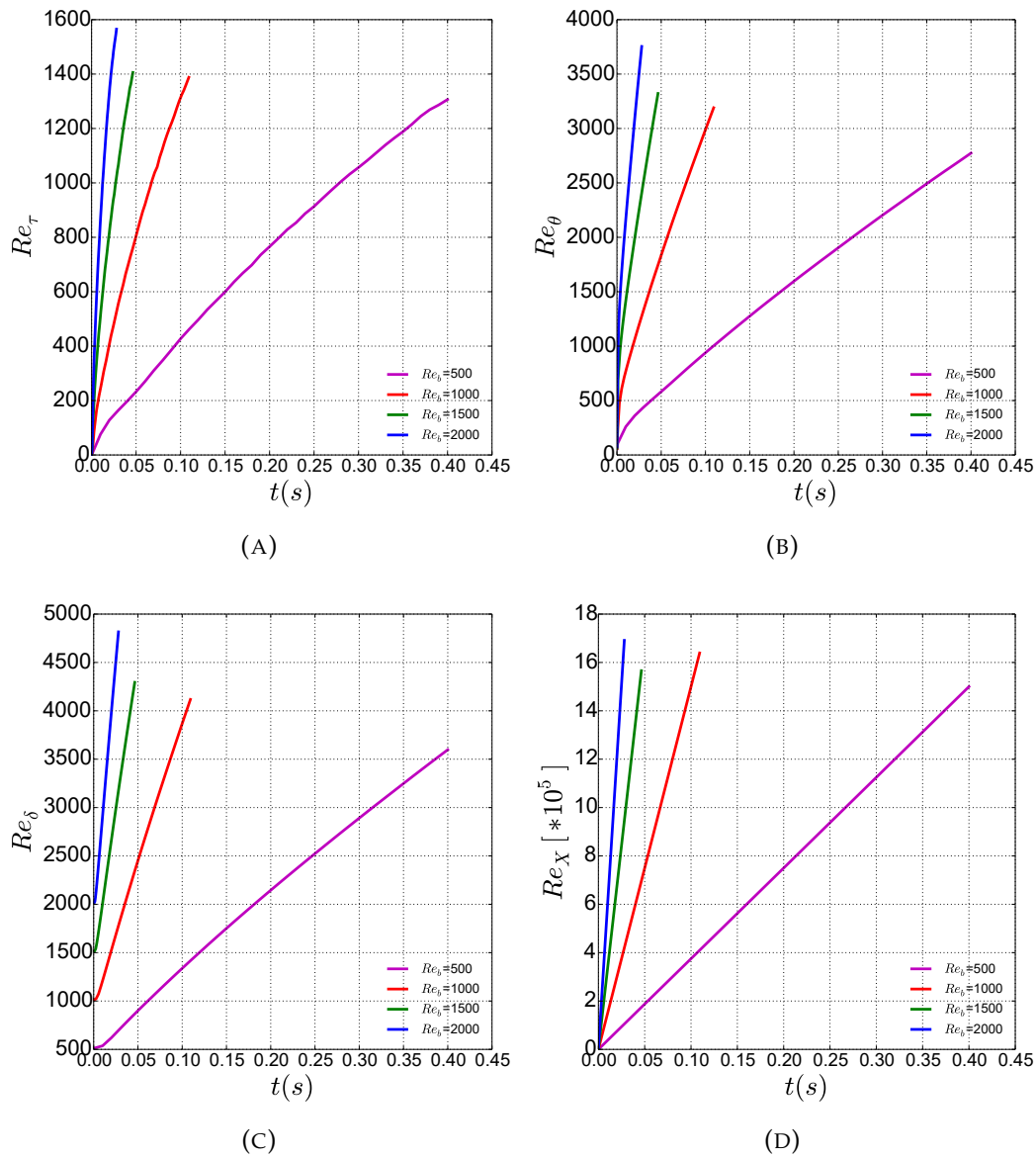


FIGURE 4.17: The quantities (A) Re_τ , (B) Re_θ , (C) Re_δ and (D) Re_X as a function of time.

The above discussed global properties are varied with Re_θ , where Re_θ represents the instants. It would be interesting to check behaviour of these properties directly varied with time as well. Next, the ODT structural properties are presented as a function of time for (A) Re_τ , (B) Re_θ , (C) Re_δ and (D) Re_X plotted in Figure 4.17 for the four bulk Reynolds numbers $Re_b \in \{500, 1000, 1500, 2000\}$ investigated. The DNS results for these quantities with time is not available, hence only the ODT properties are presented and discussed.

All the properties, as expected, are growing with time. The Re_τ value, shown in Figure 4.17 (A), are very high for higher Re_b within a very short time

interval. As discerned from the figure, Re_τ is approximately 1600 for $t < 0.05$ s for $Re_b = 2000$, whereas this value is < 1400 even for $t = 0.40$ s for $Re_b = 500$. This behaviour is similar for Re_θ , Re_δ and Re_X shown in Figure 4.17 (B-D) as well. Note that Re_θ represents time analogous and it is expected linearly growing with time which is discerned in the figure. In addition, Re_X is also directly proportional to time, as explained above and is confirmed here.

The quantities (A) δ_{99} and (B) θ as a function of time are presented in Figure 4.18 for all four bulk Reynolds numbers $Re_b \in \{500, 1000, 1500, 2000\}$ considered for TBL flow configuration. Both the quantities are growing linearly with time. However, δ_{99} value achieved is approximately 0.02 m and θ is 0.002 m for $Re_b = 2000$. Whereas, these values for $Re_b = 500$ are approximately 0.06 and 0.006 m, respectively. The $Re_b = 2000$ case is done for very small simulation time because the statistics compared with DNS for this case is achieved within short duration.

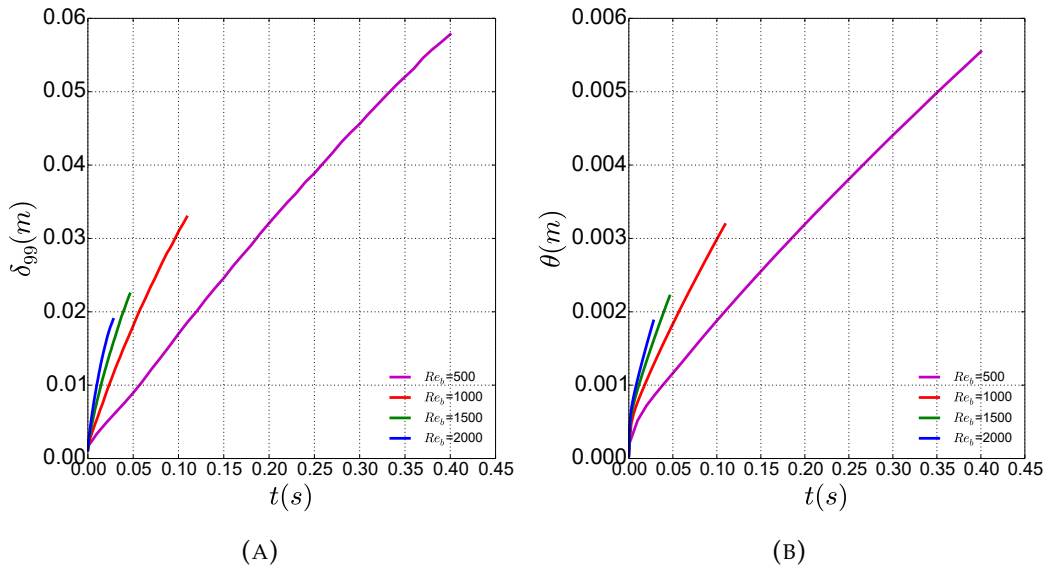


FIGURE 4.18: The quantities (A) δ_{99} and (B) θ as a function of time.

Next, the shape factor H is varied with time and is shown in Figure 4.19 for all four bulk Reynolds numbers $Re_b \in \{250, 500, 1000, 1500, 2000\}$. The trend for this figure is consistent with the Figure 4.15 (B) discussed above which means that the H is converging with time. For $Re_b = 500$, H have been almost converged indicating a fully developed flow, whereas, for higher bulk Reynolds numbers, i.e., $Re_b = 1000, 1500$ and 2000 , the H profile is still in the transitions to turbulence. For these higher Re_b case, the simulation time needs to be significantly increased to achieve fully developed turbulence flow.

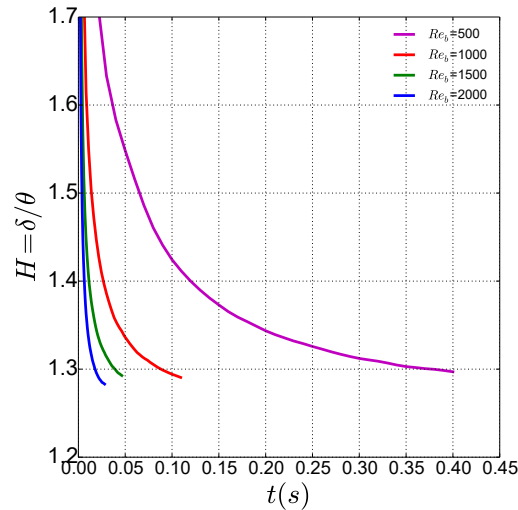


FIGURE 4.19: The quantity H as a function of time.

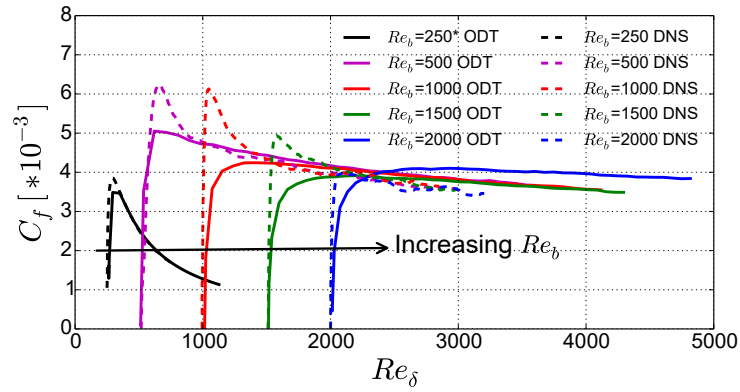
Figure 4.20 displays the variation of skin friction coefficient, $C_f = 2/(U_b^+)^2$ with (A) Re_δ , (B) Re_θ and (C) Re_X Reynolds number for five discrete bulk Reynolds numbers, i.e. $Re_b = [250, 500, 1000, 1500, 2000]$. C_f is important since it has direct influence on the nature of the flow and represented as the ratio of the wall shear stress to the dynamic pressure. The asymptotic values achieved for skin friction coefficient for all Re_b are mentioned in Table 4.1.

Figure 4.20(A) implies that the value of Re_δ is increased with increasing Re_b and the opposite is observed for temporal development of turbulent boundary layer represented by C_f . Nevertheless, the ODT results shows a similar behaviour as the reference DNS data from [50], with slight under-prediction of the C_f peaks using ODT methodology. The peak height can be modified by changing the model parameters. However, the parameters show influence on the velocity statistics as well. All the profiles finally collapses onto each other. It can be observed that for the laminar case, i.e., $Re_b = 250$, the value of skin friction coefficient is $\sim 4 \times 10^{-3}$. However, for other cases, i.e., $Re_b = [500, 1000, 1500, 2000]$, the value of C_f decreases from $\sim 5 \times 10^{-3}$ to 4×10^{-3} , showing better agreement with DNS for higher Re_b numbers.

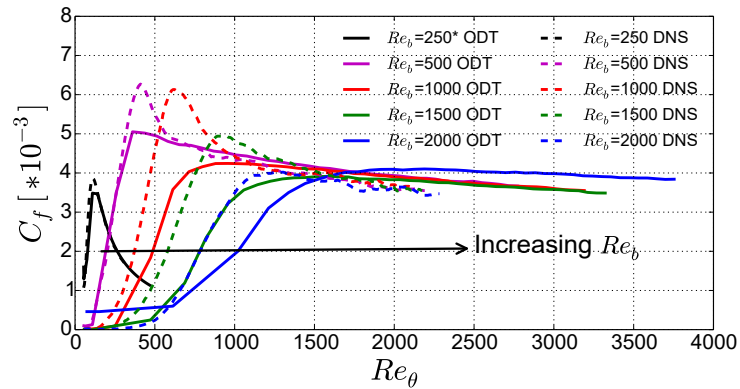
Figure 4.20 (B) shows the development of C_f with Re_θ . Initially, the profiles for ODT show deviation from the DNS data and finally with the slight delay, these profiles approaches towards each other similar to DNS indicating asymptotic insensitivity to the initial Re_b . Similar to Re_δ , the behavior of C_f with Re_θ is very similar to the DNS profiles reported by [50] with slight under-prediction of the C_f peaks by ODT which depends on the model parameters. With the selected set of optimal model parameters, however, the qualitative trends are sufficiently well reproduced, as well as the collapse in the fully turbulent state along with the lower and higher order statistics. This behaviour once again hints at the predictive capabilities and the overall consistency of the ODT model.

Figure 4.20 (C) shows the variation of C_f with Re_X . The C_f profile behaves differently with Re_X as compared to its behavior with Re_δ and Re_θ . In the two previous cases, we found a fair collapse of all the profiles at larger

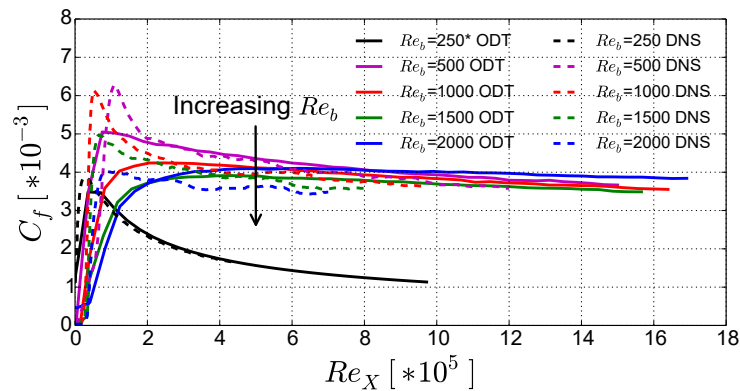
Re_θ , however, for this case the collapse is not achieved and there is a clear scattering of the profiles. The same behavior is observed for the DNS case [50].



(A)



(B)



(C)

FIGURE 4.20: Skin friction coefficient C_f as a function of (A) Re_δ , (B) Re_θ and (C) Re_X . In the case of ODT, $Re_b = 250^*$ represents the laminar solution. For comparison, the reference DNS data from [50] is shown.

4.6 Coefficients in the Transient and Asymptotic State

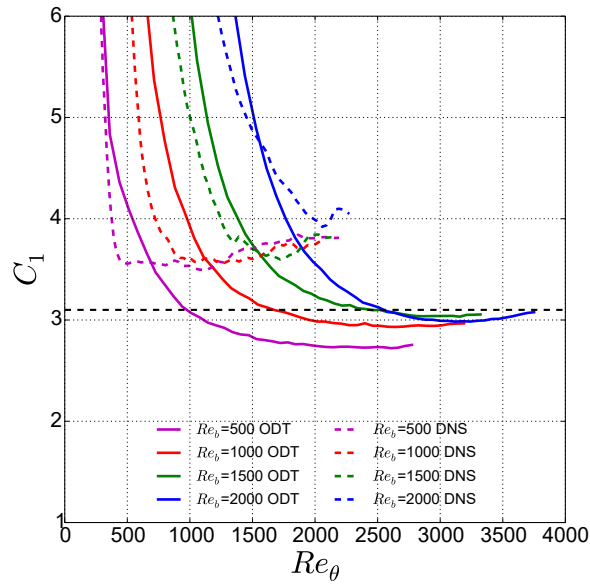
The temporal development and the asymptotic values of the coefficients C_1 and C_2 are addressed in this section. The coefficients, (A) C_1 and (B) C_2 obtained with ODT as a function of Re_θ in comparison with the DNS data [50] are shown in Figure 4.21. The DNS as well as the ODT results exhibit an initial transient phase in which the values of C_1 and C_2 drop very rapidly. Here, this temporal behavior is shown in a normalized fashion due to the transformation of the time axis to the momentum Reynolds number Re_θ . Both ODT and reference DNS suggest once again the existence of an approximately universal asymptotic state that is approached for large Re_θ when the system has ‘forgotten’ its initial condition. This state is characterized by $C_{1,ref} \sim 4.0$ and $C_{2,ref} \sim 25$ in the available reference data [119, 125, 50] but somewhat lower values in ODT, which are $C_1 \sim 3.1$ and $C_2 \sim 17$ and these asymptotic values of the ODT solutions are given by dashed lines in Figure 4.21 (A) and (B).

Based on the coefficients, C_1 and C_2 , the asymptotic state is approximately reached for $Re_\theta > Re_b$ in the reference DNS [50] but delayed to somewhat larger values of Re_θ for ODT (factor 1.5). This suggests that the dynamics of both the transient and asymptotic parts of the solution are different in ODT. Nevertheless, it is remarkable that the lower-order stand-alone ODT model is able to capture the relevant flow physics reasonably well.

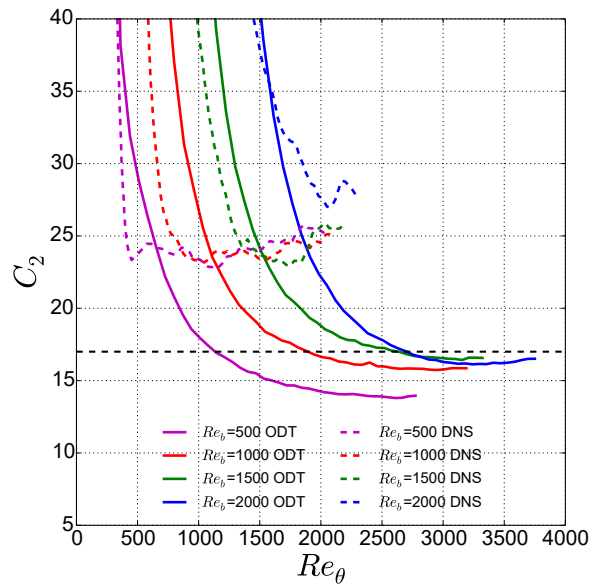
The relatively small range of Reynolds numbers investigated is another aspect and this raises the questions whether and to which extent the temporal development changes, even in the DNS, when Re_b is increased. The reference DNS for the highest available Reynolds number, $Re_b = 2000$, seemingly has not yet reached the asymptotic state up to $Re_\theta \sim 2300$ and it seems to require longer to reach the asymptotic state that manifests itself by a rather abrupt change of the slope of C_1 and C_2 . This in case of ODT solutions is different, where C_1 and C_2 level out more gradually towards high Re_θ . The solution for the smallest Reynolds number, $Re_b = 500$, exhibits systematically lower values of the coefficients than the other ones. This is likely due to the specific choice of the ODT model parameters for the TBL flow configuration. As discussed above, the similarity properties of the ODT solution suggests that the systematically lower values of C_1 and C_2 are consistent with the limitations of the lower-order formulation.

The semi-empirical equation discussed earlier is finally presented in order to quantitatively address the balance for the asymptotic ODT state. The different contributions to the semi-empirical equation for ODT as well as the available reference DNS [50] are summarised in Table 4.2. A re-analysis of published data was done to obtain the reference values. A similar quantification has not been conducted so far in the relevant literature to the best of our knowledge. This is also used to quantify the consistency of theory, DNS and ODT. Note that both DNS and ODT are well within a 10% error margin of the empirical prediction across the range $500 \leq Re_b \leq 2000$ investigated. Furthermore it can be seen in Table 4.2 that the relative error decreases for ODT with increasing Re_b . This error is non-monotonic for the reference DNS

which may be related to an insufficiently developed turbulent state. The relative errors are comparable for the largest $Re_b = 2000$ investigated for ODT and DNS. A larger Reynolds number yields a broader range of scales and, thus, a more featureless, ‘stochastic’, state of the flow which leads to the expectation that the ODT modeling error reduces with increasing Reynolds number and has been confirmed for other applications (e.g. [96, 98, 126]). The numerical values noted in Table 4.2 might therefore depend on the Reynolds number.



(A)



(B)

FIGURE 4.21: Integral coefficients characterizing the TBL as function of Re_θ , (A) C_1 and (B) C_2 . For comparison, the reference DNS data from [50] is shown.

TABLE 4.2: Contributions to the semi-empirical equation for constant coefficients C_1 and C_2 in the asymptotic state of the TBL. The ODT and DNS results are given as $C_1 \sim 3.1$ and $C_2 \sim 17$ for ODT (dashed lines in Figure 4.21) and $C_1 \sim 4$ and $C_2 \sim 25$ for DNS [50]. AE and RE denote the absolute and relative error of the balance of the semi-empirical equation.

Re_b	U_b^+	θ/δ_{99}	C_1/U_b^+	$C_2/(U_b^+)^2$	AE	RE	
500	ODT	22.5	0.09595	0.1378	0.0336	0.0082	8.5%
	DNS	23.5	0.1268	0.1702	0.0453	0.0019	1.5%
1000	ODT	22.6	0.09687	0.1372	0.0333	0.0070	7.2%
	DNS	23.2	0.1255	0.1724	0.0464	0.0005	0.4%
1500	ODT	22.8	0.09867	0.1360	0.0327	0.0046	4.7%
	DNS	23.6	0.1320	0.1695	0.0449	0.0074	5.6%
2000	ODT	23.4	0.09884	0.1325	0.0310	0.0027	2.7%
	DNS	23.7	0.1268	0.1688	0.0445	0.0025	2.0%

4.7 In Closing

The chapter presented a detailed validation for the temporally developing turbulent boundary layer. Using the selected model parameters (discussed in Appendix C), the various velocity statistics and important global properties for boundary layer-type flows are compared with the available reference DNS data from [50, 41]. Further statistics for TBL at higher Reynolds numbers is provided in Appendix F.

Chapter 5

Spatially Developing Turbulent Boundary Layer

In this chapter, the main focus is applying the spatial ODT (S-ODT) formulation to investigate the spatially developing turbulent boundary layer (SBL). This chapter is divided into several sections discussing about domain size sensitivity towards the statistics, simulation results for two bulk velocities in comparison with the DNS data and finally the results from Chapter 4, i.e., for TBL are compared with the SBL formulation. A detailed parameter sensitivity for selecting optimal set of parameters in case of SBL configuration is presented in Appendix G and the physical model parameters used to carry out the simulations presented in this chapter are used as $\alpha = 2/3$, $C = 6$, and $Z = 600$. Some of the results discussed in this chapter have been published in [112] and [127].

5.1 Influence of Domain

The influence of the domain size on velocity statistics is analyzed in this section. This is done for different Re_θ as a prerequisite check to make sure that the simulations performed on various domain sizes within the Reynolds number variation campaign would remain unaffected by any domain size considered. To capture the boundary effects onto the flow, the domain size is increased. It also verifies if the increasing boundary layer sizes are accommodated in case of ODT similar to the reference DNS. In [128], the asymptotic suction boundary layer investigation via LES reported a strong dependence of the boundary layer thickness on domain dimensions. The large eddies in the outer region of the flow are suppressed by a very small domain size. The wake strength exhibited by the flow in very small domain are entirely vanished, once the spanwise domain exceeds approximately two boundary layer thickness [129]. The authors indicates that at these domain sizes, the boundary layer thickness and friction Reynolds number may acquire box-size independent values.

The mean streamwise velocity and the rms profiles at $Re_\theta \approx 2000, 4000$ and 8000 using the optimal set of physical parameters in comparison with the

DNS and LES data from [41, 82] are shown in Figure 5.1, 5.2 and 5.3, respectively. ODT simulations are carried out for two domains, $D1 = 45,000\nu/U_b$ and $D2 = 90,000\nu/U_b$ and here the domain size D has been selected in bulk units, i.e., ν/U_b .

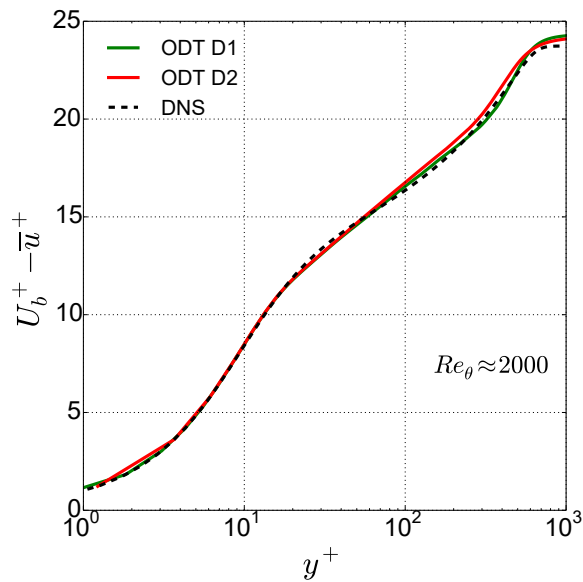
The simulations performed with increased domain size for $Re_\theta \approx 2000$ (Figure 5.1) show identical results to the reference DNS data for both the domain sizes considered for the mean as well as rms velocity profiles. In Figure 5.2 at $Re_\theta \approx 4000$, the profiles are in good agreement with the DNS data for both domain sizes. However, Figure 5.3 shows that at $Re_\theta \approx 8000$, the rms profile for $D1$ is not matching with LES and there is some part missing. Nevertheless, the mean velocity profile for this Re_θ is acceptable for both domain sizes considered in comparison with the LES.

The trend for rms profile for $D1$ is same for the model parameters C and Z considered in Appendix G. Hence, $D2$ is considered for simulations at $Re_\theta \approx 8000$ to capture the boundary effects onto the flow. The increasing boundary layer sizes are not accommodated for $D1$ and this domain size is discarded for higher momentum Reynolds numbers.

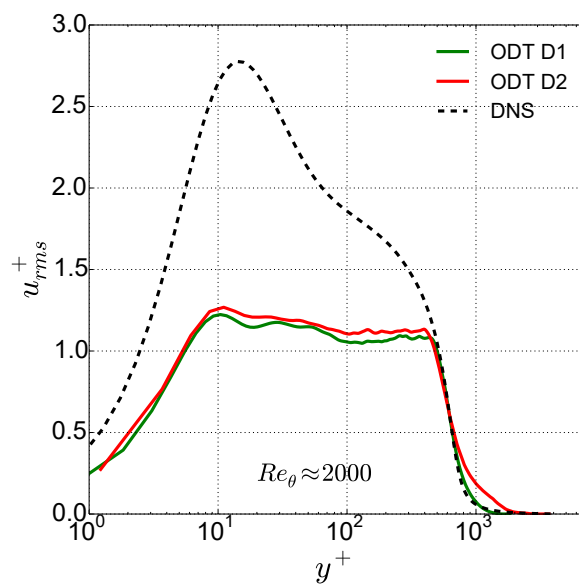
5.2 Variation of Bulk Reynolds Numbers

This section presents various velocity profiles (up to 4th order) at several Re_θ . For $Re_\theta \approx 2000, 4000$ and 8000 the ODT results are shown in comparison to the available reference DNS data from [41] and LES data from [82]. To further analyse the influence of various statistics with increasing Re_θ , the ODT results are given at $Re_\theta \approx 12000, 16000$ and 20000 . Note that the preliminary results for velocity statistics up to 4th order for $Re_\theta \approx 2000$ are published in [112]. Here, the investigation is extended for higher Re_θ . Some of the structural properties, like Re_τ , H and C_f as a function of Re_θ up to $\approx 27,000$ are also shown. The bulk velocity is varied to extend this investigation to determine the predictive capabilities of the model on various statistics. The reference DNS data is available for bulk velocity $U_b = 12$ m/s (indicated as $U1$ in figures) and for the ODT model, in addition, the simulations are also performed for $U_b = 24$ m/s (indicated as $U2$ in figures). The physical model parameters remain fixed for this purpose which are $\alpha = 2/3$, $C = 6$ and $Z = 600$.

Figure 5.4(A,B) illustrate the simulation set-up for two bulk velocities, i.e., (A) $U_b = 12$ m/s and (B) $U_b = 24$ m/s. To initiate transitions, the velocity U_b is provided at the bottom wall and propagation of turbulence is observed at several streamwise positions. Velocity field is shown on a ODT domain on y -axis which is same for both bulk velocities ($D1$ for the present case) and on x -axis, is the streamwise location. Note that x -axis does not represent complete streamwise domain, instead, the streamwise location represent only a screenshot for a particular position. Since position can be represented by Re_θ so different Re_θ corresponding to the streamwise locations are provided in the figure. Figure 5.4(A) depicts the snapshots for $U_b = 12$ m/s at $Re_\theta = [686, 2223, 3767, 4643, 6104]$ (representing different streamwise position on the x -axis) from (i-v), respectively. It can be seen from the snapshots

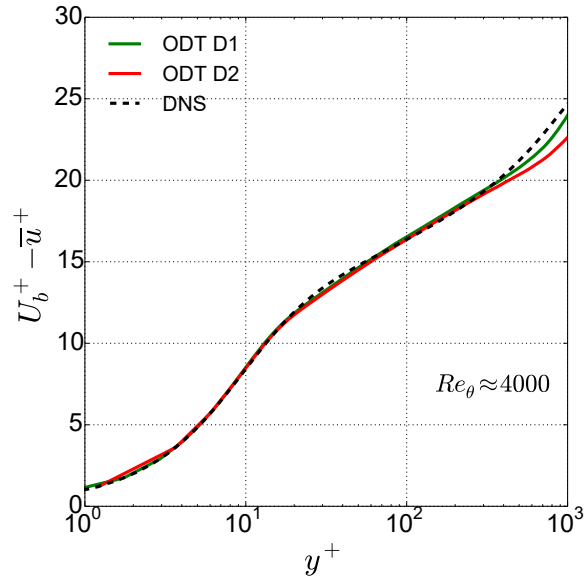


(A)

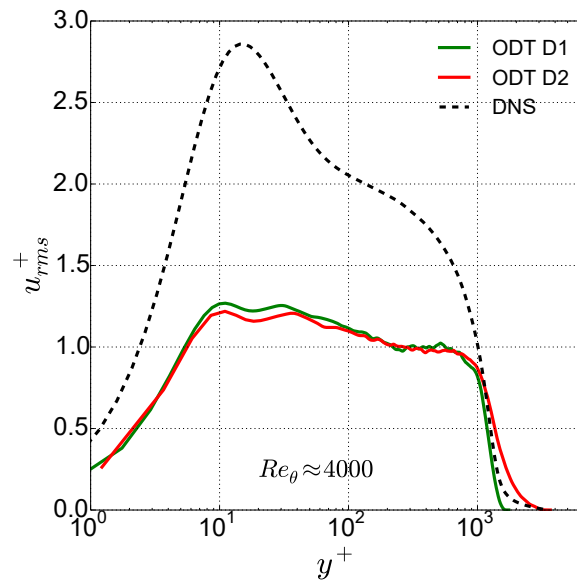


(B)

FIGURE 5.1: Normalized wall-normal profiles of the (A) mean streamwise velocity and (B) rms velocity at $Re_\theta \approx 2000$ for $D1$ and $D2$ domain size. ODT results are shown in comparison to the reference DNS [41] at the matched Re_θ .

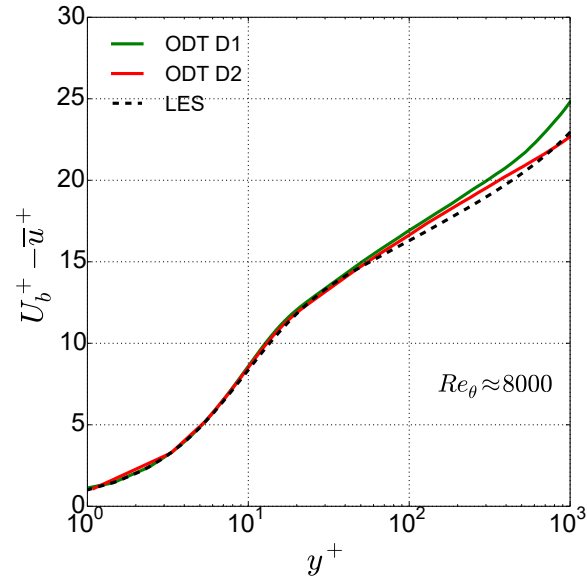


(A)

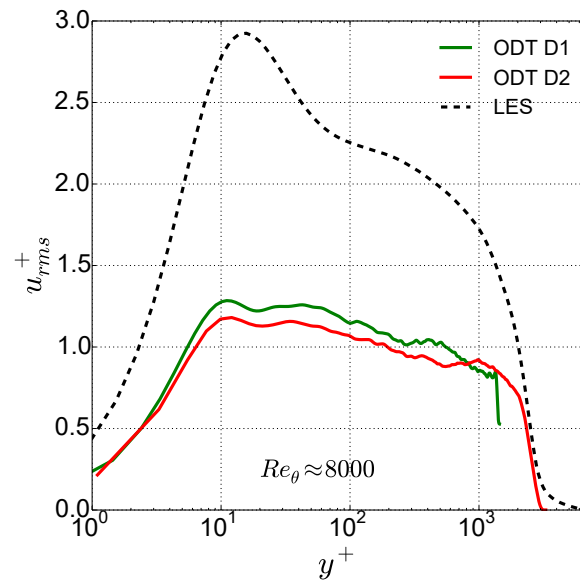


(B)

FIGURE 5.2: Normalized wall-normal profiles of the (A) mean streamwise velocity and (B) rms velocity at $Re_\theta \approx 4000$ for $D1$ and $D2$ domain size. ODT results are shown in comparison to the reference DNS [41] at the matched Re_θ .



(A)



(B)

FIGURE 5.3: Normalized wall-normal profiles of the (A) mean streamwise velocity and (B) rms velocity at $Re_\theta \approx 8000$ for $D1$ and $D2$ domain size. ODT results are shown in comparison to the reference LES [82] at the matched Re_θ .

that for $Re_\theta = 686$, i.e. in the initial stage (Figure 5.4(A)(i)), the fluctuations are less than higher Re_θ . The turbulence is propagated, however, away from the wall with streamwise location. It is increased for higher Re_θ . The general information for Figure 5.4(B) ($U_b = 24$ m/s) remains consistent with Figure 5.4(A). When these visualizations are compared with the different bulk velocities, it is found that the transitions to turbulence depends on Re_θ as well as U_b . The transitions to turbulence are started earlier for higher U_b and are further increased with streamwise position. The snapshots for both the U_b are at the same location but the values for Re_θ are higher for larger U_b at same location.

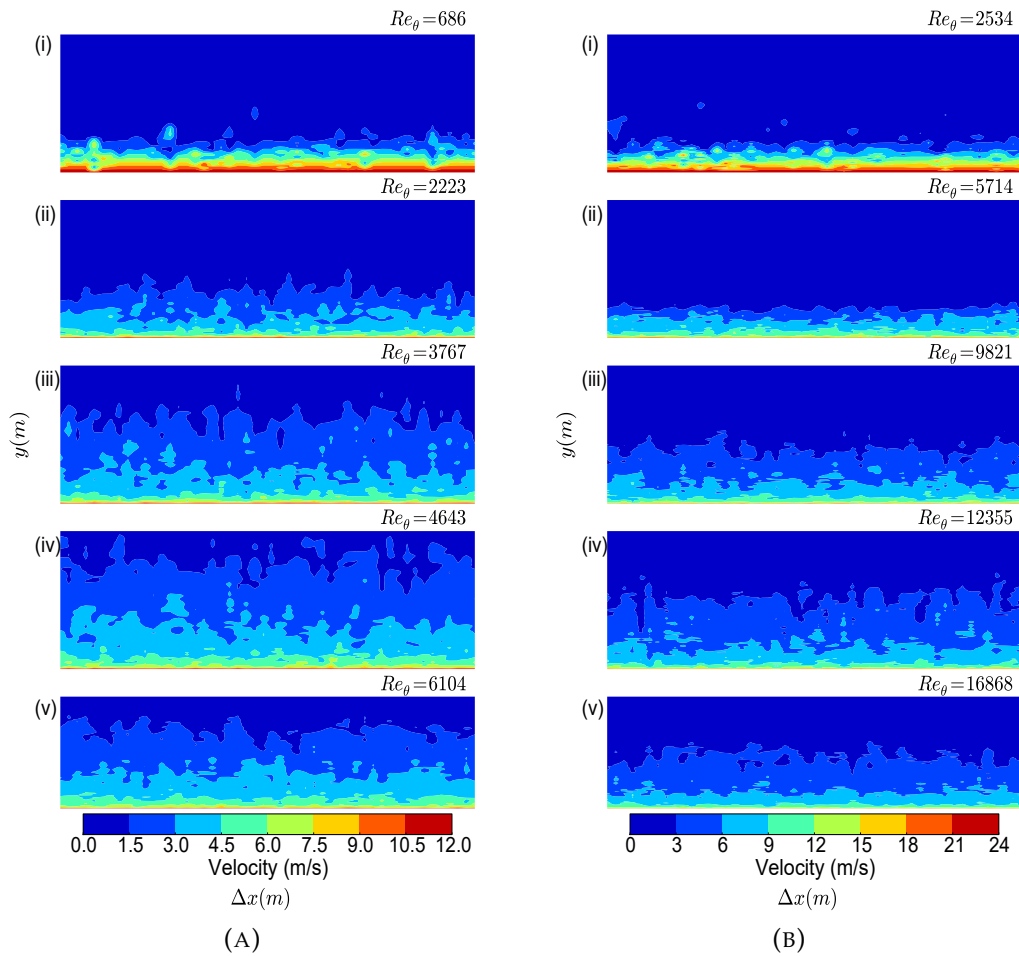


FIGURE 5.4: Velocity field with domain on y -axis (in m) and streamwise location on x -axis (in m) in terms of corresponding Re_θ for two bulk velocities (A) $U_b = 12$ m/s and (B) $U_b = 24$ m/s.

The spatially developing turbulent velocity boundary layer is shown in Figure 5.5 (a,b) for the bulk velocities investigated above, i.e., (a) $U_b = 12$ m/s and (b) $U_b = 24$ m/s. The velocity boundary layer is shown on the ODT domain on y -axis (same as the figure discussed above). This is growing with streamwise location on x -axis. The Re_θ are calculated corresponding to

particular location on x -axis. This figure illustrates the dependence of propagation of transitions to turbulence with streamwise position as well as on U_b . For both U_b , the flow is in fully turbulent state and Re_θ reached are very high. For $U_b = 12$ m/s in Figure 5.5 (a), the value for Re_θ is 601 and the corresponding location in Figure 5.5 (b) Re_θ is 2355 which indicates that Re_θ is increasing with U_b . This figure shows that ODT is capable to capture the behavior of the velocity boundary layer which is growing spatially.

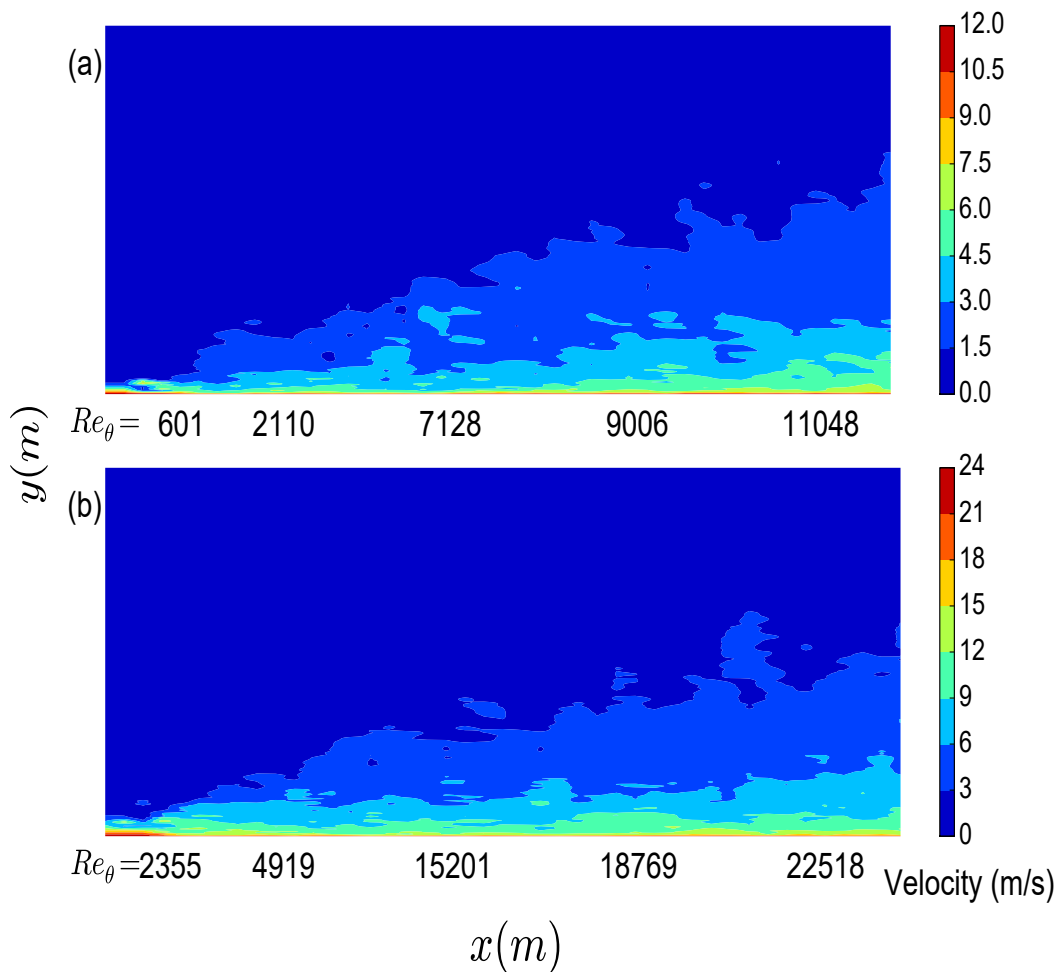


FIGURE 5.5: Velocity boundary layer development with domain on y -axis (in m) and streamwise location on x -axis (in m) in terms of corresponding Re_θ for bulk velocity (a) $U_b = 12$ m/s and (b) $U_b = 24$ m/s. The figure illustrate the influence of U_b on the velocity boundary layer.

Next, the spatially developing turbulent velocity boundary layer is shown in Figure 5.6 for the bulk velocity $U_b = 12$ m/s. In this figure streamwise positions are shown on x -axis instead of Re_θ (discussed above). The ODT domain on y -axis remains same as above.

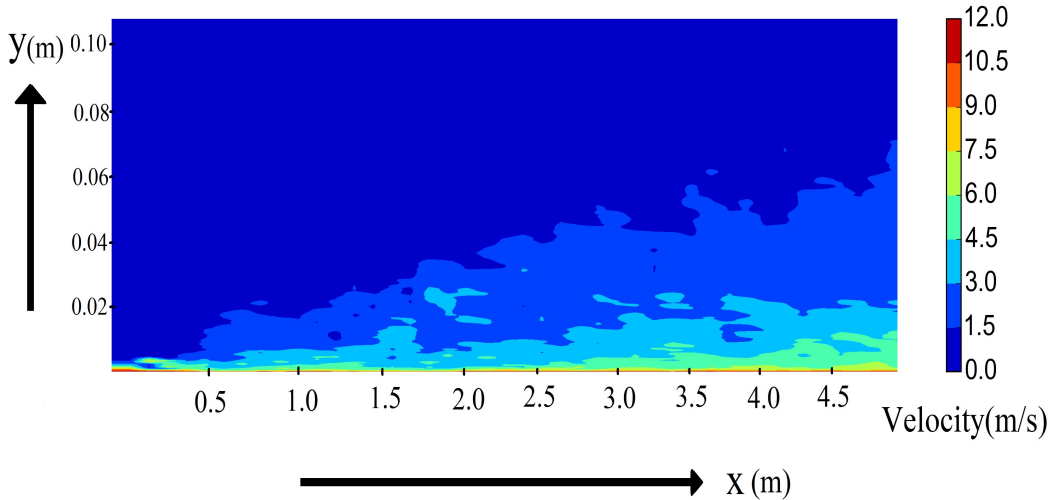


FIGURE 5.6: Velocity boundary layer development with domain on y-axis (in m) and streamwise location on x-axis (in m) for bulk velocity $U_b = 12$ m/s. The figure illustrate the influence of U_b on the velocity boundary layer.

5.2.1 First and Second Order Velocity Statistics

Figure 5.7 (A) displays the mean streamwise velocity profile as a function of the wall-normal coordinate in viscous units at $Re_\theta \sim 2000$ for domain $D1$ and $D2$ along with the DNS and LES reference from [41, 82]. The statistics is given for two bulk velocities, i.e., $U1 = 12$ m/s and $U2 = 24$ m/s. On y-axis We have $U_b^+ - \bar{u}^+$ due to the simulation set up used for the present study. The ODT profile shows very good agreement with the reference data for this Re_θ for $D1$ as well as $D2$ for lower U_b , i.e., $U1$ but not for $U2$. This indicates that the profiles are fully turbulent for $U1$ using both domain sizes. These profiles are in transient to turbulence for $U2$. The higher bulk velocity captures transitions in the flow. The main aim to use two U_b is to check influence of variation of bulk velocity on various statistics. However, we do not have reference data for $U2$. Nevertheless, the ODT model shows the ability to capture transitions from the inner to the buffer layer, and further into the log-region for $U1$ with both domain sizes.

Figure 5.7 (B) shows the mean streamwise velocity profile as a function of wall-normal coordinate in viscous units for $Re_\theta \approx 4000$. This is also shown for two bulk velocities (U_b), $U1 = 12$ and $U2 = 24$ m/s in comparison with the DNS and LES data [41, 82] at corresponding Re_θ . The general trend for this Re_θ remains same as explained for $Re_\theta \approx 2000$ for Figure 5.7 (A). The

transitions to turbulence are captured for higher bulk velocity up to $Re_\theta \approx 4000$.

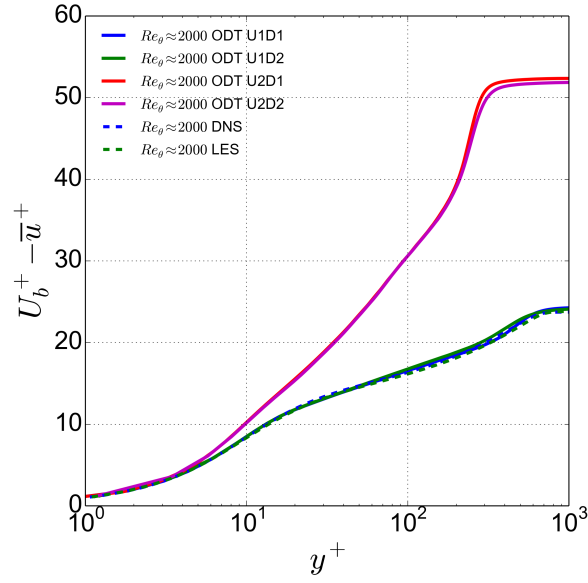
Next, in Figure 5.8 the mean streamwise velocity profile as a function of the wall-normal coordinate in viscous units is displayed at $Re_\theta \sim 8000$ for domain $D1$ and $D2$ in comparison with the LES reference from [82]. Along with the comparison, the profiles for several other Re_θ , as $Re_\theta \approx 12000, 16000$ and 20000 are also presented to check the influence of growing Re_θ on the mean velocity profile. The profiles for SBL, produced by ODT, at all Re_θ for $U1 = 12$ m/s as well as $U2 = 24$ m/s using both domain sizes are very much similar to the LES [82] data for $Re_\theta \approx 8000$. This indicated that the mean velocity has reached fully turbulent state even for $U2$ at $Re_\theta \approx 8000$. In the inner layer, i.e., $y^+ < 10$, the velocity profile is independent of U_b as well as domain size. However, some deviations from reference data are captured only in the outer log-region for growing Re_θ and also with domain variation. Nevertheless, the model captures variations for the mean velocity for all Re_θ from the inner region to the buffer region and further in the log-region.

Note that the ODT model shows very good agreement with the DNS and LES data for lower bulk velocity at all Re_θ and at higher Re_θ for higher bulk velocity using both domain size for the spatially developing turbulent boundary layer.

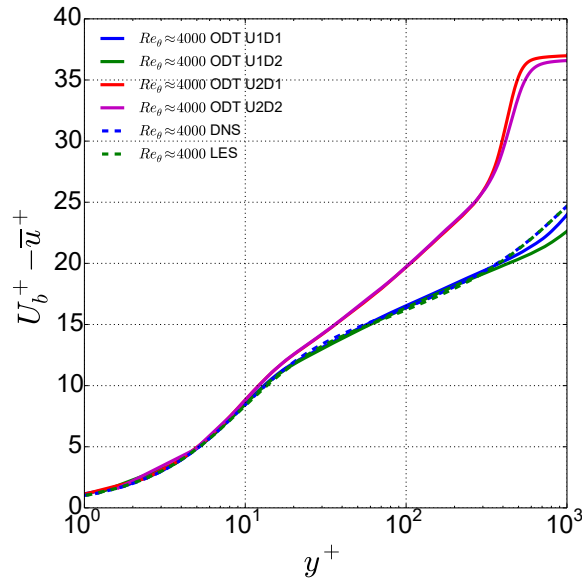
Figure 5.9 shows the pre-multiplied mean velocity gradient, i.e., the indicator function, $y^+ (\partial \bar{u}^+ / \partial y^+)$, as a function of wall-normal coordinate for the SBL configuration at $Re_\theta \approx 2000$ and 4000 for two bulk velocities investigated. The ODT results are shown in comparison with the reference DNS [41]. The pre-multiplied mean velocity aids in assessing if there is a logarithmic region in the mean velocity profile. The ODT profile for lower bulk velocity in Figure 5.9 (A) shows good quantitative agreement with the reference data and for higher bulk velocity at same Re_θ captures transition to turbulence. This behaviour is consistent with the mean streamwise velocity profile discussed above. The curves are dependent on U_b for $Re_\theta \approx 2000$ and for $Re_\theta \approx 4000$, the profiles are independent of U_b only in the inner region.

The indicator profile for higher bulk velocity achieves fully turbulent state with increasing Re_θ as shown in Figure 5.10. This figure presents the indicator function as a function of wall-normal coordinate at $Re_\theta \approx 8000$ for two bulk velocities considered above in comparison with the reference LES data [82]. At this Re_θ , the profiles from inner region to the buffer region, remains unaffected for the bulk velocities but dependent on U_b only in the outer log-region. For $U2 = 24$ m/s at $Re_\theta \approx 8000$, the profile still shows sensitivity towards initial conditions and it captures the initial transitions. However, these transitions were dominant for $Re_\theta \approx 2000$ and 4000 when compared to $Re_\theta \approx 8000$. Large noise components are noticed in the outer region which might be due to the large but less frequently occurring eddy events.

The von Kármán constant, K , of the law of the wall is defined as the inverse of the indicator function in the logarithmic region. This addresses the similarity properties. K in the present case is obtained by averaging the indicator function over $40 \leq y^+ \leq 300$. Note that ODT can reproduce but not confirm the value of K . This is because the physical model parameters are tuned to match the mean profile. To achieve the statistical convergence large



(A)



(B)

FIGURE 5.7: The mean streamwise velocity profile as a function of the wall-normal coordinate (in viscous units) at (A) $Re_\theta \approx 2000$ and (B) $Re_\theta \approx 4000$ for $U1$ and $U2$ as bulk velocities, 12 and 24 m/s, respectively. For reference, DNS and LES data from [41, 82] at $Re_\theta \approx 2000$ and 4000 is plotted.

ensemble sizes are required. This would not influence the overall observations about the results. The qualitative trends from the DNS and LES are confirmed for lower bulk velocity at all three Re_θ .

The root mean square (rms) of the normalized streamwise velocity component ($u_{rms}^+ = \sqrt{u'^2}/u_\tau$) as a function of normalized wall-normal coordinate in viscous units is depicted in Figure 5.11 at (A) $Re_\theta \sim 2000$ and (B) $Re_\theta \sim 4000$

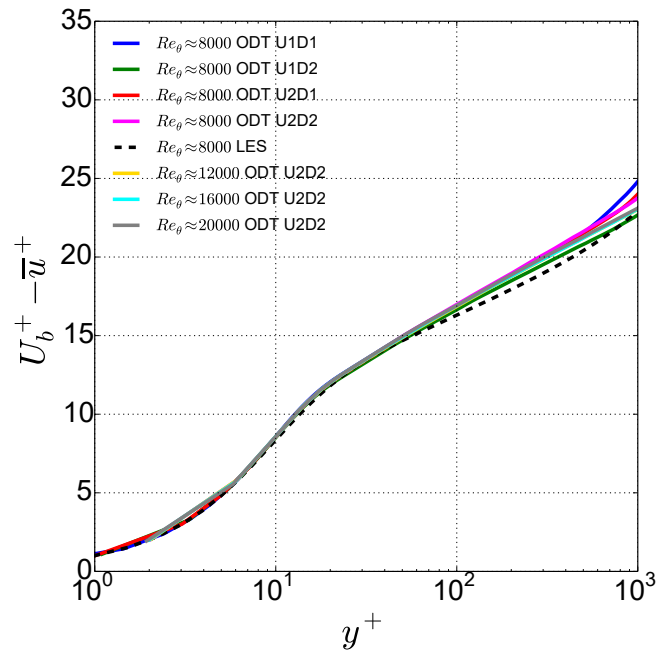
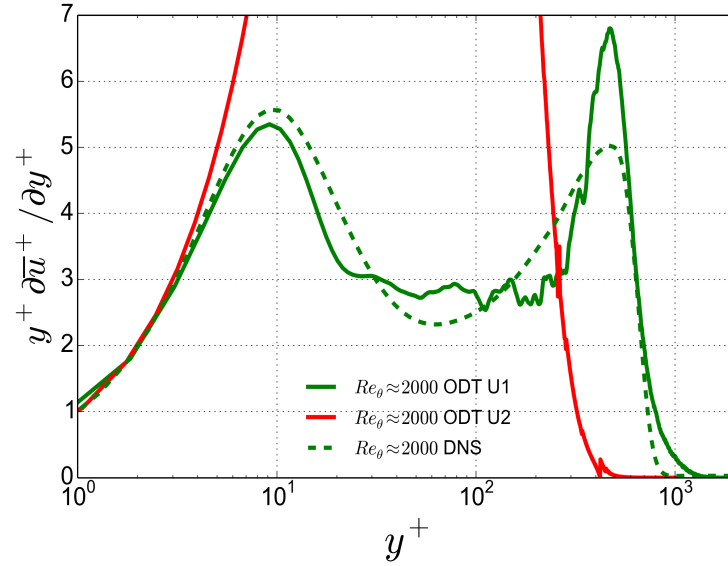


FIGURE 5.8: The mean streamwise velocity profile as a function of the wall-normal coordinate (in viscous units) at $Re_\theta \approx 8000$ in comparison with the LES data at corresponding Re_θ from [82] is shown. The ODT results are presented for $U1$ and $U2$ as bulk velocities, 12 and 24 m/s for several higher Re_θ .

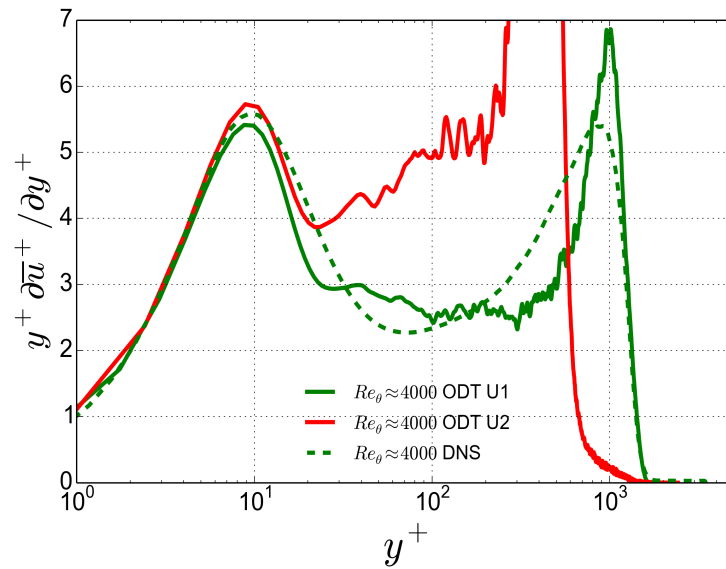
for $U1$ and $U2$ as bulk velocities, 12 and 24 m/s, respectively for two domain sizes considered for investigation. For comparison, the reference DNS data from [41] and LES data from [82] at $Re_\theta \approx 2000$ and 4000 is plotted. As usual, the peak amplitude remains under-predicted by ODT compared to the reference data for both domain sizes at lower bulk velocity. For higher bulk velocity, the profiles are in transition to turbulence for both Re_θ . The under-predicted peak can be optimized by choosing small value of the model parameter C . But in that case the velocity profile tends towards a laminar profile. This ODT modeling artifact has already been reported in the literature by [84] and can be avoided by retaining some 3-D information of the flow.

The double peak arising near to the wall, $y^+ \approx 10$, represents an artifact generated by the topology of the triplet map close to the wall and is seen only for lower bulk velocity. This peak is not seen for high bulk velocity due to transitions. The origin of this peak is explained in more detail by [89]. Although the peak is under-predicted for rms, some general trends from the reference data are confirmed with the ODT for the given initial condition and for the chosen physical parameters.

The rms profile in Figure 5.12 is shown at $Re_\theta \approx 8000$ for two bulk velocities and for two domain sizes in comparison with the reference LES data from [82] at corresponding Re_θ . ODT results are presented for several higher Re_θ as well. The ODT rms profiles are under-predicted for all Re_θ given in figure. For this Re_θ , bulk velocities does not affect the the rms profiles much and all profiles have achieved fully turbulent state. However, domain size selected



(A)



(B)

FIGURE 5.9: Indicator function versus wall-normal coordinate (in viscous units) at (A) $Re_\theta \approx 2000$ and (B) $Re_\theta \approx 4000$ for $U1$ and $U2$ as bulk velocities, 12 and 24 m/s, respectively. For comparison, the reference DNS data from [41] at $Re_\theta \approx 2000$ and 4000 is plotted.

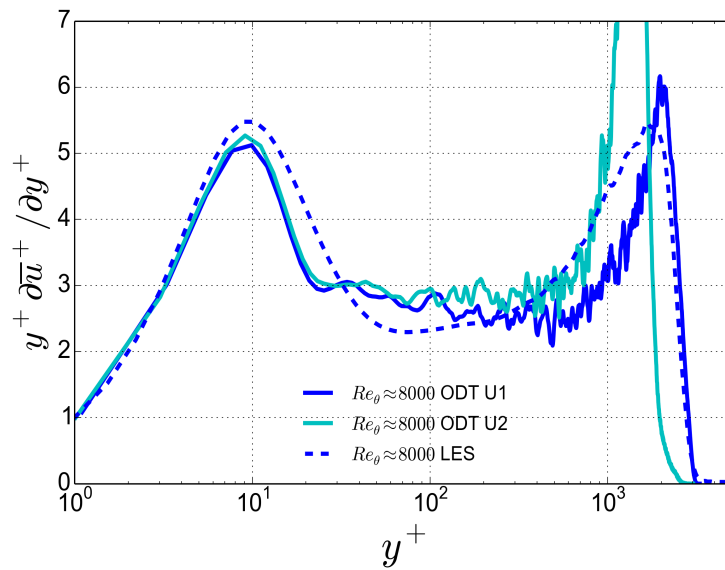
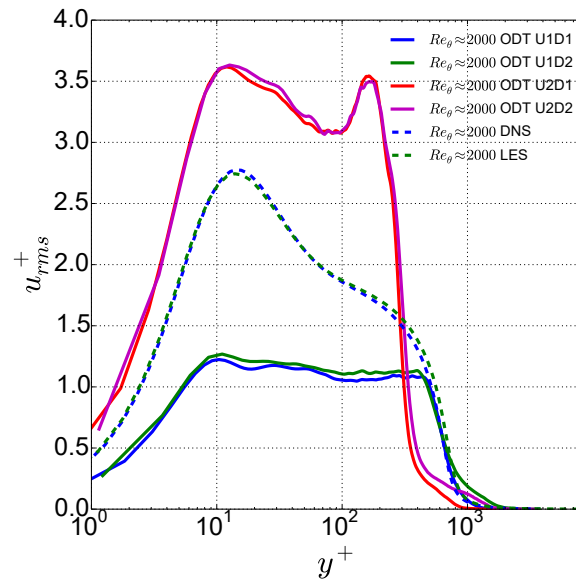


FIGURE 5.10: Indicator function versus wall-normal coordinate (in viscous units) at $Re_\theta \approx 8000$ for $U1$ and $U2$ as bulk velocities, 12 and 24 m/s, respectively. For comparison, the reference LES data from [82] at same Re_θ is plotted.

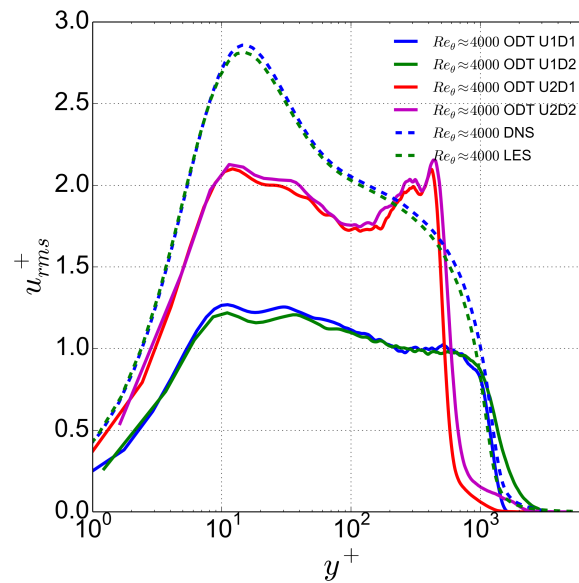
affects the profiles. $D1$ fails to capture growing turbulent boundary layer at $Re_\theta \approx 8000$ and capture only for lower Re_θ . $D2$ presents good fit for rms profile in comparison to the LES data at higher Re_θ . The ODT implementation for the SBL case confirms the double peak near the wall for this Re_θ as well.

Figure 5.13 shows the profiles for the normalized Reynolds shear stresses as a function of the wall-normal coordinate in viscous units, $(\overline{u'v'}/u_\tau^2)$, for (A) $Re_\theta \approx 2000$ and (B) $Re_\theta \approx 4000$ in comparison with the reference DNS and LES data from [41, 82]. The calculation of Reynolds shear stresses are based on the changes of the velocity profiles due to eddies and is explained in detail in [28], Appendix C. A peak is observed in the outer log-region for Reynolds shear stresses at both Re_θ for both bulk velocities and both domain sizes. For higher bulk velocity, this is due to the transitions but for Reynolds shear stresses, these transitions are captured even for lower bulk velocity. Another different observation for Reynolds shear stress is that the profiles show sensitivity towards domain sizes considered as well unlike the mean and rms velocity profiles for both Re_θ .

Figure 5.14 shows that the peak captured in the outer log-region is not seen in case of higher Re_θ , i.e., at $Re_\theta \approx 8000$ for the lower U_b . The Reynolds shear stress profiles are under-predicted in comparison to the reference LES data [82] and the outer peak disappears for $D1$ but some signs are observed for $D2$. This peak is attributed to the transient effects at lower Re_θ indicating that some of the simulated boundary layers are still developing. This indicates that the flow have not reached to the final turbulent equilibrium state. This behaviour was observed for TBL as well, as discussed in [109] and also in earlier chapter of the thesis. However, in case of TBL, the peak was observed till $Re_\theta \approx 1968$ and no transient effects were seen at $Re_\theta \approx 2500$. But in the



(A)



(B)

FIGURE 5.11: The root mean square velocity profile, as a function of wall-normal coordinate (in viscous units) at (A) $Re_\theta \approx 2000$ and (B) $Re_\theta \approx 4000$ for $U1$ and $U2$ as bulk velocities, 12 and 24 m/s, respectively. For comparison, the reference DNS data from [41] and LES data from [82] at $Re_\theta \approx 2000$ and 4000 is plotted.

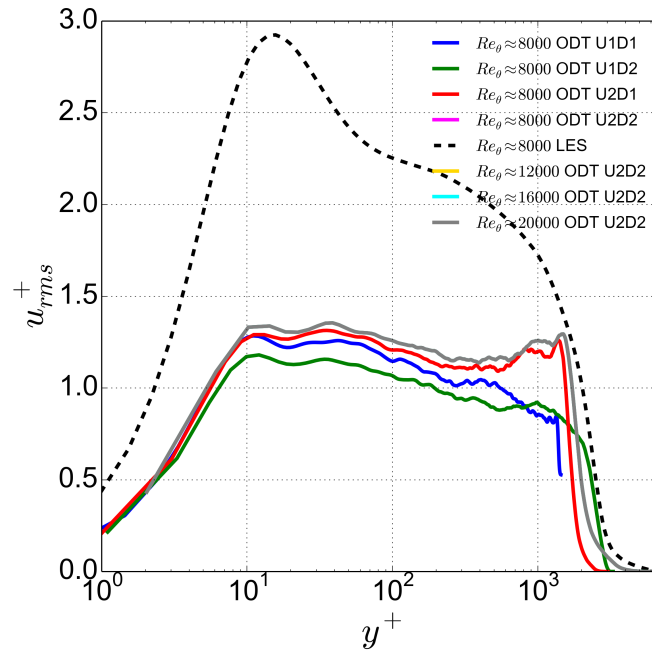
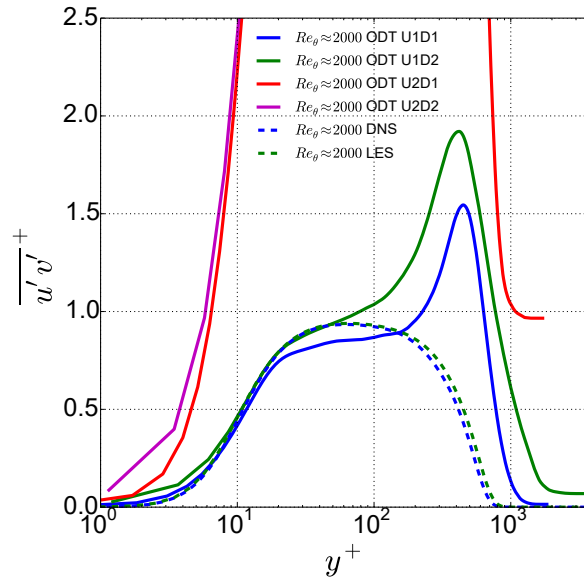


FIGURE 5.12: The root mean square velocity profile, as a function of wall-normal coordinate (in viscous units) at $Re_\theta \approx 8000$ for $U1$ and $U2$ as bulk velocities, 12 and 24 m/s, respectively. For comparison, the reference LES data from [82] at $Re_\theta \approx 8000$ is plotted. ODT results are presented for several higher Re_θ as well.

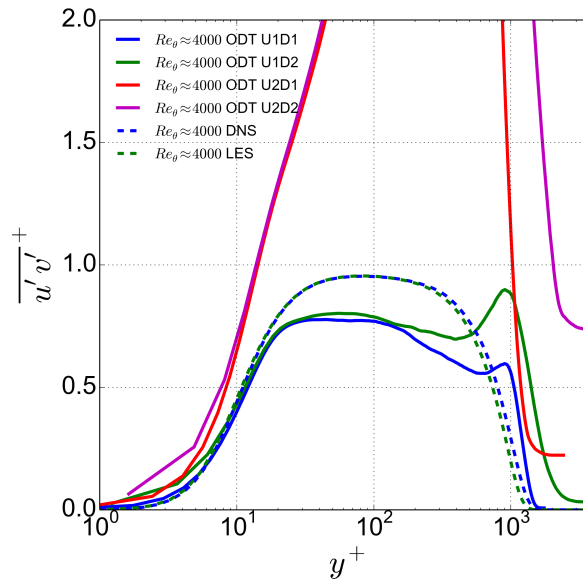
SBL case, this peak is observed till $Re_\theta \approx 4000$ and disappears till $Re_\theta \approx 7500$. A prolonged transient effects in case of SBL is reported in comparison to TBL [109]. These transient effects are, however, highly sensitive for U_b as seen from Figure 5.13 and Figure 5.14. The ODT model, in general, takes longer to transition to a fully turbulent state for higher bulk velocity than the lower bulk velocity. The effects of transient flow are observed up to $Re_\theta \approx 20,000$ for higher bulk velocity. It is noted that the Reynolds shear stresses for the suction boundary layer [96] were reported to be over-predicted and for TBL [109] case these profiles were in good agreement compared to the DNS data. Whereas in the present SBL configuration, these profiles are under-predicted as compared to the DNS and LES data [41, 82].

5.2.2 Higher Order Velocity Statistics

The turbulent production in the flow is calculated as $-\overline{u'v'}^+ \frac{\partial \overline{u}^+}{\partial y^+}$ and plotted as a function of wall-normal coordinate in viscous units in Figure 5.15 at (A) $Re_\theta \sim 2000$ and (B) $Re_\theta \sim 4000$ for $U1$ and $U2$ as bulk velocities, 12 and 24 m/s, respectively for two domain sizes. For comparison, the reference DNS data from [41] and LES data from [82] at same Re_θ is plotted.. The production for both Re_θ in SBL cases shows reasonable agreement with the available reference data at matched U_b (lower bulk velocity) for $D1$ as well as $D2$. Some transient effects are captured in turbulent production mechanism at both Re_θ



(A)



(B)

FIGURE 5.13: Profiles of the Reynolds shear stresses at (A) $Re_\theta \approx 2000$ and (B) $Re_\theta \approx 4000$ for $U1$ and $U2$ as bulk velocities, 12 and 24 m/s, respectively. All quantities are functions of the wall-normal coordinate (in viscous units). For comparison, the reference DNS data from [41] and LES data from [82] at $Re_\theta \approx 2000$ and 4000 is shown.

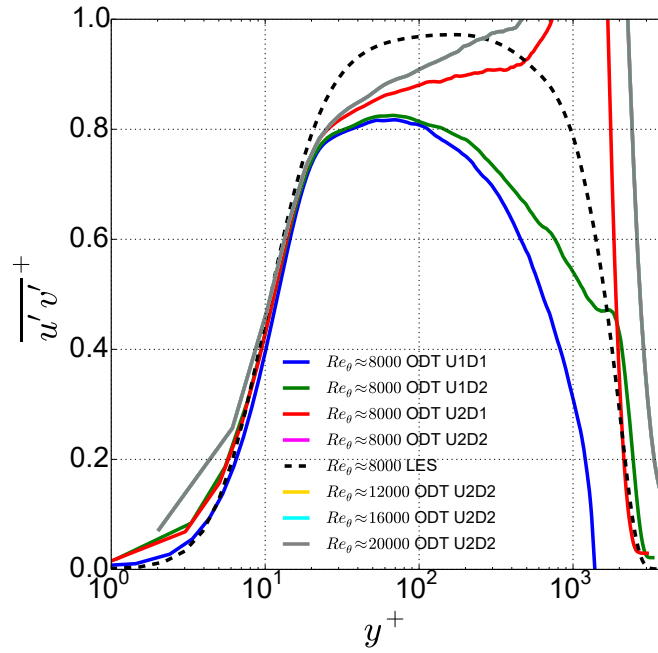
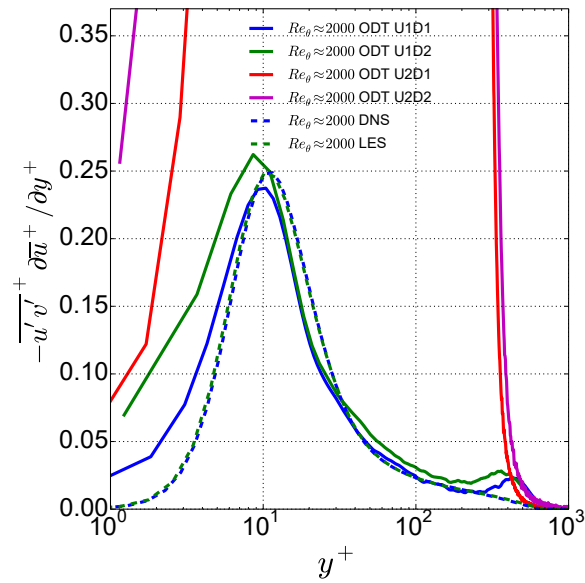


FIGURE 5.14: Profiles of the Reynolds shear stresses at $Re_\theta \approx 8000$ for $U1$ and $U2$ as bulk velocities, 12 and 24 m/s, respectively. All quantities are functions of the wall-normal coordinate (in viscous units). For comparison, the reference LES data from [82] at $Re_\theta \approx 8000$ is shown. ODT results are presented for several higher Re_θ as well.

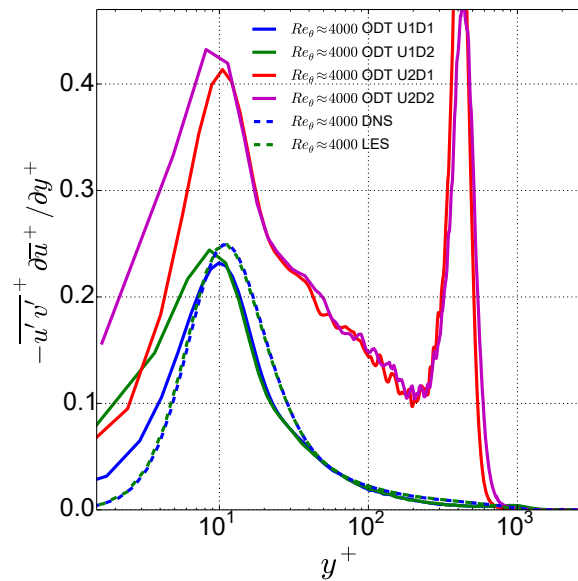
for higher bulk velocity for both domain sizes. These effects are expected since production is calculated with the mean velocity and the Reynolds shear stress. Such transient effects were observed in case of Reynolds shear stress profiles at the same Re_θ . Nevertheless, for $U1 = 12$ m/s, the Reynolds shear stresses profiles for both Re_θ using both domain sizes show agreement with the reference data.

In case of $U2 = 24$ m/s, an extra peak is noted in the outer region at higher Re_θ which is similar to the rms velocity profile and Reynolds shear stresses. At lower Re_θ , i.e., ≈ 4000 , the instabilities are dominant in the flow for the SBL configuration. The transient effects are removed for statistics at higher Re_θ . The idea behind carrying out the ODT simulations for $U2 = 24$ m/s is to analyze the influence of bulk velocity on the statistics and we do not have DNS or LES data to compare with for this case. Figure 5.16 shows good agreement for ODT turbulent production with the reference LES data at $Re_\theta \approx 8000$ for both bulk as well as domain sizes.

The skewness of the streamwise velocity component, $-\overline{u'^3}/u_{rms}^3$, as a function of wall-normal coordinate in viscous units at $Re_\theta \sim 2000$ is depicted in Figure 5.17 (A) for $U1$ and $U2$ as bulk velocities, 12 and 24 m/s, respectively for $D1$ and $D2$. For comparison, the reference DNS data from [41] and LES data from [82] at same Re_θ is shown in dashed lines. The figure shows that the ODT model, using both domain sizes, tends to over-predict the positive skewness near the wall i.e. $y^+ < 10$ for lower bulk velocity and over-predict



(A)



(B)

FIGURE 5.15: Turbulent kinetic energy production as a function of the wall-normal coordinate (in viscous units) at (A) $Re_\theta \approx 2000$ and (B) $Re_\theta \approx 4000$ for $U1$ and $U2$ as bulk velocities, 12 and 24 m/s, respectively. For comparison, the reference DNS data from [41] and LES data from [82] at $Re_\theta \approx 2000$ and 4000 is shown.

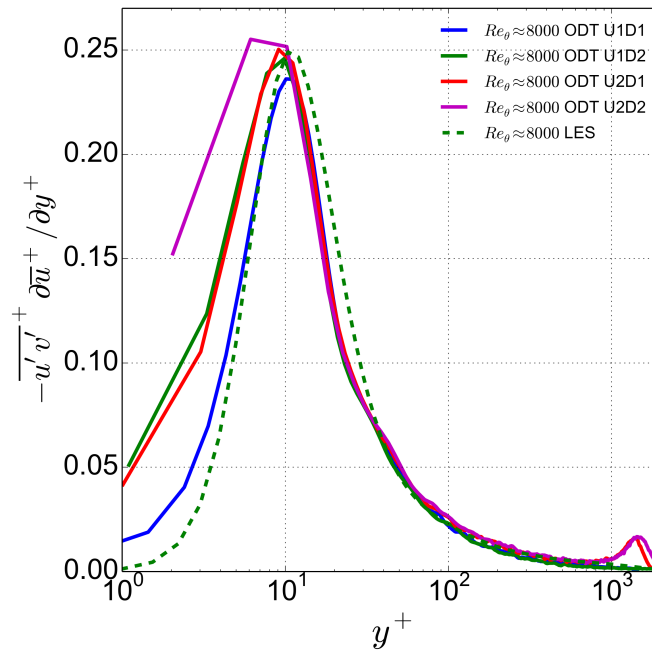


FIGURE 5.16: Turbulent kinetic energy production as a function of the wall-normal coordinate (in viscous units) at $Re_\theta \approx 8000$ for $U1$ and $U2$ as bulk velocities, 12 and 24 m/s, respectively. For comparison, the reference LES data from [82] at $Re_\theta \approx 8000$ is shown. ODT results are presented for several higher Re_θ as well.

for higher bulk velocity. The skewness profile show agreement with the reference data in the outer region between $10 < y^+ < 500$ for lower bulk velocity. However, there are large disagreements and very different trends in the outer-log region, where DNS profiles exhibit a sudden increase in the skewness values and this feature is not captured by ODT. This is presumably attributed to the missing 3-D information. Nevertheless, this figure illustrates the potential of ODT to calculate the third order velocity statistics. A similar behaviour is reported for a TBL using ODT ([109]). The ODT profiles are qualitatively consistent with the reference data.

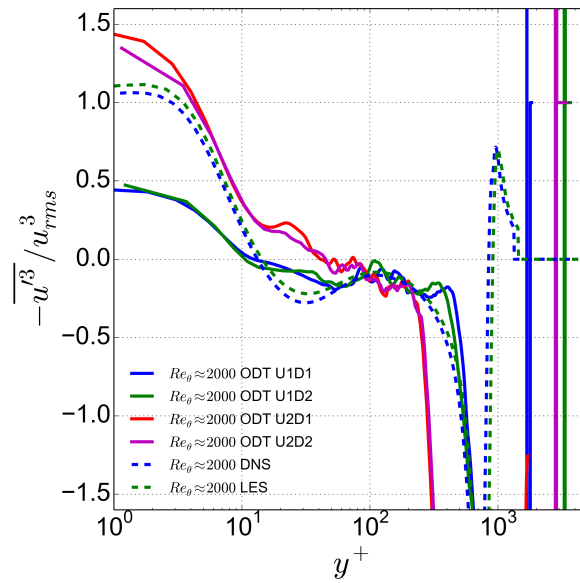
The skewness of the streamwise velocity component is plotted in Figure 5.17 (B) for $Re_\theta \approx 4000$ for SBL in comparison with the reference DNS and LES data. The qualitative trends for this Re_θ are consistent with the reference DNS and LES data as well as for $Re_\theta \approx 2000$. A suction boundary layer [96] reported considerable different behaviour for skewness as compared to SBL. As for $Re_\theta \approx 2000$, the positive skewness using ODT is under-predicted in the inner region, i.e., $y^+ < 10$, and in the outer region between $10 < y^+ < 500$, shows good agreement with the reference data. Some of the flow structures are not captured in the outer-region for spatial ODT formulations similar to the temporal formulation. The reference data exhibit a sudden increase in the skewness value in the outer-log region which is not captured by ODT. The reference data suggests negative skewness at the edge of the turbulent region. There, the mean of u is very close to zero which indicates that negative- u

excursions dominate the skewness. However, in ODT neither the triplet map nor viscous transport can cause u to extend outside its initial bounds $[0, U_b]$ and only kernels can give negative u . Even if kernels give negative u , this is a more limited mechanism for generating negative u than the mechanisms available in DNS associated with pressure fluctuations, etc. Note that this reasoning about negative u is not applicable in the interior of the boundary layer, where the mean of u is positive so negative u is not needed to produce negative skewness. Consistent with this, the negative skewness is found in the interior but not at the edge.

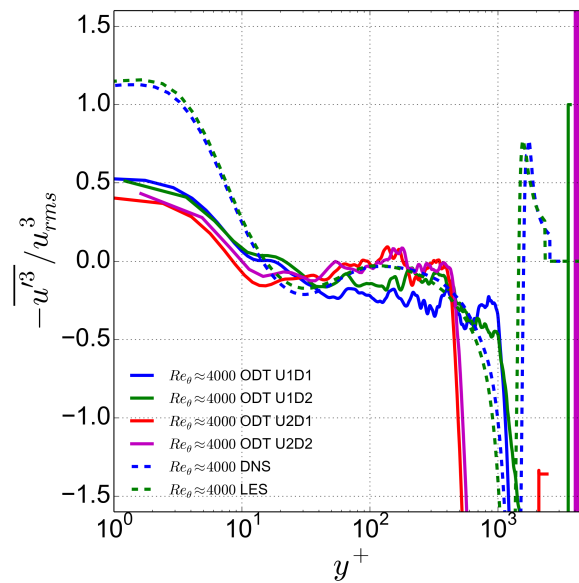
Similar to rms and Reynolds shear stress, the transient effects are captured for skewness profile at lower Re_θ for higher U_b with the general trends being consistent. For higher Re_θ shown in Figure 5.18, the third order velocity statistics from reference data in [82] are in good agreement for both bulk velocities. The figure also presents the ODT simulation results for several higher Re_θ as well.

Figure 5.19 shows the flatness of the streamwise velocity component, i.e., $\overline{u'^4}/u_{rms}^4$, as a function of wall-normal coordinate (in viscous units) at (A) $Re_\theta \approx 2000$ and (B) $Re_\theta \approx 4000$ for $U1$ and $U2$ as bulk velocities, 12 and 24 m/s, respectively for two domain sizes as $D1$ and $D2$. For comparison, the reference DNS data from [41] and LES data from [82] at corresponding Re_θ is shown in dashed lines. Additionally, Figure 5.20 shows the flatness of the streamwise velocity component at $Re_\theta \approx 8000$ for both bulk velocities and for both domain sizes in comparison with the reference LES data from [82] at corresponding Re_θ .

ODT highly under-predicts the fourth-order velocity statistics in the inner region near the wall, i.e., $y^+ < 8$ and agrees with reference data in outer log-region for lower bulk velocity. For higher bulk velocity, initial transitions are captured at lower Re_θ and the profiles are consistent with other profiles at higher Re_θ . The flatness is over-predicted in the region between $8 < y^+ < 600$ for SBL and in case of TBL, this region was reported as $10 < y^+ < 80$. A Gaussian flatness with a value close to three is observed close to the wall for the ODT results for all bulk velocities using both domain except for higher bulk velocity at lower Re_θ . In general, ODT is more Gaussian than the DNS. This can be attributed to the 3-D eddy motions and vortex stretching which leads to inhomogeneity but remains unresolved in ODT. The full 3-D instabilities exhibited by the reference data are absent in the ODT model. The profile shows agreement with the reference data only in the outer log-region. Like rms profiles, in case of flatness as well, we might need to retain some 3-D information in a non-standalone application of ODT in order to reproduce fourth-order velocity statistics to overcome this limitation [84, 103, 108], thus, allowing simulations of much more complex flows. Unlike the skewness, the sign of u has no bearing on the flatness. Due to this, ODT reproduces flatness rather well in the far fields.



(A)



(B)

FIGURE 5.17: The skewness of the streamwise velocity component as a function of wall normal coordinate (in viscous units) at (A) $Re_\theta \approx 2000$ and (B) $Re_\theta \approx 4000$ for $U1$ and $U2$ as bulk velocities, 12 and 24 m/s, respectively. For comparison, the reference DNS data from [41] and LES data from [82] at $Re_\theta \approx 2000$ and 4000 is shown.

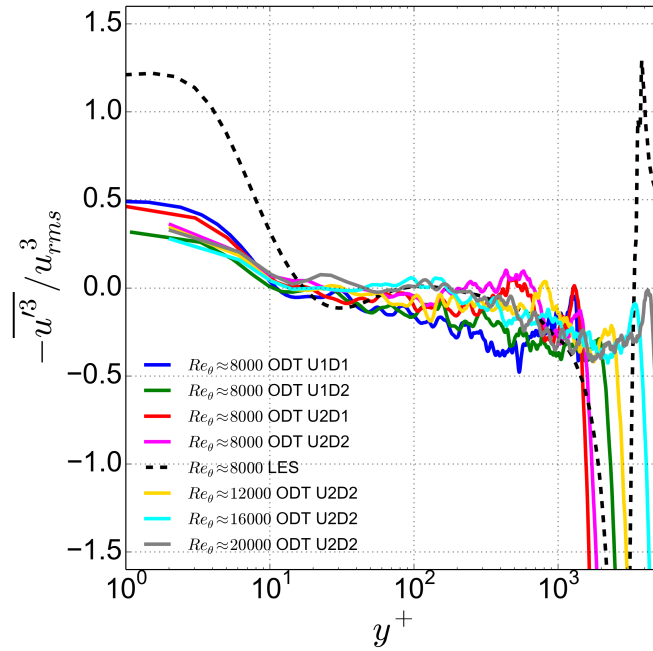
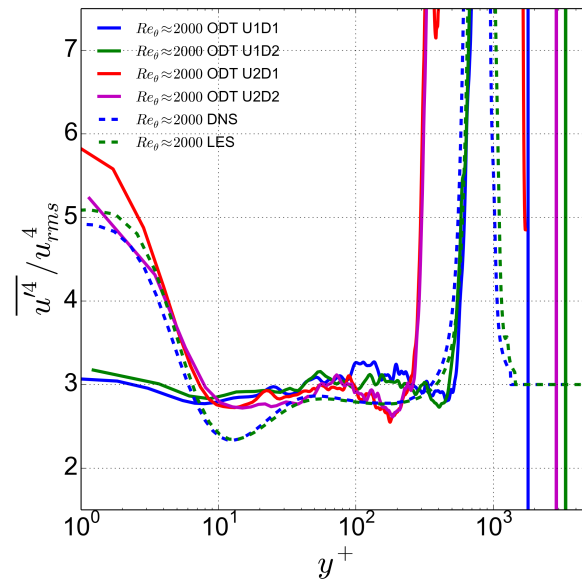


FIGURE 5.18: The skewness of the streamwise velocity component as a function of wall normal coordinate (in viscous units) $Re_\theta \approx 8000$ for $U1$ and $U2$ as bulk velocities, 12 and 24 m/s, respectively. For comparison, the reference LES data from [82] at $Re_\theta \approx 8000$ is shown. ODT results are presented for several higher Re_θ as well.

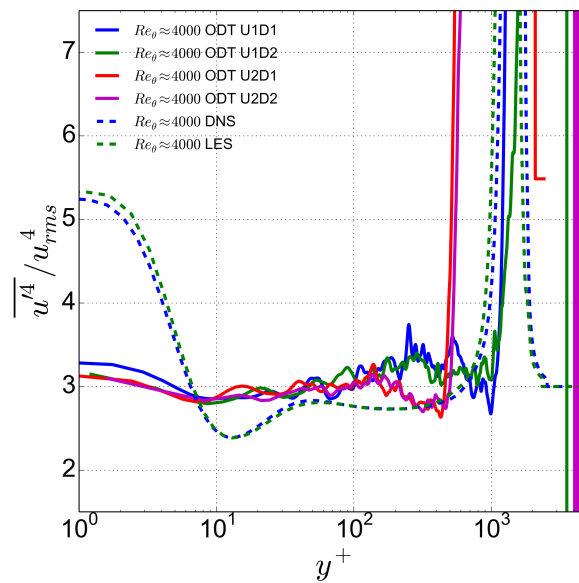
5.3 Variation of the Structural Properties with Re_θ

For the SBL configuration, the ODT structural properties, i.e., friction Reynolds number (Re_τ), shape factor (H) and skin friction coefficient (C_f) with Re_θ are discussed in this section in comparison with the reference DNS data from [41] up to $Re_\theta \approx 4300$ and LES data from [82] up to $Re_\theta \approx 8300$. These simulations are performed on a larger domain, i.e., $D2 = 90,000\nu/U_b$ in order capture the boundary effects onto the flow even at very high Re_θ ($\approx 27,000$). For $U1 = 12$ m/s, the Re_θ value is in the range $\approx [600 - 14,000]$ and for $U2 = 24$ m/s, the range is $\approx [2300 - 27,000]$. The values of the properties achieved at the last sampled Re_θ are provided in Table 5.1.

The turbulence is further quantified in the near-wall region and Figure 5.21 is shown to obtain a functional relation for Re_τ in terms of Re_θ for two bulk velocities. Re_τ is calculated using u_τ and δ_{99} and values are given in Table 5.1. The Figure shows linear behaviour of the quantity with variation of Re_θ . A power-law relation is obtained as $Re_\tau = 0.89 \times Re_\theta^{0.89}$ to provide a good fit for the ODT data. This equation also relates Re_τ with Re_θ . It can be used to convert between the two Reynolds numbers. For comparison, the DNS data up to $Re_\theta \approx 4300$ and the LES data up to $Re_\theta \approx 8300$ from [41, 82] is shown with dashed lines. However, the ODT flow properties are shown up to $Re_\theta \approx 14,000$ for lower U_b and up to $Re_\theta \approx 27,000$ for higher U_b . This quantity is, in general, good agreement with the available reference data.



(A)



(B)

FIGURE 5.19: The flatness of the streamwise velocity component as a function of wall normal coordinate (in viscous units) at (A) $Re_\theta \approx 2000$ and (B) $Re_\theta \approx 4000$ for $U1$ and $U2$ as bulk velocities, 12 and 24 m/s, respectively. For comparison, the reference DNS data from [41] and LES data from [82] at $Re_\theta \approx 2000$ and 4000 is shown.

TABLE 5.1: The simulations results for friction Reynolds number Re_τ , displacement Reynolds number $Re_{\delta_{99}}$, momentum thickness Reynolds number Re_θ (f for final value of the quantities), skin friction C_f , von Kármán's constant K and shape factor H .

Case	$Re_{\tau,f}$	$Re_{\delta_{99},f}$	$Re_{\theta,f}$	$Re_{X,f}$ [10^6]	C_f [10^{-3}]	K	H
U1C1	3138	1808	8241	47	2.54	0.26	1.54
U1C2	4142	16,774	10,086	47	3.96	0.44	1.66
U1Z1	3789	15,345	9546	47	3.40	0.34	1.61
U1Z2	3750	15,188	9480	47	3.42	0.36	1.60
U1	4762	19,285	13,821	47	3.44	0.38	1.40
U2	9391	37,412	27,604	188	2.38	0.33	1.38

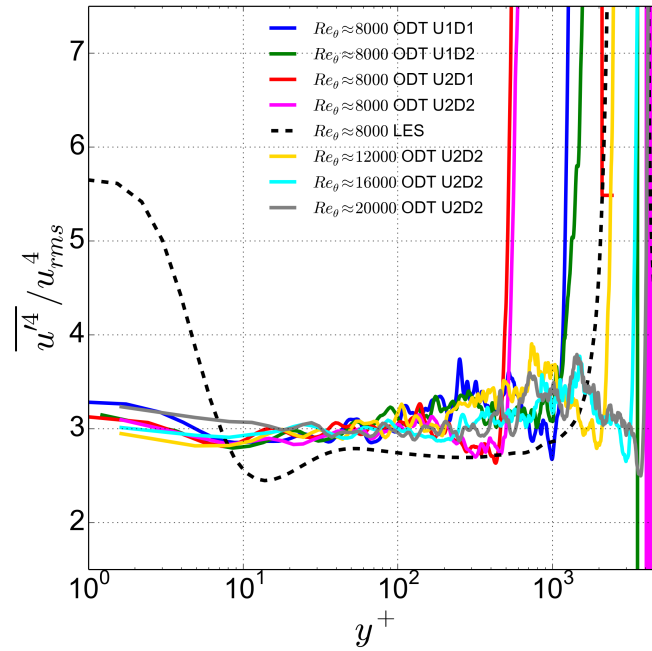


FIGURE 5.20: The flatness of the streamwise velocity component as a function of wall normal coordinate (in viscous units) at $Re_\theta \approx 8000$ for $U1$ and $U2$ as bulk velocities, 12 and 24 m/s, respectively. For comparison, the reference LES data from [82] at $Re_\theta \approx 8000$ is shown. ODT results are presented for several higher Re_θ as well.

The shape factor (H) defined as the ratio of the displacement thickness and momentum thickness, i.e., $H = \delta/\theta$ is plotted with variation of Re_θ in Figure 5.22 for different bulk velocities. Table 5.1 summarises the asymptotic values achieved for the shape factor. This quantity gives a direct quantitative estimation of the mean streamwise velocity profile independent of the skin friction. The figure also shows the DNS results up to $Re_\theta \approx 4300$ and the LES results up to $Re_\theta \approx 8300$ from [41, 82]. A convergence of the shape factor is seen at higher Re_θ but the ODT data does not show good agreement with the reference data unlike TBL [109]. In the small Re_θ range, a different Re_θ trend is noted for the reduced order model. However, a different trend at low Re_θ value is reported even in case of DNS [41]. ODT under-predicts the value for the shape factor in the range from $2000 < Re_\theta < 8000$ in comparison with the reference data. It is worth noting the behaviour for this property for a one-dimensional model.

Next, the development of the skin friction coefficient, $C_f = 2/(U_b^+)^2$, with Re_θ for two bulk velocities up to very high Re_θ ($\approx 27,000$) (see Table 5.1) is shown in Figure 5.23. The coefficient, C_f is defined as the ratio of the wall shear stress to the dynamic pressure. The behaviour for SBL flow configuration is very much similar to the TBL configuration reported in [109]. The profile for ODT show deviation initially from the DNS data. Although as it reaches the final turbulent equilibrium state, it finally merge towards the reference data. This shows asymptotic insensitivity to the initial conditions. Also, in case of

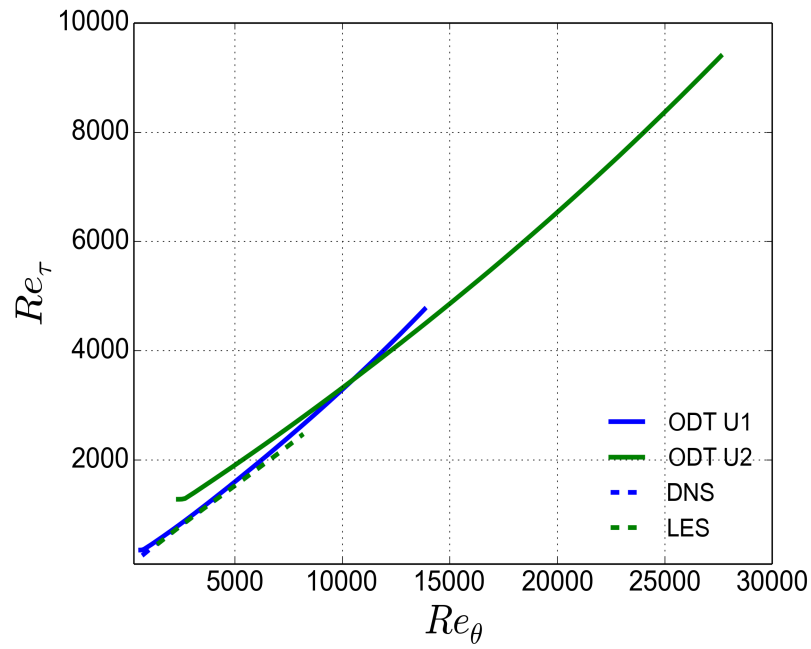


FIGURE 5.21: The quantity Re_τ as a function of Re_θ for $U1$ and $U2$ as bulk velocities, 12 and 24 m/s, respectively. For comparison, the reference DNS data from [41] and LES data from [82] is shown.

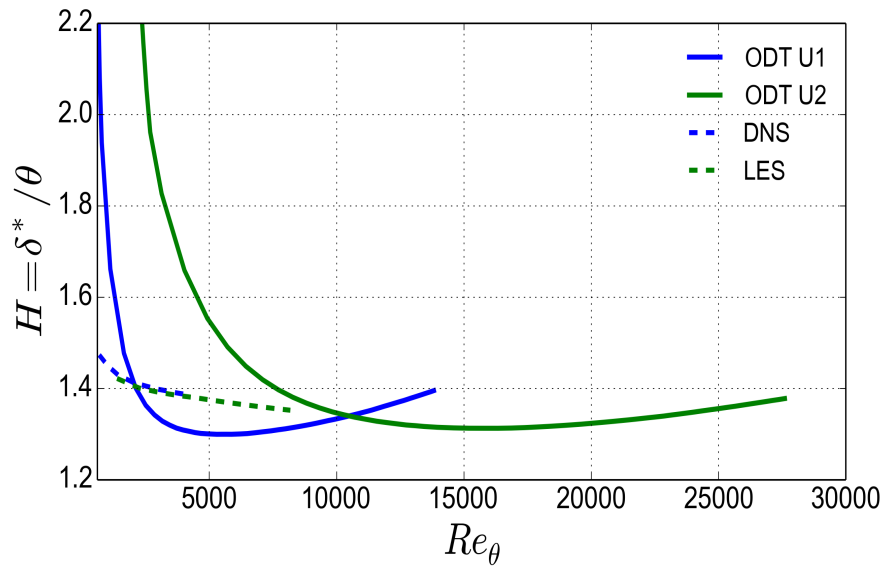


FIGURE 5.22: The quantity H as a function of Re_θ for $U1$ and $U2$ as bulk velocities, 12 and 24 m/s, respectively. For comparison, the reference DNS data from [41] and LES data from [82] is shown.

DNS [44], the laminar-turbulent transition is induced at different Re_θ . These transitions depends on tripping and as a result of transition, DNS exhibit typical overshoots of C_f . A different behaviour of the DNS simulations in the

region $Re_\theta = 200 - 1000$ due to the transition mechanism is reported in [44]. The behavior of C_f for the ODT model is similar to the DNS and LES profiles reported in [41, 82] from $Re_\theta \approx 2500$ onward with a slight under-prediction of the C_f for $U1 = 12$ m/s. However, in the small Re_θ range, a inconsistent trend with respect to Re_θ is observed in case of the reduced order model in comparison with the reference data. The C_f peak amplitude could be improved by changing the model parameters. However, with the chosen combination of parameters, the qualitative trends are sufficiently well reproduced, as well as the collapse into the fully turbulent state along with the lower and higher order statistics. This confirming once more the capability of ODT to predict such properties.

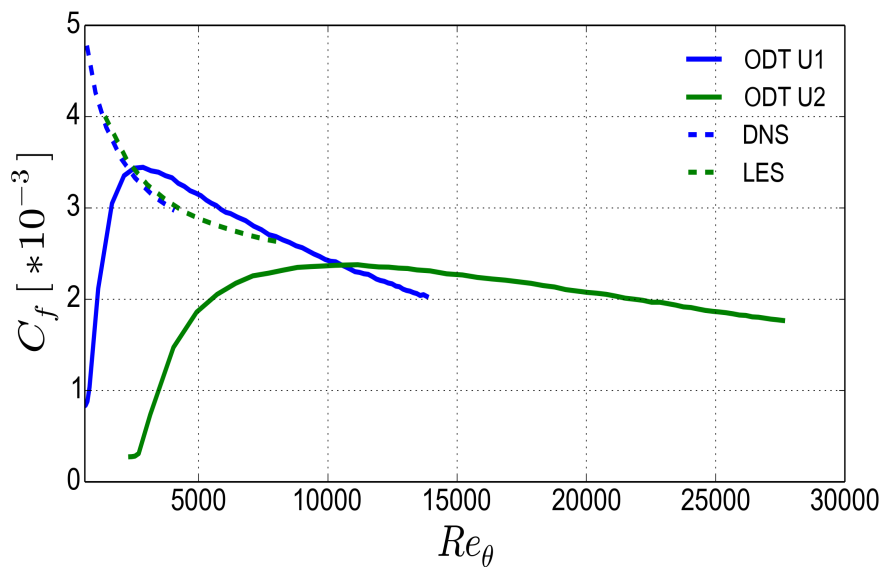


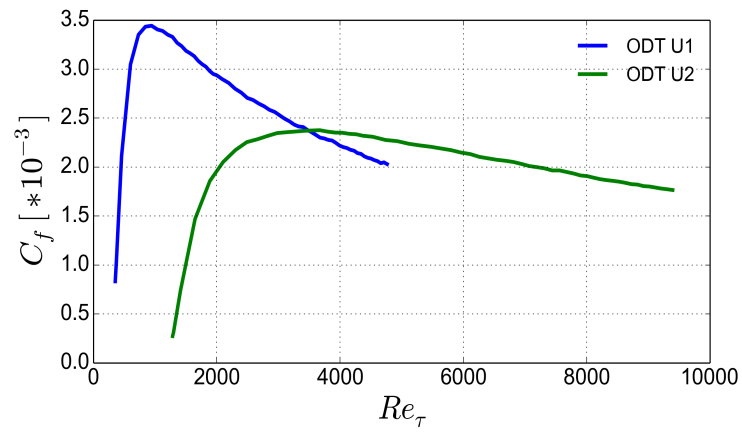
FIGURE 5.23: Skin friction coefficient C_f as a function of Re_θ for $U1$ and $U2$ as bulk velocities, 12 and 24 m/s, respectively. For comparison, the reference DNS data from [41] and LES data from [82] is shown.

The development of the skin friction coefficient, C_f is now shown with (A) Re_τ , (B) Re_δ (C) Re_X for $U1$ and $U2$ as bulk velocities, 12 and 24 m/s, respectively in Figure 5.24 only for ODT simulations. Table 5.1 summarises the asymptotic values for all these quantities. The reference data is not available for these quantities for SBL configuration. Here, these quantities are not discussed in detail.

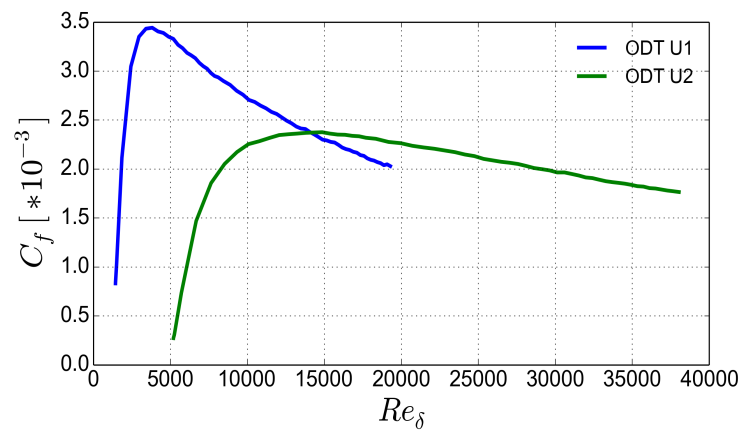
Figure 5.25 displays variation of Re_δ with Re_θ and Figure 5.26, variation of H with (A) Re_τ and (B) Re_δ for $U1$ and $U2$ as bulk velocities, 12 and 24 m/s, respectively only for ODT simulations.

5.4 Comparison between TBL and SBL

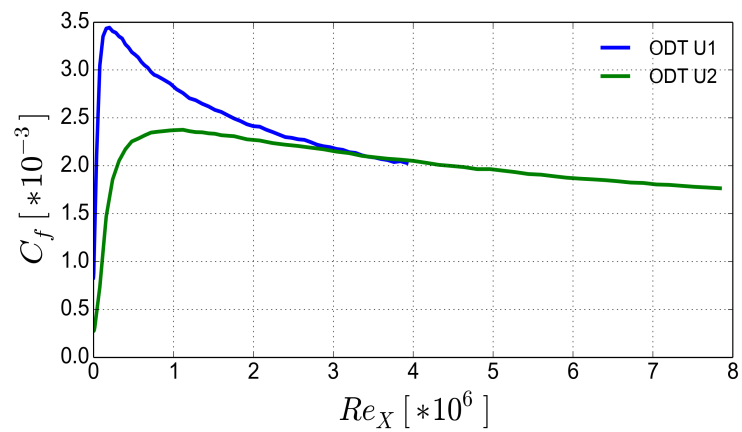
A comparison between TBL and SBL flow characteristics for various velocity statistics up to 4th order and some of the global properties with the spatial



(A)



(B)



(C)

FIGURE 5.24: Skin friction coefficient C_f as a function of (A) Re_τ , (B) Re_δ (C) Re_X for U1 and U2 as bulk velocities, 12 and 24 m/s, respectively.

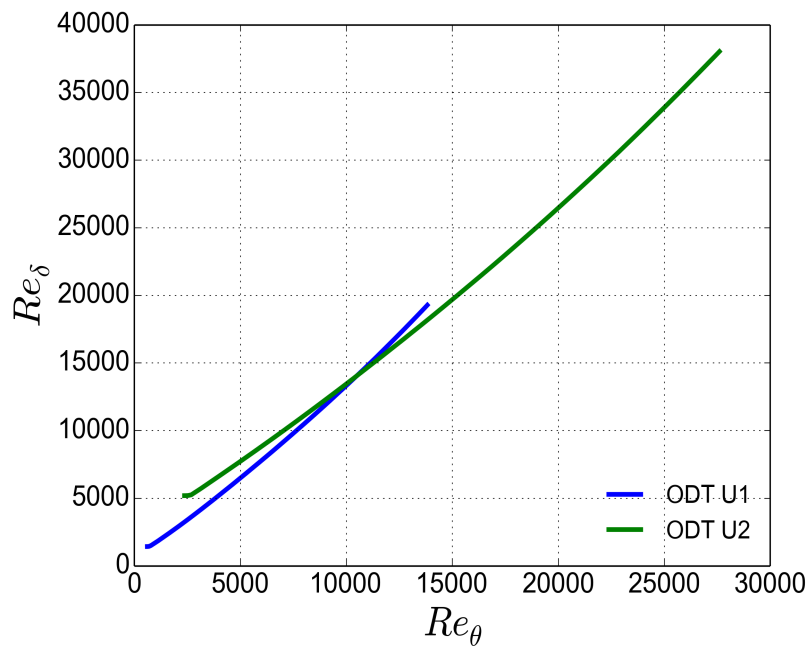


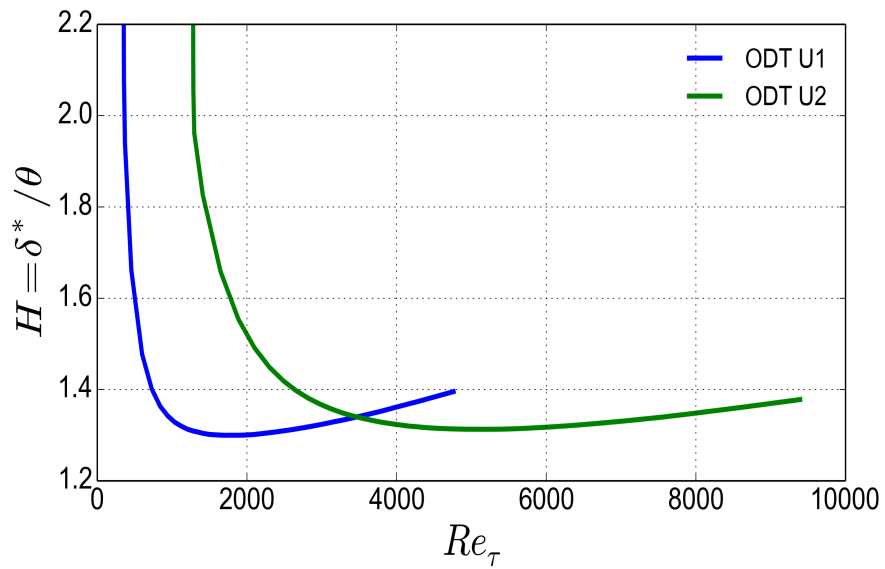
FIGURE 5.25: The quantity Re_δ as a function of Re_θ for $U1$ and $U2$ as bulk velocities, 12 and 24 m/s, respectively. Reference data is not available for this quantity.

and temporal DNS features is presented in this section.

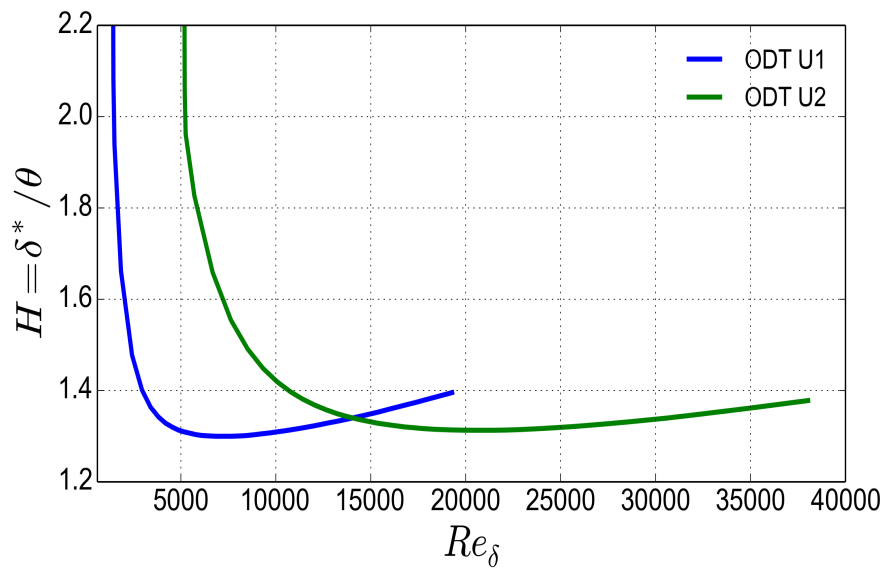
The mean streamwise velocity profile as a function of wall-normal coordinate in viscous units at $Re_\theta \approx 1968$ for the present case, i.e., the SBL flow configuration along with the TBL configuration reported in [109] is shown in Figure 5.27. Note that the profiles for SBL and TBL for ODT simulations overlap on to each other up to $y^+ \approx 200$ and deviate from $y^+ > 200$ onward. However, there is a difference observed in outer-log region between spatial [41] and temporal [50] DNS profiles as well. The accountability for such difference can be given to different initial and boundary conditions. In case of SBL, the initial condition is laminar profile for ODT as well as DNS. For TBL case, tan hyperbolic profile is used in [50, 109]. The bulk velocities used are also different as $U_b = 12$ m/s for SBL and $U_b = 15$ m/s for TBL cases. The selection of the optimal parameter for the individual flow configurations also explains the difference in outer-log region in case of ODT than DNS.

Figure 5.28 shows the pre-multiplied mean velocity gradient, i.e., the indicator function, $y^+ (\partial \bar{u}^+ / \partial y^+)$, as a function of wall-normal coordinate. This figure includes the profiles for the SBL and TBL flow configuration for the ODT methodology at $Re_\theta \approx 2000$ and the reference spatial DNS data at corresponding Re_θ . The reference data for temporally developing turbulent boundary layer is not available.

The profiles for SBL and TBL configurations for ODT model overlap on to each other up to $y^+ \approx 150$ and minor deviation are observed in range $150 < y^+ < 300$ which increases from $y^+ > 300$ onward. These differences in the outer-log region are noted earlier for TBL as well as SBL cases with increasing bulk Reynolds numbers. We report that for this comparison between SBL and



(A)



(B)

FIGURE 5.26: The quantity H as a function of (A) Re_τ and (B) Re_δ for $U1$ and $U2$ as bulk velocities, 12 and 24 m/s, respectively.

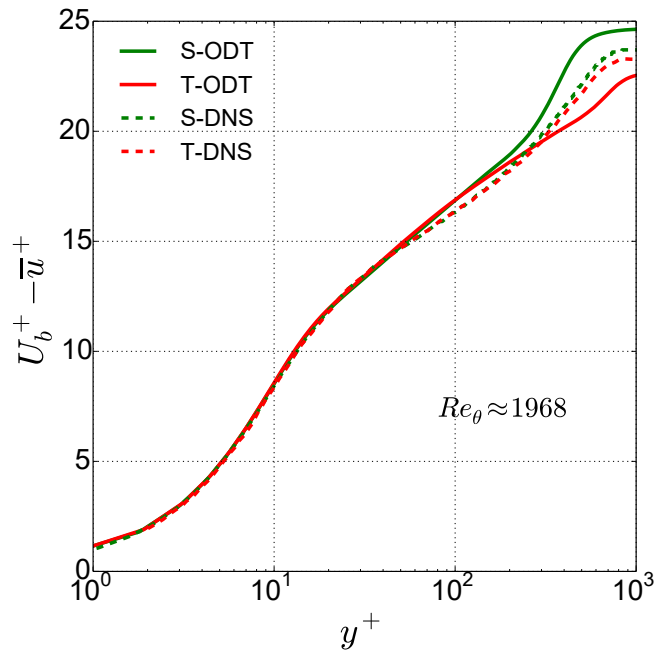


FIGURE 5.27: Normalized wall-normal profiles of the mean streamwise velocity component as a function of wall normal coordinate (in viscous units) at $Re_\theta \approx 1968$ for spatial and temporal ODT formulation. For reference, spatial DNS data from [41] and temporal DNS data from [50] at same Re_θ is shown in dashed lines.

TBL, we have different bulk Reynolds numbers. This could also be due to the different initial and boundary conditions. Additionally, the selected optimal parameter for the individual flow configurations are also different.

Figure 5.29 (A) depicts the rms of the normalized streamwise velocity component as a function of the normalized wall-normal coordinate in viscous units is at $Re_\theta \approx 1968$ for SBL and TBL, ODT and DNS. Some minor discrepancies are noticed from ODT as well as DNS simulations. The C parameter plays important role in improving rms peaks. Lower C values can be utilized for modifying the rms peak. However, $C = 9$ is used for TBL and $C = 6$ for SBL. The SBL peak is slightly under-predicted as compared to TBL. Other reasons for the discrepancies remain same as explained for mean streamwise velocity profile. These are distinct initial and boundary conditions and the model physical parameter selected for the flow configurations. The statistics, however, is presented for SBL and TBL at same Re_θ (≈ 1968). Nevertheless, TBL as well SBL flow configuration under-predict the rms peak as compared to DNS. The qualitative trend of the flow dynamics is captured well with a reduced order model.

The profile for the normalized Reynolds shear stresses as a function of the wall-normal coordinate in viscous units, for both SBL and TBL ODT configurations are shown in Figure 5.29(B). The TBL data is shown at $Re_\theta \approx 1968$. The SBL data is shown at ≈ 1968 and ≈ 7500 . For comparison, the reference data from [41, 50], both at $Re_\theta \approx 1968$ is also plotted. For SBL configuration,

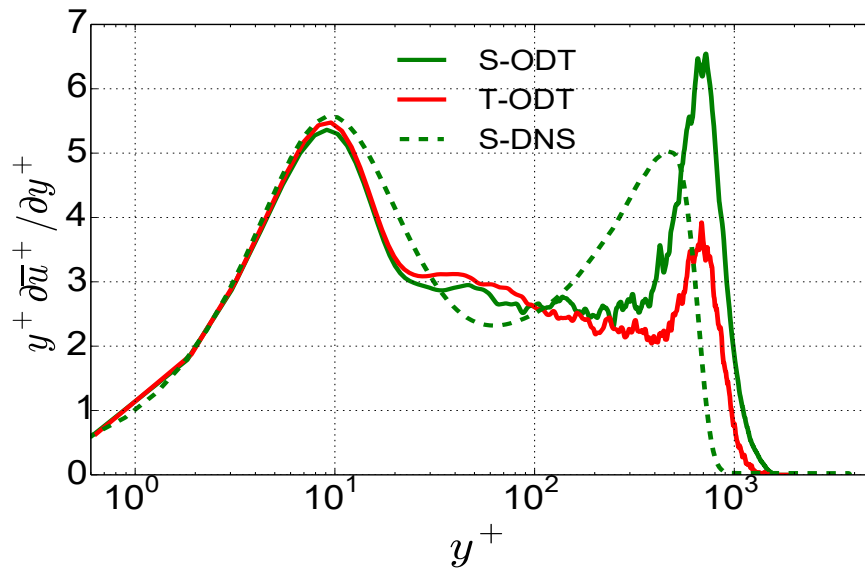
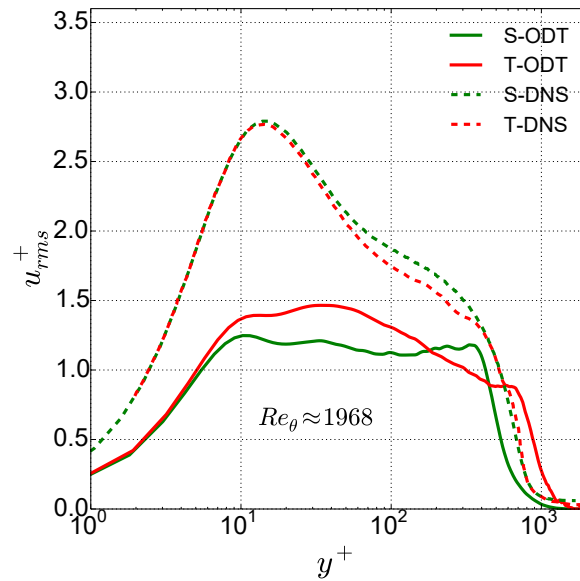


FIGURE 5.28: Indicator function versus wall-normal coordinate (in viscous units) at $Re_\theta \approx 1968$ for spatial and temporal ODT formulation. For reference, spatial DNS data from [41] at same Re_θ is shown in dashed line.

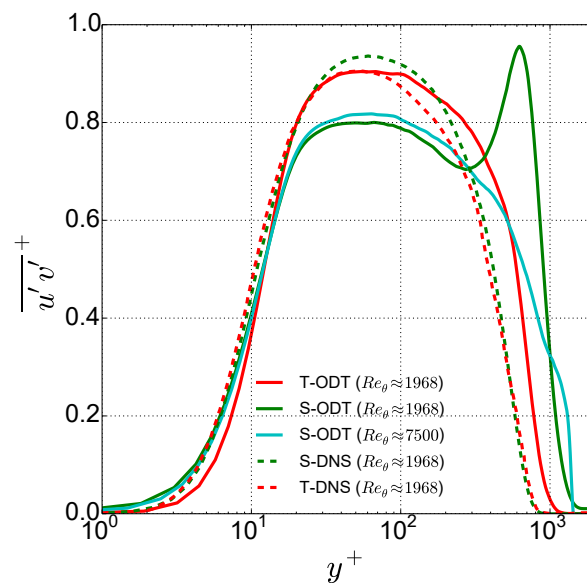
a peak in outer-log region at $Re_\theta \approx 1968$ is reported due to transient effects and these effects were reported for TBL using ODT model in [109], however, only up to $Re_\theta \approx 2500$. Although, these transient effects for the present case are noticed up to $Re_\theta \approx 7500$. In case of the ODT model, the SBL peak is slightly under-predicted in comparison with TBL. Note that the general shape is captured by ODT using spatial as well temporal configuration.

The turbulent production in the flow is plotted as a function of wall-normal coordinate in viscous units in Figure 5.30 at (A) $Re_\theta \approx 1968$ and (B) $Re_\theta \approx 2000$ for spatial and temporal ODT formulation. For reference, spatial DNS and LES data from [41, 82] at same Re_θ is shown in dashed lines. Temporal reference data is not available for these profiles as well. Here, the factors responsible for creating difference between SBL and TBL remains same as explained for other profiles, which are different (a) initial conditions, (b) boundary conditions, (c) bulk velocity and (d) optimal set of physical model parameter, for the individual flow configurations. Additionally, it is important to mention that the Re_θ up to which flow capture transitions to turbulence is much higher in case of SBL as compared to TBL for the ODT model. The Re_θ considered here is very small ($Re_\theta \approx 1968$ and $Re_\theta \approx 2000$).

The skewness of the streamwise velocity component is plotted as a function of wall-normal coordinate in viscous units in Figure 5.31 (A) at $Re_\theta \approx 2000$ for spatial and temporal ODT profiles. This is done in comparison with the reference spatial DNS in [41] and temporal DNS in [50]. The qualitative trend for the present SBL configuration is consistent with the TBL configuration for the ODT simulations discussed in earlier chapter. Also these profiles for ODT are consistent with the reference DNS data for considered Re_θ . For both, SBL and TBL flow configurations, the positive skewness using reduced order

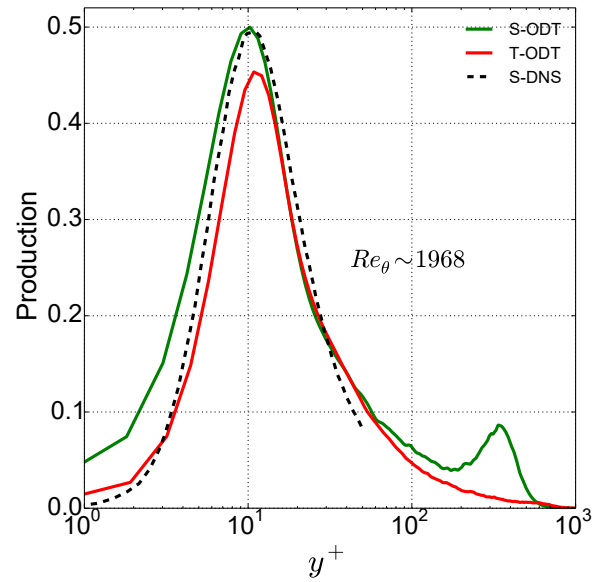


(A)

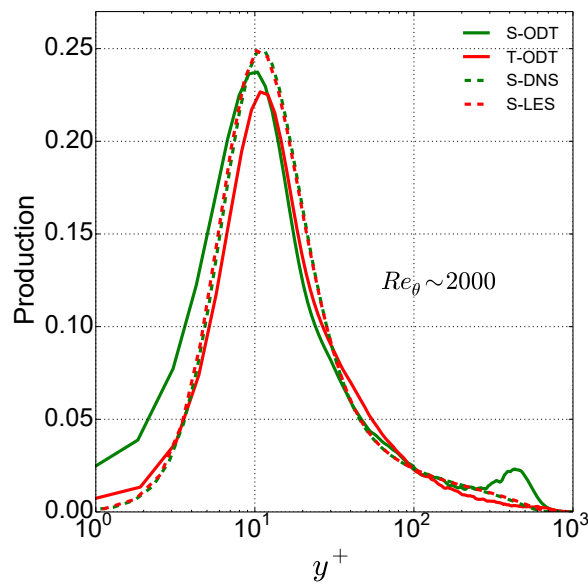


(B)

FIGURE 5.29: The (A) rms of the streamwise velocity component and (B) Reynolds shear stresses profile as a function of wall normal coordinate (in viscous units). The rms profiles are shown at $Re_\theta \approx 1968$ for SBL as well as TBL configuration and the Reynolds shear stresses at $Re_\theta \approx 1968$ for TBL and at $Re_\theta \approx 1968, 7500$ for SBL ODT formulation. For reference, spatial DNS data from [41] and temporal DNS data from [50] at $Re_\theta \approx 1968$ is shown in dashed lines.



(A)



(B)

FIGURE 5.30: Turbulent kinetic energy production as a function of the wall-normal coordinate (in viscous units) for (A) $Re_\theta \approx 1968$ and (B) 2000 for spatial and temporal ODT formulation. For reference, spatial DNS data from [41] and spatial LES data from [82] at same Re_θ is shown in dashed lines.

model formulation is under-predicted as compared to the reference DNS data in the inner region and in the outer-region, some of the flow structures are not captured for TBL as well SBL configuration.

The flatness of the streamwise velocity component is depicted in Figure 5.31 (B) as a function of wall-normal coordinate in viscous units at $Re_\theta \approx 2000$ for spatial and temporal ODT profiles. For reference, the DNS data from [41, 50] is also plotted. The qualitative trend for flatness profiles are also consistent for the SBL and TBL configuration for ODT methodology and with reference DNS data plotted with dashed lines. The Gaussian flatness value for both cases considered is near to three. The profiles are under-predicted in inner-region in comparison with the reference DNS data.

Skin friction coefficient C_f as a function of (A) Re_δ and (B) Re_X for spatial and temporal ODT formulation is shown in Figure 5.32. For reference, temporal DNS data from [50] is shown in dashed lines.

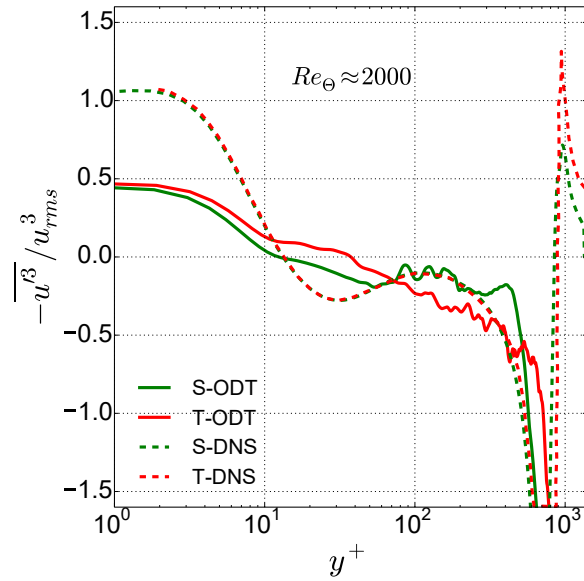
Despite several differences (which are initial and boundary conditions, bulk velocity, physical model parameters) in the the simulations carried out for SBL and TBL flow configurations for ODT methodology, the profiles for C_f with Re_δ for both configurations shown in Figure 5.32 (A) collapses onto each other at higher Re_δ . The TBL profile is available up to very small Re_δ but it is expected that if the simulations for TBL are carried out for long duration up to higher Re_δ then it may overlap with the SBL profile. Moreover, the peak in the initial stage is under-predicted for SBL as compared to the TBL due to different C opted.

Figure 5.32 (B) for C_f with Re_X shows different behaviour than with Re_δ . The C_f variation with Re_X seems parallel for SBL and TBL flow configurations for ODT model. However, these profiles might collapse at very high Re_X but the range for Re_X is not same for both cases. It can be commented that for SBL, C_f seems to achieve asymptotic state for very high Re_X but for TBL the profile has not reached asymptotic state.

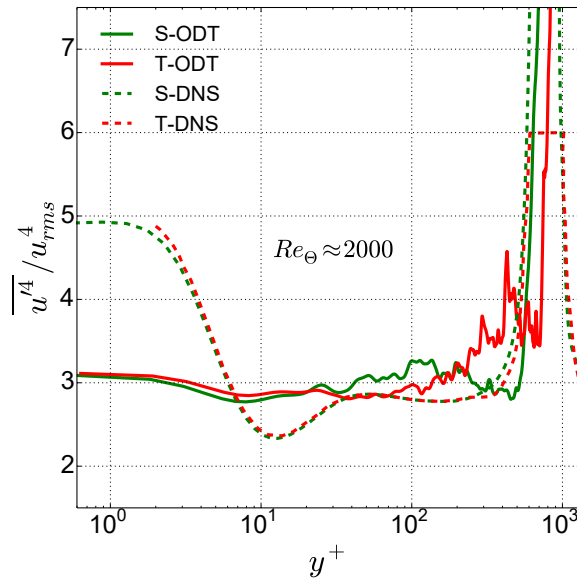
Next, (A) skin friction coefficient C_f and (B) shape factor H , as a function of Re_θ for spatial and temporal ODT formulation is shown in Figure 5.33. For reference, spatial DNS and LES data from [41, 82] and temporal DNS data from [50] at same Re_θ is shown in dashed lines.

Note that for ODT, TBL data is available up to $Re_\theta \approx 3500$ and SBL data up to $Re_\theta \approx 14000$. Figure 5.33 (A) captures initial transitions for all profiles for ODT as well as DNS and LES up to $Re_\theta \approx 2000$. At higher Re_θ , TBL profiles are expected to collapse with SBL profiles for ODT and reference data. However, due to limited data range for TBL profiles for ODT and DNS, it can not be verified in the present work and remain open to verify in future investigations related to boundary layer-type flows.

The shape factor H variation with Re_θ in Figure 5.33 (B) also captures transitions to turbulence up to certain Re_θ and is expected to show some similar trend only at very high Re_θ . Nevertheless, the trends are consistent with the earlier simulations for SBL and TBL flow configuration using the ODT model discussed in previous chapter and above in this chapter. It is also worth comparing these quantities for one-dimensional model for the considered formulations.

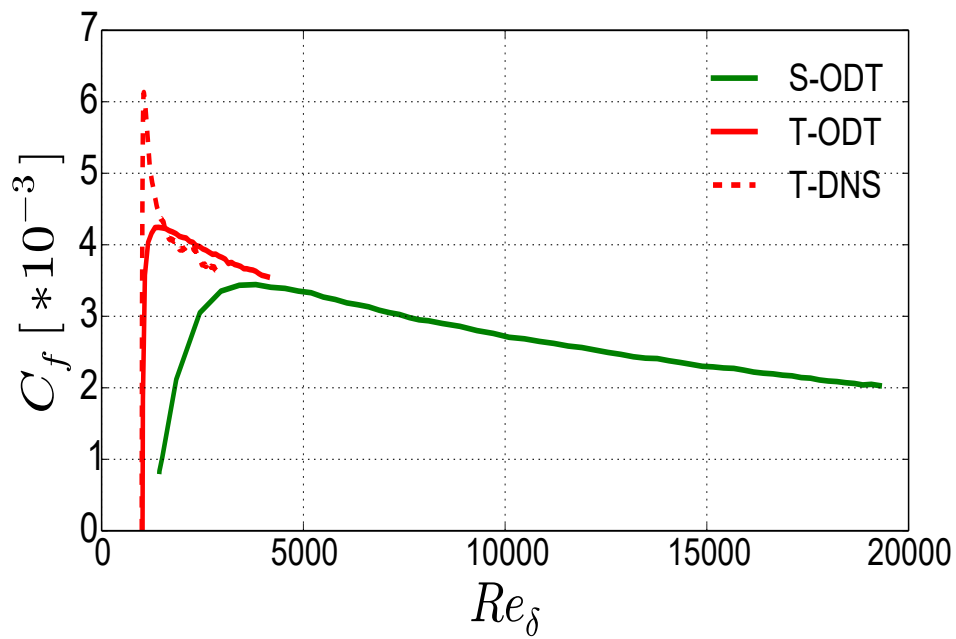


(A)

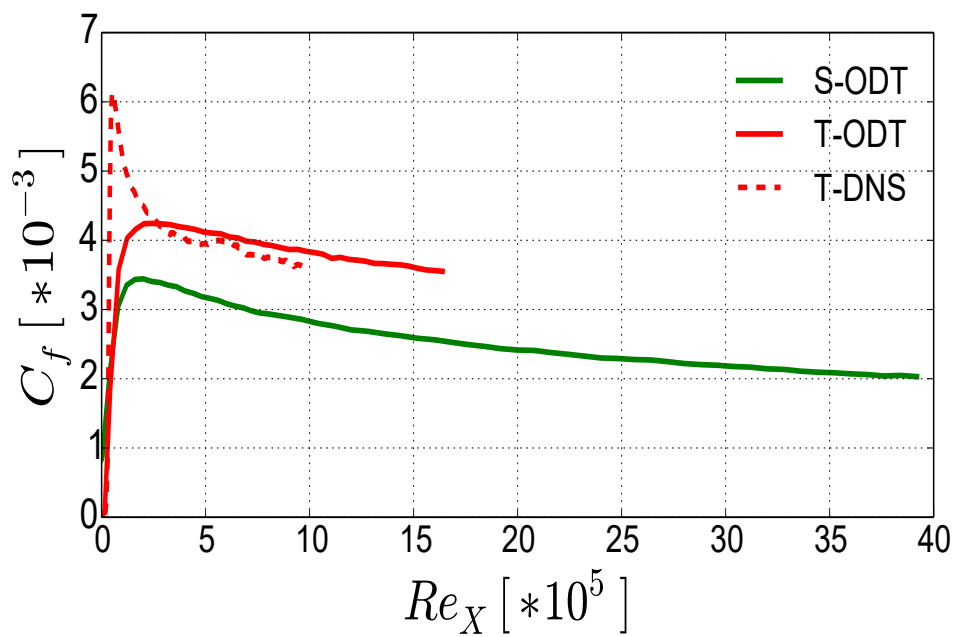


(B)

FIGURE 5.31: The (A) skewness and (B) flatness of the stream-wise velocity component as a function of wall normal coordinate (in viscous units) at $Re_\theta \approx 2000$ for spatial and temporal ODT formulation. For reference, spatial DNS data from [41] and temporal DNS data from [50] at same Re_θ is shown in dashed lines.



(A)

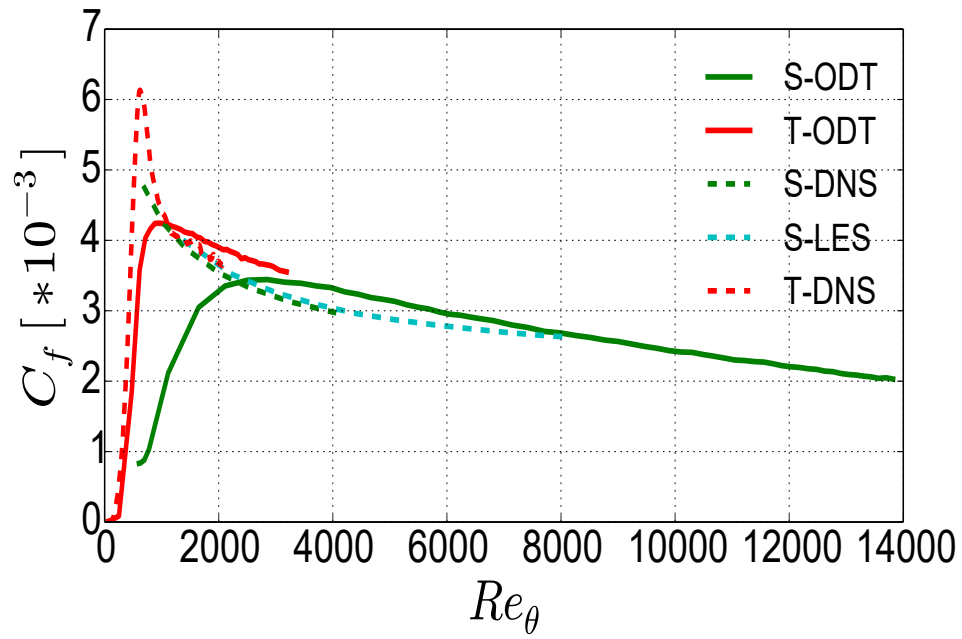


(B)

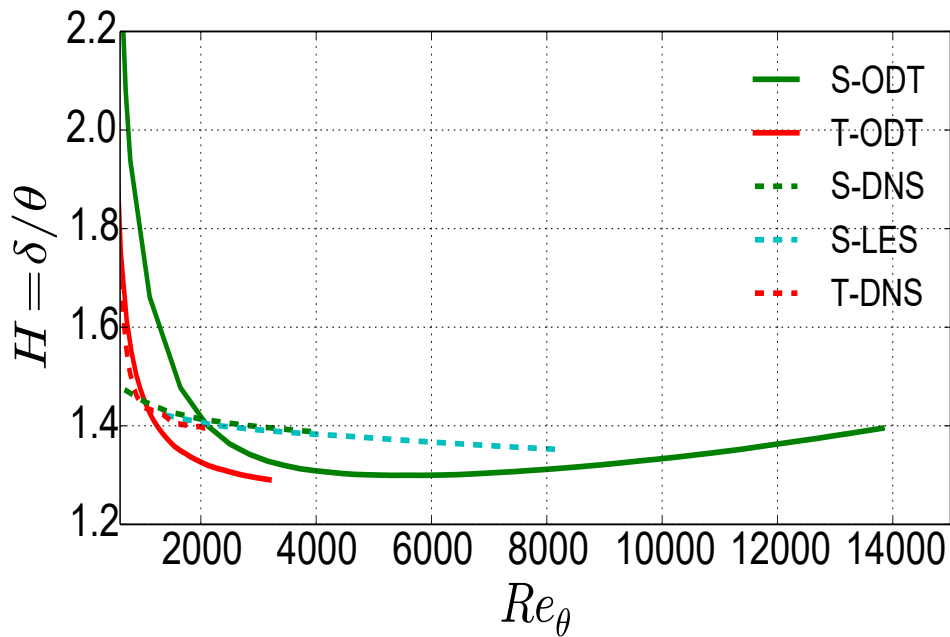
FIGURE 5.32: Skin friction coefficient C_f as a function of (A) Re_δ and (B) Re_X for spatial and temporal ODT formulation. For reference, temporal DNS data from [50] is shown in dashed lines.

The spatial reference data for this quantity is not available.

Figure 5.34 displays variation of the quantity Re_δ as a function of Re_θ for spatial and temporal ODT formulation. For comparison, the reference temporal DNS data from [50] is shown. Spatial reference is not available for this



(A)



(B)

FIGURE 5.33: (A) Skin friction coefficient C_f and (B) shape factor H as a function of Re_θ for spatial and temporal ODT formulation. For reference, spatial DNS and LES data from [41, 82] and temporal DNS data from [50] is shown in dashed lines.

quantity. The profiles collapse onto each other and shows very good agreement for SBL and TBL ODT simulation with the temporal DNS results. Re_δ increases with increasing Re_θ and shows linear behaviour. The values reached

for T-ODT for Re_δ is ≈ 4000 and $Re_\theta \approx 3500$ and for S-ODT, $Re_\delta \approx 20000$ and $Re_\theta \approx 14000$.

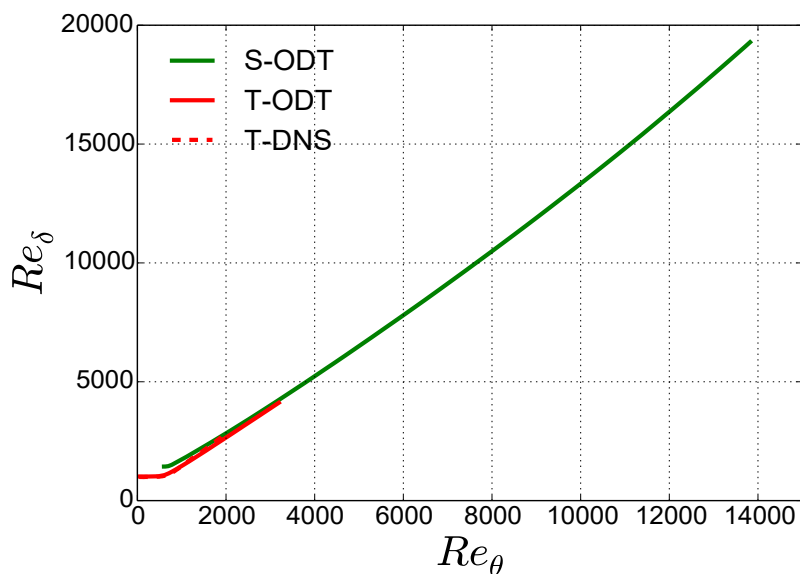


FIGURE 5.34: The quantity Re_δ as a function of Re_θ for spatial and temporal ODT formulation. For comparison, the reference DNS data from [50] is shown.

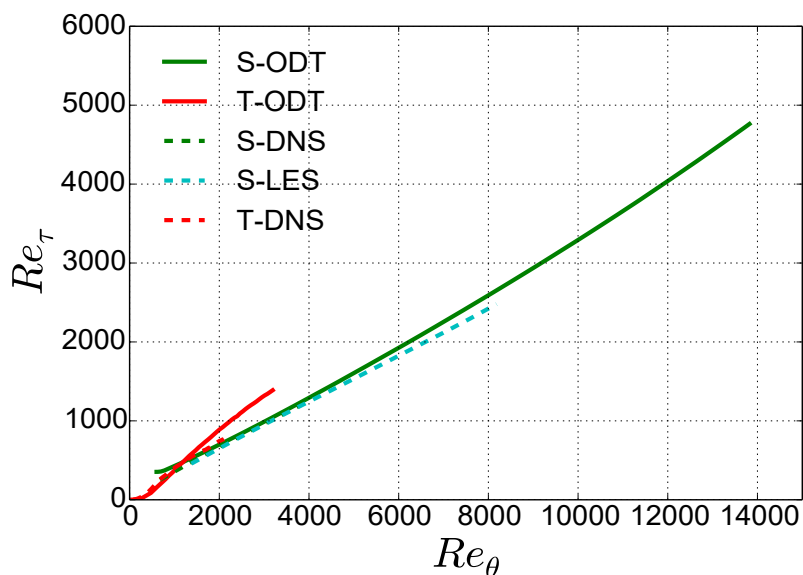


FIGURE 5.35: The quantity Re_τ as a function of Re_θ for spatial and temporal ODT formulation. For reference, spatial DNS and LES data from [41, 82] and temporal DNS data from [50] is shown in dashed lines.

Figure 5.35 displays variation of the quantity Re_τ a function of Re_θ for spatial and temporal ODT formulation. For reference, spatial DNS and LES data

from [41, 82] and temporal DNS data from [50] is shown in dashed lines. S-ODT, S-DNS and S-LES show good agreement with each other and T-ODT matches with T-DNS. However, the spatial results for ODT, DNS as well LES do not show agreement with the temporal results produced with ODT and DNS. In general, Re_τ increases with increasing Re_θ for spatial as well as temporal formulation. A linear behaviour of the quantity Re_τ is noted with Re_θ . The values reached for T-ODT for Re_τ is ≈ 1500 and $Re_\theta \approx 3500$ and for S-ODT, $Re_\tau \approx 6000$ and Re_θ same as above ≈ 14000 .

5.5 In Closing

The chapter discusses a detailed validation for the spatially developing turbulent boundary layer. The selection of optimal physical model parameters is presented in Appendix G. These selected model parameters are used to investigate various velocity statistics and important global properties for boundary layer-type flows and are compared with the available reference DNS and LES data from [41, 82]. The various velocity statistics and global properties are compared for S-ODT and T-ODT with reference data for boundary layer-type problems.

Chapter 6

SBL with Uniform Blowing

In this chapter, the well validated spatial ODT formulation in earlier chapter is extended further by applying uniform blowing on the bottom wall. Blowing and suction are two important aspects to reduce or enhance drag. The uniform blowing is presented in this chapter, whereas the suction case is presented elsewhere [96]. Various velocity statistics as a function of wall-normal coordinate and several global properties for boundary layer varied with Re_θ in comparison with the reference LES data are discussed in detail in the chapter. Since the ODT model is sensitive towards model physical parameters, a detailed parametric study is conducted to choose the optimal set of these parameters and presented in Appendix H.

6.1 Velocity Statistics for Uniform Blowing Configuration

In this section, velocity statistics up to 4th order at some selected stream-wise location represented by Re_θ as $Re_\theta \approx 1407, 2082$ and 2395 is discussed. These results are presented in comparison to the available reference LES data form [64] at same Re_θ . For the comparison purpose, some of the DNS profiles from simple SBL configuration without blowing from [41] are also used as not all the statistic is available for the uniform blowing flow configuration. Additional, some of the structural properties, for example, Re_τ , H and C_f as a function of Re_θ are also discussed as these quantities are very important for boundary layer-type flows especially with uniform blowing. The simulations are performed for one free-stream velocity. The optimal set of physical model parameters are fixed as $\alpha = 2/3$, $C = 6$, $Z = 100$, and the two-thirds large-eddy suppression mechanism.

6.1.1 First and Second Order Velocity Statistics

The mean streamwise velocity profile as a function of the wall-normal coordinate in viscous units for $Re_\theta \approx 1407, 2082$ and 2395 with (A) uniform blowing in SBL and at $Re_\theta \approx 1811$ and 2047 (B) without blowing for a fixed free-stream

velocity along with the LES reference data [64] (dashed line) is depicted in Figure 6.1.

For the selected optimal parameters, the ODT profiles shows very good agreement with the reference LES data for all Re_θ for uniform blowing case. The velocity profile is independent of Re_θ from the inner region to the buffer region up to $y^+ < 200$, whereas, in the outer region, the profile for lowest Re_θ , i.e., $Re_\theta \approx 1407$ is close to the wall. This moves away from the wall with increasing Re_θ for uniform blowing in turbulent boundary layer. Note that this behaviour of profiles with increasing Re_θ is similar to the reference LES data [64] shown with dashed line in Figure 6.1 (A). This illustrates the ability of the ODT model to capture the variations for the mean velocity from inner region to the buffer region and further into the log-region for the spatially developing turbulent boundary layer with uniform blowing.

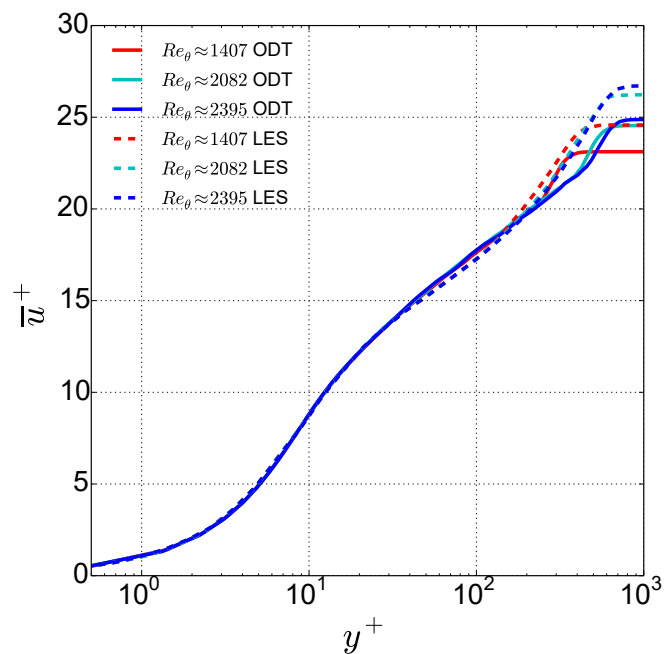
The optimal set of model parameters for without blowing case is not the same as for uniform blowing case. Nevertheless, for the selected model parameters, the mean streamwise velocity profiles for without blowing at both Re_θ considered show excellent agreement with the reference data as shown in Figure 6.1 (B).

Note that the physical model parameters selected for uniform blowing case are $\alpha = 2/3$, $C = 6.0$, $Z = 100$ and two-thirds LS suppression mechanism. Whereas, for without blowing case these parameters are $\alpha = 2/3$, $C = 4.5$, $Z = 600$ and frac domain LS suppression mechanism. In general the C parameter is important for boundary layer-type flows as seen in previous SBL and TBL investigation. However, the Z parameter is found very important for blowing configuration considered here. Small eddies might be important for blowing case and hence a low Z value is used for the same.

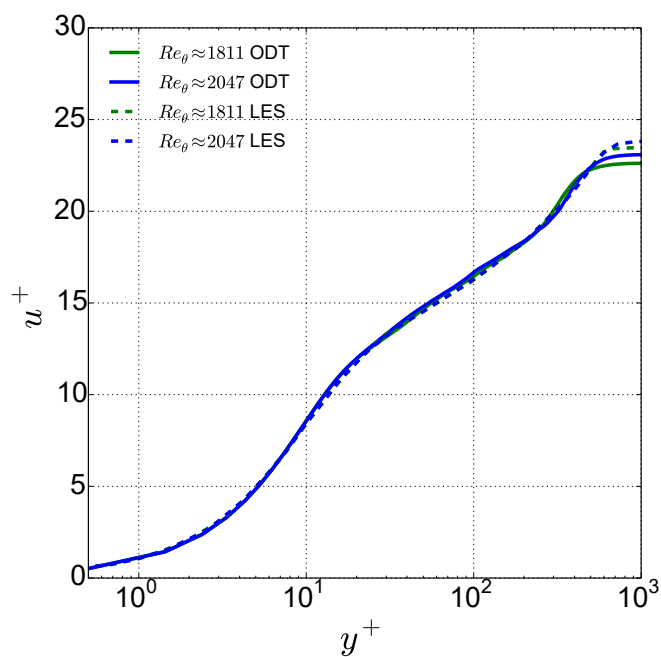
The pre-multiplied mean velocity gradient, i.e., the indicator function is shown in Figure 6.2 for $Re_\theta \approx 1407, 2082$ and 2395 with (A) uniform blowing in SBL and at $Re_\theta \approx 1811$ and 2047 (B) without blowing for a fixed free-stream velocity. Note that the LES data for comparison is not available for this profile and the DNS data of a fully turbulent zero pressure gradient SBL from [44] is used in the plot as a black dashed line at $Re_\theta \sim 2000$. The indicator function calculated as $y^+ (\partial \bar{u}^+ / \partial y^+)$, is varied as a function of wall-normal coordinate (in viscous units) for uniform blowing and without blowing configuration.

The indicator function is important as it aids in assessing if there is a logarithmic region in the mean velocity profile and the log-region is identified in the velocity profile by a constant region in the plot. It is known that this constant region start appearing only at fairly large Reynolds number regime. The profiles are noted as independent of Re_θ from the inner to the buffer region. There is dispersion in the profiles in the region far away from the wall. The variation of indicator function with growing Re_θ in the outer log-region is similar to the mean streamwise velocity explained above.

The von Kármán constant K of the law of the wall is considered in order to address the similarity properties. K is determined as the inverse of the pre-multiplied mean velocity gradient, i.e., indicator function in the logarithmic region and it is obtained for the present case by averaging indicator function over $25 < y^+ < 150$ (given in Table 6.1 for $Re_\theta \approx 2395$). $K = 0.32$ for the



(A)



(B)

FIGURE 6.1: The mean streamwise velocity profile as a function of the wall-normal coordinate (in viscous units) at $Re_\theta \approx 1407, 2082$ and 2395 with (A) uniform blowing in SBL and at $Re_\theta \approx 1811$ and 2047 (B) without blowing. For comparison, the reference LES data for uniform blowing as well as without blowing configuration from [64] at corresponding Re_θ are shown.

spatially developing turbulent boundary layer with uniform blowing. The ODT model is capable to capture the qualitative trends from the reference DNS data using the estimated set of physical model parameters.

Figure 6.2 (B) shows indicator function for no blowing case for two Re_θ . The observation for this profiles remains consistent with the other cases, for example, for blowing case explained above as well as with SBL and TBL configurations presented in previous chapters.

Figures 6.3 displays the root mean square (rms) of the streamwise velocity component ($u_{rms}^+ = \sqrt{u'^2}/u_\tau$) as a function of the normalized wall-normal coordinate in viscous units for $Re_\theta \approx 1407, 2082$ and 2395 with (A) uniform blowing in SBL and at $Re_\theta \approx 1811$ and 2047 (B) without blowing in comparison with the LES reference data [64].

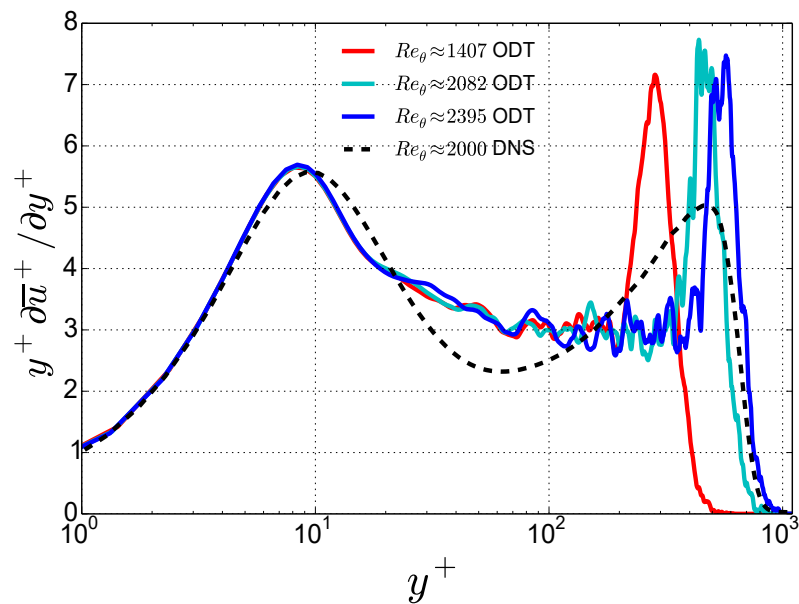
It is known from previous studies [28, 29, 89, 96, 109] that the ODT model under-predicts the rms peaks due to missing 3-D information. Therefore, some 3-D information [84, 94, 130, 131] needs to be retained to get a good fit for the rms profiles using ODT in comparison to reference LES [64]. The peak value for rms profile can be improved by choosing small value of the model parameter C which however, have the direct effect on the slope of the mean streamwise velocity.

For blowing configuration shown in Figures 6.3 (A), the general trend for rms is similar to reference LES [64] with increasing Re_θ . The rms profiles remain unaffected in the inner region up to $y^+ < 10$ and are sensitive to Re_θ from $y^+ > 10$ onward. The peak amplitude for blowing is directly proportional to the Re_θ . The ODT implementation for uniform blowing also confirm a very weak double peak in region $10 < y^+ < 50$. This peak in the vicinity of the wall might be due to the artifacts generated by the topology of the triplet map close to a wall [89]. This peak was also reported in the temporally developing turbulent boundary layer [109].

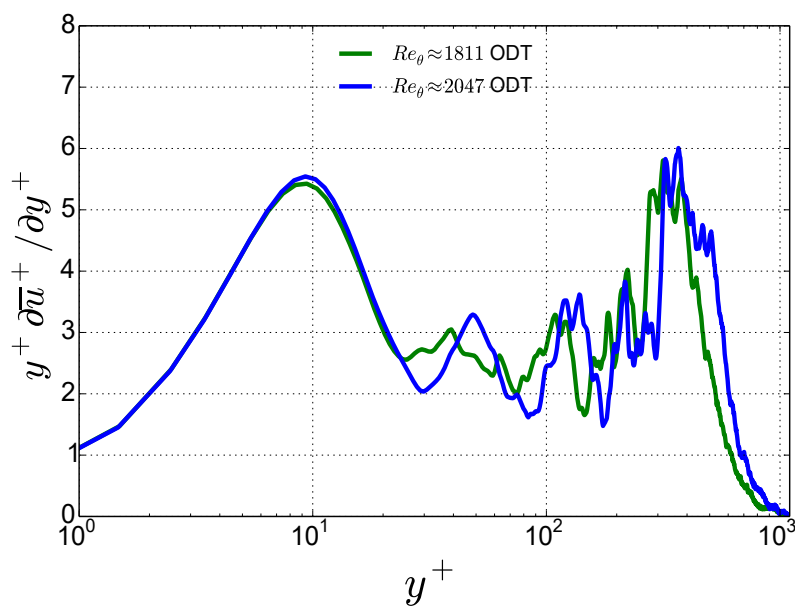
An additional peak in the outer log-region was reported in [112] at small Re_θ and in [109] at all Re_θ which was attributed purely to the transient flow or to the effect of the initial conditions in [112]. This peak was also sensitive to the LS method used and time window selected in [109]. For the present uniform blowing configuration, the same LS method is used as it was in [109] but no time window is used since the streamwise position is used to calculate Re_θ instead of instant. This peak is also discerned in the reference DNS results for high bulk Reynolds number [50] and it has decreased after the initial transient has passed leaving a 'shoulder'. This 'shoulder' appears in reference LES data as well [64] which hints that ODT seems to capture this general property of the outer layer dynamics of the boundary layer.

When compared with the TBL and SBL case without blowing [109, 112], and with blowing case for same simulation set-up which is used for blowing in Figures 6.3 (B), a slight increase in the rms amplitude by blowing is noted. This is due the reduced skin friction coefficient which is discussed below.

Figures 6.4 shows the profiles for the normalized Reynolds shear stresses as a function of the wall-normal coordinate in viscous units, $(\overline{u'v'}/u_\tau^2)$, for $Re_\theta \approx 1407, 2082$ and 2395 with (A) uniform blowing in SBL and at $Re_\theta \approx 1811$ and 2047 (B) without blowing. The reference data from [64] is plotted with

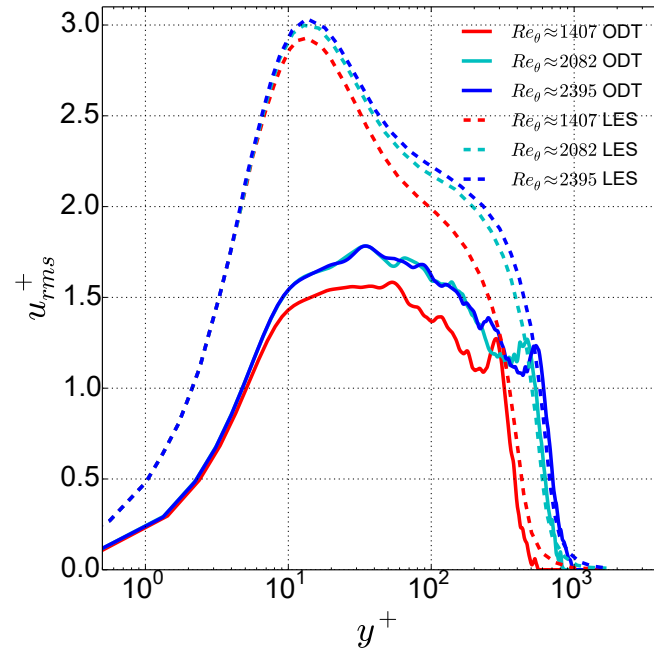


(A)

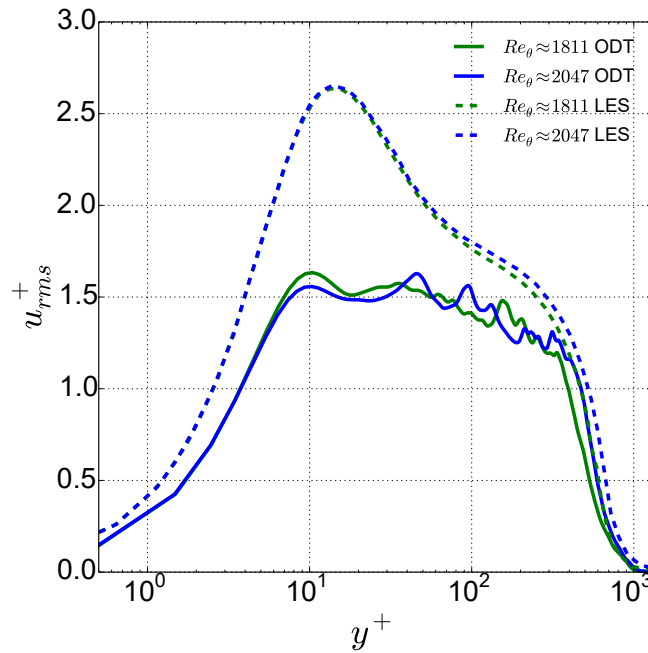


(B)

FIGURE 6.2: The indicator function as a function of wall-normal coordinate (in viscous units) at $Re_\theta \approx 1407, 2082$ and 2395 with (A) uniform blowing in SBL and at $Re_\theta \approx 1811$ and 2047 (B) without blowing configuration. For comparison, the reference DNS data for the SBL configuration from [44] at $Re_\theta \sim 2000$ is given by a black dashed line. The reference data for blowing case is not available for indicator function.



(A)



(B)

FIGURE 6.3: The streamwise root-mean-square velocity profiles versus wall-normal coordinate (in viscous units) at $Re_\theta \approx 1407, 2082$ and 2395 with (A) uniform blowing in SBL and at $Re_\theta \approx 1811$ and 2047 (B) without blowing. For comparison, the reference LES data from [64] at corresponding Re_θ is shown for uniform blowing as well as without blowing configuration.

dashed lines for corresponding Re_θ for blowing as well as without blowing case. Note that the calculation of Reynolds shear stresses is different in ODT. The Reynolds shear stress calculations are based on the changes of the velocity profiles due to eddies which is explained in detail in [28] Appendix C.

An additional peak was reported in temporal and spatial ODT formulations used for boundary layer investigation in [109, 112] which is not captured for the uniform blowing configuration shown in Figures 6.4(A). This peak is however, captured for the without blowing case in Figures 6.4 (B) using same simulation set-up as used for blowing case. This suggests that the flow dynamics may be different for different flow configurations and not all profiles behave in similar fashion.

The qualitative trend for Reynolds shear stress profiles show agreement with the LES data [64], however, the profiles are under-predicted as compared to the reference data. The Reynolds shear stresses for the suction boundary layer [96] were also reported to be over-predicted compared to the reference DNS data. For the temporally developing turbulent boundary layer, the Reynolds shear stresses were in very good agreement with the DNS results. Whereas, it was slightly under-predicted for spatially developing turbulent boundary layer. This aids another sign of confidence in the predictive capabilities of ODT for the selected flow configuration.

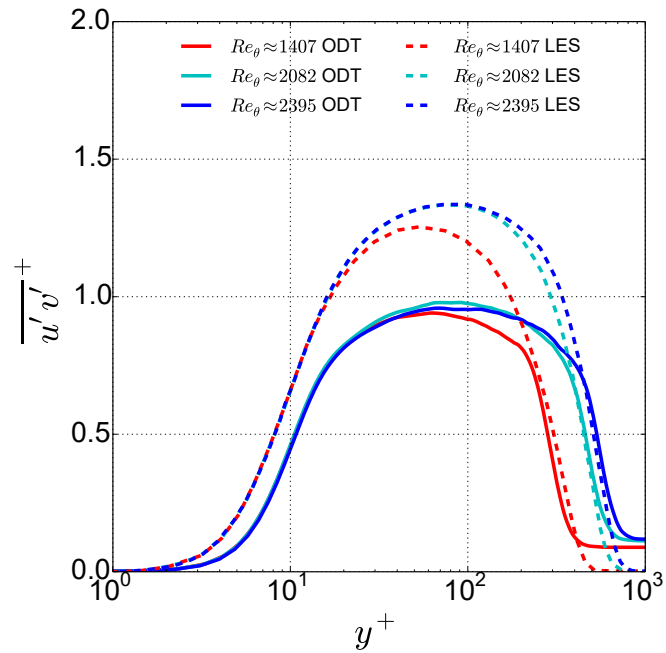
When Figures 6.4 (A) is compared with Figures 6.4 (B), the magnitude for Reynolds shear stress in both the cases is different. For blowing configuration, it is ≈ 1.0 , whereas, for without blowing case it is ≈ 0.9 . As expected, the Reynolds shear stress is slightly increased for blowing configuration.

6.1.2 Higher Order Velocity Statistics

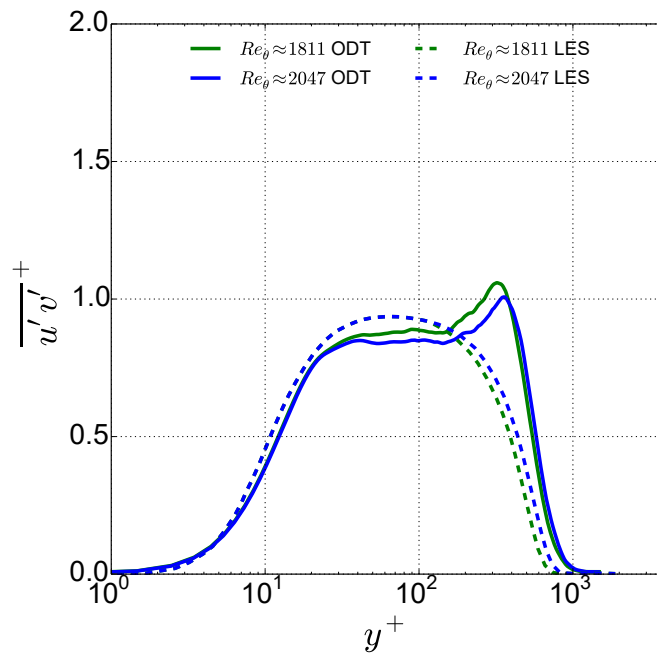
The turbulent production as a function of wall-normal coordinate in viscous units is depicted in Figure 6.5. The turbulent production is calculated as $-\overline{u'v'}^+ \frac{\partial \overline{u}^+}{\partial y^+}$. The figure displays production for $Re_\theta \approx 1407, 2082$ and 2395 with (A) uniform blowing in SBL and at $Re_\theta \approx 1811$ and 2047 (B) without blowing configuration. The production data for reference LES for selected Re_θ is not available and a modest comparison is made by using DNS data without blowing from [41] at comparable Re_θ , i.e., $Re_\theta \approx 2000$.

As expected in case of uniform blowing shown in Figure 6.5 (A), the peak of production is noted slightly over-predicted for ODT simulations in comparison to the DNS data. This might be due to the reduction in skin friction coefficient for present configuration because for the case without blowing shown in Figure 6.5 (B), this peak is under-predicted. This indicates that ODT is capable to capture flow dynamics for blowing configuration. Nevertheless, the qualitative trend remains unaltered for the blowing configuration when compared to other cases in earlier chapters and dependence of production on Re_θ is not observed. Note that the Reynolds shear stress profiles shown above are under-predicted, but the production curve is very close to the reference data, suggesting the $\partial u / \partial y$ is over-predicted.

Figure 6.6 depicts the skewness of the streamwise velocity component, $-\overline{u'^3} / u_{rms}^3$, as a function of the wall-normal coordinate in viscous units, y^+ .

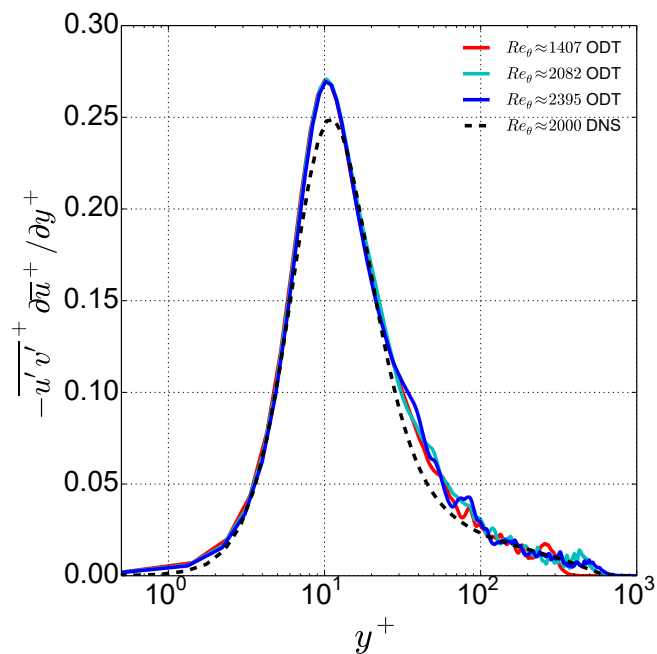


(A)

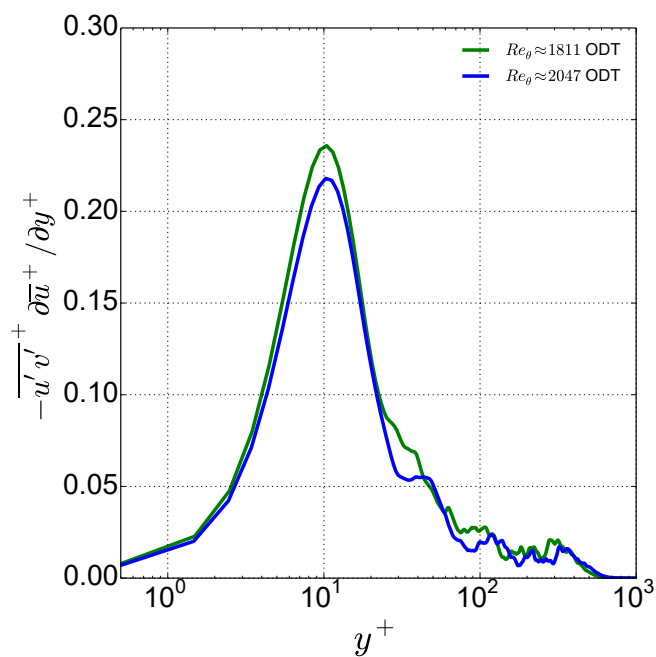


(B)

FIGURE 6.4: The profiles of the Reynolds shear stresses versus wall-normal coordinate (in viscous units) at $Re_\theta \approx 1407, 2082$ and 2395 with (A) uniform blowing in SBL and at $Re_\theta \approx 1811$ and 2047 (B) without blowing. For comparison, the reference LES data from [64] at corresponding Re_θ is shown for uniform blowing as well as without blowing configuration.



(A)



(B)

FIGURE 6.5: Turbulent kinetic energy production as a function of the wall-normal coordinate (in viscous units) at $Re_\theta \approx 1407, 2082$ and 2395 with (A) uniform blowing in SBL and at $Re_\theta \approx 1811$ and 2047 (B) without blowing configuration. For comparison, the reference DNS data from [41] at $Re_\theta \approx 2000$ is shown for SBL configuration without blowing.

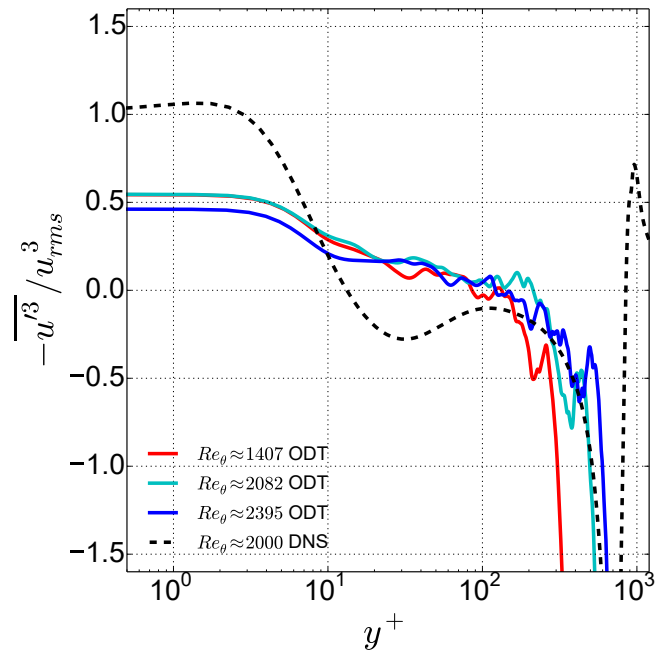
Note that we do not have reference LES data for blowing configuration at higher order velocity statistics and like production, DNS data from [41] at $Re_\theta \approx 2000$ is shown for comparison. For ODT, the profiles are displayed at $Re_\theta \approx 1407, 2082$ and 2395 with (A) uniform blowing in SBL and at $Re_\theta \approx 1811$ and 2047 (B) without blowing configuration.

The behaviour for skewness in case of blowing case shown in Figure 6.6 (A) is similar to the spatial and temporal simulations without blowing reported in [109, 112] in inner region, i.e., $y^+ < 10$. Some deviations are discerned in the buffer region, $10 < y^+ < 100$, for the blowing configuration in comparison to the spatial boundary layer without blowing [112]. The skewness for blowing and without blowing using same simulation set-up shown in Figure 6.6 (A) and (B) also show deviations in inner as well as buffer region from each other. Nevertheless, the skewness profiles are consistent with the temporal simulations performed using T-ODT [109]. The behaviour for skewness was different in case of a suction boundary layer as well [96]. The ODT results are observed qualitatively consistent with the DNS data considered. The dependence of skewness on Re_θ is dominant in the outer log-region, i.e., $y^+ > 300$ which is consistent with other statistics discussed above. More details regarding the skewness produced using the ODT model are already covered in TBL as well as SBL chapter and also in [109, 112].

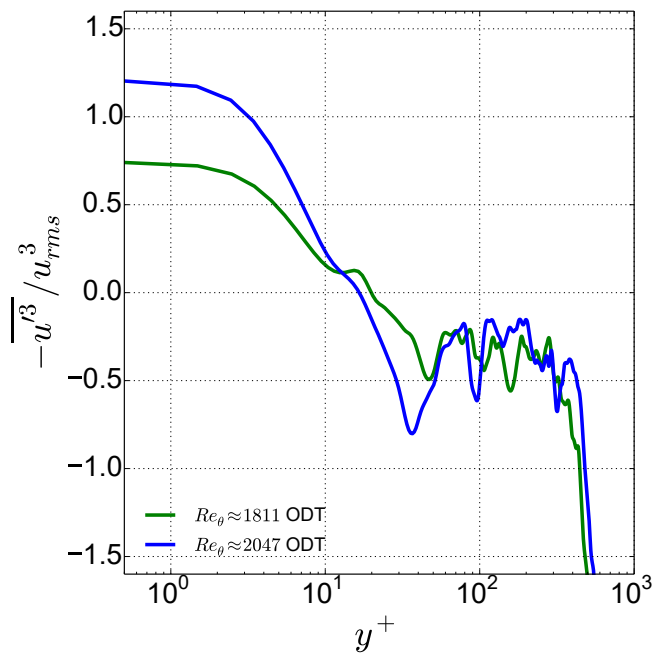
The flatness of the streamwise velocity component, $\overline{u'^4} / u_{rms}^4$, as a function of wall-normal coordinate in viscous units is displayed in Figure 6.7 for (A) uniform blowing case at $Re_\theta \approx 1407, 2082$ and 2395 and (B) without blowing case at $Re_\theta \approx 1811$ and 2047 . For comparison, the DNS data from [41] at $Re_\theta \approx 2000$ is shown in dotted lines for planar spatially developing turbulent boundary layer.

The flatness profiles are under-predicted in inner region for $y^+ < 10$, near the wall and over-predicted in the buffer region in the range $10 < y^+ < 40$. The fourth order velocity statistics show reasonable agreement with the reference DNS data along a certain y range from moderate to large distance from the wall. Like the mean velocity profiles and the rms profiles, flatness shown in Figure 6.7 (A) also show dependency on Re_θ in outer log-region which is consistent with other statistics for blowing case. The outer layer statistics in ODT are dominated by the kernel-mechanism which is explained in detail in [109, 112].

In general, ODT is more Gaussian than DNS and three is the Gaussian flatness value for the ODT model which might be due to DNS being more dynamic compared to the ODT model. Giving some more context, note that the ensemble is built by ODT simulation runs. These runs have identical initial conditions but different random number sequences and are realized by initializing with different random seeds. On average, all ensemble members develop in time in a similar way. But all of them are uncorrelated when looking at the flow profiles at a particular point in time. This property manifests itself by virtually perfect Gaussianity of the point statistics. This would be different in DNS. For example, when a similar ensemble of flow profiles would be constructed from the spanwise direction as these profiles would be spatially correlated (provided they are reasonably close to each other) which is not the

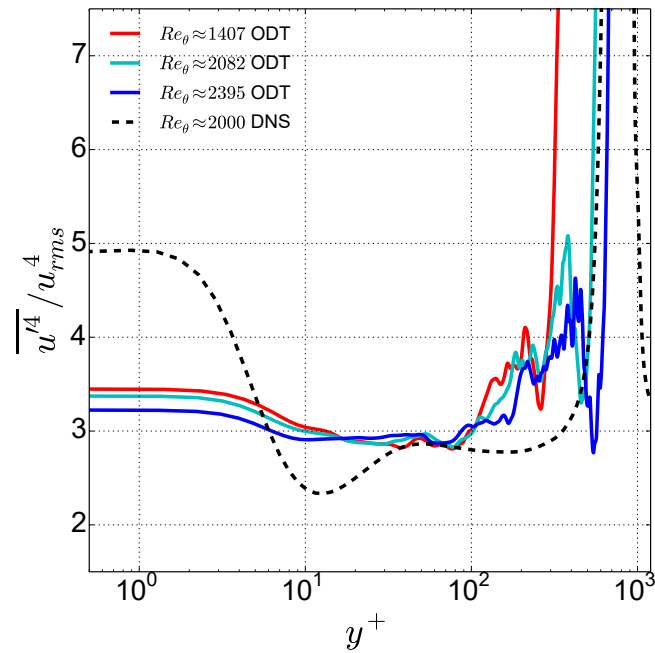


(A)

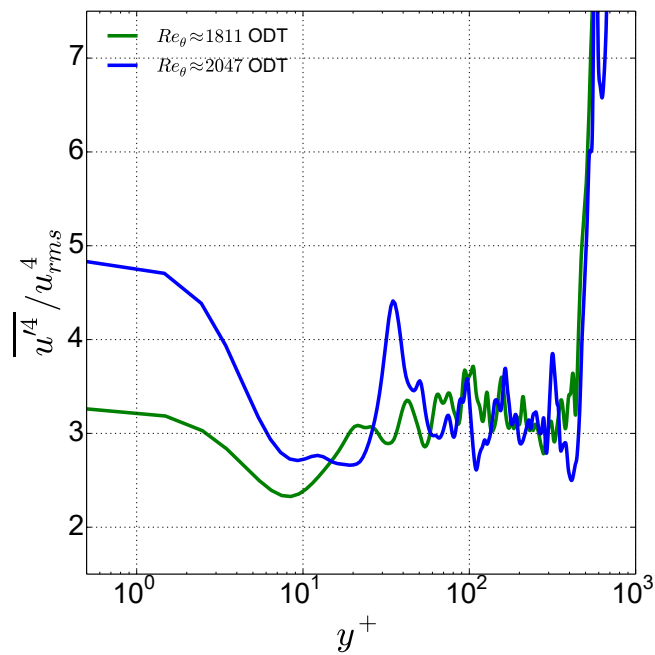


(B)

FIGURE 6.6: Profiles of the skewness of the streamwise velocity fluctuations as a function of the wall-normal coordinate in viscous units at $Re_\theta \approx 1407, 2082$ and 2395 for (A) uniform blowing and at $Re_\theta \approx 1811$ and 2047 (B) without blowing configuration. For comparison, the reference DNS data from [41] at $Re_\theta \approx 2000$ is shown for SBL configuration without blowing.



(A)



(B)

FIGURE 6.7: Profiles of the flatness of the streamwise velocity fluctuations as a function of the wall-normal coordinate in viscous units at $Re_\theta \approx 1407, 2082$ and 2395 for (A) uniform blowing and at $Re_\theta \approx 1811$ and 2047 (B) without blowing configuration. For comparison, the reference DNS data from [41] at $Re_\theta \approx 2000$ is shown for SBL configuration without blowing.

case for the present ODT application.

The flatness disagreement with the reference DNS data is attributed to the missing 3-D information and some 3-D information of the flow needs to be retained to reproduce the 4th order velocity statistics. A non-standalone application of ODT, referred as ODTLES [103, 132] can be used to overcome above limitation. ODTLES permits the simulations of much more complex flows by partially removing the one-dimensional constraint.

Figure 6.7 (B) shows flatness profiles for without blowing case using same simulation set-up as used for the blowing configuration. These profiles deviates from profiles shown in Figure 6.7 (A) in inner as well as outer region. Profiles in Figure 6.7 (A) are more scattered in outer region but profiles in Figure 6.7 (B) are scattered more in inner region and collapses onto each other for both Re_θ in outer region.

6.2 Variation of the Global Properties with Re_θ

In this section, some of the global properties are presented as a function of Re_θ . These quantities are shown below and are frictional Reynolds number (Re_τ), shape factor (H), and skin friction coefficient (C_f) with Re_θ up to $Re_\theta \approx 2500$ for uniform blowing configuration and up to $Re_\theta \approx 3000$ for without blowing case. The respective cases considered are represented as 'B-' for blowing and 'NC-' for no control in the figures discussed below for a fixed free-stream velocity. The reference LES data from [64] is plotted for comparison in dashed line for all the global properties. Table 6.1 gives the values of the properties achieved at the last sampled Re_θ .

Figure 6.8 displays the variation of Re_τ with Re_θ . This quantity further quantify the turbulence in the near-wall region. The spatial development of Re_τ is calculated using u_τ and δ_{99} and the values achieved are given in Table 6.1. The figure also obtains a functional relation for the two Reynolds numbers, i.e., Re_τ in terms of Re_θ . A linear behaviour of the quantities is noted. For the blowing configuration, a power-law relation is obtained as $Re_\tau = 0.61 \times Re_\theta^{0.92}$ to provide a good fit for the ODT data and this equation can be used to convert between Re_τ and Re_θ . This relation for without blowing configuration is reported as $Re_\tau = 0.76 \times Re_\theta^{0.89}$. Note that the value reached for Re_τ at any Re_θ is less in case of uniform blowing in comparison to without blowing configuration and a decrease of Re_τ with blowing is observed for LES as well [64]. The ODT flow properties are generally in good agreement with the reference LES data from [64].

The shape factor is calculated as the ratio of the displacement thickness to the momentum thickness, $H = \delta/\theta$ and plotted over Re_θ as shown in Figure 6.9. For reference, the LES data from [64] in dashed lines for uniform blowing as well as without blowing configuration is also shown.

The quantity H allows a direct quantitative estimation of the mean stream-wise velocity profile which is independent of the skin friction. The ODT profiles does not show good agreement with the LES data, however, an increase in H by blowing is noted. This is similar to the reference data. In that sense, ODT

TABLE 6.1: The simulations results for friction Reynolds number Re_τ , displacement Reynolds number $Re_{\delta_{99}^*}$, momentum thickness Reynolds number Re_θ (f for final value of the quantities), skin friction C_f , von Kármán's constant K and shape factor H .

Case	$Re_{\tau,f}$	$Re_{\delta_{99}^*,f}$	$Re_{\theta,f}$	$Re_{X,f}$ [10^6]	C_f [10^{-3}]	K	H
U1C1	848	3435	2479	1.2	4.04	0.28	1.38
U1C2	900	3646	2680	1.2	4.52	0.33	1.36
U1Z1	890	3604	2626	1.2	4.51	0.30	1.37
U1Z2	860	3483	2450	1.2	4.22	0.30	1.37
U1L1	933	3779	2818	1.2	5.11	0.34	1.34
U1L2	929	3764	2818	1.2	5.08	0.35	1.34
U1	876	3548	2583	1.2	4.30	0.32	1.37

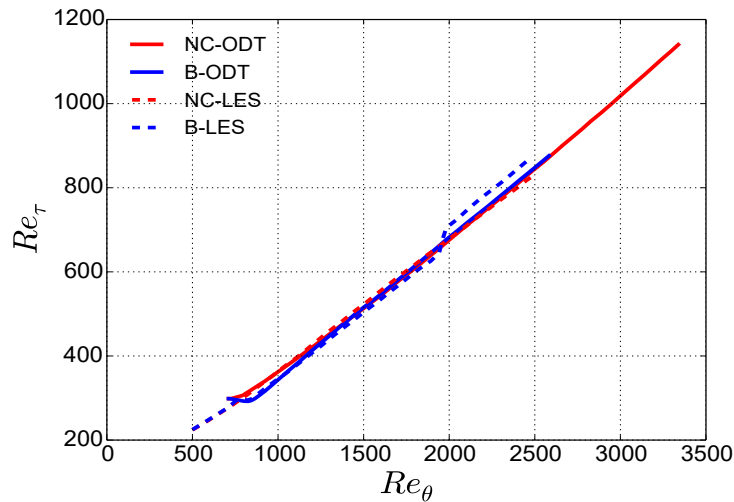


FIGURE 6.8: The quantity Re_τ as a function of Re_θ up to $Re_\theta \approx 3000$ for uniform blowing (represented as 'B-') and without blowing (represented as 'NC-' meaning 'no control') configuration. For comparison, the reference LES data from [64] is shown for corresponding configurations.

capture the flow dynamics for the blowing configuration very well and this indicates that the blowing can promote flow separation [64]. The shape factor is under-predicted by ODT and in the small Re_θ range a different Re_θ trend is observed for the reduced order model. However, this trend is consistent with our earlier work [109, 112] and also at low Re_θ , a different trend is spotted in case of DNS as well [41]. The values achieved for H for the cases considered for the present study is provided in Table 6.1.

Finally, the development of skin friction coefficient, $C_f = 2/(U_b^+)^2$, is shown with Re_θ for both cases with and without blowing using the ODT model. For reference, the LES data from [64] for fixed free-stream velocity in Figure 6.10 is plotted. C_f is calculated as the ratio of the wall shear stress to the dynamic pressure and like shape factor, skin friction coefficient also show different trends in comparison to LES data initially. But the trend is consistent with the earlier ODT applications [109, 112]. The laminar-turbulent transition is induced at different Re_θ in case of DNS [44] and DNS exhibit typical overshoots of C_f depending on tripping and as a result of transition, the profiles using ODT methodology are slightly over-predicted as compared to the reference data for the selected physical model parameters. However, it was under-predicted for [109, 112]. The peak height can be modified by altering the model parameters. Nevertheless, the qualitative trends are sufficiently well reproduced with the selected set of model parameters.

Figure 6.10 also confirms the increase in the boundary layer thickness and decrease in the skin friction for uniform blowing configuration. This is similar to the reference LES data reported in [64]. $\sim 15\%$ of the drag reduction is achieved in case of blowing. In spite of the weak amplitude of the control, flow dynamics for blowing configuration are captured using a reduced order model. This confirms once more the overall consistency and the capability of

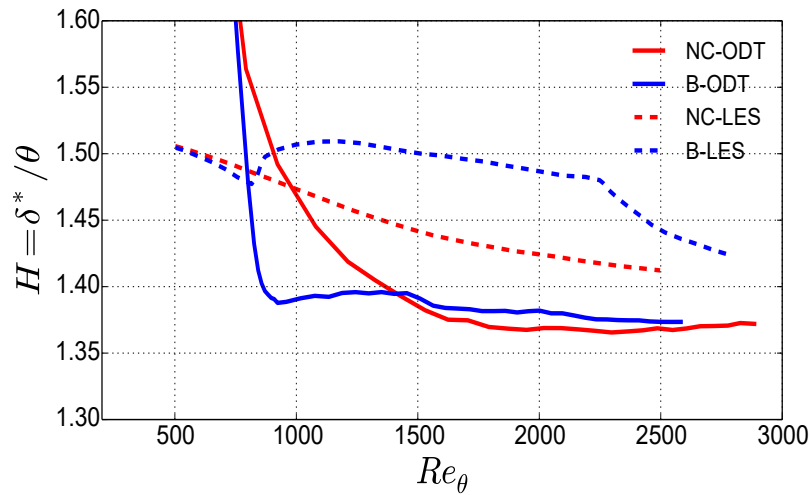


FIGURE 6.9: The quantity H as a function of Re_θ up to $Re_\theta \approx 3000$ for uniform blowing (represented as 'B-') and without blowing (represented as 'NC-' meaning 'no control') configuration. For comparison, the reference LES data from [64] is shown for corresponding configurations.

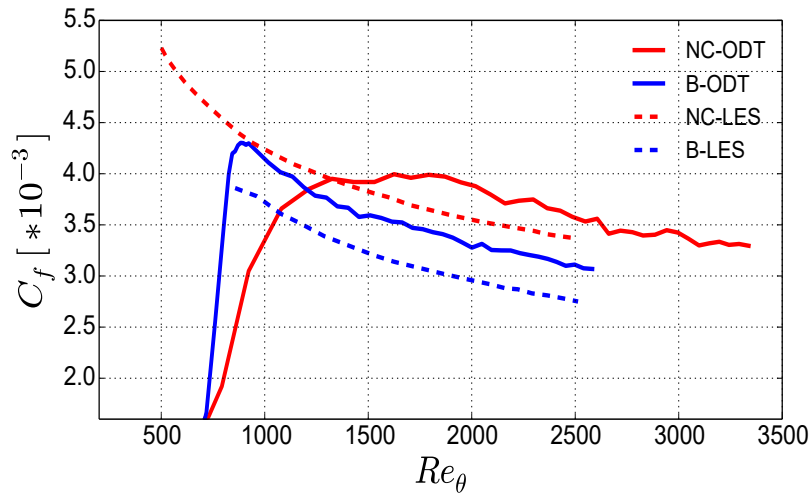


FIGURE 6.10: Skin friction coefficient C_f as a function of Re_θ up to $Re_\theta \approx 3000$ for uniform blowing (represented as 'B-') and without blowing (represented as 'NC-' meaning 'no control') configuration. For comparison, the reference LES data from [64] is shown for corresponding configurations.

the ODT model to predict such properties.

6.3 In Closing

In this chapter, the ODT model is utilized to investigate effect of uniform blowing in a spatially developing turbulent boundary layer. Various velocity statistics up to 4th order and some of the global properties important for blowing case are presented in comparison with the reference LES and DNS data. The selection of optimal physical model parameters is presented in Appendix H.

Chapter 7

Comparison with Experiments

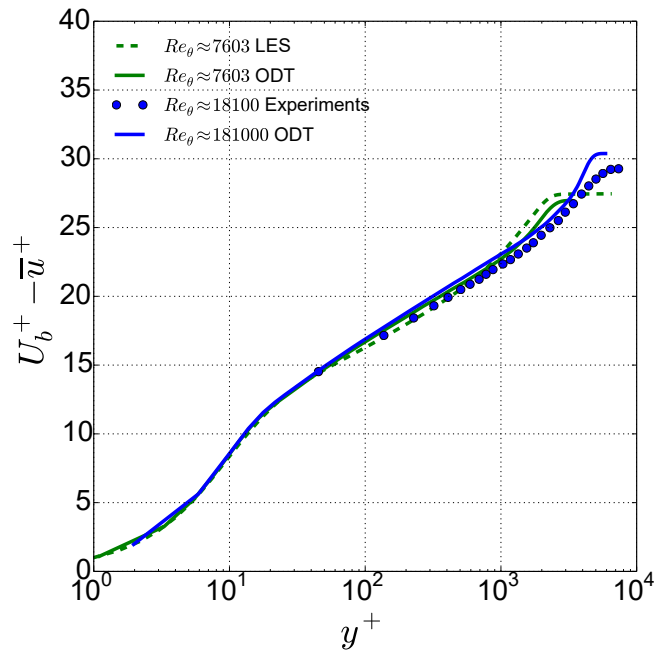
The well validated spatial ODT formulation discussed in previous chapters is here utilized for comparing ODT results with the experiments conducted at BTU (chair of Prof. Egbers) in collaboration with the University of Lille, CNRS, France. The comparison is done for a flat plate turbulent boundary layer at high Reynolds number to demonstrate the capability of the ODT model to capture flow dynamics at computationally high Reynolds numbers and to present the state of the art. Various velocity statistics as a function of wall-normal coordinate for boundary layer for a single Re_θ are given in this chapter in comparison with the reference experiment results [133]. We do not show the comparison with all the Re_θ discussed for experiments, rather we consider only one Re_θ which is highest for experiments.

7.1 The Logarithmic Law of the Wall

The mean streamwise velocity profile as a function of the wall-normal coordinate in viscous units at $Re_\theta \approx 7603$ for LES [82] and $Re_\theta \approx 18100$ for experiments [133] is depicted in Figure 7.1. The general trend for the velocity profile is consistent with the other cases discussed in the previous chapters and hence, to avoid repetition, these trends are not discussed again in this chapter.

The problem with experiments is the examination of fluctuations and statistical values measured very close to the wall. As reported in [133] and can also be seen from Figure 7.1 that the first measured point in case of experiments for $Re_\theta \approx 18100$ is at $y^+ = 45$. Whereas, in case of ODT, at $Re_\theta \approx 7603$, the profile shows similar behaviour as LES [82] and successfully captures the near wall dynamics. At $Re_\theta \approx 18100$, the ODT model captures the first data point at $y^+ = 2$.

The pre-multiplied mean velocity gradient, i.e., the indicator function is shown in Figure 7.2 at $Re_\theta \approx 7603$ and 18100 for LES and experiments, respectively, along with the ODT results at both Re_θ . The indicator function is calculated as $y^+ (\partial \bar{u}^+ / \partial y^+)$, and is varied as a function of wall-normal coordinate (in viscous units).



(A)

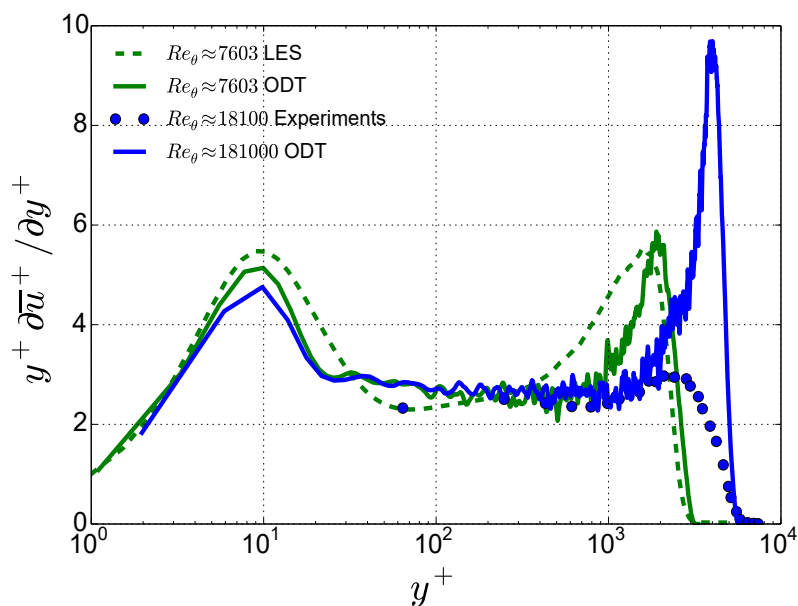
FIGURE 7.1: The mean streamwise velocity profile as a function of the wall-normal coordinate (in viscous units) at $Re_\theta \approx 7603$ for reference LES [82] and ODT along with the experiment data [133] at $Re_\theta \approx 18100$ in comparison with the ODT results.

As seen in Figure 7.1, that there is a linear region in the mean velocity profile starting from $y^+ = 30$ up to $y^+ = 1000$ which is pretty flat in Figure 7.2, identifying the log-region in the velocity profile. This constant region is confirmed at the given Re_θ as it is known that it start appearing only at fairly large Reynolds number regime. Note that the first measured point in case of experiments is at $y^+ \approx 60$, whereas in case of ODT the first data point is at $y^+ = 2$.

7.2 Second Order Velocity Statistics

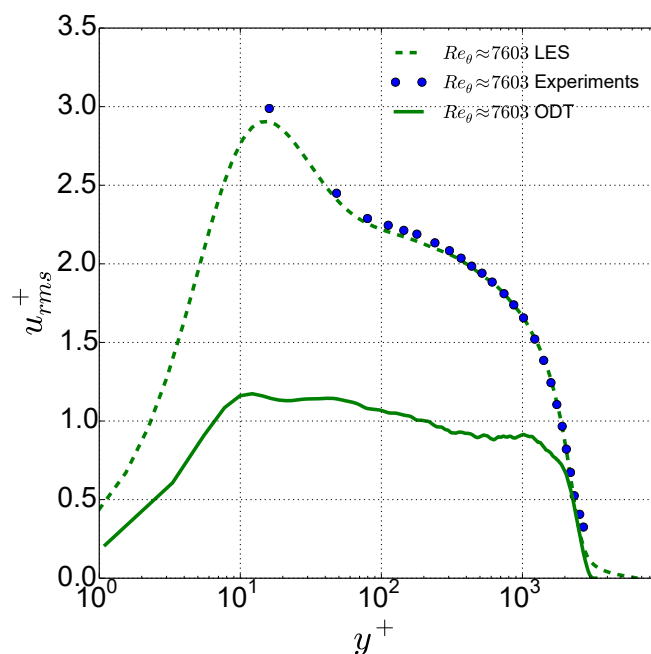
Figures 7.3 displays the root mean square (rms) of the streamwise velocity component ($u_{rms}^+ = \sqrt{u'^2}/u_\tau$) as a function of the normalized wall-normal coordinate in viscous units at $Re_\theta \approx 7603$ for LES and experiments along with the ODT results.

It is discussed in earlier chapters and also known from previous studies, for example, [28, 29, 89, 96, 109] that the ODT model under-predicts the rms peaks due to missing 3-D information. Hence, some 3-D information [84] needs to be retained to get a good fit for the rms profiles using ODT in comparison to reference LES and experiments. In case of rms profile as well, the first measured point in case of experiments is at $y^+ \approx 20$, whereas ODT can capture near wall dynamics.



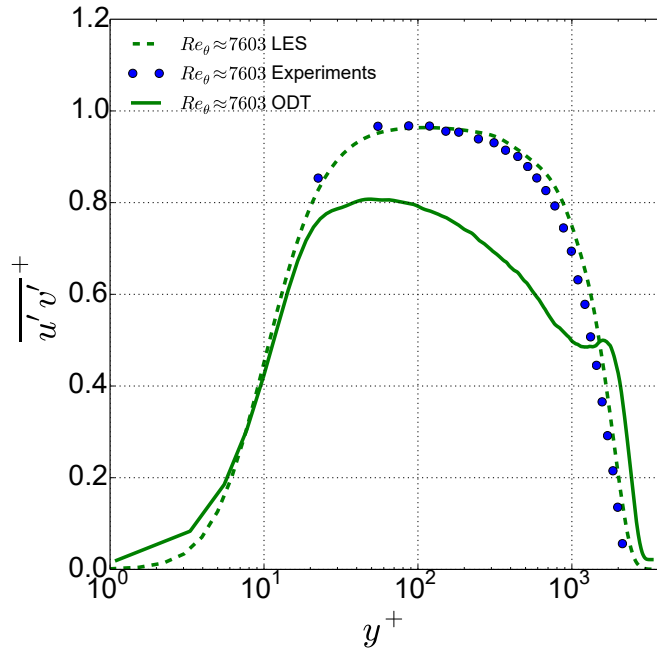
(A)

FIGURE 7.2: The indicator function as a function of the wall-normal coordinate (in viscous units) at $Re_\theta \approx 7603$ for reference LES [82] and ODT along with the experiment data [133] at $Re_\theta \approx 18100$ in comparison with the ODT results.



(A)

FIGURE 7.3: The streamwise root-mean-square velocity profiles versus wall-normal coordinate (in viscous units) at $Re_\theta \approx 7603$ for reference LES [82] and the experiment data [133] in comparison with the ODT results.



(A)

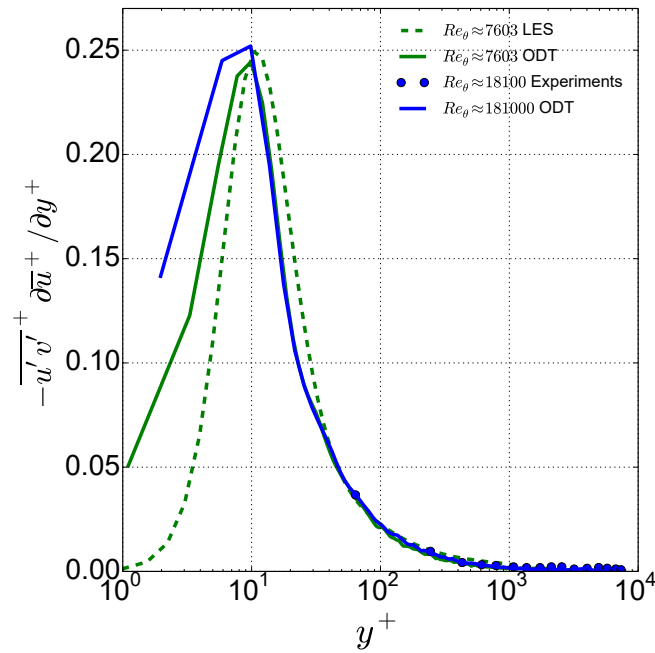
FIGURE 7.4: The profiles of the Reynolds shear stresses versus wall-normal coordinate (in viscous units) at $Re_\theta \approx 7603$ for reference LES [82] and the experiment data [133] in comparison with the ODT results.

Figure 7.4 shows the profiles for the normalized Reynolds shear stresses as a function of the wall-normal coordinate in viscous units, $(\overline{u'v'}/u_\tau^2)$, at $Re_\theta \approx 7603$ for LES and experiments along with the ODT results. The Reynolds shear stress calculations in case of ODT are based on the changes of the velocity profiles due to eddies [28] Appendix C.

An additional peak is reported for Reynolds shear stress in outer log-region similar to previous cases. For details regarding this peak, the reader is referred to the previous chapters of the thesis. Like rms profiles discussed above, the first measured point for Reynolds shear stresses in case of experiments is also around $y^+ \approx 20$ and ODT captures near wall dynamics.

7.3 Higher Order Velocity Statistics

The turbulent production as a function of wall-normal coordinate in viscous units is depicted in Figure 7.5 which is calculated as $-\overline{u'v'}^+ \frac{\partial \overline{u}^+}{\partial y^+}$. The figure displays production at $Re_\theta \approx 7603$ and 18100 for LES and experiments, respectively, along with the ODT results. As discussed for the previous profiles above, the ODT model is good in capturing the near wall dynamics and shows the first data point for production at around $y^+ \approx 2$. Whereas, the first measured point in case of experiments is around $y^+ \approx 60$.



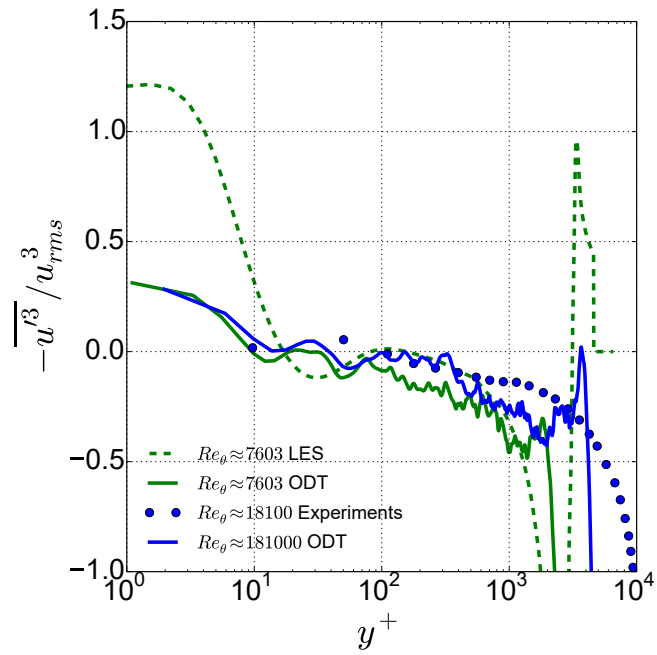
(A)

FIGURE 7.5: Turbulent kinetic energy production as a function of the wall-normal coordinate (in viscous units) at $Re_\theta \approx 7603$ for reference LES [82] and ODT along with the experiment data [133] at $Re_\theta \approx 18100$ in comparison with the ODT results.

Figure 7.6 depicts the skewness of the streamwise velocity component, $-\overline{u'^3}/u_{rms}^3$, as a function of the wall-normal coordinate in viscous units, y^+ . The profiles are shown at $Re_\theta \approx 7603$ for reference LES [82] and ODT along with the experiment data [133] at $Re_\theta \approx 18100$ in comparison with the ODT results.

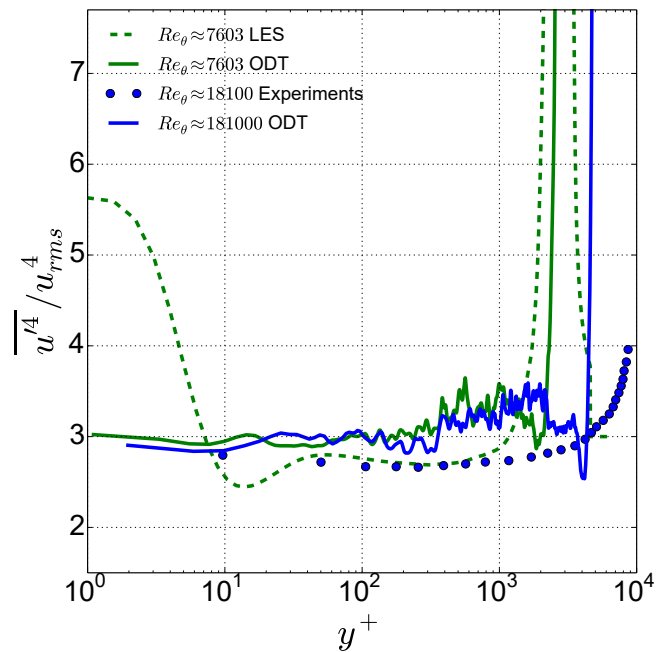
The behaviour for skewness for the present case is similar to the other cases discussed in the previous chapter and hence, the reader is referred to the previous chapters of the thesis for a detailed discussion regarding the skewness profiles. Note that the first measured point for the skewness profile in case of experiments is at $y^+ = 1$.

The flatness of the streamwise velocity component, $\overline{u'^4}/u_{rms}^4$, as a function of wall-normal coordinate in viscous units is displayed in Figure 7.7 at $Re_\theta \approx 7603$ for reference LES [82] and ODT along with the experiment data [133] at $Re_\theta \approx 18100$ in comparison with the ODT results. The flatness profile is consistent with the previous cases, for example, TBL, SBL and SBL with uniform blowing. As mentioned above, the ODT model captures the near wall dynamics successfully, whereas, experiments show the first measured point at $y^+ = 1$.



(A)

FIGURE 7.6: Same as Figure 7.5, but profiles of the skewness of the streamwise velocity fluctuations.



(A)

FIGURE 7.7: Same as Figure 7.5, but profiles of the flatness of the streamwise velocity fluctuations.

7.4 In Closing

In this chapter, the ODT model is utilized to compare the velocity statistics with experiments conducted at BTU in collaboration with the University of Lille, CNRS, France. The main aim of this chapter is to compare the ODT results with experiments at high Re_θ . Various velocity statistics up to 4th are presented in comparison with the reference LES and experimental data.

Chapter 8

Conclusions & Outlook

8.1 Conclusions

The role of turbulent boundary layers in numerous applications in the atmospheric sciences, engineering and industry, have led to extensive studies of such kind of flows over the last decades. Spatial and temporal approaches have been used to analyze the incompressible as well as the compressible boundary layers. Further, to control the flow for turbulent wall-bounded flows, the mechanism of adding or removing mass through a porous surface, have led to extensive studies of such kind of flows.

In this thesis, the ODT model has been applied for the first time to incompressible temporally and spatially developing turbulent boundary layers. Additionally, the effect of uniform blowing in a spatially developing turbulent boundary layer is investigated. The ODT model resolves the flow variables along a 1-D computational domain. In this model, the viscosity effects are represented by the deterministic diffusion equation and the turbulent advection by stochastic mapping events. From earlier studies, it is known that the ODT results are sensitive to the choice of model parameters. So, first the physical model parameters, α , C , Z and LS suppression mechanism are validated for each flow configurations.

For the TBL configuration, the ODT model is able to capture various relevant features of the reference DNS data to a reasonable extent for the model parameter values $C = 9$, $Z = 400$, $\alpha = 2/3$ and the two-thirds large eddy suppression method. Using the calibrated model parameters, various bulk Reynolds numbers from the range $250 \leq Re_b \leq 2000$ have been investigated for ODT methodology in comparison to the available reference DNS [50] results. The velocity statistics such as mean, root mean square, turbulent stresses, skewness and flatness as wall-normal profiles is obtained which was then extended to turbulence spectra and global properties, that is, the skin friction coefficient and various similarity Reynolds numbers.

For the TBL configuration the mean streamwise velocity matches to the available reference DNS results up to a good degree for all bulk and momentum Reynolds numbers investigated showing the ability of ODT to capture flow

dynamics ranging from the viscous sublayer through the buffer layer and all the way into the logarithmic layer. The rms peak amplitude is under-predicted compared to the reference data which is a well-known limitation of the lower-order formulation (e.g. [28, 29, 89]) and might be alleviated in future by a 3-D expansion of the model, the so-called ODTLES [84, 88, 108], which aims to retain the 3-D information. The profiles of the Reynolds shear stresses match well with the reference DNS. The skewness of the streamwise velocity component is under-predicted in the inner region ($y^+ < 10$) of the TBL solution and over-predicted in the buffer region ($10 < y^+ < 30$). ODT is able to reproduce the flatness values of the streamwise velocity component in large y range.

Several global properties also show very good agreement with the reference DNS data. A semi-empirical balance equation for the asymptotically self-similar state of the TBL have been diagnostically investigated with the aid of ODT which suggests that ODT exhibits somewhat different asymptotically self-similar solutions than the reference DNS. Both ODT and DNS fulfill the semi-empirical balance with a relative error which is well below 10% for all bulk Reynolds numbers investigated for the TBL configuration.

Further, for the SBL configuration, the model parameters used are, $\alpha = 2/3$, $C = 6$, $Z = 600$ and the frac domain large eddy suppression mechanism. The calibration procedure for the model parameters was carried out at $Re_\theta \approx 4000$ in comparison with the reference DNS data from [41] at the same Re_θ . For SBL, the influence of domain on velocity statistics at different Re_θ for two domain sizes is also analysed.

The calibrated model parameters and domain size same as the available reference data is used to carry out the simulation for the SBL set-up and the velocity statistics such as mean, root mean square, turbulent stresses, skewness, flatness and indicator function as wall-normal profiles produced from ODT is compared to the reference DNS and LES data from [41, 82] at $Re_\theta \approx 2000, 4000$ and 8000 for two bulk velocity. The structural properties variation with Re_θ is discussed for this configuration as well.

For the SBL configuration the results are consistent with the TBL configuration and the mean streamwise velocity matches to the reference DNS results up to a good degree. The peak amplitude of the root mean square velocity profiles is under-predicted compared to the reference data for this case as well and the Reynolds shear stresses profile shows an additional peak in the outer region for $Re_\theta = 2000$ and 4000 due to transient effects which get resolved for higher Re_θ , i.e., at $Re_\theta = 8000$ and the profiles are slightly under-predicted in comparison with the reference DNS and LES data from [41, 82] at all Re_θ .

The skewness of the streamwise velocity component is slightly under-predicted in the inner region, over-predicted in the buffer region and the flatness of the streamwise velocity component is only matched reasonably in the logarithmic region similar to the TBL case. The flow properties for example, C_f , H and Re_τ as a function of Re_θ shows moderate agreement with the available reference DNS and LES data and all the profiles capture transient effects for higher bulk velocity at lower Re_θ .

A comparison between SBL and TBL flow configurations is also presented

using ODT with each other and with DNS at $Re_\theta \approx 1968$ up to 2nd order statistics and at $Re_\theta \approx 2000$ for 3rd and 4th order velocity statistics and most of the flow properties remain the same for both the approaches.

Next, the ODT model is applied to analyse the blowing boundary layer-type flow and the ODT results are compared to the available reference LES data at various momentum thickness Reynolds numbers. For this purpose, the model parameters are calibrated in comparison with the LES data from [64] at various Re_θ and the optimal set of the model parameters is $\alpha = 2/3$, $C = 6$, $Z = 100$ and two-thirds large eddy suppression method. The calibrated model parameters are then used for further simulations to produce the velocity statistics such as mean, root mean, turbulent stresses as wall-normal profiles and the ODT results are compared with the LES [64] at various streamwise locations.

For uniform blowing case, the mean streamwise velocity profile shows good agreement to the reference LES data. The well known artifact of the model is also confirmed and the peak amplitude of the rms velocity profile is under-predicted compared to the LES data and the cross-stress profiles show qualitative agreement with a overall under-prediction in comparison to the LES profiles. The higher order velocity statistics are provided in comparison with DNS of spatially developing turbulent boundary layer without blowing from [41]. An increase in H is observed using blowing configuration and this is consistent with the reference LES data, however, the overall shape factor profile does not show good agreement with the reference data. $\sim 15\%$ of the drag reduction is achieved in case of blowing using the ODT model hence, confirming the overall consistency and the capability of the ODT model to predict such properties.

The ODT model achieves considerable reduction in cost due to reduction in dimensionality and it makes ODT an interesting tool for investigating such flows for high Reynolds numbers. The comparison presented in this thesis suggests that ODT is able to reproduce several DNS and LES velocity statistics for the temporally and spatially developing turbulent boundary layer without blowing as well as with uniform blowing.

8.2 Outlook

As discussed in the previous section, in this thesis a number of different investigations on turbulent boundary layer using ODT have been performed successfully. In this section, an overview of the issues is presented which could have been addressed in the course of this work, for example, additional important flow types and modeling aspects to either improve the present results or to analyse a new case study.

The primary aim for the present study is to understand the model behaviour and the flow physics captured for the simple configurations using the stand-alone ODT model. However, the ODT model is restricted to 1-D effects. Hence, to remove this restriction, a natural continuation of the present work

is the extension of the ODT model into ODTLES formulation as ODTLES retains the large structure information and accounts for 3-D effects. ODTLES formulation may be promising to predict complex flows and higher order velocity statistics accurately and it is also expected that the rms and Reynolds stresses might improve significantly with this formulation [84, 103]. However, ODTLES formulation uses the temporal ODT rather than spatial ODT.

Another alternative, which is more challenging, is to work aspects of the near-wall cycle as in [134] into the ODT model. In [134], the approach is followed from [135] and the evolution equations are Fourier transformed in the streamwise and spanwise directions. In the ODT model [28], the individual eddies are viewed as Fourier wave packets. However, there are discrepancies noted reflecting the absence of wave phenomena in the model. Further following [29], the kernel $K(y)$ may be viewed as a wavelet construct and is used to measure available energy and to implement energy transfers. Like a wavelet, the kernel is effectively a local filter that selects fluctuations whose length scales are comparable to the eddy size l and thus enforces the correspondence between the eddy size and the scale of the dynamics governing its occurrence. This may be regarded as a matter of definition rather than a physical principle, because the turbulent eddy is a concept rather than a physical observable. It is analogous to a normal mode of a linear system, but has no precise definition owing to the strong nonlinearity of the Navier-Stokes equations. If a turbulent eddy is heuristically defined as motion in response to local forcing at a given length scale, then the use of a wavelet-type construct to characterize the forcing can be viewed as a consistency requirement rather than a physical modeling assumption. Therefore, to analyse the aspects of the near-wall cycle, Fourier transformation of the kernels is needed which is not implemented in the model so far. However, it is under consideration due to the practical applications and to extend the model towards Quantum mechanics in order to obtain solution of the Schrodinger equations to describe the evolution of a wave function in time.

It is also important to note that the advection term is not considered in the present ODT algorithm as v is the advection velocity perpendicular to the wall. In case of channel flow this advection can be neglected due to imposition of the boundary conditions, however, in the case of boundary layer, v is not zero on the complete domain and cannot be neglected. Nevertheless, it is verified for the present study that this term does not influence the results at the considered Reynolds's numbers. However, the effect of this term is more dominant for very high Reynolds numbers and high Re demands the inclusion of the missing advection term. So, in further investigations the magnitude of the error has to be measured. This can be done in two ways. First, by modifying the governing equations of the model where continuity equation is used in momentum equation to get a quadratic PDE as discussed in [28] (Appendix C, equation C4). This equation does not assume a low order approximation for the advecting velocity, but rather solve directly the momentum flux in conservative formulation. However, the equation in conservative formulation is a second order PDE and it would be expensive to solve. Second, by modifying kernel operation which is currently in progress.

Since, the ODT model has not been applied enough to investigate turbulent boundary layer, there are several directions to extend the study. Another very interesting application aiming at skin friction drag reduction is performed by heating or cooling the wall surface. The present thesis deals with zero pressure gradient (ZPG), so it is very important for technical applications to investigate the effect of adverse pressure gradient (APG) as boundary layer separation is dominant in APG.

Appendix A

Turbulent Kinetic Energy

The turbulence kinetic energy (TKE) is defined as the mean kinetic energy per unit mass associated with the eddies in the turbulent flow and is characterised by measured rms velocity fluctuations. The TKE can be calculated based on the closure method, i.e. a turbulence model in case of RANS equations. Here, only the budgets of TKE are explained however, for a detailed derivation the reader is referred to [1].

The TKE is defined as the half the sum of the variances, i.e., the square of the standard deviations of the velocity components given as,

$$\mathcal{K} = \frac{1}{2} \left(\overline{(u')^2} + \overline{(v')^2} + \overline{(w')^2} \right), \quad (\text{A.1})$$

where the difference between the instantaneous and the average velocity is the turbulent velocity component, i.e.,

$$u' = u - \bar{u}, \quad (\text{A.2})$$

with the mean as,

$$\bar{u}' = \frac{1}{T} \int_0^T (u(t) - \bar{u}) dt = 0, \quad (\text{A.3})$$

and the variance as,

$$\overline{(u')^2} = \frac{1}{T} \int_0^T (u(t) - \bar{u})^2 dt \geq 0. \quad (\text{A.4})$$

The TKE produced by friction, fluid shear or external forces at integral scale is transferred to the turbulence energy cascade which is then dissipated by viscous forces at the Kolmogorov scale and this process is expressed as [1],

$$\frac{D\mathcal{K}}{Dt} + \nabla \cdot \mathcal{T}' = \mathcal{P} - \epsilon, \quad (\text{A.5})$$

where the first and second terms on the left hand are the mean-flow material derivative and the turbulence transport, respectively. The terms on the right hand side are the production and and the dissipation. Further, the full form

of the TKE equations is given below (ignoring the buoyancy term) with the assumption that the density and viscosity are constant,

$$\underbrace{\frac{\partial \mathcal{K}}{\partial t}}_{\text{Local derivative}} + \underbrace{\bar{u}_j \frac{\partial \mathcal{K}}{\partial x_j}}_{\text{Advection}} = - \underbrace{\frac{1}{\rho} \frac{\partial \overline{u'_i p'}}{\partial x_i}}_{\text{Pressure diffusion}} - \underbrace{\frac{1}{2} \frac{\partial \overline{u'_j u'_j u'_i}}{\partial x_i}}_{\text{Turbulent transport } \mathcal{T}} + \underbrace{\nu \frac{\partial^2 \mathcal{K}}{\partial x_j^2}}_{\text{Molecular viscous transport}} - \underbrace{\overline{u'_i u'_j} \frac{\partial \bar{u}_i}{\partial x_j}}_{\text{Production } \mathcal{P}} - \underbrace{\nu \frac{\partial u'_i}{\partial x_j} \frac{\partial u'_i}{\partial x_j}}_{\text{Dissipation } \epsilon}. \quad (\text{A.6})$$

Appendix B

ODT Model Details

B.1 Eddy Sampling

An eddy rate distribution, $\lambda(l, y_0, t)$ and the eddy turnover, τ , has been discussed earlier in Chapter 2. Here, an event rate $R(t)$ is considered and defined by Equation B.1. $R(t)$ is the cumulative event rate of all possible eddy events for a given time. Using this variable it is now possible to define the joint Probability Density Function (PDF), Λ , from Equation B.2,

$$R(t) = \int \int \lambda(l, y_0, t) dl dy_0 \quad (\text{B.1})$$

$$\Lambda(l, y_0, t) = \frac{\lambda(l, y_0, t)}{R(t)} \in [0, 1]. \quad (\text{B.2})$$

To sample an eddy, a random number between 0 and 1 is selected. This number corresponds to a single eddy event when using the joint PDF, Λ . This eddy event is then applied to the flow.

To advance simulation time, a time step, dt is sampled via a Poisson process. A Poisson process is a stochastic method for modeling the time at which a random event occurs. It can be constructed from the event rate of the process we intend to model. In present case, this rate is the eddy event rate, $R(t)$. After implementing the eddy a random time-step is sampled from the distribution of Equation B.3,

$$\phi(dt) = \exp(-R(t)dt). \quad (\text{B.3})$$

B.2 Eddy Sampling: the smart way

The eddy sampling technique described in the previous section is computationally too expensive to be considered in real life applications. An alternative procedure, which is implemented in current ODT codes, is explained in this section.

Instead of calculating the event rate $R(t)$, a predefined value of a trial event rate, R_t , is used to sample the time step of the process. For each time-step an eddy size and length will be sampled and a trial will occur. If the eddy passes the trial, it will be implemented. Else, a new time step will be sampled and a new trial will occur until a viable eddy is found.

The eddy trial starts by sampling a time-step, dt^* , from the distribution of Equation B.4. Then, two distinct probability functions, one for the eddy location, $F(y_0)$, and another for the eddy size, $G(l)$, which must be provided, are sampled. It's not overly important what these two functions look like, however, the closer they are to the actual probability functions for an eddy size and location the more effective the whole process will be. Typically a uniform distribution is used for the eddy location and an exponential distribution for the eddy size,

$$\phi(dt^*) = \exp(-R_T dt^*). \quad (\text{B.4})$$

For the sampled eddy, the same procedure from the previous section is performed, culminating in the calculation of the eddy rate, λ , for this specific eddy. The acceptance probability, AP , for an eddy can be defined as the joint probability of the eddy rate, the two sample functions for the eddy size and location, and the event rate. This acceptance probability is then compared with a randomly selected number, $PP_{RNG} \subset [0, 1]$. If the acceptance probability is larger, the eddy is implemented,

$$\text{if } AP \equiv \frac{\lambda(l, y_0, t)}{F(l)G(y_0)R_T} > PP_{RNG} \Rightarrow \text{Implement eddy!} \quad (\text{B.5})$$

The eddy trial process is repeated until one eddy is accepted. Upon acceptance, the flow state is moved forward by the sum of all the time-steps sampled until the eddy acceptance, $dt = dt_0^* + dt_1^* + \dots + dt_n^*$, and the eddy is implemented.

For this approach to be equivalent to the one described in the previous section, one condition must be met: $R_T \gg R(t)$. Although $R(t)$ is never explicitly calculated, we can guarantee that this condition is respected if most of the eddy trials fail.

We want the average acceptance rate of Equation B.5 to be of around 2%. If it's much higher than this, the aforementioned condition can not be guaranteed, and this process is not equivalent to the one from the previous section. If it's lower the process will be inefficient and too many eddy samples will be performed before an eddy is implemented. To adjust the process we can modify, R_T , to reach the desired acceptance ratio.

Appendix C

Model Parameter Sensitivity for TBL

In this Appendix we analyse the influence of various model parameters on several velocity statistics of boundary layer type flows. The sensitivity study focus on the temporally developing turbulent boundary layer. Here, 4 major physical model parameters are discussed and the numerical parameters are discussed in previous chapters. The analysis is carried out only for physical parameters because other ODT applications demonstrates that these parameters influence the results and it is important to calibrate these parameters for any flow configuration before making a final choice for analysing the flow dynamics. Numerical parameters do not influence the results, although improves the efficiency of the model.

For the TBL configuration, our starting point is the set of model parameters for the asymptotic suction boundary layer [96]. These parameters depend on the physics included and the forcing mechanism used and unfortunately cannot be taken over directly. Previous studies have shown that the ODT model parameters are not universal, for example, non-reacting and reacting jets [100, 92, 98], mixing layers [85], thermal convection [86], and wall-bounded flows [28, 84, 87, 126]. These studies suggest that the optimal model parameters (usually) become asymptotically independent of the Reynolds number which is a strong property of the model. This property makes ODT an interesting candidate for forward modeling of high-Reynolds-number turbulent flows as discussed in Chapter 4.

In this section, we estimate the ‘physical’ ODT model parameters, α , C , Z , and the large-eddy suppression. We have discussed the sensitivity of the results to parameter variations using a well-documented TBL reference case for $Re_b = 1000$ that has developed up to $Re_\theta \sim 1968$. Conventional velocity statistics and global properties of boundary layer are discussed by comparing ODT results to those of the available reference DNS [50].

The velocity statistics presented here consider a time-averaging window encompassing several eddy events in addition to the ensemble-based procedure. The mean velocity profiles obey the same near-wall similarity solution for all ODT solutions discussed in this section. Solely the friction velocities u_τ

are distinct as can be inferred from the non-constant value of the normalized free-stream velocity U_b^+ among the cases.

C.1 Variation of the Model Parameter α

The pressure fluctuations may not be universal [29] and that the pressure fluctuations do not necessarily imply a maximization of the inter-component kinetic energy transfer, therefore, the model parameter α has been introduced to control the exchange of the turbulent energy between the three velocity components. This parameter takes values in the range $[0, 1]$, where 0 means no and 1 maximal transfer of the kinetic energy. For $\alpha = 2/3$, equipartition of the energies is approximated which can be interpreted as a tendency to small-scale isotropy [29]. The ODT model parameters $C = 9$, $Z = 400$, and the two-thirds large-eddy suppression were kept fixed here for calibrating the α parameter.

Figure C.1 shows profiles of the mean streamwise velocity for various α normalized in inner (A, B) and outer (C, D) scale. ODT results are shown in comparison to the reference DNS of [50] for $Re_b = 1000$ at (A) $Re_\theta \sim 1100$ (B) $Re_\theta \sim 1968$. The mean profiles shown in Figure C.1 (A, B) exhibit an increase of the slope of the logarithmic region ($30 < y^+ < 300$) and the normalized free-stream velocity with α . The viscous sublayer ($y^+ < 20$), however, remains unaffected. This hints at a dependency of u_τ on the energy redistribution mechanism, Note that the solutions for ODT remains same for both the Re_θ considered here.

The variability of the flow profiles with u_τ raised the question that to what extent these profiles are influenced by the representation of the boundary layer growth and temporal development of the turbulent flow. This is addressed by showing the streamwise mean velocity, $U_b^- - \bar{u}^- = (U_b - \bar{u})/U_b$ (here $U_b^- = 1$) (scaled to outer units) in Figures C.1(C, D). The profiles of the streamwise velocity at both Re_θ collapse very well for all the α values considered specially in the range $y^- = y/\delta_{99} > 0.6$ for the TBL configuration. This indicates that the growth of the outer layer as well as the large-scale dynamics are comparable in the respective cases.

The optimal value is $\alpha = 2/3$ and this implies a tendency to equipartition and small-scale isotropy of the turbulent flow. This value is consistent with the Re_θ which is a important observation as it shows that the α become asymptotically independent of the Reynolds number.

Figure C.2 shows profiles of the root mean square (rms) velocity, $u_{rms}^+ = \sqrt{u'^2}/u_\tau$, for various α normalized in inner (A, B) and outer (C, D) scale. ODT results are shown in comparison to the reference DNS of [50] for $Re_b = 1000$ at (A) $Re_\theta \sim 1100$ (B) $Re_\theta \sim 1968$.

The qualitative trend for the rms velocity profiles shown in Figure C.1 (A, B) is consistent with the available reference data [50]. The peak value is, however, under-predicted with the ODT methodology in comparison to the

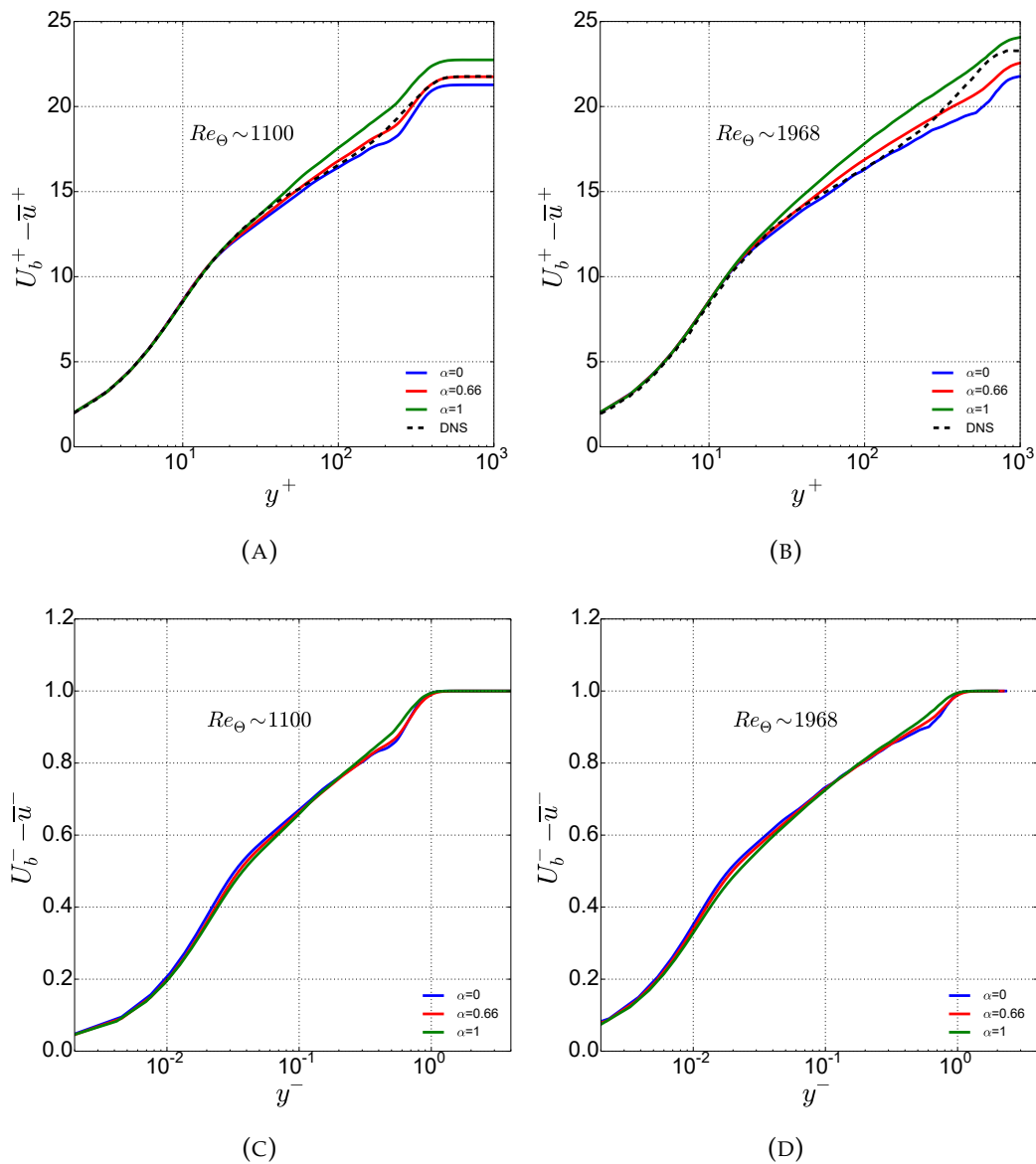


FIGURE C.1: Normalized wall-normal profiles of the mean streamwise velocity for various values of the model parameter α for $Re_b = 1000$ at (A) $Re_\theta \sim 1100$ (B) $Re_\theta \sim 1968$. ODT results are shown in comparison to a reference DNS [50]. The model parameters $C = 9$, $Z = 400$ and the large-eddy suppression are fixed. (C, D) Same data as in (A, B) but normalized with the outer velocity, U_b , and length scale, δ_{99} . The superscripts '+' and '-' indicate normalization with inner and outer units, respectively.

DNS data. The profile in the inner region ($y^+ < 5$) and in the outer log region ($y^+ > 400$) does not depend on α . The most sensitive region for α is $10 < y^+ < 400$.

Figure C.2 also indicates that the normalized streamwise rms velocity fluctuations decrease with increasing α from the buffer layer onward ($y^+ > 10$). The main features for any α are retained for the rms profiles. However, it fails

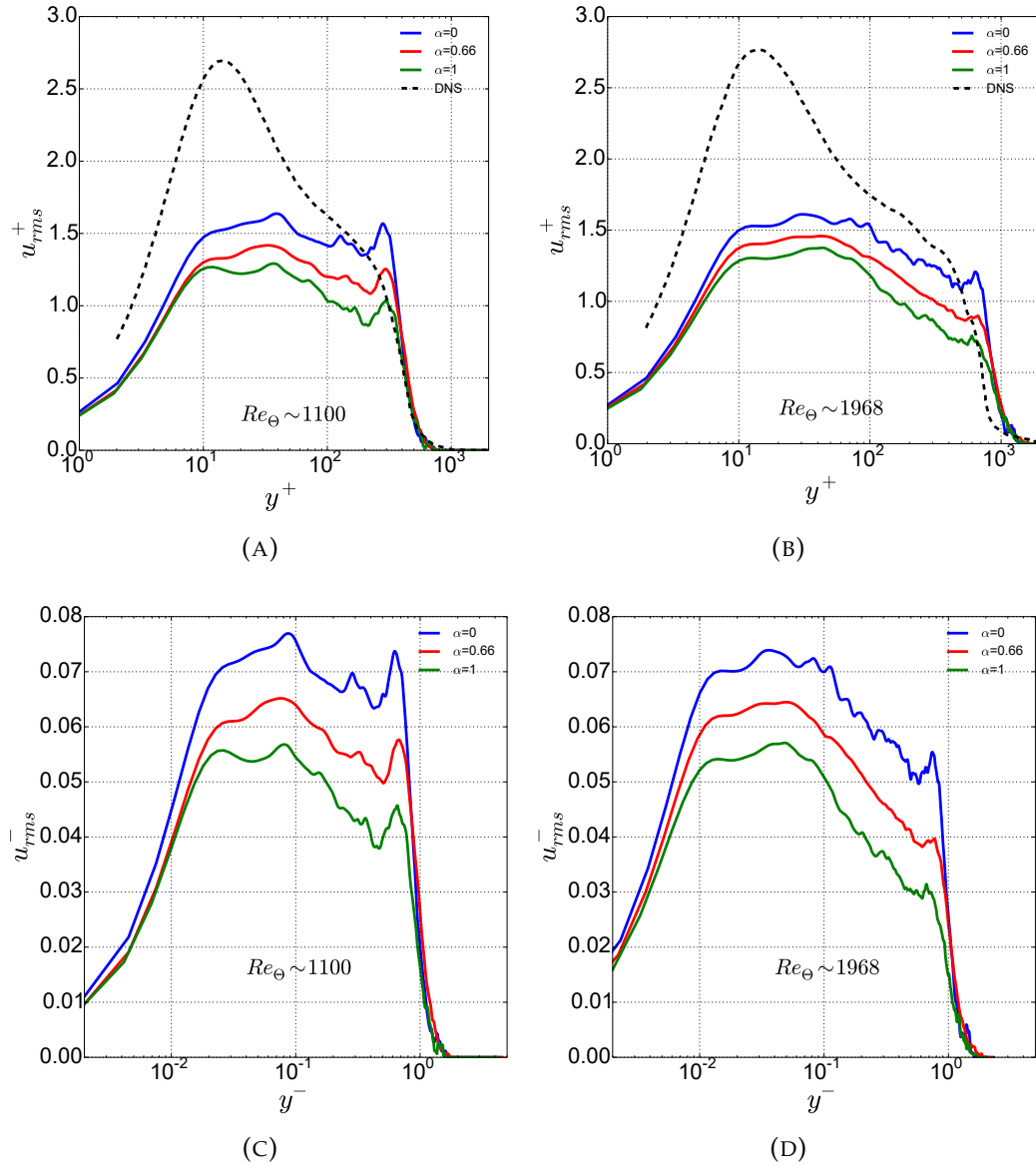


FIGURE C.2: Normalized wall-normal profiles of the rms streamwise velocity for various values of the model parameter α for $Re_b = 1000$ at (A) $Re_\theta \sim 1100$ (B) $Re_\theta \sim 1968$. ODT results are shown in comparison to a reference DNS [50]. The model parameters $C = 9$, $Z = 400$ and the large-eddy suppression are fixed. (C, D) Same data as in (A, B) but normalized with the outer velocity, U_b , and length scale, δ_{99} . The superscripts ‘+’ and ‘-’ indicate normalization with inner and outer units, respectively.

to capture the near-wall fluctuation peak. This is a well-known limitation of the model [28, 29, 89]. For $\alpha = 0$, all kinetic energy resides in the u component and for $\alpha \rightarrow 1$, the energy exchange increases towards its maximum possible value, which results in a smaller u_τ and larger U_b^+ . Hence, the momentum transfer across the logarithmic region and from the fluid to the wall depends on the energy redistribution.

Figure C.2 (C, D) shows the rms velocity, $u_{rms}^- = \sqrt{u'^2}/U_b$, scaled to outer units. The figure suggests that the rms velocity profiles shown in Figure C.2 (C, D) imply that the height variation of the corresponding profiles in Figure C.2 (A, B) is not solely due to the variation of u_τ .

We conclude that ODT is able to capture the first and second order moments of the streamwise velocity for the selected Reynolds numbers in comparison with the reference DNS. The optimal value selected is $\alpha = 2/3$.

C.2 Variation of the Model Parameter C

The overall occurrence of the eddies is controlled by the parameter C , referred as turbulence strength parameter. The simulations are carried out for three C values i.e. $C = [6, 9, 12]$. The analysis is done for $Re_b=1000$ at $Re_\theta \sim 1100$ and 1968. While analyzing the influence of C parameter, all other parameters are kept constant as $Z = 400$, $\alpha = 0.66$ as well as usage of the two-thirds suppression mechanism.

Figure C.3 shows the influence of the model parameter C on the mean streamwise velocity normalized by (A,B) inner units and (C,D) outer units at (A,C) $Re_\theta \sim 1100$ and (B,D) $Re_\theta \sim 1968$. The mean profile presented in Figure C.3(A,B) shows that the slope of the normalized velocity profile in the free-stream velocity U_b^+ as well as the logarithmic region are directly influenced by the C parameter. For small C , the velocity profile tends towards a laminar profile and u_τ decreases and for large C , u_τ increases. For small C values the level of turbulence is reduced due to implementation of less eddies. For large C , the turbulence intensity have increased. The similarity properties of the inner layer ($y^+ < 10$) remain unaffected by C similar to the parameter α . The mean velocity profile exhibits good agreement for $C = 9$ with the reference DNS data [50] for both Re_θ .

Figure C.3(C) and (D) shows that the profiles collapses better in the outer log-region, i.e., specially in the range $y^- = y/\delta_{99} > 1$ when normalised by outer units for the TBL configuration. However, the profiles of the streamwise velocity at higher Re_θ collapse very well as compared to small Re_θ , i.e., $Re_\theta \sim 1100$. It was observed that the profiles in Figure C.1 showed better horizontal alignment when normalised by outer units because α have less effect than C on the occurrence of large eddies that control boundary layer growth.

Figure C.4 shows the influence of the model parameter C on the rms velocity normalized by (A,B) inner units and (C,D) outer units at (A,C) $Re_\theta \sim 1100$ and (B,D) $Re_\theta \sim 1968$. The shape of the rms profiles is the same for all the values of C considered. Interestingly, the fluctuation magnitude is inversely proportional to C and implies less rms for larger turbulence intensity. The behaviour is counterintuitive. This can be understood by a much flatter mean state in the more turbulent case such that turbulence is sustained by much weaker available (shear-extractable) energies. This indicates less velocity fluctuations and less shear. However, ODT keeps underestimating the rms from the buffer until the log region for any value of C investigated similar to

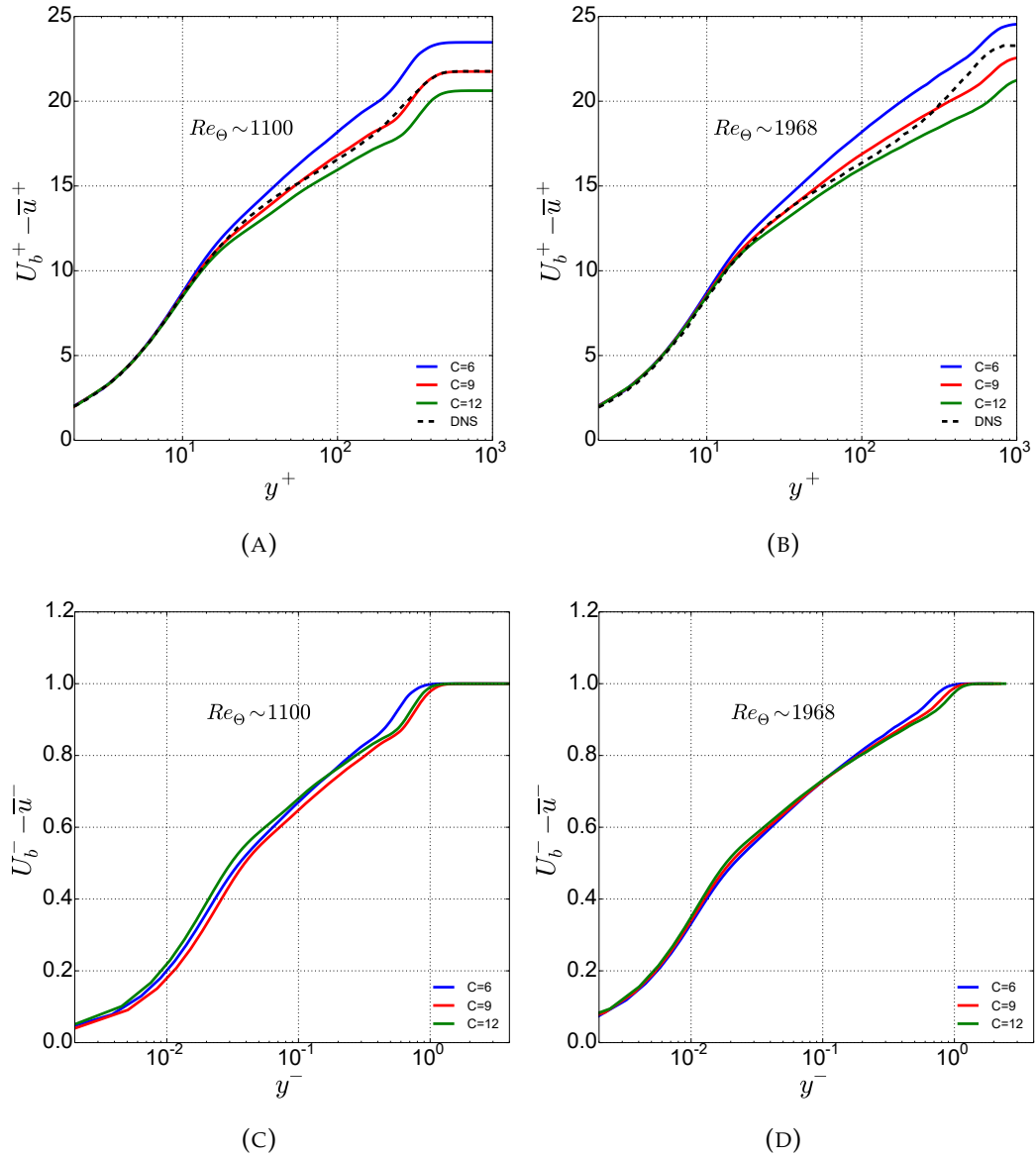


FIGURE C.3: Normalized wall-normal profiles of the mean streamwise velocity for various values of the model parameter C for $Re_b = 1000$ at (A) $Re_\theta \sim 1100$ (B) $Re_\theta \sim 1968$. ODT results are shown in comparison to a reference DNS [50]. The model parameters $\alpha = 2/3$, $Z = 400$ and the large-eddy suppression are fixed. (C, D) Same data as in (A, B) but normalized with the outer velocity, U_b , and length scale, δ_{99} . The superscripts '+' and '-' indicate normalization with inner and outer units, respectively.

α parameter. We therefore consider $C = 9$ obtained for the mean profile as optimal value.

Figure C.4 (C, D) shows the rms velocity, $u_{rms}^- = \sqrt{u'^2}/U_b$, scaled to outer units. Similar to α parameter, this figure also suggests that the rms velocity profiles shown in Figure C.4 (C, D) imply that the height variation of

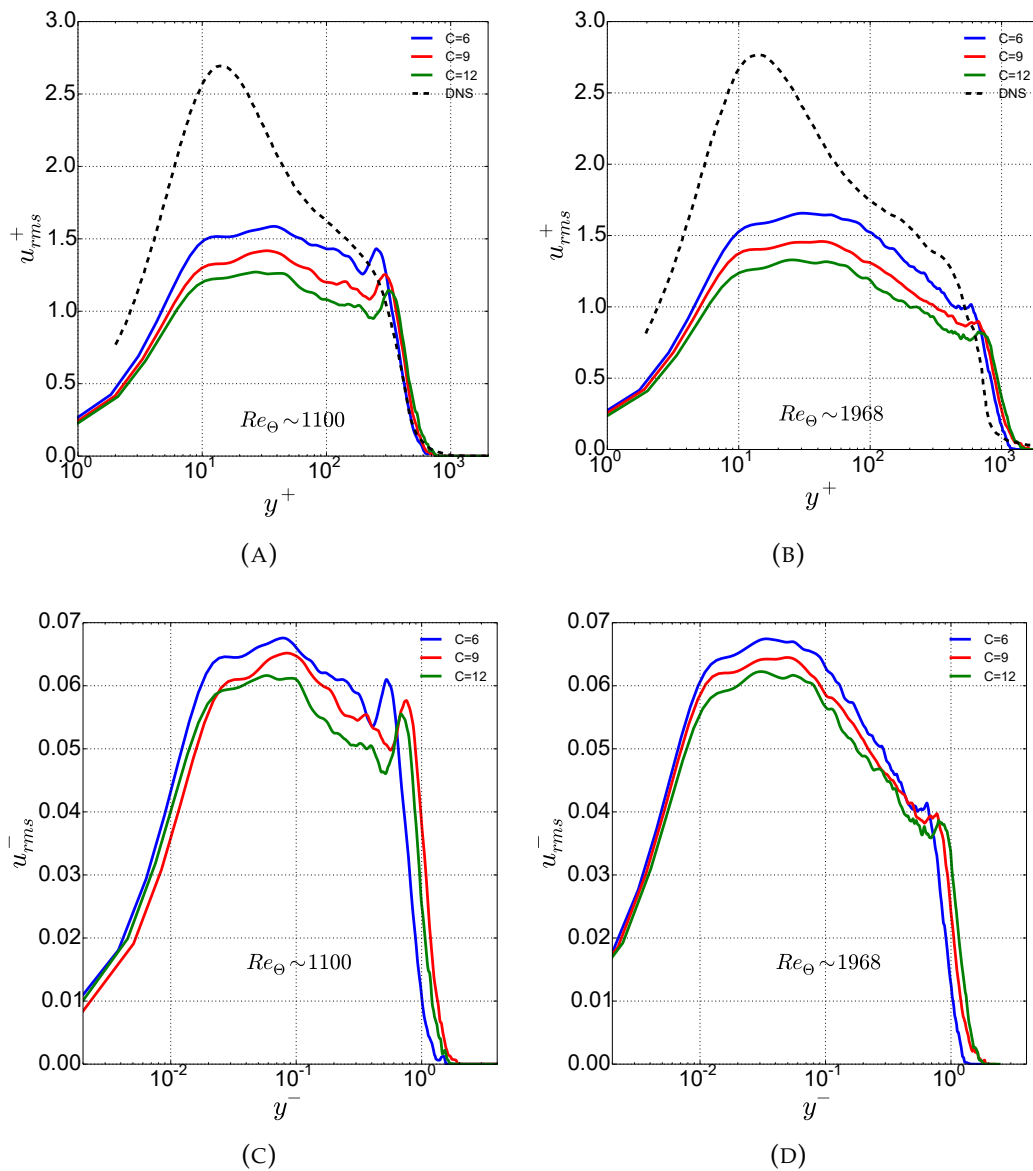


FIGURE C.4: Normalized wall-normal profiles of the rms streamwise velocity for various values of the model parameter C for $Re_b = 1000$ at (A) $Re_\theta \sim 1100$ (B) $Re_\theta \sim 1968$. ODT results are shown in comparison to a reference DNS [50]. The model parameters $\alpha = 2/3$, $Z = 400$ and the large-eddy suppression are fixed. (C, D) Same data as in (A, B) but normalized with the outer velocity, U_b , and length scale, δ_{99} . The superscripts '+' and '-' indicate normalization with inner and outer units, respectively.

the corresponding profiles in Figure C.4 (A, B) is not solely due to the variation of u_τ .

The results for variation of C for $Re_b=1000$ at (A, C) $Re_\theta \sim 1100$ and (B, D) $Re_\theta \sim 1968$ with $\alpha = 2/3$, $Z = 400$ and the two-thirds suppression method fixed are demonstrated in Figure C.5 for the cross stress profile, scaled in (A, B) inner and (C, D) outer units.

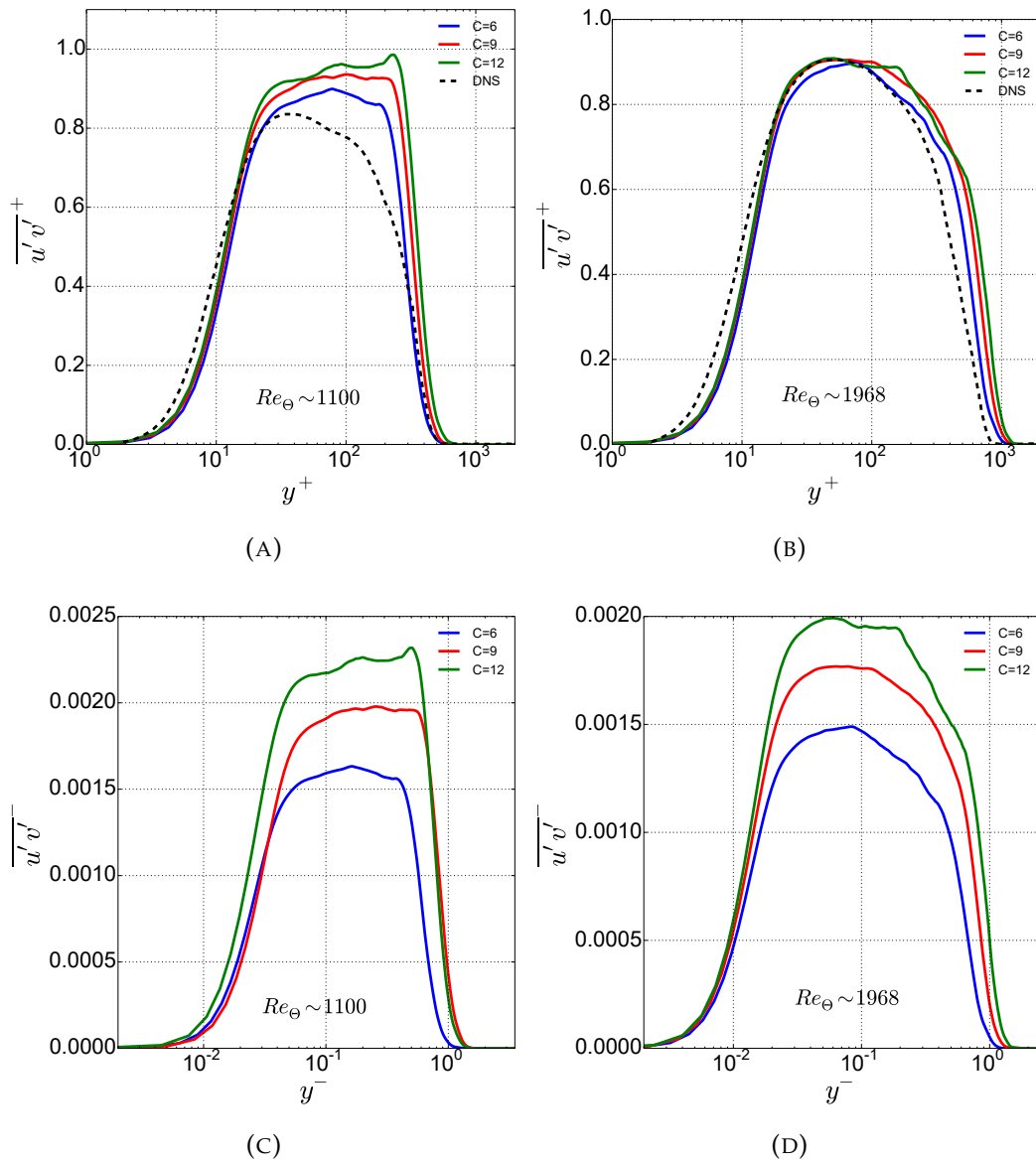


FIGURE C.5: Normalized wall-normal profiles of the cross stresses for various values of the model parameter C for $Re_b = 1000$ at (A) $Re_\theta \sim 1100$ (B) $Re_\theta \sim 1968$. ODT results are shown in comparison to a reference DNS [50]. The model parameters $\alpha = 2/3$, $Z = 400$ and the large-eddy suppression are fixed. (C, D) Same data as in (A, B) but normalized with the outer velocity, U_b , and length scale, δ_{99} . The superscripts '+' and '-' indicate normalization with inner and outer units, respectively.

The profile matches well with the DNS results for all C values considered for the investigation for higher Re_θ , i.e., $Re_\theta \sim 1968$ shown in Figure C.5 (B). However, for $Re_\theta \sim 1100$ in Figure C.5 (A), the profiles are dependent on value of C only in the region $50 < y^+ < 300$ and in this region, the magnitude for cross stress is minimum for lowest C , i.e., $C = 6$. The magnitude is directly proportional to C for cross stress profiles which is opposite to rms profiles. Nevertheless, the ODT profiles agrees with the DNS results for both Re_θ for

$C = 9$.

Note that Figure C.5 (C) and (D) shows the dependence of outer units on cross stress profiles with variation of C parameter unlike the mean streamwise and rms velocity discussed above. We report that the height variation at both Re_θ for C parameter is strong for cross stress profiles. The height change for the cross stress profiles normalized with outer units is increasing with increasing the value of C .

ODT is able to capture the first and second order moments of the streamwise velocity for the selected Reynolds numbers in comparison with the reference DNS for $C = 9$ and hence this value is used for further investigation for TBL configuration.

To further check the affect of the C parameter on higher statistics we have considered skewness. Figure C.6 shows the skewness of the streamwise velocity component for variation of C for $Re_b=1000$ at (A, C) $Re_\theta \sim 1100$ and (B, D) $Re_\theta \sim 1968$ with $C = 9$, $Z = 400$ and the two-thirds suppression method fixed, scaled in (A, B) inner and (C, D) outer units.

For all C values, the parameter slightly influences the skewness in the inner region with under-predicted amplitude and in the outer log region with over-predicted amplitude as compared to the reference DNS data [50]. Nevertheless, the skewness profiles are qualitatively consistent for all C considered. However, $C = 9$ gives a better fit for lower velocity statistics discussed for the mean streamwise and rms velocity profile than the other C values. The skewness in the inner region increases with decreasing C value. For example for $C = 12$, the skewness is less as compared to the skewness for $C = 6$ as shown in Figure C.6 (A) and (B). However, the skewness in the outer region show opposite trend and increases with increasing C value.

Note that the qualitative trends for the skewness of the streamwise velocity component are consistent for both Re_θ considered for the present configuration and behaves in a similar way. Figure C.6 (C, D), scaled with outer units on x -axis does not change from Figure C.6 (A, B). This suggests that the higher order velocity statistics is independent of the scaling. Note that the scaling on y -axis is same for all the figures.

The quantities (A) Re_τ , (B) H , (C) Re_δ and (D) Re_X as a function of Re_θ for various values of the model parameter C for $Re_b = 1000$ is shown in Figure C.7. For comparison, the reference DNS data from [50] is shown in dashed line. The model parameters $\alpha = 2/3$, $Z = 400$ and the large-eddy suppression are fixed. Figure C.7 (A) shows that the value of Re_τ converges towards the reference DNS value for more turbulence intensity, i.e., for higher C values. It diverges away for less turbulence intensity, i.e., $C = 6$. However, we have considered the optimal value of the C parameter according to the establishment of log-law and we use $C = 9$ for investigating TBL flow configuration.

For H variation with Re_θ , the value for ODT solution is close to the reference DNS data considered for $C = 6$ shown in Figure C.7 (B). The H behaves opposite as compared to Re_τ with the variation of C parameter. The H value moves away from the DNS results with increasing C . For $C = 9$ and 12, the H profile is similar. Figure C.7 (C) indicates that Re_δ variation with Re_θ in

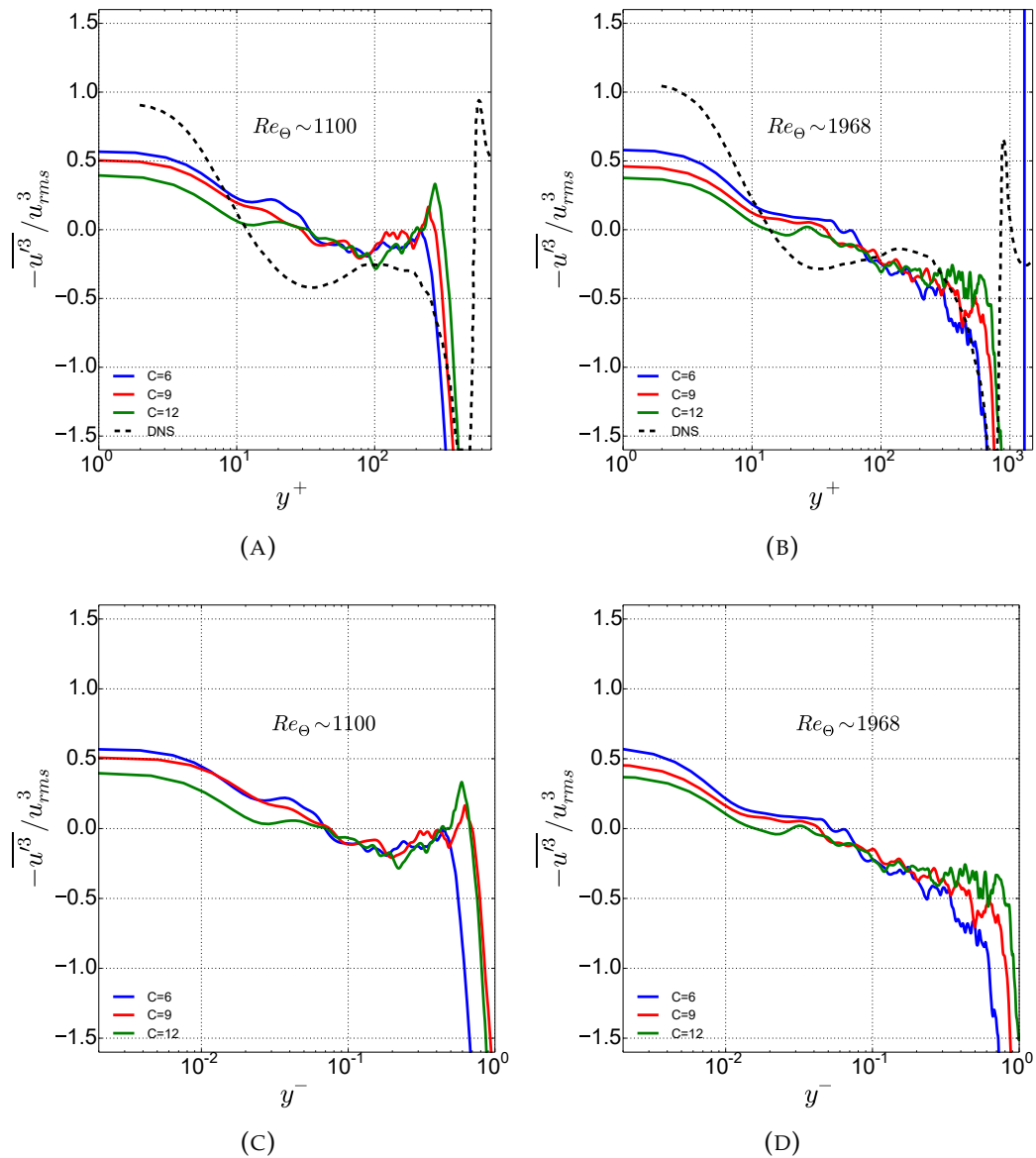


FIGURE C.6: Normalized wall-normal profiles of the skewness of the streamwise velocity for various values of the model parameter C for $Re_b = 1000$ at (A) $Re_\theta \sim 1100$ (B) $Re_\theta \sim 1968$. ODT results are shown in comparison to a reference DNS [50]. The model parameters $\alpha = 2/3$, $Z = 400$ and the large-eddy suppression are fixed. (C, D) Same data as in (A, B) but normalized with the outer velocity, U_b , and length scale, δ_{99} . The superscripts '+' and '-' indicate normalization with inner and outer units, respectively.

independent of the C parameter which is consistent with the α parameter. Re_X shows good agreement with the reference DNS data for $C = 9$ as shown in Figure C.7 (D). The profile for Re_X deviates and diverges from the DNS results for both $C = 6$ and $C = 12$. The Re_X value tends to increase significantly for low C values i.e. for $C = 6$ and decrease for high C ($C = 12$).

Skin friction coefficient C_f as a function of (A) Re_δ , (B) Re_θ and (C) Re_X

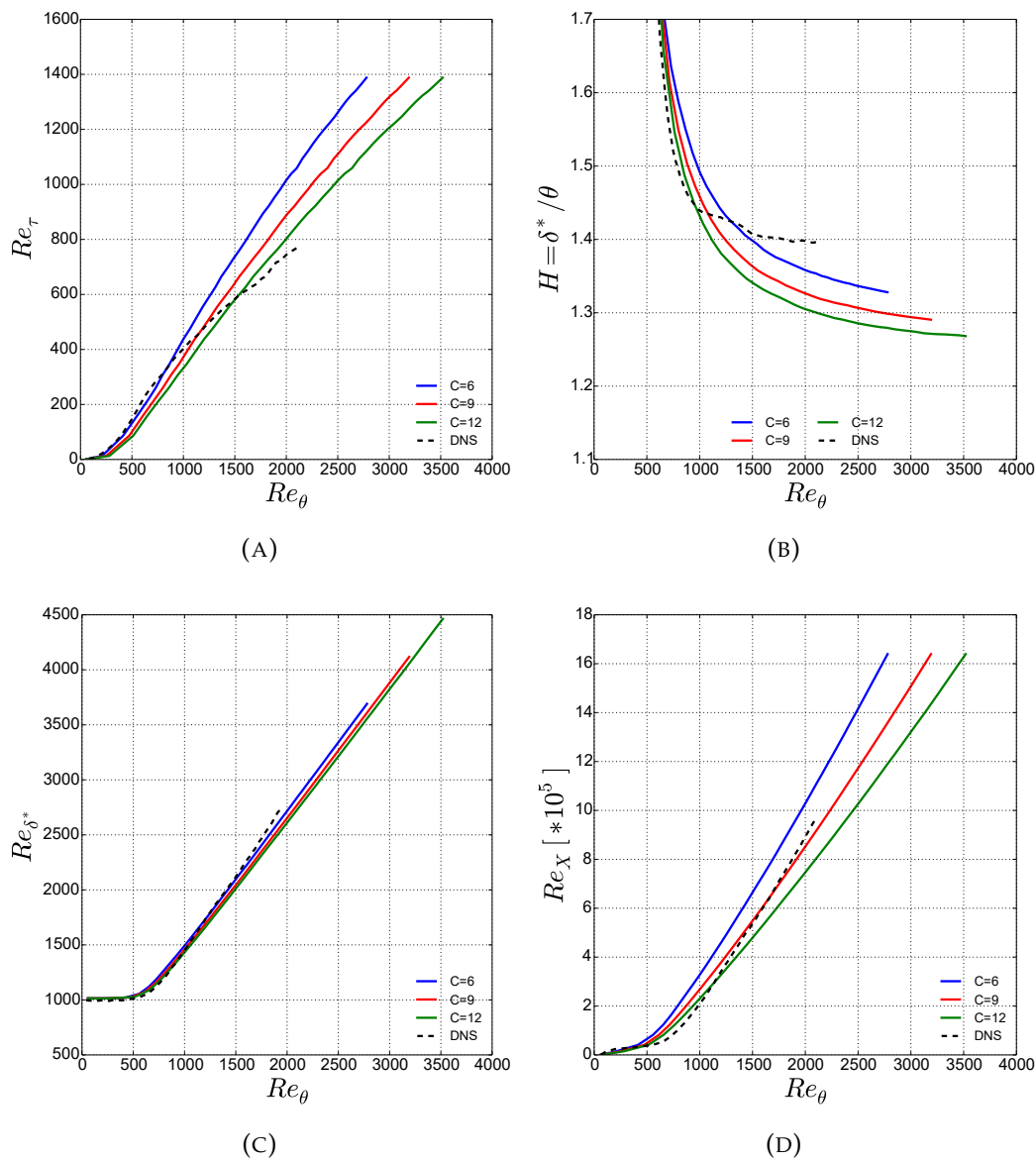
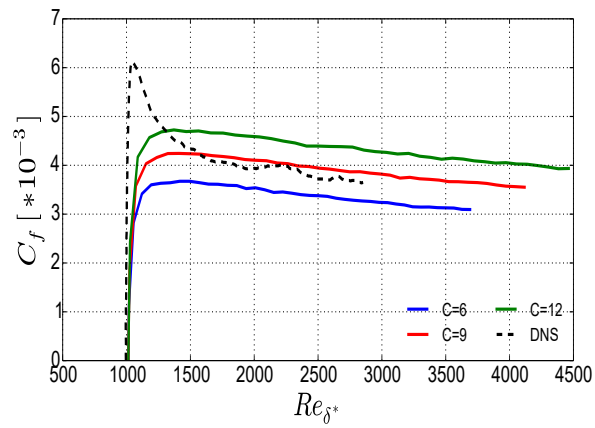
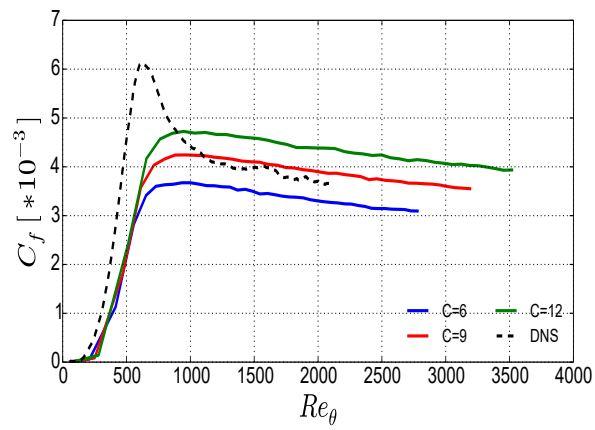


FIGURE C.7: The quantities (A) Re_τ , (B) H , (C) Re_δ and (D) Re_x as a function of Re_θ for various values of the model parameter C for $Re_b = 1000$. For comparison, the reference DNS data from [50] is shown. The model parameters $\alpha = 2/3$, $Z = 400$ and the large-eddy suppression are fixed.

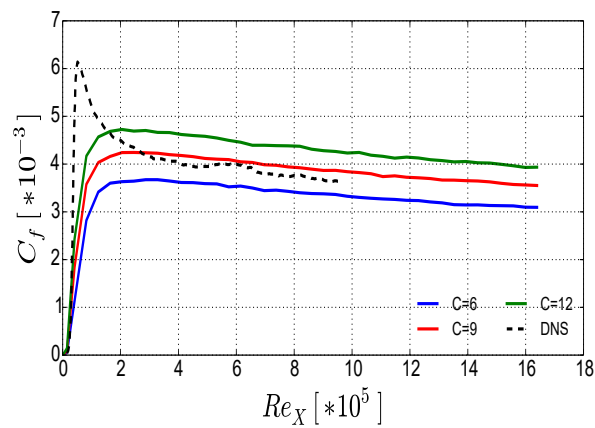
for various values of the model parameter C for $Re_b = 1000$ is shown in Figure C.8. For comparison, the reference DNS data from [50] is shown. The model parameters $\alpha = 2/3$, $Z = 400$ and the large-eddy suppression are fixed for this analysis. The skin friction coefficient peak is dependent on C parameter. However, the peak is under-predicted for all C values considered in comparison with the reference DNS data from [50]. The peak is more close to the DNS data for higher C values and decreases with decreasing C . Nevertheless, the profiles for all C values converges for higher Re_θ . For higher Re_θ , the skin friction coefficient shows good agreement for $C = 9$ and hence,



(A)



(B)



(C)

FIGURE C.8: Skin friction coefficient C_f as a function of (A) Re_{δ} , (B) Re_{θ} and (C) Re_X for various values of the model parameter C for $Re_b = 1000$. For comparison, the reference DNS data from [50] is shown. The model parameters $\alpha = 2/3$, $Z = 400$ and the large-eddy suppression are fixed.

we choose $C = 9$ for analyzing the temporally developing turbulent boundary layer.

C.3 Variation of the Model Parameter Z

This parameter is used to suppress the small eddies that are smaller than the Kolmogorov scale to increase the performance of the model. In ODT, for wall bounded flows, especially in the buffer layer, the behavior of 3-D eddies is different from the 1-D representation and by excluding some slightly larger eddies than the Kolmogorov ones ($Z > 1$), the position of the buffer layer in the ODT solutions can be matched to DNS [84]. We have varied the Z value in the range $Z = [200, 400, 600]$ while keeping other parameters constant i.e. $C = 9$, $\alpha = 0.66$ and the two-thirds LS mechanism. The analysis is done for $Re_b=1000$ at $Re_\theta \sim 1100$ and 1968.

Figure C.9 depicts the influence of the model parameter Z on the mean streamwise velocity normalized by (A,B) inner units and (C,D) outer units at (A,C) $Re_\theta \sim 1100$ and (B,D) $Re_\theta \sim 1968$. It can be seen from Figure C.9(A) and (B) that the change of the Z parameter has no effect in the logarithmic region. Although, the change from the linear region towards the logarithmic region is highly influenced by this parameter. Mainly the start of the buffer region is controlled by the Z parameter. When $Z = 200$, there is an earlier start of the buffer layer in the velocity profile and the opposite is observed for $Z = 600$. The TBL, in general seems to be less sensitive to Z than the other parameters discussed above. For $Z = 400$, the profile is in good agreement with the DNS profile reported in [50] for both Re_θ , i.e., for $Re_\theta \sim 1100$ as well as $Re_\theta \sim 1968$ and this agrees with the optimal value reported for the asymptotic suction boundary layer [96] and is close to the values used for turbulent channel flows [89, 126].

The mean profile presented in Figure C.9(A,B) also confirms that the slope of the logarithmic region of the mean profile remain virtually unaffected and the free-stream velocity U_b^+ in the logarithmic region is directly influenced by the Z parameter. For large Z , u_τ decreases and for small Z , u_τ increases. For small Z values, the small eddies are included in the flow and for large Z values, these small eddies are ignored which improves the performance of the model. The similarity properties of the inner layer ($y^+ < 10$) remain unaffected by this parameter similar to the other parameters discussed earlier. The mean velocity profile exhibits good agreement for $Z = 600$ with the reference DNS data [50] for both Re_θ for TBL configuration considered here.

Figure C.9(C) and (D) shows that the profiles collapse better in the outer log-region, i.e., specially in the range $y^- = y/\delta_{99} > 1$ when normalised by outer units for the TBL configuration. However, the profiles of the streamwise velocity at both Re_θ collapse very well for Z parameter as compared to the C parameter. The mean streamwise velocity profiles for the Z and α parameters obtain a large horizontal collapse in comparison to the C parameter. This was expected as the C parameter effects the occurrence of the large eddies and plays a key role in boundary layer dynamics.

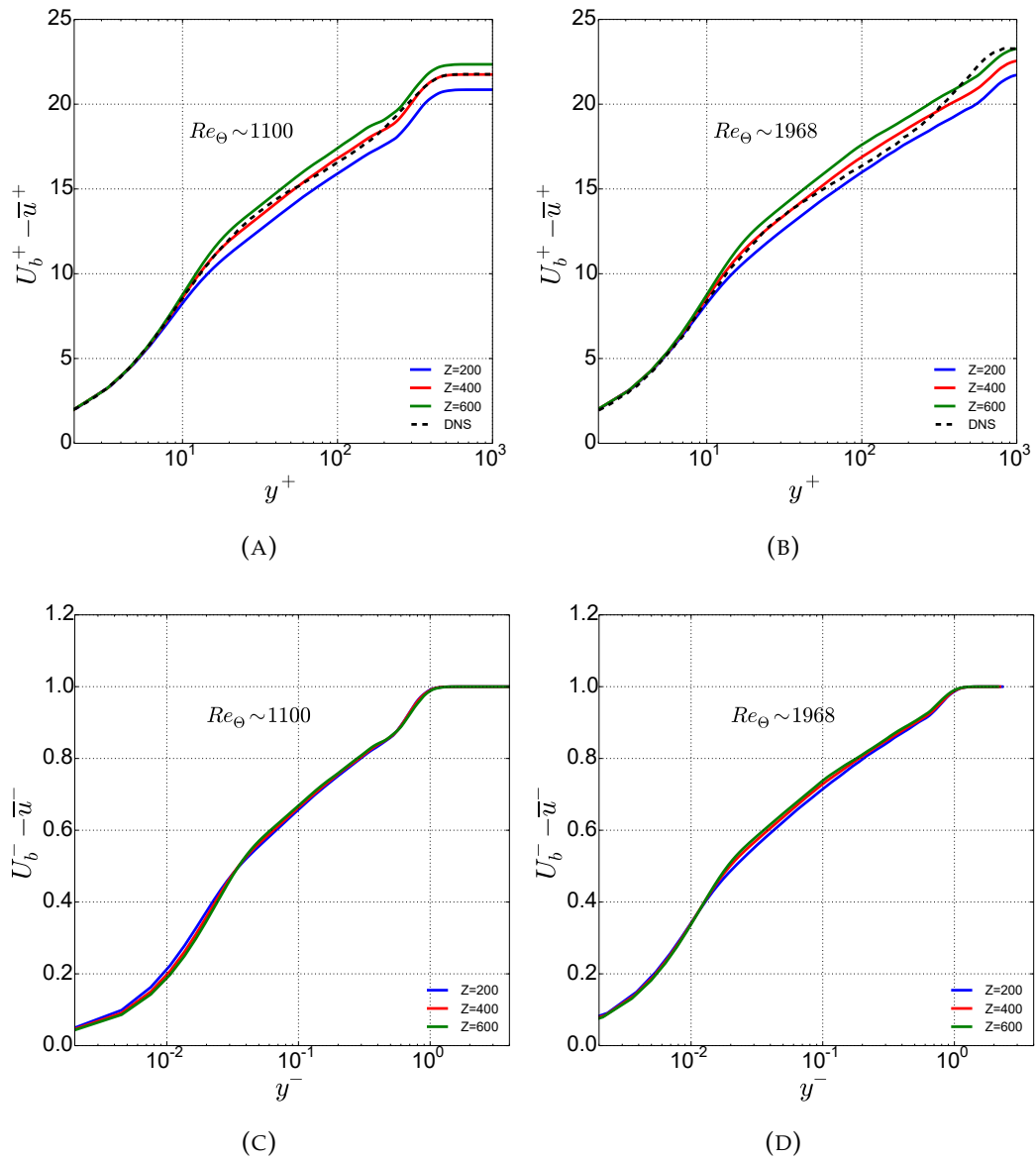


FIGURE C.9: Normalized wall-normal profiles of the mean streamwise velocity for various values of the model parameter Z for $Re_b = 1000$ at (A) $Re_\theta \sim 1100$ (B) $Re_\theta \sim 1968$. ODT results are shown in comparison to a reference DNS [50]. The model parameters $\alpha = 2/3$, $C = 9$ and the large-eddy suppression are fixed. (C, D) Same data as in (A, B) but normalized with the outer velocity, U_b , and length scale, δ_{99} . The superscripts '+' and '-' indicate normalization with inner and outer units, respectively.

Figure C.10 displays the influence of the model parameter Z on the rms velocity normalized by (A,B) inner units and (C,D) outer units at (A,C) $Re_\theta \sim 1100$ and (B,D) $Re_\theta \sim 1968$. The other optimal parameters are kept constant for this purpose. Like other parameters discussed above, the shape of the rms profiles is the same for all the values of Z considered. The rms velocity profiles are less sensitive towards Z parameter unlike for C and α . Only the

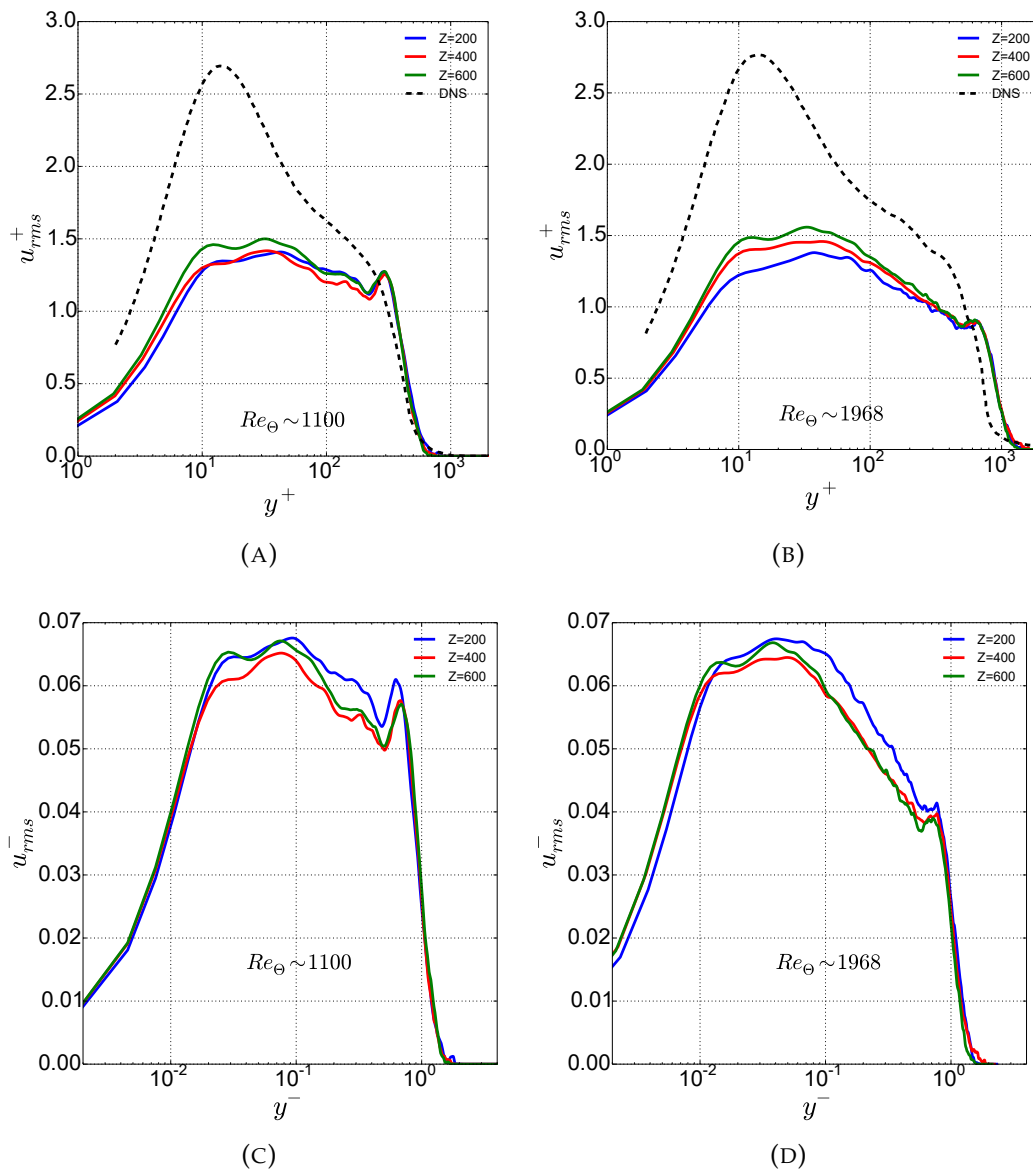


FIGURE C.10: Normalized wall-normal profiles of the rms streamwise velocity for various values of the model parameter Z for $Re_b = 1000$ at (A) $Re_\theta \sim 1100$ (B) $Re_\theta \sim 1968$. ODT results are shown in comparison to a reference DNS [50]. The model parameters $\alpha = 2/3$, $C = 9$ and the large-eddy suppression are fixed. (C, D) Same data as in (A, B) but normalized with the outer velocity, U_b , and length scale, δ_{99} . The superscripts '+' and '-' indicate normalization with inner and outer units, respectively.

peaks seem to vary slightly with Z . ODT underestimate the rms from the buffer until the log region for any value of Z investigated similar to α and C parameters. We therefore consider $Z = 600$ obtained for the mean profile as optimal value for further simulations.

Figure C.10 (C, D) shows the rms velocity, $u_{rms}^- = \sqrt{u'^2}/U_b$, scaled to

outer units. Similar to α and C parameter, this figure also suggests that the rms velocity profiles shown in Figure C.10 (C, D) imply that the height variation of the corresponding profiles in Figure C.10 (A, B) is not due to the variation of u_τ as the height variation for outer as well as inner units is consistent for both Re_θ considered.

Since, ODT is able to capture the low order moments of the streamwise velocity for the selected Reynolds numbers in comparison with the reference DNS for $Z = 600$, we select this value for further investigation for TBL configuration.

C.4 Influence of the LS Mechanism

To avoid unphysically large eddy event which are rare to occur, Large eddy Suppression (LS) mechanism is used in different ways. The simulations are performed for three different mechanisms: 1) The eddies are allowed only when the simulation elapsed time is greater than the eddy turnover time. This is known as the 'elapsed time mechanism'. 2) When shear associated with the eddy implementation is highly concentrated in a narrow position range and causes the insertion of an eddy then this can be avoided by using the 'two-thirds mechanism'. 3) These eddies can be suppressed by simply suppressing those eddies whose size exceeds by a given fraction of the domain size, referred as the 'frac domain mechanism'. Additionally, we have presented the results when no eddy suppression mechanism is implemented (referred as 'none' mechanism). The study is done for $Re_b = 1000$ at $Re_\theta \sim 1100$ and $Re_\theta \sim 1968$. The influence of these suppression mechanisms on various velocity statistics and global properties is analysed and presented next. While performing the simulations with LS, all the other parameters are kept constant as $\alpha = 0.66$, $C = 9$ and $Z = 400$.

Figure C.11 depicts the influence of the LS mechanism on the mean streamwise velocity as a function of wall normal coordinates at (A) $Re_\theta \sim 1100$ and (B) $Re_\theta \sim 1968$. In the logarithmic region, there is no influence of LS as shown in Figure C.11(A) and (B). The influence is observed in the region $y^+ > 20$ and the velocity profile agrees with the DNS data for the two-thirds LS mechanism. On the other hand, for the other two suppression mechanisms and also for the none mechanism, the profile is under-predicted as compared to DNS. For the elapsed time mechanism, the profile in the buffer region is the same as for the frac domain and the none mechanisms but is slightly different in outer log region. The profiles with the frac domain and the none mechanisms overlap with each other. We conclude that the viscous sublayer and the logarithmic region are only weakly affected by the large-eddy suppression methods. This matches qualitatively the expectation since large eddy events are expected to affect mainly the outer layer ($y^+ > 300$).

Note that when the outer layer is modified due to too many large eddy events, the distribution of the smaller ones is modified indirectly and, consequently, the momentum transport is affected across the entire boundary

layer. This alters u_τ and also the normalized free-stream velocity U_b^+ , which depends weakly on the large-eddy suppression as seen in the figure.

The two-thirds suppression mechanism has the largest effect on the low-order velocity statistics (see Figure C.11) and for the other two suppression mechanisms and also without suppression, the mean profiles are underestimated in comparison to the reference DNS [50]. The profiles obtained without the suppression (labeled with ‘none’) as well as with the elapsed time and frac domain methods are within the statistical confidence level, identical to each other up to $y^+ \sim 100$.

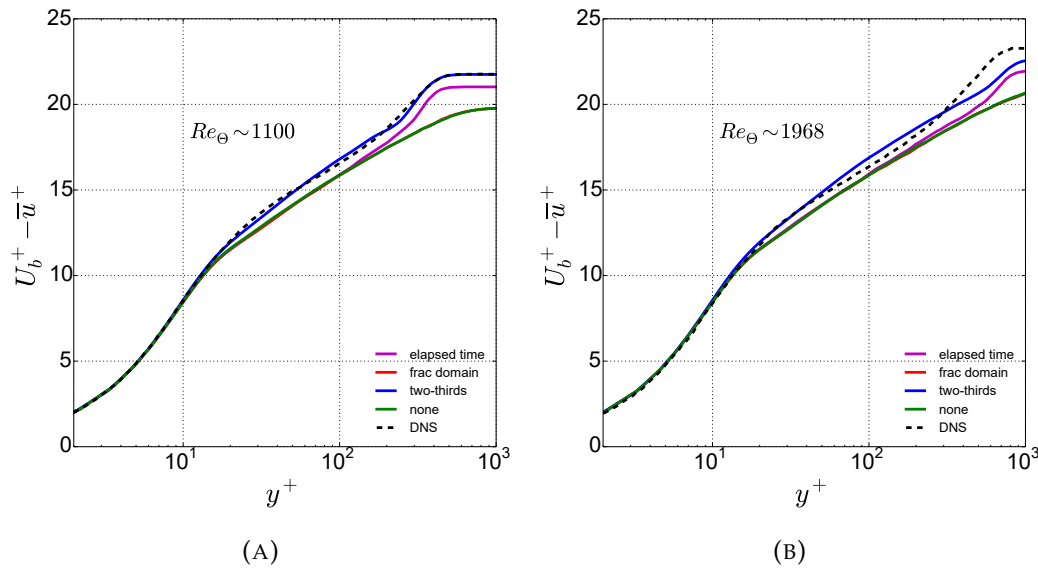


FIGURE C.11: Normalized wall-normal profiles of the mean streamwise velocity for various large-eddy suppression methods for $Re_b = 1000$ at (A) $Re_\theta \sim 1100$ (B) $Re_\theta \sim 1968$. ODT results are shown in comparison to a reference DNS [50]. The model parameters $\alpha = 2/3$, $C = 9$ and $Z = 400$ are fixed.

Figure C.12 displays the influence of the LS mechanism on the rms velocity as a function of wall normal coordinates (in viscous units) at (A) $Re_\theta \sim 1100$ and (B) $Re_\theta \sim 1968$. The other optimal parameters are kept fixed for investigating influence of LS mechanism. For rms profile, shown in Figure C.12 (A) and (B), the elapsed time, the frac domain and the none mechanisms almost overlap with each other in the buffer region, while the two-thirds LS mechanism show slightly more amplitude in this region. Whereas, in the outer region, two-thirds and elapsed time mechanisms collapse onto each other and frac domain and none mechanism collapse onto each other as well. Also, elapsed time and two-thirds mechanisms show an additional peak in the outer log-region at both Re_θ and this peak is not discerned in other two mechanism and this peak also appears as a ‘shoulder’ in the reference DNS [50]. The curves are under-predicted than DNS results for all the cases. The frac domain and the none mechanisms vary from other two mechanisms in the outer region with better agreement for the two-thirds LS mechanism to the DNS data.

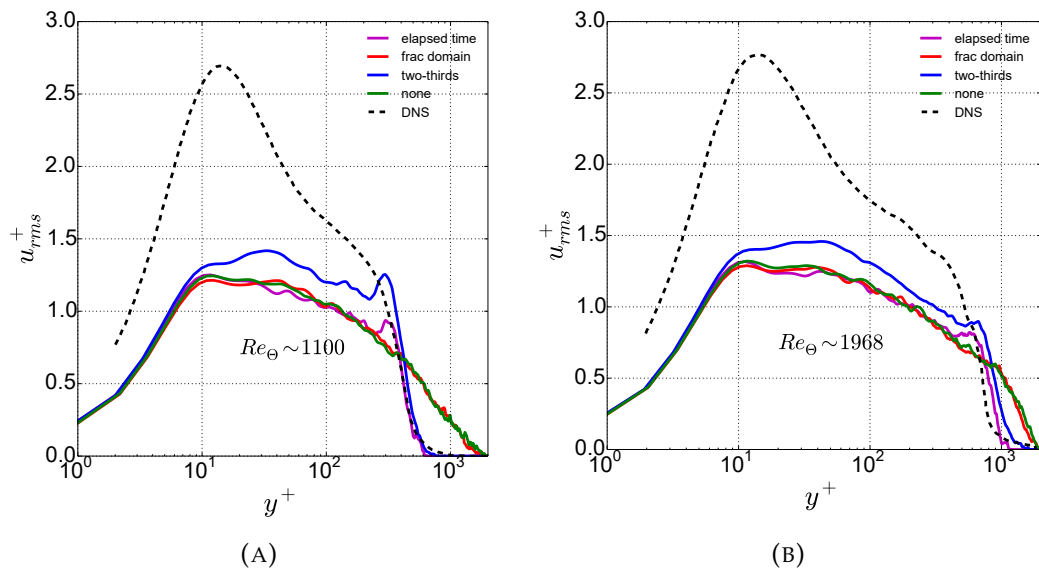


FIGURE C.12: Same as above but for the rms streamwise velocity.

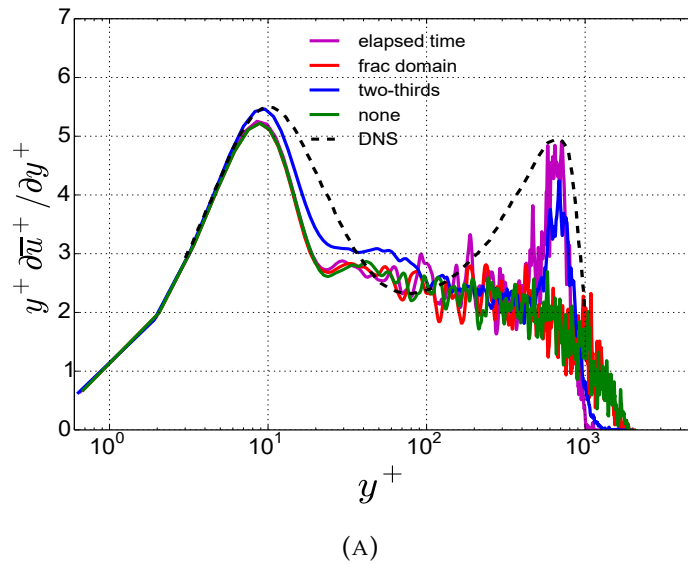


FIGURE C.13: The indicator function versus wall-normal coordinate (in viscous units) for various large-eddy suppression methods for $Re_b = 1000$ at $Re_{\theta} \sim 1968$. For comparison, the reference DNS data for the SBL from [44] at $Re_{\theta} \sim 2000$ is given by a black dashed line. The model parameters $\alpha = 2/3$, $C = 9$ and $Z = 400$ are fixed.

Figure C.13 shows indicator function for various LS methods normalized with the wall normal coordinates (in viscous units) at $Re_{\theta} \sim 1968$ for $Re_b = 1000$. ODT results are shown in comparison to the reference DNS of [41]. As expected, the LS method influence the indicator function mostly in the outer region, i.e., in the region $y^+ > 100$. The curve for frac domain traces the curve for none mechanism and the elapsed time and two-thirds trace each

other. The profiles for all LS methods behaves in a similar fashion in the inner region. However, the function is under-predicted as compared to the reference DNS for frac domain and none methods and agrees fairly well for other two mechanisms.

Appendix D

Influence of Initial Conditions

An extra peak has been captured in the outer log-region for rms, cross stress and turbulent production for the TBL configuration. This additional peak has also been captured for the SBL configuration, however, it is dominant in the TBL formulation. Here we discuss about the additional peak captured in turbulent production.

We noticed three main factors that are responsible for this peak. As addressed before, first, this peak is neglected for higher averaging window. Second, it also disappears for the LS methods (frac domain and none) and discerned for the elapsed time and two-thirds mechanisms. The third reason for this peak could be transient effects and hence, we see this peak only for lower Re_θ .

The turbulent production as a function of the wall-normal coordinate in the flow is shown for higher bulk Reynolds number, i.e., $Re_b = 2000$ at four different instant in Figure D.1. The optimal set of parameters for the TBL configuration are used for this purpose. $Re_b = 2000$ case is considered because for this case the peak was discerned even for $Re_\theta \sim 1968$, whereas for lower Re_b it disappears at higher Re_θ .

This figure shows production at (A) $Re_\theta \sim 1212$, (B) $Re_\theta \sim 1694$, (C) $Re_\theta \sim 2054$ and (D) $Re_\theta \sim 2384$. The extra peak in outer log-region is dominant for $Re_\theta \sim 1212$ and the magnitude of the peak reduces with increasing Re_θ . This peak disappears for $Re_\theta \sim 2054$ and higher Re_θ . Hence, the figure demonstrates the influence of transient effects or initial condition on velocity statistics for the temporally developing turbulent boundary layer.

A similar behaviour for rms and cross stresses have also been observed. Here, the rms and cross stresses profiles are not shown and these profiles are discussed in Chapter 4. It is assumed from the above analogy that initial conditions have influence on lower order velocity statistics.

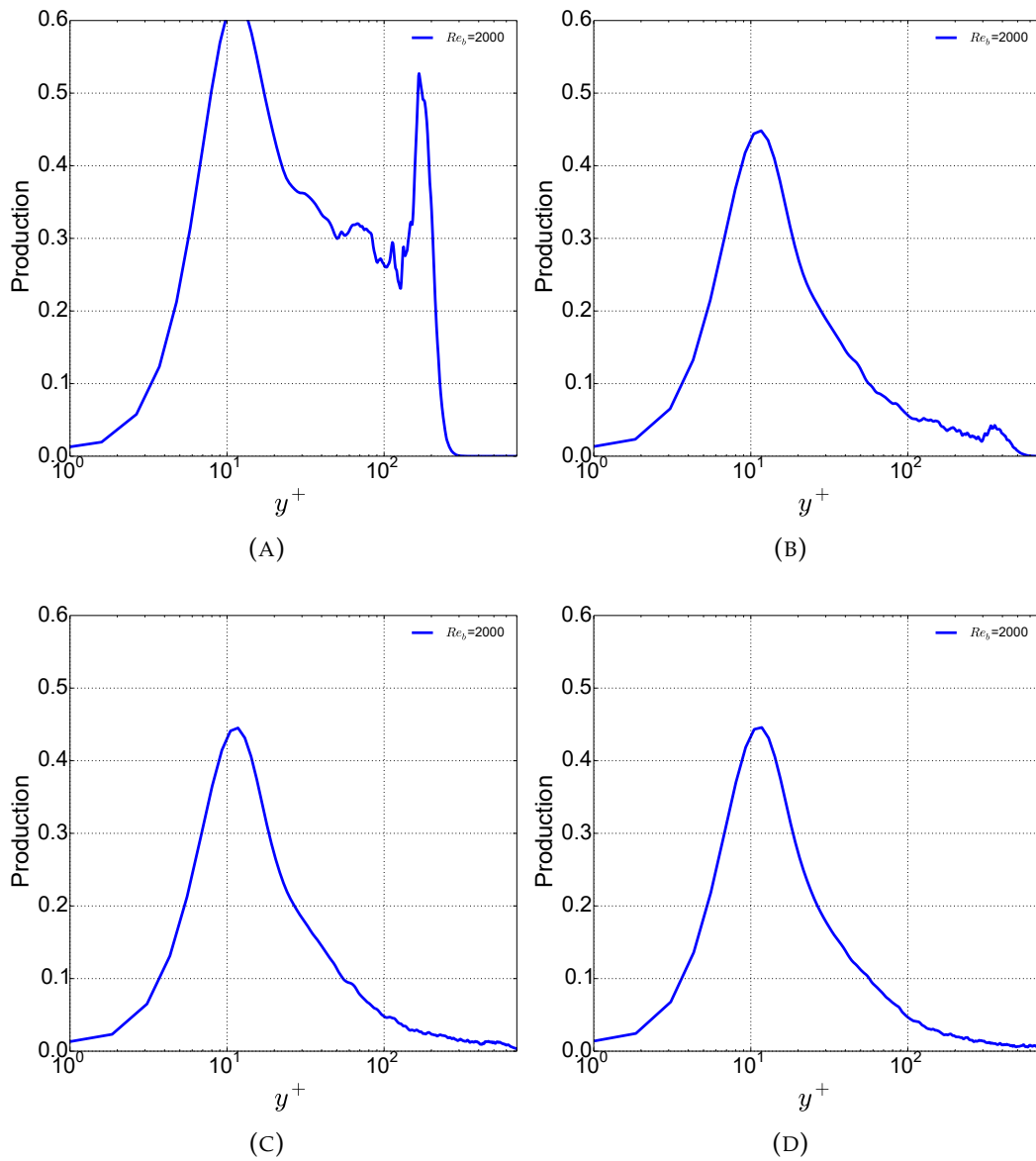


FIGURE D.1: Turbulent kinetic energy production as a function of the wall-normal coordinate (in viscous units) for (A) $Re_{\theta} \sim 1212$, (B) $Re_{\theta} \sim 1694$, (C) $Re_{\theta} \sim 2054$ and (D) $Re_{\theta} \sim 2384$ to analyse the influence of initial conditions.

Appendix E

Generation of Energy Spectra in ODT

As described earlier, there are two possible choices while comparing the 1-D turbulence spectra between ODT and DNS for the temporally developing boundary layer application case. These choices are explained below.

E.1 Generation of Time-Dependent Energy Spectra

Turbulence spectra are usually obtained for applications with a characteristic homogeneous, stationary and isotropic turbulence, as explained in [136]. The cross power spectral density or co-spectrum is defined as the Fourier transform of the fluctuating velocity autocorrelation,

$$\bar{S}(k, t) \equiv \int_{-\infty}^{\infty} e^{-\hat{i}kr} R(r, t) dr, \quad (\text{E.1})$$

here \hat{i} indicates the representation of the complex base with $\hat{i}^2 = -1$. k is the wavenumber and $R(r, t)$ is the fluctuating velocity autocorrelation,

$$R(r, t) = \overline{u'(y, t)u'^*(y + r, t)}. \quad (\text{E.2})$$

It is calculated as follows.

1. Firstly, the wall-normal positions corresponding to the uniform anisotropy y^+ range discussed for isotropy indicator is calculated. This can be done once the average velocity profile $U_b - \bar{u}(y, t)$ has been obtained, given that the normalization parameter $u_\tau(t)$ is required. It determines a range of cells $j_l < j < j_l + N_j$ corresponding to the uniform anisotropy range $y_l^+(t) < y^+(t) < y_h^+(t)$ discussed earlier. All of the averaged and fluctuating quantities are calculated within this range and it has a length $Y_{ODT}(t)$. A fixed and equidistant diagnostic grid for all of the calculations is used here. A C-spline interpolation is used to interpolate the solutions from the adaptive ODT grid to the diagnostic grid.

2. Next, a spatially filtered velocity is defined as $\widehat{u}(t)$ which is within the range $y_l^+(t) < y^+(t) < y_h^+(t)$. This represents the characteristic velocity of the uniform anisotropy range,

$$\widehat{u}(t) = \frac{1}{Y_{ODT}} \sum_{j-j_l=\alpha=0}^{N_j-1} u_\alpha(y, t) \Delta y_\alpha. \quad (\text{E.3})$$

Note that it is possible to obtain an ensemble average across N realizations of this quantity, which is symbolized as $\overline{\widehat{u}}(t)$.

3. The fluctuating velocity field is calculated as $u'(y, t) = u(y, t) - \widehat{u}(t)$ for each realization.
4. To obtain the cross power spectral density the product of the filtered Fourier transform and its complex conjugate from the fluctuating velocity field is estimated [137, 124] which is equal to the Fourier transform of the convolution, large ‘*’, of the windowed fluctuating velocity field with itself,

$$\widehat{S}(\widehat{k}, t) = \mathcal{F}\{Wu'\} \mathcal{F}^*\{Wu'\} = \mathcal{F}\{(Wu') * (Wu')^*\}. \quad (\text{E.4})$$

The superscript ‘*’ represents the complex conjugate and W is the Hanning window (full cosine taper) as in [137, 124]. Now, averaging over realizations would result in Eq. (E.1). In order to find $\widehat{S}(\widehat{k}, t)$, we first calculate the autocorrelation of the windowed fluctuating velocity field. Then the ensemble average of the autocorrelation is estimated and then the Fourier transform of the result is obtained.

5. The discrete Fourier transform of an N_j point record is calculated as,

$$\mathcal{F}_m\{\cdot\} = \sum_{j-j_l=\alpha=0}^{N_j-1} (\cdot)_\alpha e^{-\frac{2\pi i \alpha m}{N_j}} \quad m = 0, \dots, N_j - 1 \quad (\text{E.5})$$

6. Here, the largest wavenumber is $k = |\widehat{k}| = 2/\Delta y = 2N_j/\delta_{99}$, being $\Delta y/2$ the smallest length-scale according to the Nyquist-Shannon sampling theorem. $2/\delta_{99}$ is thus the smallest wavenumber. Using the discrete notation in general, $k_m = 2(m+1)/\delta_{99}$.
7. As $\overline{\widehat{S}}(\widehat{k}, t) = \overline{\widehat{S}}^*(-\widehat{k}, t)$, the one-sided (real) energy spectra are calculated as $\overline{S}(k, t) = 2 \left| \Re\{\overline{\widehat{S}}(\widehat{k}, t)\} \right|$.
8. A constant c is calculated, such that $\overline{\Phi}(k, t) = c\overline{S}(k, t)$ for the final normalization of the ensemble-averaged spectra. Here Φ is the turbulence kinetic energy spectral density with units m^3/s^2 . The constant c satisfies the condition $\overline{u'u'}(Re_\theta, y^+) = \int_{-\infty}^{\infty} \overline{S}(k, t) dk$ [137, 124, 50]. Using

our definition of k , $dk = (2/\delta_{99})dm$, i.e., for the discrete version, the integral becomes a sum and we formally replace dm by $\Delta m = 1$, thus,

$$c = \frac{\overline{u'u'}(Re_\theta, y^+)}{\frac{2}{\delta_{99}} \sum_{m=0}^{N_j-1} \overline{S_m}(k_m, t)}. \quad (\text{E.6})$$

9. $\overline{\Phi}(k, t)$ is normalized in the friction units with the friction velocity u_τ and the Kolmogorov length-scale $\eta = \nu/u_\tau$. The wavenumber k is normalized by the inverse of the Kolmogorov length-scale $1/\eta$ ($k^+ = \eta/\Delta y^+$).

E.2 Generation of Position-Dependent Energy Spectra

The Taylor's hypothesis is used for the calculation of the position-dependent energy spectra and the procedure in the ODT model is analogous to that shown in [124]. The cross power spectral density or co-spectrum is defined as,

$$\overline{S}(k_x, y) \equiv \frac{\widehat{u}(y)}{2\pi} \int_{-\infty}^{\infty} e^{-i k_x \widehat{u}(y) \tau} R(y, \tau) d\tau. \quad (\text{E.7})$$

Above $R(y, \tau)$ is the fluctuating velocity autocorrelation defined as,

$$R(y, \tau) = \overline{u'(y, t)u'^*(y, t + \tau)}. \quad (\text{E.8})$$

1. Firstly, the wall-normal position corresponding to the desired y^+ is calculated where the energy spectrum is needed. This step is done for every realization, considering the instantaneous velocity profile. An equidistant time grid is used for all of the calculations discussed here.
2. A time-filtered velocity, $\widehat{u}(y)$ is defined as,

$$\widehat{u}(y) = \frac{1}{T} \sum_{\alpha=0}^{N_t-1} u_\alpha(y, t) \Delta t_\alpha. \quad (\text{E.9})$$

N_t represents the number of time intervals sampled in T , with T as an averaging time interval that starts at the smallest Re_θ value after which all velocity profiles are independent of Re_b (fully turbulent regime) and ends at the predefined input t_{end} for every simulation. Similar to the time-dependent spectrum, it is possible to obtain an ensemble average across N realizations $\overline{\widehat{u}}(y)$,

$$\overline{\widehat{u}}(y) = \frac{1}{N} \sum_{n=1}^N \widehat{u}(y). \quad (\text{E.10})$$

3. The fluctuating velocity field is calculated as $u'(y, t) = u(y, t) - \widehat{u}(y)$ for each realization.

4. The calculation are similar as in the time-dependent spectrum and the Fourier transform is defined analogous to Eq. (E.5). The cross power spectral density is acquired as in Eq. (E.4), with the additional multiplication factor $\widehat{u}(y)/(2\pi)$ as specified by Eq. (E.7).

5. The largest wavenumber [124] is equivalent to

$$k_x(y) = |\widehat{k}_x(y)| = 2 \left[2\pi / \left(\Delta t \widehat{u}(y) \right) \right] = 4\pi N_t / (T \widehat{u}(y)) \quad (\text{E.11})$$

and the smallest wavenumber is

$$4\pi / (T \widehat{u}(y)) \quad (\text{E.12})$$

In general, $k_{x,m}(y) = 4\pi (m + 1) / (T \widehat{u}(y))$.

6. The calculation for $\overline{S}(k_x, y)$ is analogous to the previous case of the time-dependent spectra described above. Finally, the constant c is calculated for the final normalization such that $\overline{\Phi}(k_x, y) = c \overline{S}(k_x, y)$. Here Φ is the turbulence kinetic energy spectral density with units m^3/s^2 . Similar to the time-dependent spectra, c satisfies the same condition as $\overline{u'u'}(Re_\theta, y^+) = \int_{-\infty}^{\infty} \overline{S}(k_x, t) dk_x$. The selected Re_θ used for the scaling with $\overline{u'u'}(Re_\theta, y^+)$ as well as the u_τ and δ_{99} normalization is that corresponding to the beginning of the sampling time interval.

Appendix F

TBL Results for High Bulk Reynolds Number

In the following, the ODT simulation results for high bulk Reynolds numbers, i.e., $Re_b = 2500$ and 5000 are presented. The reference DNS data is not available for these bulk Reynolds numbers and hence, only ODT results are discussed. The various statistics are discussed for the given Re_b at two Re_θ , $Re_\theta \sim 5045$ and 9075 ($\sim 10^4$). For these simulations the domain size is increased to capture boundary effects onto the flow. The optimal set of physical model parameters is taken from the validated TBL flow configuration discussed earlier. Most of the numerical model parameters are adapted according to the given Reynolds numbers and the initial condition remains unaltered for these simulations. The aim to carry out these simulation is to check the behaviour of various ODT profiles for large Reynolds numbers. In general, nothing ambiguous is observed from the results shown below and the qualitative trends for these simulations are consistent with the previous simulations.

First, the velocity statistics up to 4th order is presented for both Re_b at two Re_θ . This discussion includes the mean streamwise velocity, indicator function, rms velocity, the Reynolds stresses, production, skewness and flatness of the streamwise velocity component, all as a function of wall-normal coordinate. Next, isotropy indicator variation with wall-normal coordinate is presented. At last, some of the global properties of the boundary layer, varied with Re_θ as well as time and constant coefficient C_1 and C_2 are shown.

Figure F.1 displays the mean streamwise velocity profile as a function of the wall-normal coordinate at (A) $Re_\theta \sim 5045$ and (B) $Re_\theta \sim 9075$ for $Re_b = 2500$ and 5000 . The profiles for the lower Re_θ do not collapse onto each other only in the outer-log region as shown in Figure F.1 (A). This indicates that the transitions to turbulence are captured up to high Re_θ for high Re_b . Whereas, the higher Re_θ , i.e., $Re_\theta \sim 9075$ shows fully turbulent state and the profiles for both Re_b collapse on top of each other. Similar to the other TBL cases investigated, the influence of the initial conditions on the velocity profile is depicted in Figure F.1 (A) particularly in the outer log-region. The qualitative trend is consistent but quantitative trend can not be measured due to unavailability of reference data.

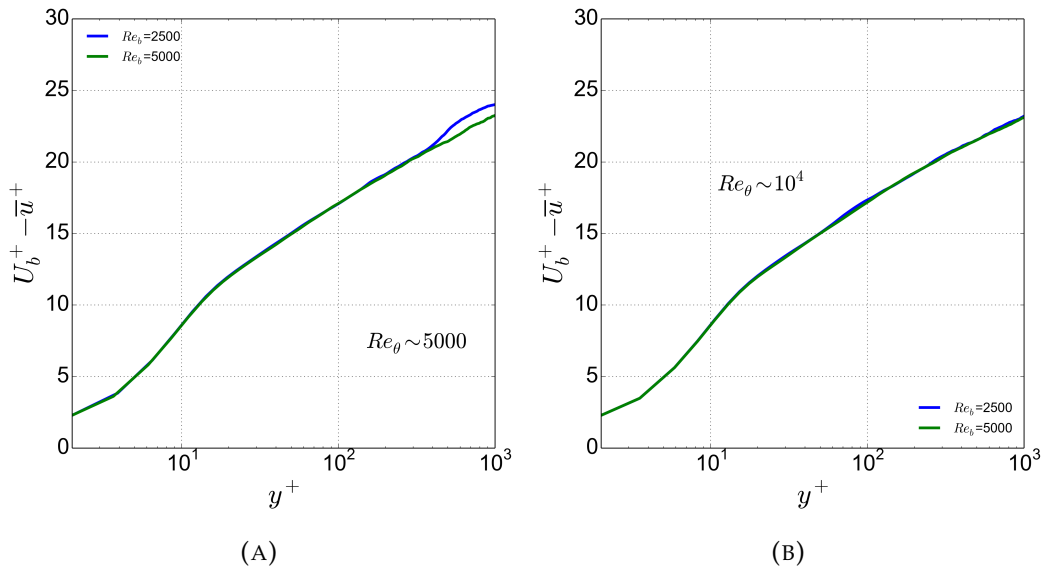


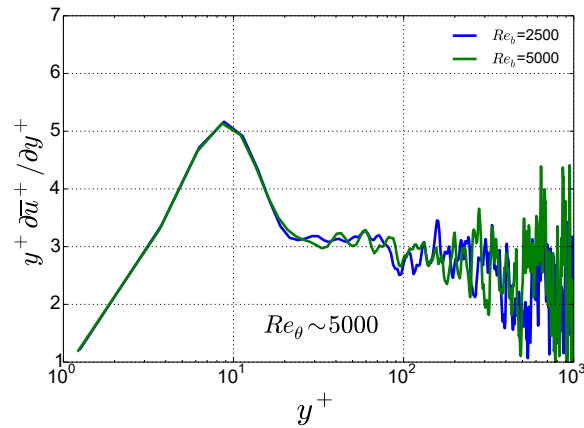
FIGURE F.1: Mean streamwise velocity profile as a function of the wall-normal coordinate (in viscous units) at (A) $Re_\theta \sim 5045$ and (B) $Re_\theta \sim 9075$ for $Re_b = 2500$ and 5000 .

The indicator function, $y^+ (\partial \bar{u}^+ / \partial y^+)$, as a function of wall-normal coordinate in viscous units is presented in Figure F.2 at (A) $Re_\theta \sim 5045$ and (B) $Re_\theta \sim 9075$ for two bulk Reynolds numbers. The curves are dependent on Re_b for both Re_θ as shown in Figure F.2 (A) and (B). A large noise component further away from the wall can be improved by using very large ensemble sizes to achieve the statistical convergence. This would not change the results. Note that for these higher Re_b , there is formation of the logarithmic region.

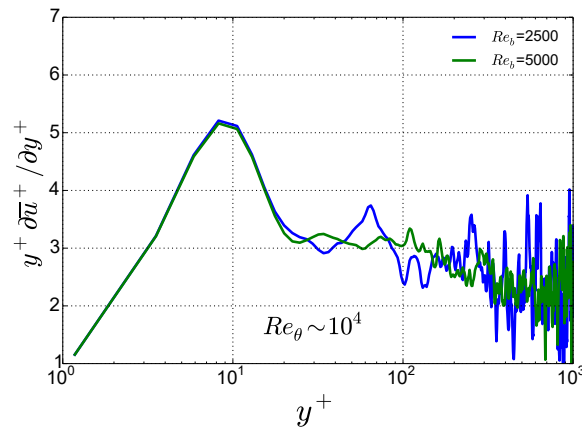
The root mean square (rms) of the normalized streamwise velocity component ($u_{rms}^+ = \sqrt{u'^2} / u_\tau$) as a function of the normalized wall-normal coordinate in viscous units is shown in Figures F.3 at (A) $Re_\theta \sim 5045$ and (B) $Re_\theta \sim 9075$ for two Re_b . To obtain the statistical convergence for rms very large ensemble sizes can be used however, it would not change the results. The qualitative trend is consistent with other rms profiles presented above. The weak double peak discerned in the vicinity of the wall for low Re_b presented earlier, is not developed for the cases considered here. However, this peak is expected for large ensemble sizes because some small traces of the peak can already be seen in Figures F.3 (A) and (B). Note that the additional peak in the outer-log region is also not captured for these cases. Rest of the features remain same as explained before and we do not discuss them here.

The normalized cross stresses as a function of the wall-normal coordinate in viscous units, $(\overline{u'v'} / u_\tau^2)$ at (A) $Re_\theta \sim 5045$ and (B) $Re_\theta \sim 9075$ are shown in Figures F.4 for $Re_b = 2500$ and 5000 . The profiles for higher Re_b , i.e., $Re_b = 5000$ at $Re_\theta \sim 5045$ (Figures F.4 (A)) are still in transition to turbulence and these profiles collapse at $Re_\theta \sim 9075$ (Figures F.4 (B)) for both Re_b .

The turbulent production as a function of the wall-normal coordinate in viscous units in the flow is shown in Figure F.5 at (A) $Re_\theta \sim 5045$ and (B) $Re_\theta \sim$



(A)



(B)

FIGURE F.2: Indicator function versus wall-normal coordinate (in viscous units) at (A) $Re_\theta \sim 5045$ and (B) $Re_\theta \sim 9075$ for $Re_b = 2500$ and 5000 .

9075 for $Re_b = 2500$ and 5000 . The curves for both Re_b collapse well onto each other for ODT simulations. The collapse is achieved for $Re_\theta \sim 5045$ as well as $Re_\theta \sim 9075$. The production mechanism, similar to other velocity statistics, for higher Reynolds numbers remains consistent with the TBL case for ODT methodology.

Figure F.6 illustrates the skewness of the streamwise velocity component as a function of the wall-normal coordinate y^+ (in viscous units) at (A) $Re_\theta \sim 5045$ and (B) $Re_\theta \sim 9075$ for both Re_b , i.e., $Re_b = 2500$ and 5000 . The ODT results for higher bulk as well as momentum Reynolds numbers are qualitatively consistent with the other lower Reynolds numbers ODT results presented earlier. Note that for $Re_\theta \sim 5045$ (see Figure F.6 (A)), the profiles for considered Re_b collapses with each other in the inner region and some deviations are observed in the outer log-region, whereas, opposite is indicated for $Re_\theta \sim 9075$ shown in Figure F.6 (B). For the higher Re_θ , the skewness profiles for both Re_b show variation in the inner region, $y^+ < 10$.

Next, in Figure F.7 the tendency of the ODT model for high Reynolds

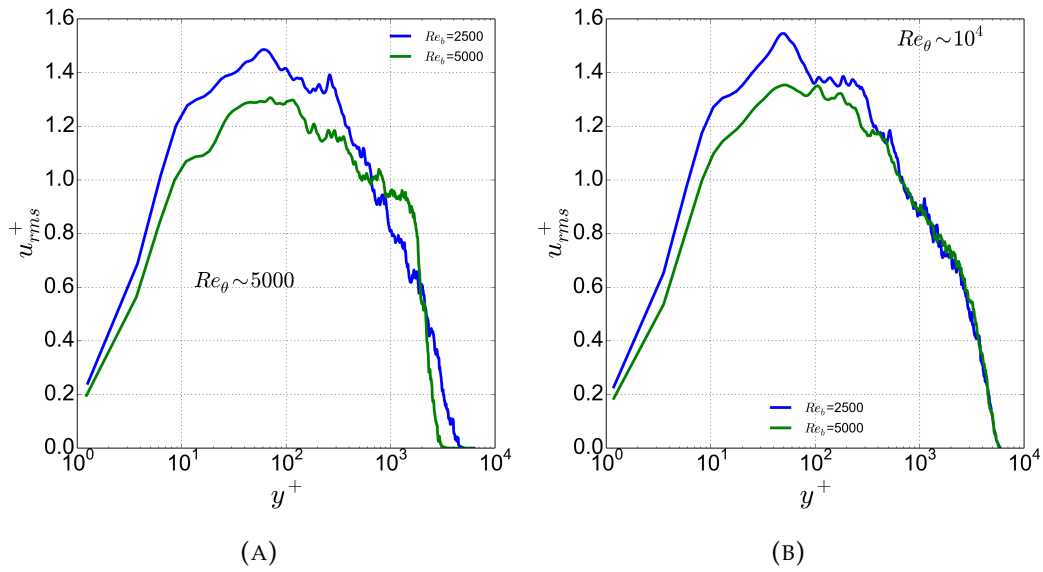


FIGURE F.3: Streamwise root-mean-square velocity profiles at (A) $Re_\theta \sim 5045$ and (B) $Re_\theta \sim 9075$ for $Re_b = 2500$ and 5000 . All quantities are functions of the wall-normal coordinate (in viscous units).

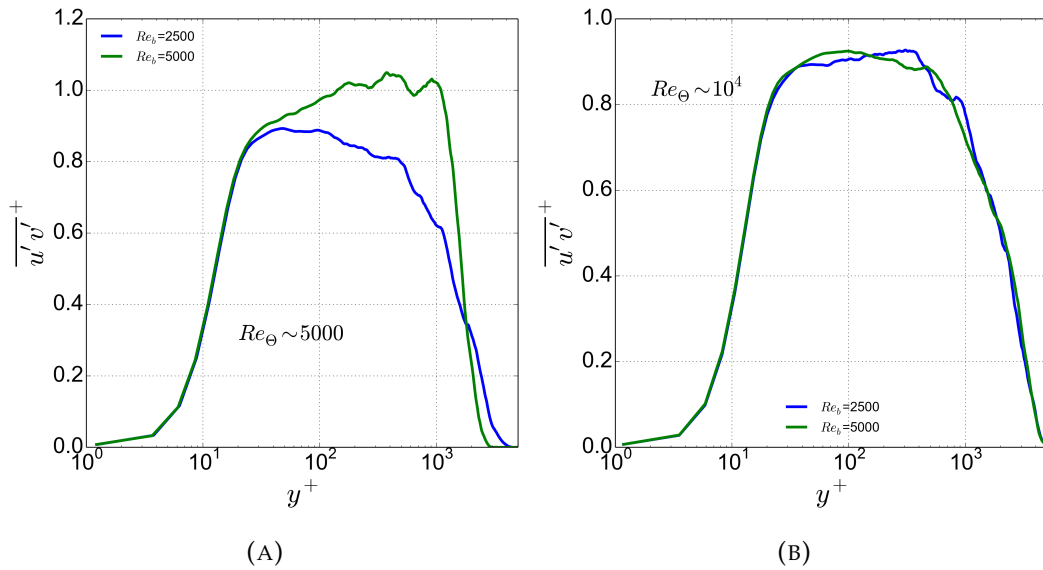


FIGURE F.4: Profiles of the cross stresses at (A) $Re_\theta \sim 5045$ and (B) $Re_\theta \sim 9075$ two bulk Reynolds numbers considered. All quantities are functions of the wall-normal coordinate (in viscous units).

numbers towards the flatness of the streamwise velocity component as a function of the wall-normal coordinate y^+ (in viscous units) is checked at (A) $Re_\theta \sim 5045$ and (B) $Re_\theta \sim 9075$ for both Re_b , i.e., $Re_b = 2500$ and 5000 . A Gaussian flatness value is in range 3 – 3.5 for the considered cases. However, there is no reference data to make further comments on the flatness

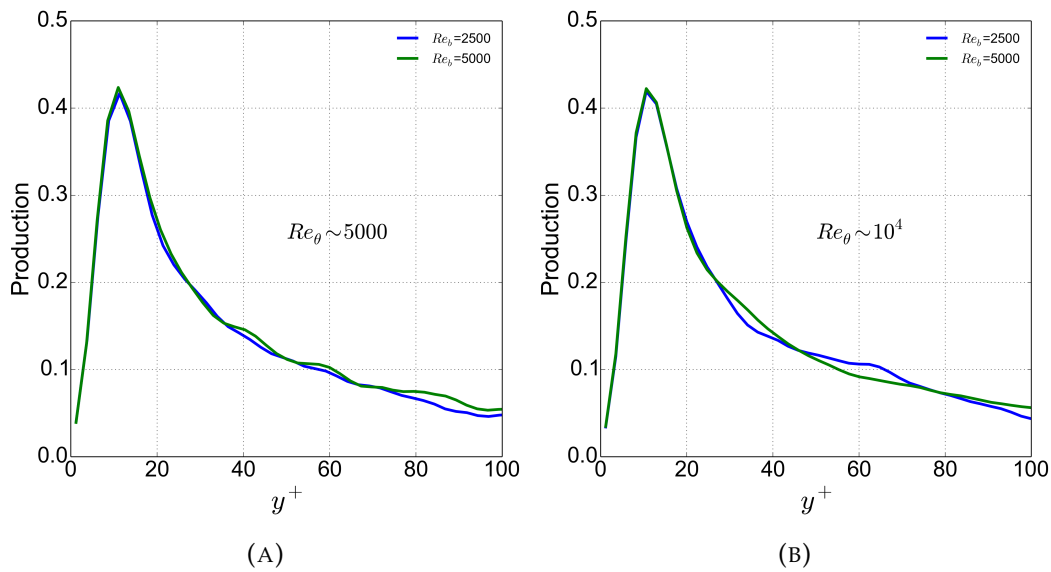


FIGURE F.5: Turbulent kinetic energy production as a function of the wall-normal coordinate (in viscous units) at (A) $Re_\theta \sim 5045$ and (B) $Re_\theta \sim 9075$ for $Re_b = 2500$ and 5000.

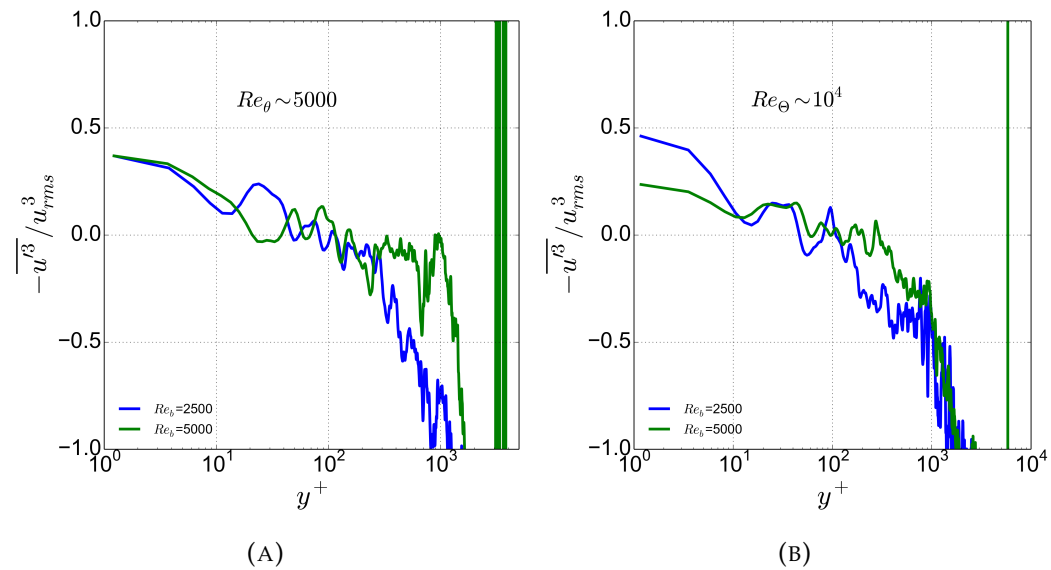


FIGURE F.6: Profiles of the skewness of the streamwise velocity fluctuations as a function of the wall-normal coordinate (in viscous units) at (A) $Re_\theta \sim 5045$ and (B) $Re_\theta \sim 9075$ for $Re_b = 2500$ and 5000.

profiles for ODT simulation. Nevertheless, the qualitative trend seems to be consistent with the well validated case presented for lower Reynolds number for the model.

Isotropy indicator v_{rms}^+ / u_{rms}^+ as a function of the wall-normal coordinate (in viscous units) at (A) $Re_\theta \sim 5045$ and (B) $Re_\theta \sim 9075$ for $Re_b = 2500$ and 5000 is displayed in Figure F.8. For $Re_\theta \sim 5045$, the isotropy indicator is consistent

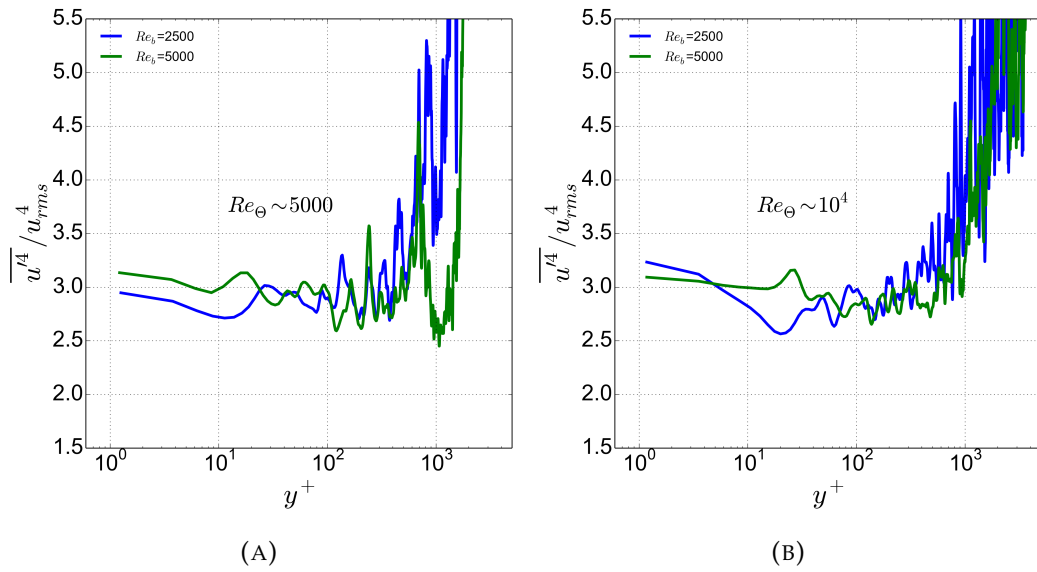


FIGURE F.7: Profiles of the flatness of the streamwise velocity fluctuations as a function of the wall-normal coordinate (in viscous units) at (A) $Re_\theta \sim 5045$ and (B) $Re_\theta \sim 9075$ for $Re_b = 2500$ and 5000 .

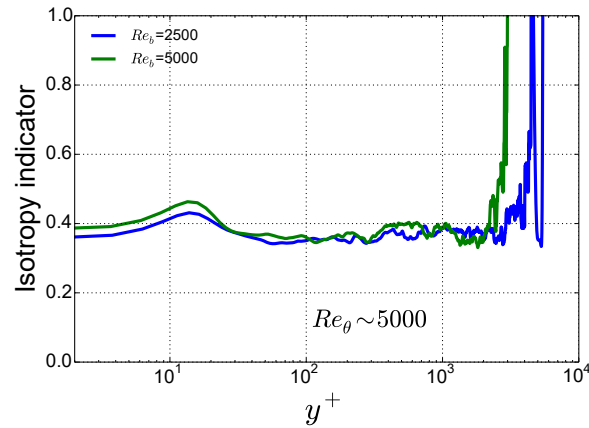
with the TBL validation case of lower Reynolds numbers. For the other case at $Re_\theta \sim 9075$, however, the indicator shows different trend for $Re_b = 2500$ in the outer log-region and the profile do not return towards $Re_b = 5000$ as it follows for $Re_\theta \sim 5045$. Nevertheless, the constant region for the large y^+ range is discerned for both Re_θ investigated.

The ODT structural properties are next shown in Figure F.9 for Re_τ as a function of (A) Re_θ and (B) time for the two bulk Reynolds numbers for $Re_b = 2500$ and 5000 .

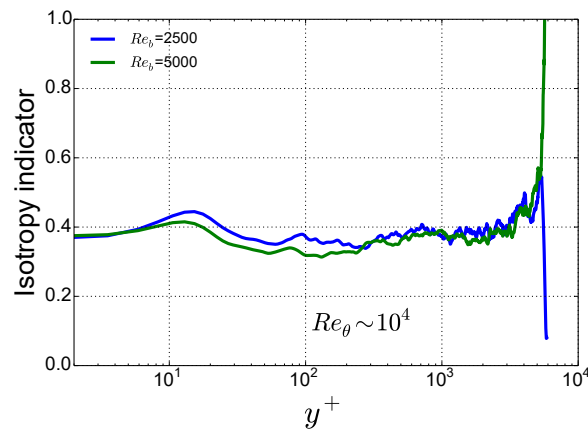
In Figure F.9 (A), Re_τ varied with Re_θ capture some initial transition to turbulence up to $Re_\theta \sim 8000$ and finally after $Re_\theta > 8000$, the profiles are collapsing onto each other. For higher Re_b ($Re_b = 5000$), the Re_τ at very high Re_θ achieves constant values and further seems to decrease. This might be a natural behaviour or it might be restricted due to selected domain size for considered Reynolds number. We have increased domain size for these simulations based on earlier simulations presented as validation for TBL formulation. Since, Re_θ represents instant, a similar behaviour is expected for Re_τ variation with time which is confirmed in Figure F.9 (B).

In Figure F.10 the shape factor H is shown as a function of (A) Re_θ and (B) time for the two bulk Reynolds numbers for $Re_b = 2500$ and 5000 . The H profile for both bulk Reynolds numbers collapse onto each other when varied with Re_θ starting from $Re_\theta \sim 8000$ (see Figure F.10 (A)). However when varied with time as in Figure F.10 (B), it tends to follow different trends for both Re_b . It seems the profiles might diverge for this case and may never collapse with each other. Any further comment for these profiles is beyond the scope of the present work.

The variation of Re_δ with Re_θ is linear after $Re_\theta > 5000$ for both Re_b and



(A)



(B)

FIGURE F.8: Isotropy indicator v_{rms}^+/u_{rms}^+ as a function of the wall-normal coordinate (in viscous units) at (A) $Re_\theta \sim 5045$ and (B) $Re_\theta \sim 9075$ for $Re_b = 2500$ and 5000 .

is shown in Figure F.11 (A). Very high values are achieved for Re_δ . In Figure F.11 (B), Re_δ with time is linear but the trends for both Re_b are different. This indicates that the global properties have this different behaviour with time which can be verified in future.

The Re_X variation with Re_θ in Figure F.12 (A) is consistent with the earlier TBL results discussed for lower Re_b in comparison with the DNS. In Figure F.12 (B), Re_X with time is linear but the profiles for both Re_b are diverging from each other. This figure hints that the domain selection might be proper and do not influence any of the quantity. In that case, decrease of some of the quantities at higher Re_θ or instants might be a general property. However, no clear comments can be made because there is no reference data for comparison.

Figure F.13 displays the variation of skin friction coefficient, C_f with (A) Re_δ , (B) Re_θ and (C) Re_X for both discrete bulk Reynolds numbers, i.e. $Re_b = 2500$ and 5000 . The general trend for skin friction coefficient is consistent with

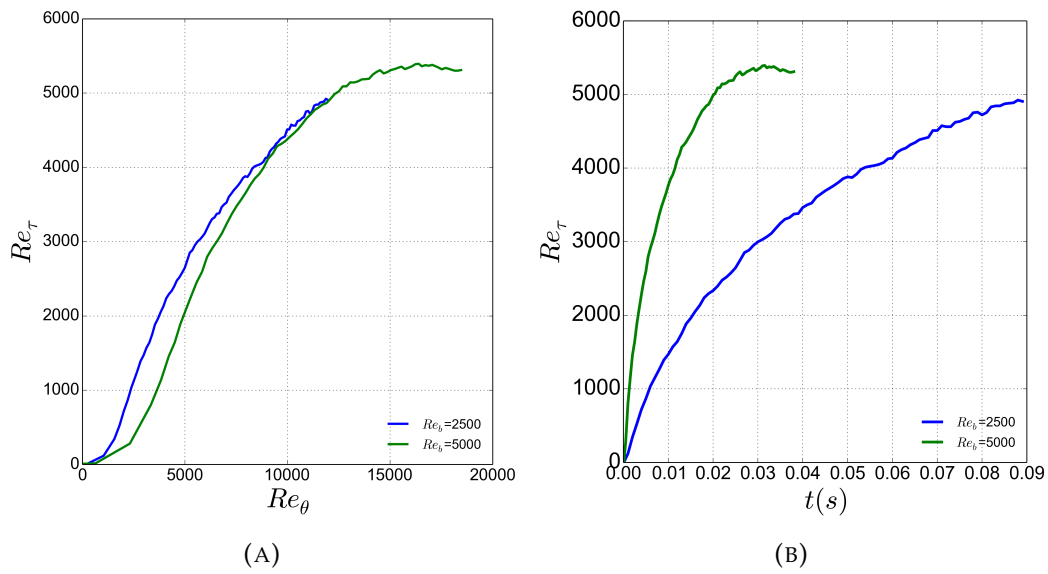


FIGURE F.9: The quantity Re_τ as a function of (A) Re_θ and (B) time for $Re_b = 2500$ and 5000 .

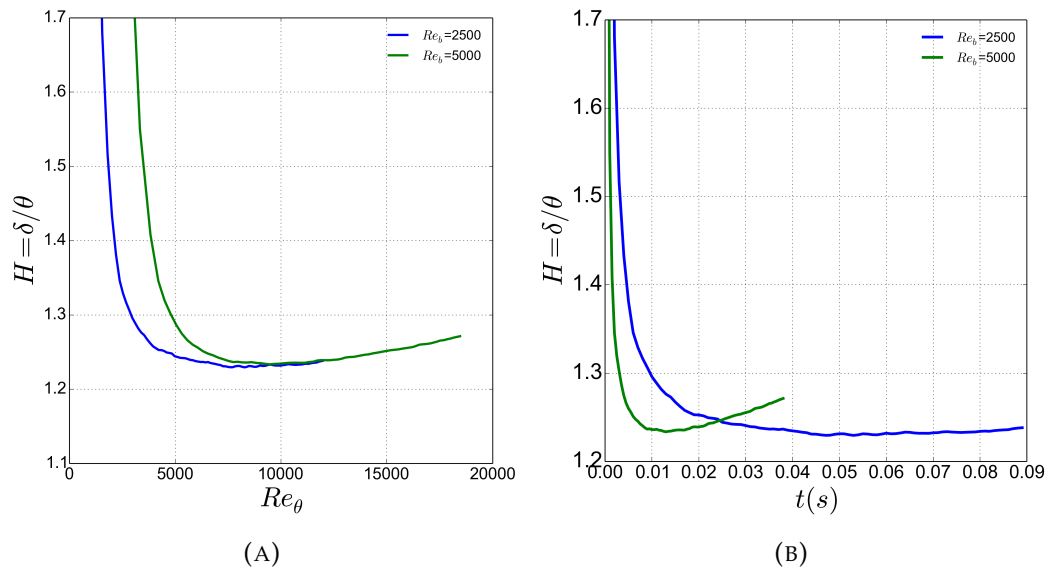


FIGURE F.10: The quantity H as a function of (A) Re_θ and (B) time for $Re_b = 2500$ and 5000 .

the well validated TBL case presented earlier. Figure F.13 (A) and (B) confirms that the value of Re_δ and Re_θ is increased with increasing Re_b (shown with arrow in the figure). Figure F.13 (C) shows that C_f profiles approaches towards each other similar to the other two profiles for both Re_b . This behaviour was different for lower Re_b presented earlier for validation of TBL configuration.

The temporal development (as a function of Re_θ) of the coefficients (A) C_1 and (B) C_2 obtained with ODT for high bulk Reynolds numbers, i.e., $Re_b = 2500$ and 5000 are displayed in Figure F.14. Unlike the universal asymptotic

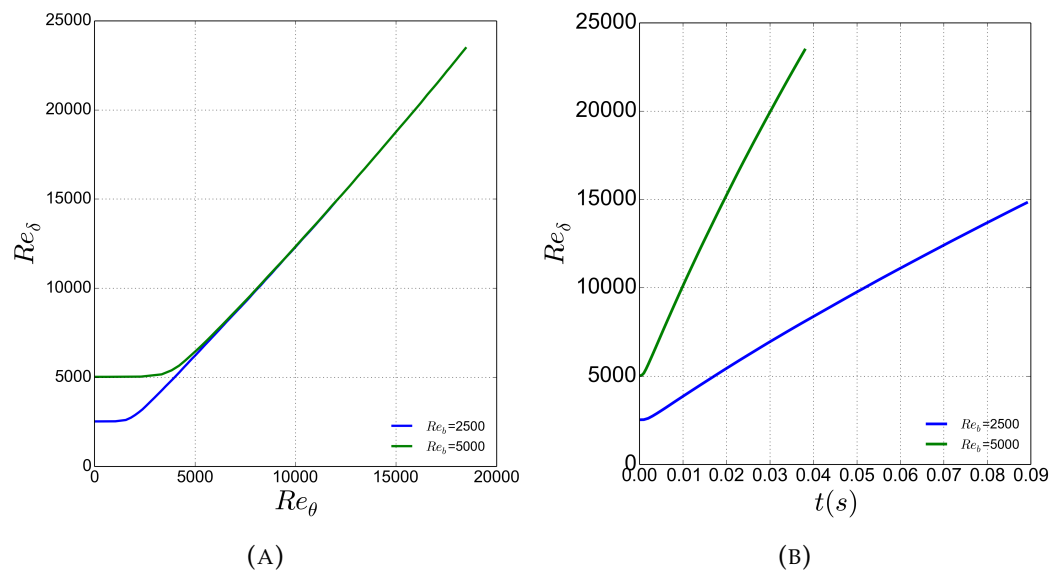


FIGURE F.11: The quantity Re_δ as a function of (A) Re_θ and (B) time for $Re_b = 2500$ and 5000.

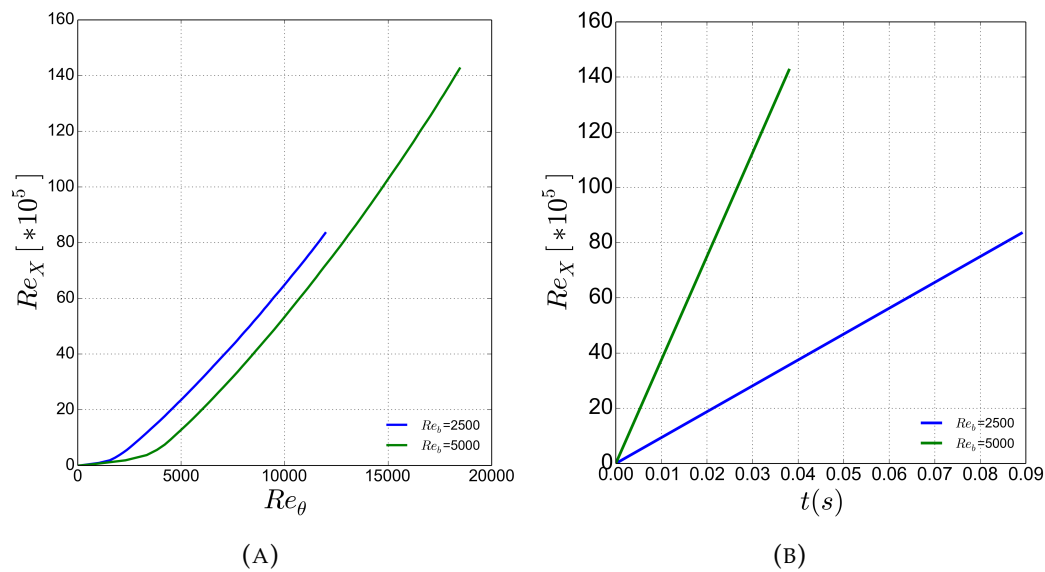
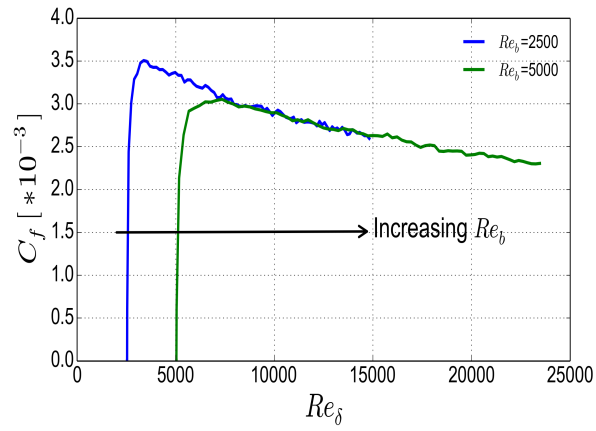
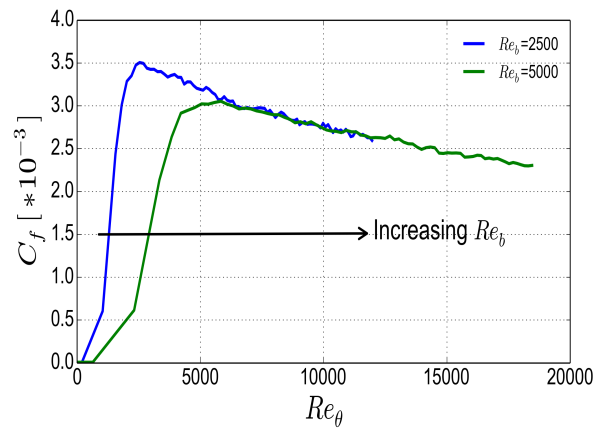


FIGURE F.12: The quantity Re_X as a function of (A) Re_θ and (B) time for $Re_b = 2500$ and 5000.

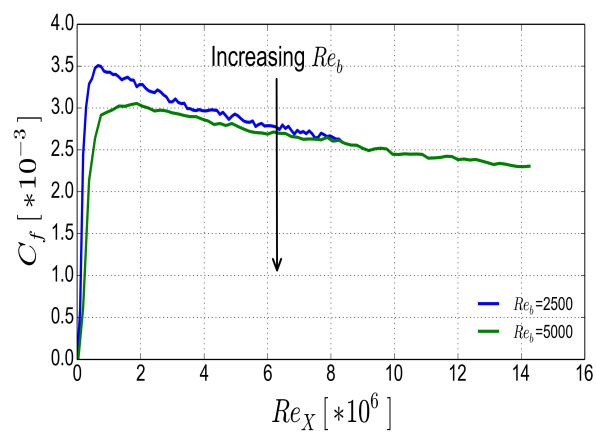
state reached for low Re_b presented before in comparison with the DNS, for the investigated Re_b , these coefficients are decreasing after $Re_\theta = 9000$. Nevertheless, the profiles for both Re_b collapses onto each other for both constants.



(A)

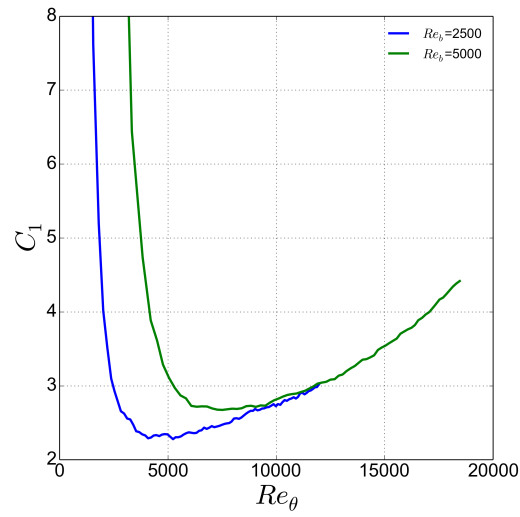


(B)

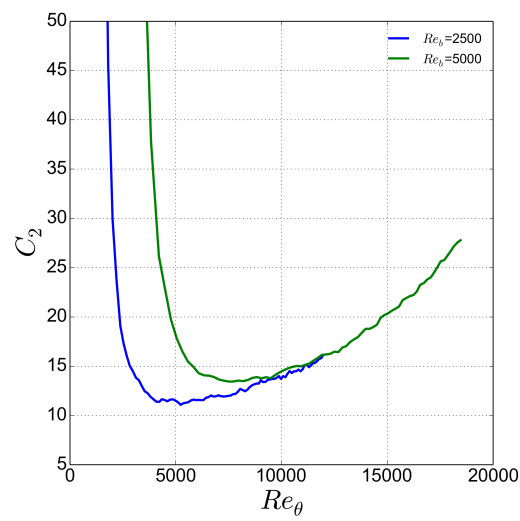


(C)

FIGURE F.13: Skin friction coefficient C_f as a function of (A) Re_δ , (B) Re_θ and (C) Re_X for $Re_b = 2500$ and 5000 .



(A)



(B)

FIGURE F.14: Integral coefficients characterizing the TBL as function of Re_θ , (A) C_1 and (B) C_2 for $Re_b = 2500$ and 5000.

Appendix G

Model Parameter Sensitivity for SBL

This Appendix discusses the sensitivity of the results for SBL configuration to the physical ODT model parameters. The important physical model parameters considered in earlier studies using ODT are α , C , Z and large eddy suppression mechanism. These parameters are explained in detail while finding optimal set of the parameters for TBL configuration and their influence on various velocity statistics and global properties of boundary layer have been presented. For the present, SBL configuration, the influence of the model parameters on all statistics is not considered, instead only the mean streamwise and rms velocity profile are discussed to find optimal set of parameters. This is done by comparing ODT results to the reference DNS [41] at several Re_θ for a fixed bulk velocity ($U_b = 12$ m/s). Note that a suitable C and Z parameter value is selected for SBL configuration. For α , equipartition of energy, i.e., $\alpha = 2/3$ is used and the default large eddy suppression mechanism [89] is applied.

In [98], to avoid tuning the model parameters, the pipe and jet flow are treated with the same set of parameters. However, in a third case, i.e., the reactive jet, the parameter C was increased to get good results in comparison with the experiments. Several other studies suggests that the ODT model parameters are not universal and cannot be taken over directly while these parameters depend on the physics included and the forcing mechanism used. These studies includes wall-bounded flows [28, 84, 87, 126], thermal convection [86], mixing layers [85] and non-reacting and reacting jets [100, 92, 98] among others. The real vortices formation in case of ODT can be different which can slightly change the turbulent properties for the given flow configuration and hence, restrict to take over these values directly from other studies. The parameters, however can be tuned at low or intermediate Reynolds number and the optimal model parameters usually become asymptotically independent of the Reynolds number. This property makes ODT an interesting tool for modeling of high-Reynolds number turbulent flows.

The starting point to fix the model physical parameters in the SBL configuration is the set of model parameters used for an asymptotic suction boundary layer [96] and a TBL [109] which is discussed in Appendix C. These cases are

considered to find parameters as they are close to the present case investigated. The value for α parameter is used as $\alpha = 2/3$ which is consistent with the previous studies and controls the exchange of the turbulent energy between the three velocity components and $\alpha = 2/3$ means equipartition of energy in the velocity components. To calibrate the parameter C or Z , the other model parameters are kept fixed. The numerical parameters used for SBL configurations are given elsewhere (see Chapter 3). The ODT simulations are carried out for $C \in \{3, 6, 9\}$ and $Z \in \{400, 600, 800\}$ and the results are discussed below. In addition, we have one more physical parameter which is used to suppress very large eddies [100, 92, 85, 89, 98], that are physically insignificant, i.e., large eddy suppression mechanism. For the SBL configuration, we take the default mechanism for large eddy suppression from earlier ODT applications.

G.1 Variation of the Model Parameter C

Referring to the TBL study in Appendix C, the C parameter, as expected was found very important. This is because it controls the overall turbulence of the flow or the frequency of the eddy events and sometimes referred as the turbulence intensity parameter. As mentioned earlier, for small C values, less eddies are implemented and the flow behaves like laminar. Opposite is observed for large C values. This exhibit the direct influence on the slope of the velocity. This parameter is optimized by varying the value of C from 3 to 9 for the mean and root mean square (rms) velocity profile at $Re_\theta \approx 2000, 4000$ and 8000 while keeping the $\alpha = 2/3$ and $Z = 600$ fixed. Validating the parameter for a range of Re_θ also confirms that the parameters become asymptotically independent of the Reynolds number.

Figure G.1 depicts the influence of the C parameter on the (A,C) mean streamwise and (B,D) the rms velocity normalised with (A,B) outer (C,D) inner units at $Re_\theta \approx 2000$. The simulations are carried out for $C \in \{3, 6, 9\}$ while keeping the other parameters fixed. The reference DNS data at same Re_θ is shown for selecting the optimal C value.

Figure G.1 (A) confirms the influence of the C parameter on the slope of the normalized velocity profile in the logarithmic region. It also effect the frictional velocity, u_τ . Less eddies are implemented for the small C values which controls the turbulence of the flow and hence the level of turbulence is reduced depicting the laminar behaviour of the velocity profile with decreased u_τ . For large C values, opposite is observed and the turbulence intensity is increased. In the inner region. i.e., $y^+ < 10$, the flow dynamics remain unaffected. Whereas there is a direct influence by the C parameter in the logarithmic region, i.e., $y^+ > 30$. A good match for the mean velocity is achieved between the ODT model and the reference DNS data for $C = 6$ for the present configuration.

The rms velocity for all the C values considered for mean streamwise velocity is depicted in Figure G.1 (B). The rms is underestimated from the buffer until the log region for any value of C investigated. $C = 6$ obtained for the

mean profile is considered for further simulations. Interestingly, the shape of the rms profile remain unaffected with the variation of C . However, the fluctuation magnitude is inversely proportional to C . The case representing less turbulence intensity, i.e., $C = 3$ shows the most rms and vice versa implying less shear and less velocity fluctuations and can be interpreted by a much flatter mean state in the more turbulent case such that turbulence is sustained by much weaker available (shear-extractable) energies.

Figure G.1 (C) shows the streamwise mean velocity, $U_b^- - \bar{u}^- = (U_b - \bar{u})/U_b$ (here $U_b^- = 1$) collapses better for the profiles in the outer log-region, i.e., specially in the range $y^- = y/\delta_{99} > 1$ when normalised by outer units for the SBL configuration. It was observed from TBL case as well that the profiles are most influence by C parameter due to the occurrence of large eddies that control boundary layer growth. Note that a fairly good large- y collapse is obtained for larger C values as $C = 3$ is plausibly an outlier because it corresponds to less developed turbulence.

Figure G.1 (D) shows the rms velocity, $u_{rms}^- = \sqrt{u'^2}/U_b$, scaled to outer units which is similar to TBL configuration and imply that the height variation of the corresponding profiles in Figure G.1 (B) is not only due to the variation of u_τ . Like, mean streamwise velocity profiles, the larger C values show large- y collapse specially in outer log-region whereas $C = 3$ show some deviations even in outer log-region for rms profiles.

Figure G.2 displays the influence of the C parameter on the (A,C) mean streamwise and (B,D) the rms velocity normalised with (A,B) outer (C,D) inner units at $Re_\theta \approx 4000$. The simulations are carried out for the same C range as considered above and other parameters are kept fixed. The reference DNS data at $Re_\theta \approx 4000$ is shown for selecting the optimal C value. The influence of C parameter on mean streamwise velocity profile for $Re_\theta \approx 4000$ re-affirms the direct influence on the slope of the normalised velocity profile in the logarithmic region as shown in Figure G.2 (A). The validation for the given Re_θ also confirms that the parameters become asymptotically independent of the Reynolds number.

The general information for the considered Re_θ remains consistent with the lower Re_θ and the parameter also effect the frictional velocity, u_τ due to implementation of less eddies for the small C values which controls the turbulence of the flow and hence the level of turbulence is reduced depicting the laminar behaviour of the velocity profile with decreased u_τ and opposite for large C values. The flow dynamics still remain unaffected in the inner region. i.e., $y^+ < 10$ and direct influence in the logarithmic region, i.e., $y^+ > 30$. A good match for the streamwise mean velocity between the ODT model and the DNS data [41] for $C = 6$ for the present configuration is achieved.

The rms velocity for all the C values as considered above for the streamwise mean velocity is shown next in Figure G.2 (B) at $Re_\theta \approx 4000$. The rms is still underestimated from the buffer until the log region, however, quantitative trend remains consistent with the trend for $Re_\theta \approx 2000$ as well as DNS. Moreover, quantitative measurement for $Re_\theta \approx 4000$ seems more close to DNS as compared to $Re_\theta \approx 2000$ case explained above and the fluctuation magnitude is inversely proportional to C . $C = 3$ shows amplitude of the peak more close

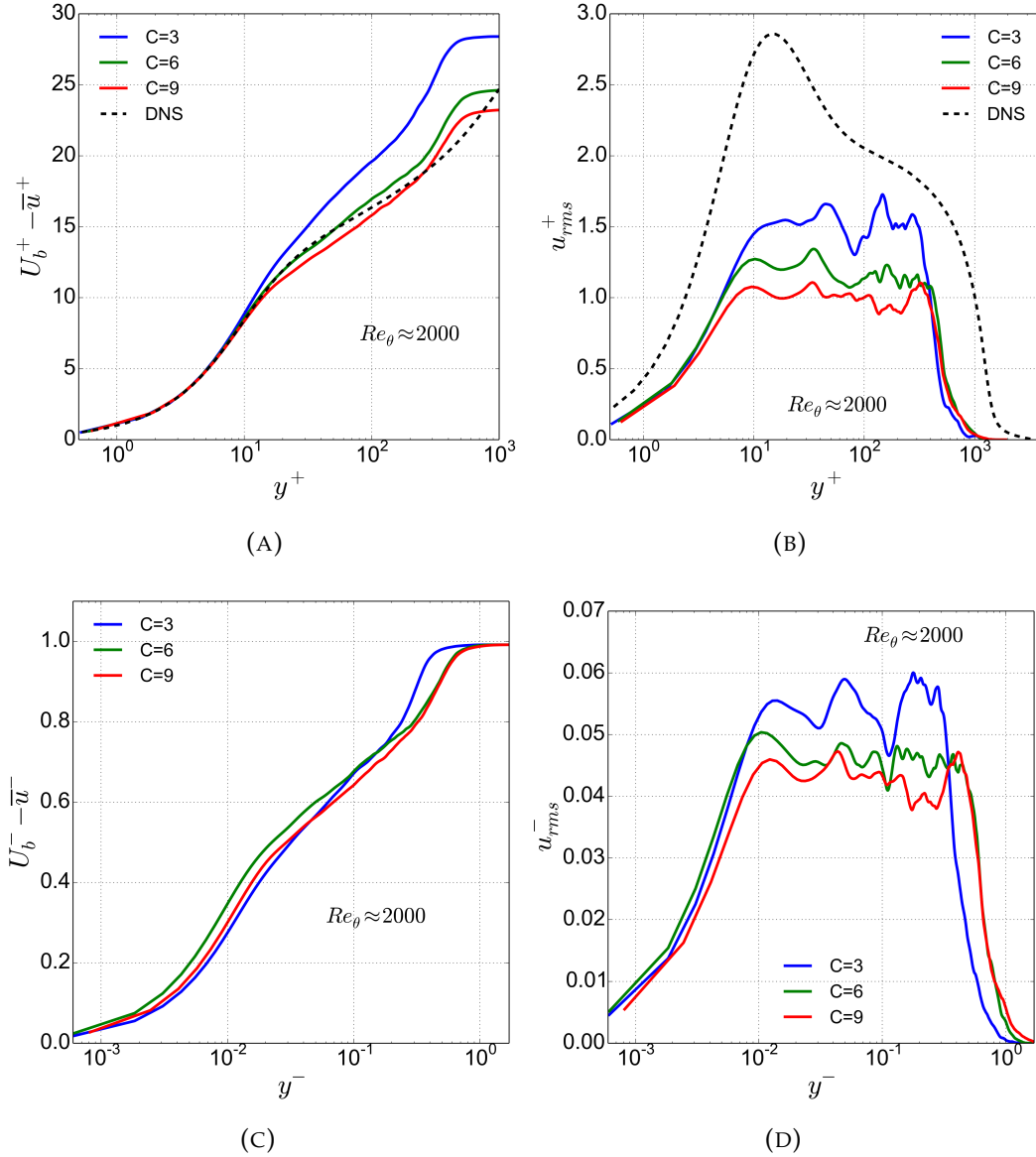


FIGURE G.1: Normalized wall-normal profiles of the (A) mean streamwise velocity and (B) corresponding rms velocity for various values of the model parameter C . ODT results are shown in comparison to the reference DNS [41] at $Re_\theta \approx 2000$. The model parameters $\alpha = 2/3$ and $Z = 600$ are fixed. (C, D) Same data as in (A, B) but normalized with the outer velocity, U_b , and length scale, δ_{99} . The superscripts '+' and '-' indicate normalization with inner and outer units, respectively.

to the DNS data, however, the same C shows that the mean velocity profile is tending towards the laminar flow due to implementation of less number of eddies. Hence, $C = 6$ obtained for the mean profile is considered for the simulations of SBL configurations.

Figure G.2 (C) shows the streamwise mean velocity at $Re_\theta \approx 4000$ normalised with the outer units. The profiles collapse better in the outer log-region, i.e., specially in the range $y^- = y/\delta_{99} > 1$ with a fairly good large- y collapse achieved for larger C values and $C = 3$ is an outlier as it corresponds to less developed turbulence. Figure G.2 (D) shows the rms velocity scaled to outer units at $Re_\theta \approx 4000$. The rms velocity profiles are consistent with $Re_\theta \approx 2000$ and general trend and deviations remain same.

Figure G.3 displays the influence of the C parameter on (A) the mean streamwise and (B) the rms velocity normalised with wall-normal coordinate in viscous units at $Re_\theta \approx 8000$. The profiles are not shown normalised with the outer units as the general trends remain same. The simulations are carried out for the same C range as done for other two Re_θ . The LES data at $Re_\theta \approx 8000$ is also shown in the figure for reference. The influence of C parameter on mean streamwise velocity profile for the considered Re_θ also remains same and show influence on the slope of the normalised velocity profile in the logarithmic region as shown in Figure G.3 (A) and remains consistent with the lower Re_θ . A good match is obtained for the streamwise mean velocity between the ODT model and the LES data [82] for $C = 6$.

The rms velocity for all the C values is shown in Figure G.3 (B) at $Re_\theta \approx 8000$. The profiles are normalised with the wall-normal coordinate in viscous units. The profiles remain consistent with the lower Re_θ , however some missing part is noted in outer log region at $Re_\theta \approx 8000$. This is a restriction imposed due to domain size selected for the simulations. To address this missing profile, different domain sizes are considered and presented in Chapter 5.

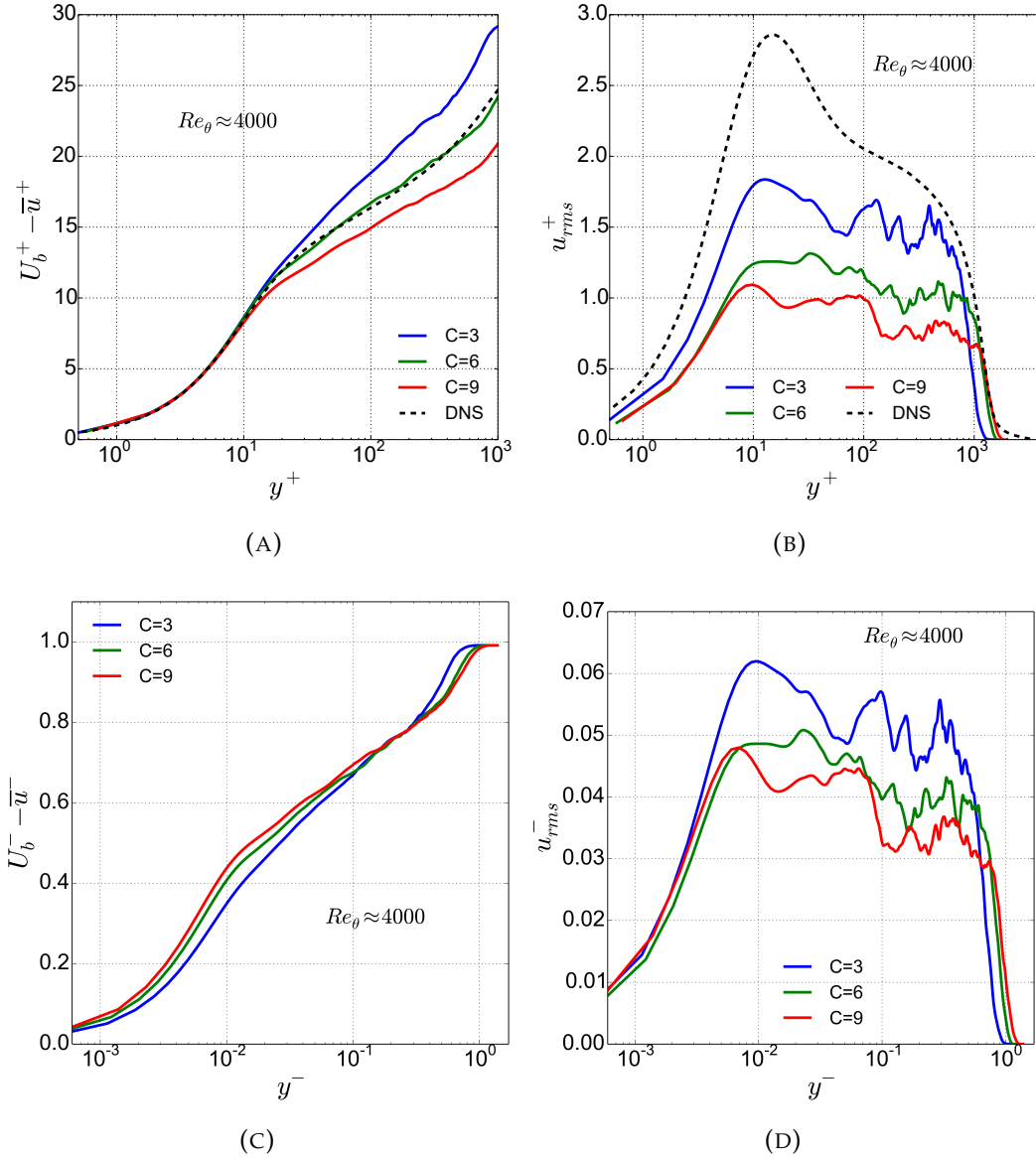


FIGURE G.2: Normalized wall-normal profiles of the (A) mean streamwise velocity and (B) corresponding rms velocity for various values of the model parameter C . ODT results are shown in comparison to the reference DNS [41] at $Re_\theta \approx 4000$. The model parameters $\alpha = 2/3$ and $Z = 600$ are fixed. (C, D) Same data as in (A, B) but normalized with the outer velocity, U_b , and length scale, δ_{99} . The superscripts '+' and '-' indicate normalization with inner and outer units, respectively.

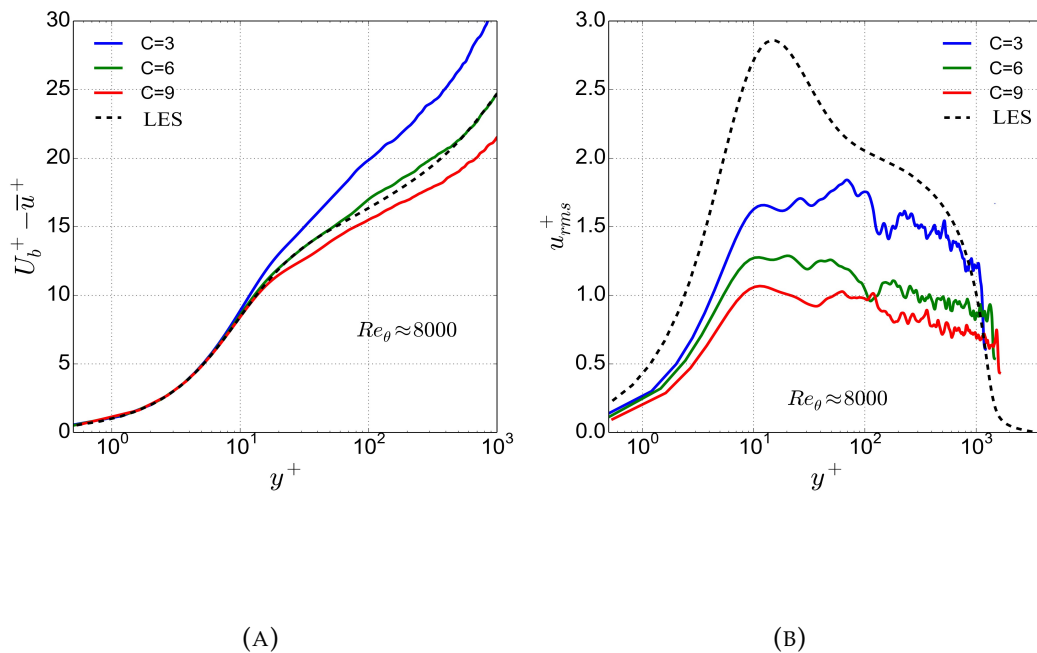


FIGURE G.3: Normalized wall-normal profiles of the (A) mean streamwise velocity and (B) corresponding rms velocity for various values of the model parameter C . ODT results are shown in comparison to the reference LES [82] at $Re_\theta \approx 8000$. The model parameters $\alpha = 2/3$ and $Z = 600$ are fixed.

G.2 Variation of the Model Parameter Z

The next model parameter considered is Z and this parameter increases the efficiency of the algorithm by suppressing the eddy events that are smaller than the Kolmogorov scale ($Z > 1$). The 3D eddies behaves in a different way for the wall bounded flows in the 1D representation of the ODT model. This behaviour is predominant in the buffer layer. Hence this parameter can be used to match the position of the buffer layer in the ODT solutions with the DNS data [84]. The same case investigated above is consider using the optimal parameters ($\alpha = 2/3$ and $C = 6$). The Z value is selected as 550, 600 and 650.

Figure G.4 depicts the influence of the Z parameter on the (A,C) mean streamwise and (B,D) rms velocity normalized with (A,B) inner and (B,D) outer units at $Re_\theta \approx 2000$ in comparison with the DNS data at same Re_θ . All the profiles shows that the mean streamwise and rms velocity are not affected much for any Z value considered for inner as well as outer units. The Z parameter is expected to have less influence on profiles for boundary layer-type flows as compared to the C parameter. The main effect of increasing Z should be an upward shift of the mean velocity profile in the logarithmic region

which is not observed for the SBL configuration. However, to confirm this shift, Z values were selected as 400, 600 and 800 and presented elsewhere. We have selected $Z = 600$ for further investigation and this also agrees with the optimal value used for turbulent channel flow [89].

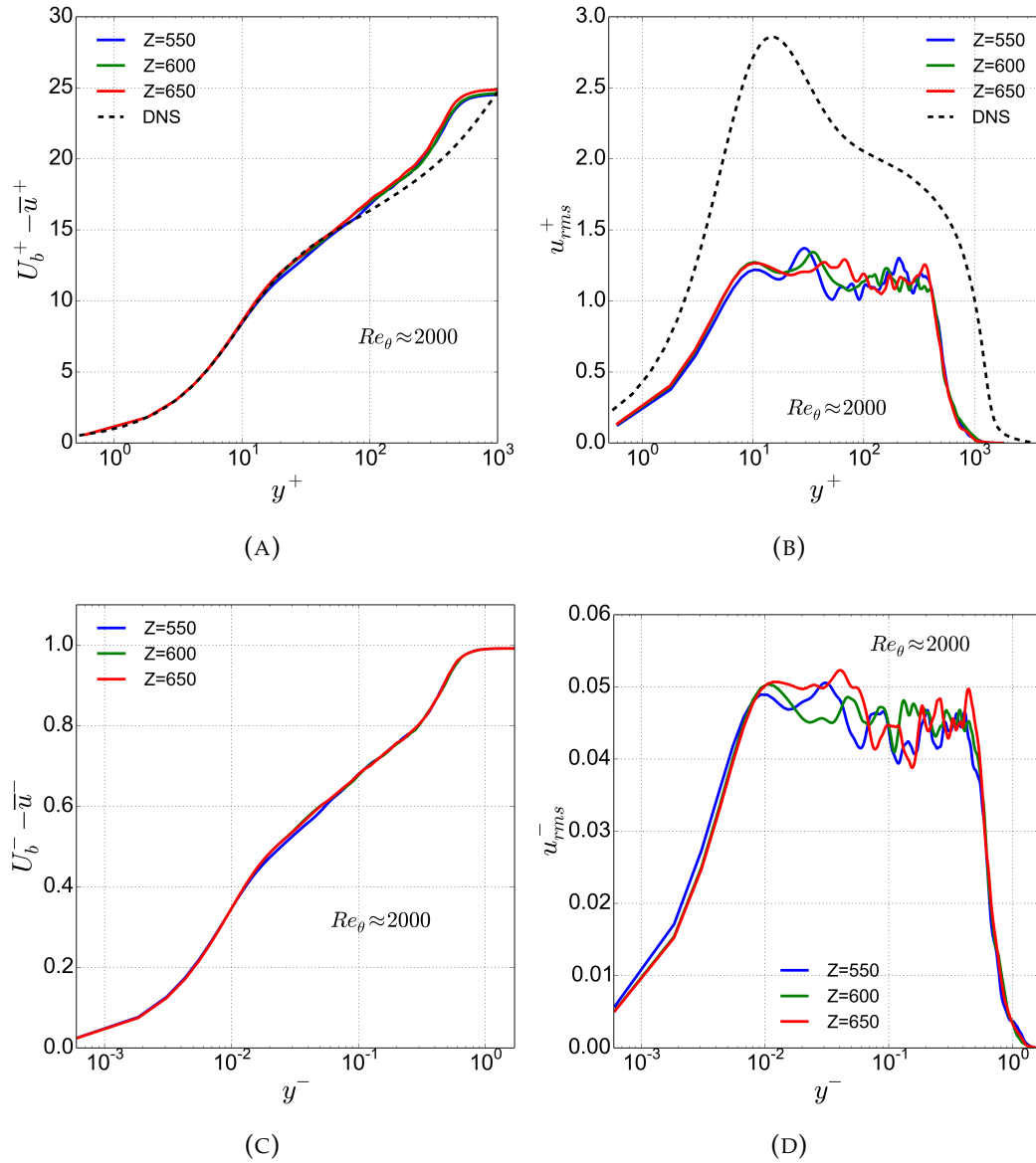


FIGURE G.4: Normalized wall-normal profiles of the (A) mean streamwise velocity and (B) corresponding rms velocity for various values of the model parameter Z . ODT results are shown in comparison to the reference DNS [41] at $Re_\theta \approx 2000$. The model parameters $\alpha = 2/3$ and $C = 6$ are fixed. (C, D) Same data as in (A, B) but normalized with the outer velocity, U_b , and length scale, δ_{99} . The superscripts '+' and '-' indicate normalization with inner and outer units, respectively.

Figure G.5 shows the influence of the Z parameter on the (A,C) mean streamwise and (B,D) the rms velocity normalised with (A,B) outer (C,D) inner

units at $Re_\theta \approx 4000$. The simulations are carried out for all Z values as done for $Re_\theta \approx 2000$ while keeping the other parameters fixed. The reference DNS data at $Re_\theta \approx 4000$ is shown in black dotted line. The profiles of the the mean streamwise and rms velocity remain unaffected for any Z value considered for inner as well as outer units at $Re_\theta \approx 4000$ as well. The general explanation for the profiles at considered Re_θ remains same as discussed above.

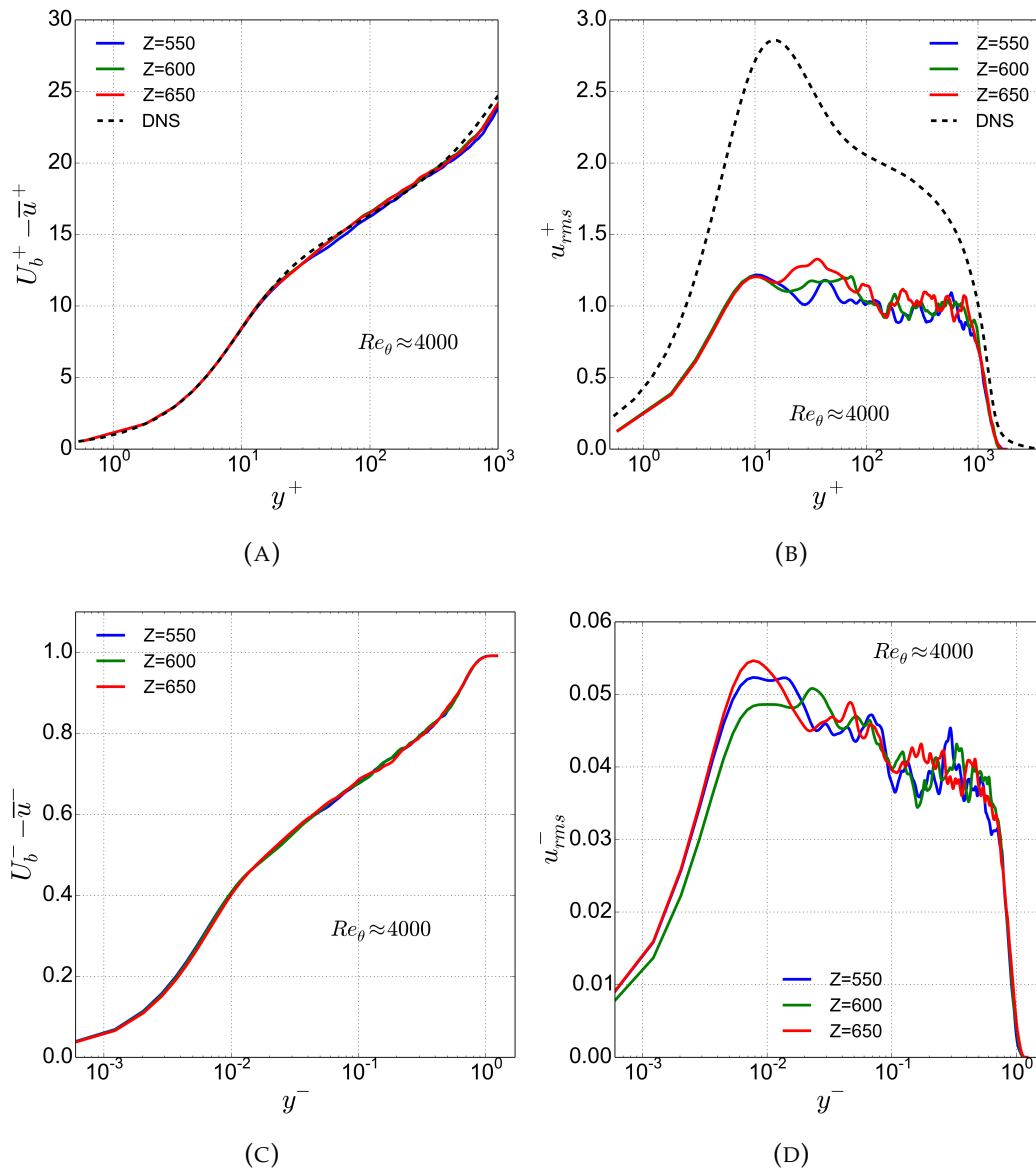


FIGURE G.5: Normalized wall-normal profiles of the (A) mean streamwise velocity and (B) corresponding rms velocity for various values of the model parameter Z . ODT results are shown in comparison to the reference DNS [41] at $Re_\theta \approx 4000$. The model parameters $\alpha = 2/3$ and $C = 6$ are fixed. (C, D) Same data as in (A, B) but normalized with the outer velocity, U_b , and length scale, δ_{99} . The superscripts '+' and '-' indicate normalization with inner and outer units, respectively.

Figure G.6 is shown for (A) the mean streamwise and (B) the rms velocity

normalised with wall-normal coordinate in viscous units at $Re_\theta \approx 8000$ for various Z values considered for the validation. The main purpose to display profiles at this Re_θ is to analyse the influence of variation of parameters at high Re_θ . The LES data at corresponding Re_θ is shown for reference. Similar to the cases explained above, the profiles of the the mean streamwise and rms velocity remain unaffected for this case as well. In general, the profiles at this Re_θ are consistent with the lower Re_θ . Note that in the outer log region at $Re_\theta \approx 8000$ for variation of Z parameter, a similar behaviour is observed which was reported for the C parameter and this point is addressed shortly.

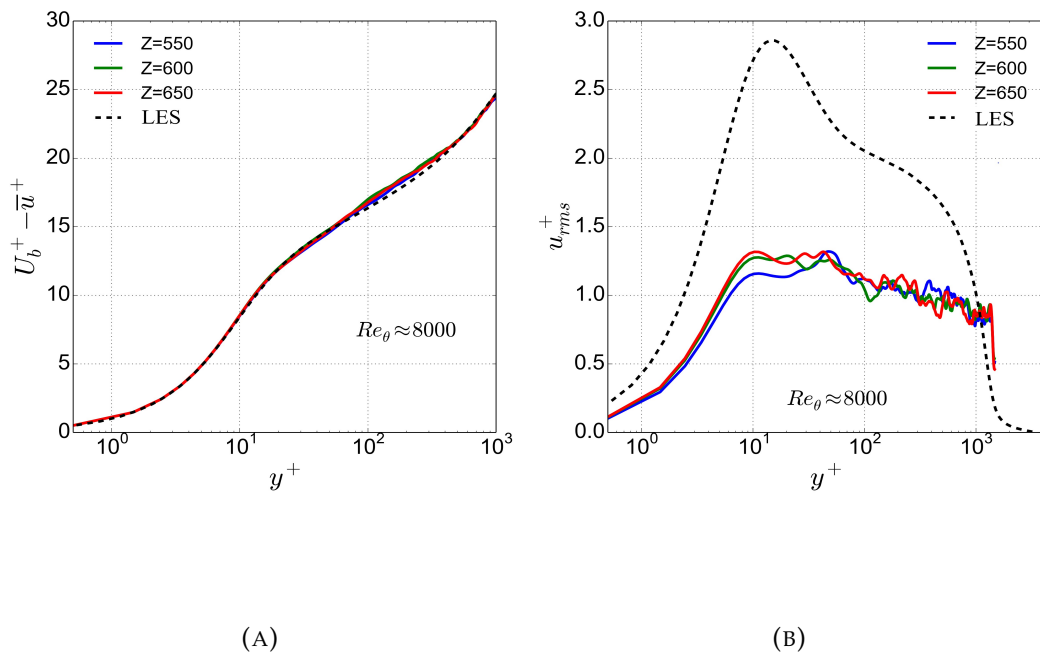


FIGURE G.6: Normalized wall-normal profiles of the (A) mean streamwise velocity and (B) corresponding rms velocity for various values of the model parameter Z . ODT results are shown in comparison to the reference LES [82] at $Re_\theta \approx 8000$. The model parameters $\alpha = 2/3$ and $C = 6$ are fixed.

Appendix H

Model Parameter Sensitivity for Uniform Blowing in SBL

The sensitivity of the results to the physical ODT model parameters (α , C , Z , and the large-eddy suppression) are discussed for each flow configurations. It was noted that these parameters are different for SBL as well as TBL. Hence, it is important to find the optimal set of the physical model parameters for blowing configuration also. For the blowing case, the ODT results are compared to the reference LES [64] at two Re_θ .

Previous studies have also indicated that these parameters cannot be taken over directly. The studies involving wall-bounded flows [28, 84, 87, 126], mixing layers [85], thermal convection [86], and non-reacting and reacting jets [100, 92, 98], shows that the ODT model parameters are not universal. The pipe and jet flow have been treated with the same set of parameters in [98] and in a third reactive jet case, C was increased to get reasonable results compared to experiments. All these studies mentioned above demonstrates that the selection of model parameters is influenced by the physics included and the forcing mechanism used in the flow. Hence, these parameters needs to be tuned for a given flow configuration.

To find the optimal set of parameters for blowing case, the set of model parameters for the asymptotic suction boundary layer [96], TBL [109] and SBL [112] cases are taken as starting point because these studies are close to our present work.

The model parameter α , transfer coefficient, controls the exchange of the turbulent energy between the three velocity components and its value can vary from zero to one and $\alpha = 2/3$ means equipartition of energy in the velocity components. In most of the previous studies the value for α is used as $2/3$ and for the present case also $\alpha = 2/3$ is selected without discussing in detail. However, statistics variation with α parameter is shown below. The other parameters C , Z , and the large-eddy suppression are calibrated against the reference LES case [64] because C and LS suppression method were found very sensitive for boundary layer-types flows shown in previous chapters. The Z parameter was not much sensitive for SBL and TBL configurations but it is found sensitive for blowing case discussed below. While calibrating one particular parameter, all other parameters are kept fixed. The range of

these parameters is very small and the ODT simulations are carried out for $C \in \{5, 6, 7\}$, $Z \in \{50, 100, 150\}$ and ‘thirds’, ‘elapsed time’ and ‘frac domain’ mechanism for large eddy suppression.

The mean velocity profile is considered for selecting the model parameters by comparing to the LES results [64]. However, higher order velocity profiles and variation of global properties with these parameters is also shown below but does not influence the choice of parameters. Note that all the profiles obey the same trend and are consistent with other studies.

H.1 Variation of the Model Parameter C

The C parameter is referred as the turbulent intensity parameter and controls the frequency of the eddy events or the overall turbulence of the flow. The flow behaves like laminar for small C values because less eddies are implemented for small values of C and opposite is observed for large values of C further exhibiting the direct influence on the slope of the velocity. ODT simulations are carried out for $C \in \{5, 6, 7\}$ for the blowing configuration at (A) $Re_\theta \approx 2082$ and (B) $Re_\theta \approx 2395$ discussed below. The other parameters are kept constant for investing considered parameter and optimal value is selected by comparing with the reference LES data [64] at the same Re_θ .

The influence of the C parameter on the mean streamwise velocity scaled with inner units, u_τ and $y_\tau = \nu/u_\tau$ and with outer units u_∞ and δ_{99} are depicted in Figure H.1 and H.2, respectively. The use of inner units are represented by the superscripts ‘+’ and outer units by ‘-’.

Figure H.1 displays the impact of the C parameter on the slope of the normalized velocity profile in the logarithmic region at (A) $Re_\theta \approx 2082$ and (B) $Re_\theta \approx 2395$. The flow dynamics remain unaltered in the inner region, i.e., $y^+ < 20$ and slope is changed in the logarithmic region, i.e., $y^+ > 30$ for both Re_θ considered. The general behaviour of the mean streamwise velocity profile with the C parameter is consistent with the earlier study for SBL and TBL cases and are not discussed again here. A good match is achieved for the mean velocity between the ODT results and reference LES data [64] for $C = 6$. This value is further used to carry out the ODT simulations. The C parameter is found most sensitive to the blowing case which is similar to the boundary layer type flow [109, 112].

Figure H.2 displays the impact of the C parameter on the frictional velocity, u_τ at $Re_\theta \approx 2082$ and this figure also illustrates how much the shape change in Figure H.1 is explained by faster boundary layer growth for larger C . A fairly good large- y collapse is obtained here and the profiles collapse very well for all C values considered in the range $y^- = y/\delta_{99} > 0.1$ suggesting that the large-scale dynamics as well as the growth of the outer layer are comparable in the two respective cases. The streamwise mean velocity is $u_\infty^- = 1$ and the outer units are most sensitive to the C parameter.

Figure H.3 shows the streamwise root-mean-square velocity profiles versus wall-normal coordinate (in viscous units) for various values of the model parameter C at (A) $Re_\theta \approx 2082$ and (B) $Re_\theta \approx 2395$. ODT results are shown

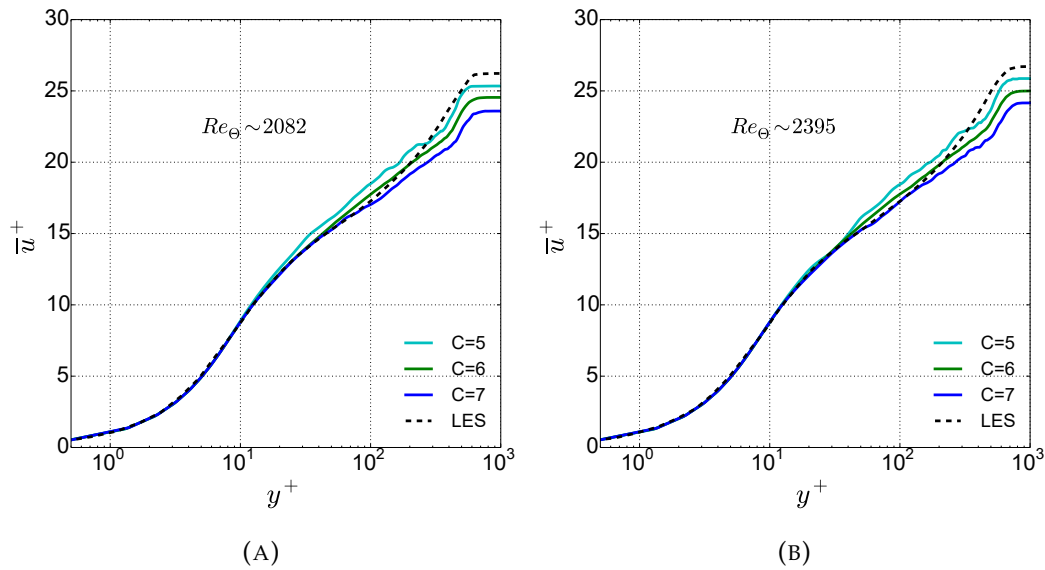


FIGURE H.1: Normalized wall-normal profiles of the mean streamwise velocity \bar{u} for various values of the model parameter C at (A) $Re_\theta \approx 2082$ and (B) $Re_\theta \approx 2395$. ODT results are shown in comparison to a reference LES [64] at corresponding Re_θ . The model parameters $\alpha = 2/3$, $Z = 100$ and the large-eddy suppression are fixed.

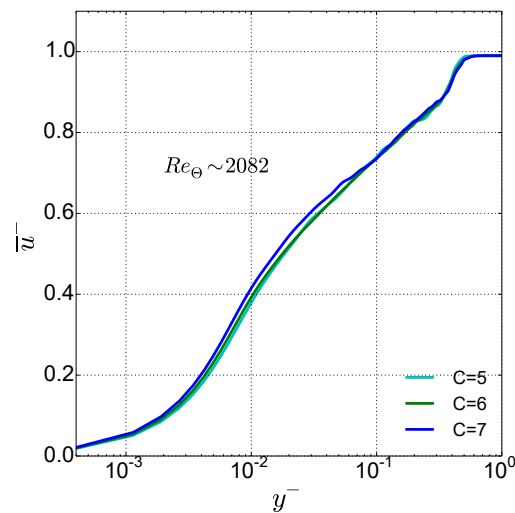


FIGURE H.2: The profiles of the mean streamwise velocity normalized with the outer units for various values of the model parameter C at $Re_\theta \approx 2082$. The model parameters $\alpha = 2/3$, $Z = 100$ and the large-eddy suppression are fixed.

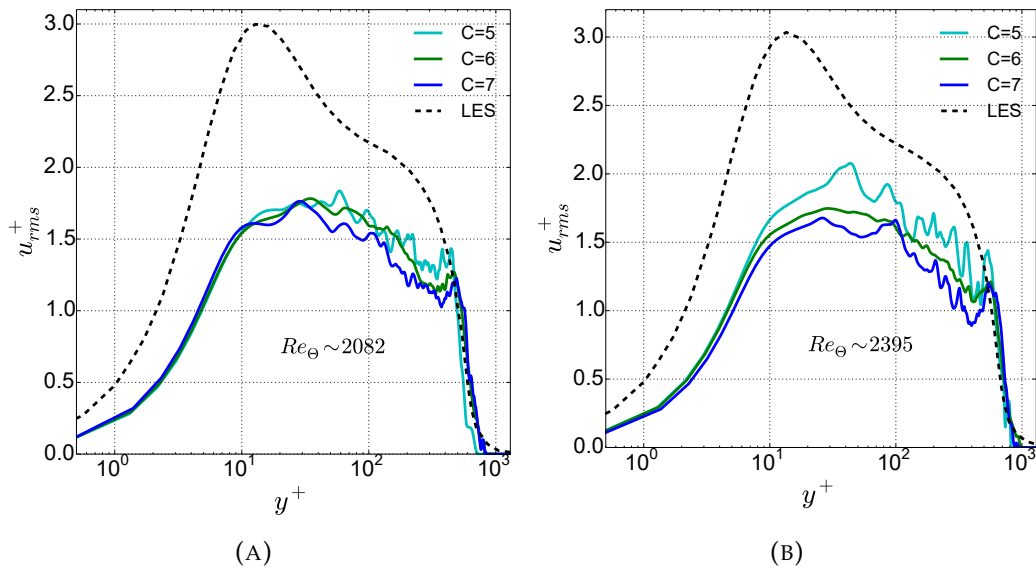


FIGURE H.3: The streamwise root-mean-square velocity profiles versus wall-normal coordinate (in viscous units) for various values of the model parameter C at (A) $Re_\theta \approx 2082$ and (B) $Re_\theta \approx 2395$. ODT results are shown in comparison to a reference LES [64] at corresponding Re_θ . The model parameters $\alpha = 2/3$, $Z = 100$ and the large-eddy suppression are fixed.

in comparison to a reference LES [64] at corresponding Re_θ . The model parameters $\alpha = 2/3$, $Z = 100$ and the large-eddy suppression are fixed. The shape of the rms profiles is the same for all the values of C considered and the overall observations are consistent with the SBL and TBL cases. Hence, the figures are shown only to check if these profiles behaves as expected or if there are some discrepancies. Since these profiles behaves as expected, they are not discussed further,

The H variation with Re_θ is shown in Figure H.4. ODT results are shown in comparison to a reference LES [64]. The model parameters $\alpha = 2/3$, $Z = 100$ and the large-eddy suppression are fixed. The profiles are sensitive towards the C parameter. These profiles are not sensitive towards any other parameters as shown below. Lower C values are more close to the reference results.

Skin friction coefficient C_f as a function of Re_θ for various values of the model parameter C is shown in Figure H.5. ODT results are shown in comparison to a reference LES [64]. The model parameters $\alpha = 2/3$, $Z = 100$ and the large-eddy suppression are fixed. Similar to shape factor, skin friction profile is close to the reference data for lower C values.

H.2 Variation of the Model Parameter Z

The model parameter Z is utilized to suppress the eddy events that are smaller than the Kolmogorov scale by using $Z > 1$ to increase the efficiency of the

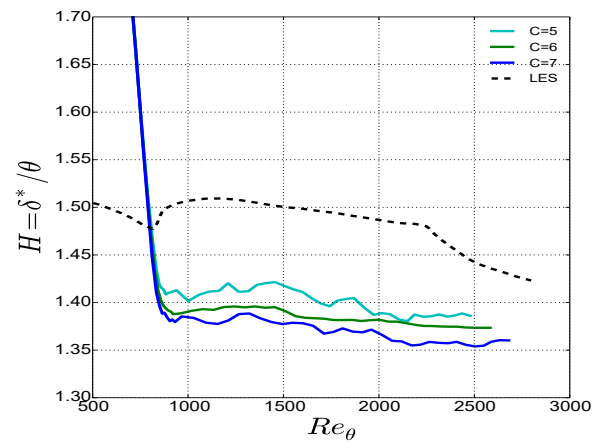


FIGURE H.4: The quantity H as a function of Re_θ for various values of the model parameter C . ODT results are shown in comparison to a reference LES [64]. The model parameters $\alpha = 2/3$, $Z = 100$ and the large-eddy suppression are fixed.

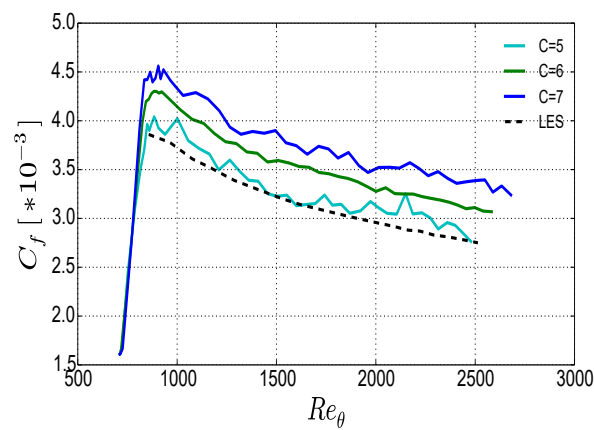


FIGURE H.5: Skin friction coefficient C_f as a function of Re_θ for various values of the model parameter C . ODT results are shown in comparison to a reference LES [64]. The model parameters $\alpha = 2/3$, $Z = 100$ and the large-eddy suppression are fixed.

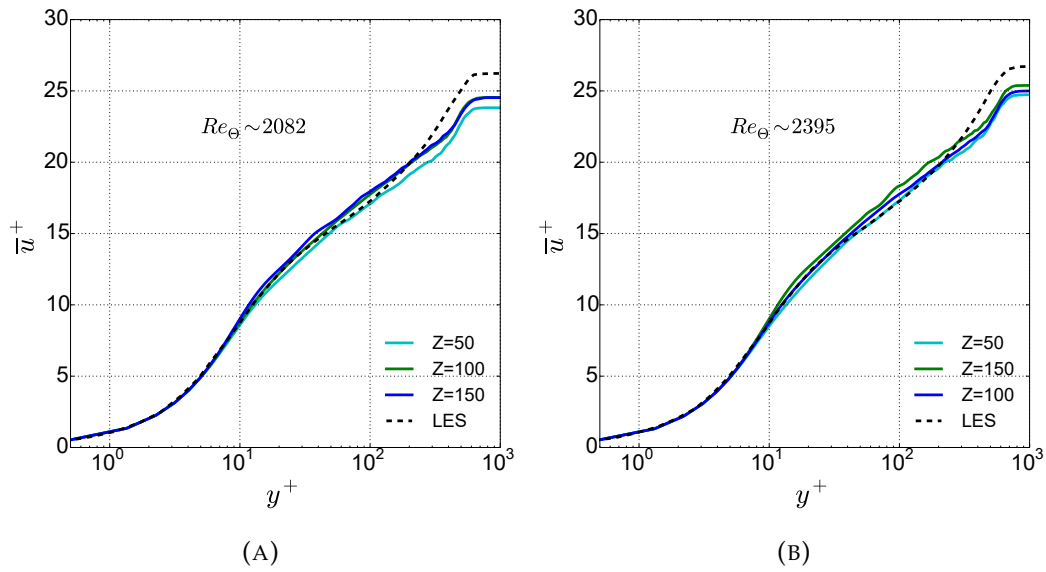


FIGURE H.6: Normalized wall-normal profiles of the mean streamwise velocity \bar{u} for various values of the model parameter Z at (A) $Re_\theta \approx 2082$ and (B) $Re_\theta \approx 2395$. ODT results are shown in comparison to a reference LES [64] at corresponding Re_θ . The other model parameters are fixed.

algorithm in the model. The Z parameter affect the starting point of the buffer layer and hence, a good match can be obtained between the ODT solutions and LES [64] data by excluding eddies slightly larger than the Kolmogorov ones by selecting $Z > 1$ [84]. ODT simulations are carried out for $Z \in \{50, 100, 150\}$ for velocity statistics up to 4th order at (A) $Re_\theta \approx 2082$ and (B) $Re_\theta \approx 2395$ and several global properties. The ODT results are presented in comparison with the LES data [64] at the same Re_θ with other parameters fixed.

Figure H.6 and Figure H.7 depicts the impact of the Z parameter on the mean streamwise velocity profile scaled with inner and outer units, respectively. The inner and outer units representation remains same as explained in previous section for the C parameter.

Figure H.6 shows that the Z parameter is less sensitive to the mean velocity profile than the C parameter for uniform blowing case for both Re_θ . The insensitivity to Z over the range chosen suggests using a wider range of Z and a higher Z range is presented elsewhere. Nevertheless, a well know effect of the Z parameter is confirmed, that is, an upward shift of the mean velocity profile in the logarithmic region with increasing Z which is due to the decrease of u_τ . In general, the profiles variation with the parameter remains consistent with previous studies.

Figure H.7 show excellent horizontal alignment of profiles because the Z parameter have less effect than the C parameter on the occurrence of large eddies. These eddies controls the boundary layer growth. For the blowing case, $Z = 100$ is used for the simulations. The value of the Z parameter considered for the uniform blowing configuration is noted smaller as compared

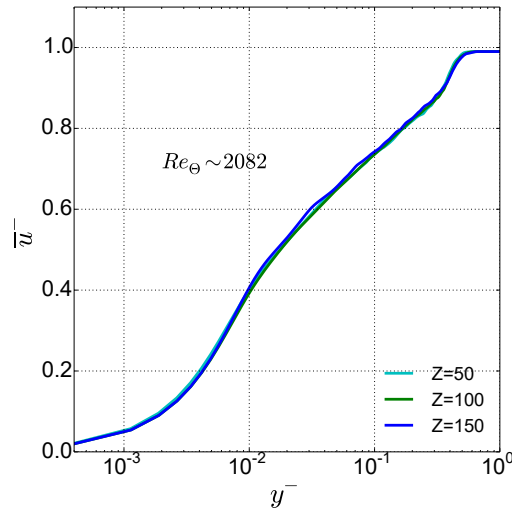


FIGURE H.7: The profiles of the mean streamwise velocity normalized with the outer units for various values of the model parameter Z at $Re_\theta \approx 2082$. The other model parameters are fixed.

to the other ODT applications [89, 98, 96, 109] indicating that the small eddies are important in case of blowing and are included to capture the flow properties.

Now, the the rms of the streamwise velocity component as a function of wall-normal coordinate is shown in Figure H.8. The profiles are shown at (A) $Re_\theta \approx 2082$ and (B) $Re_\theta \approx 2395$ for variation of Z parameter with reference data for comparison from [64] at corresponding Re_θ . The other model parameters are kept fixes while performing simulations for the Z parameter. All the profiles are consistent with the literature with variation of the Z parameter.

Variation of global properties, for example, C_f with Re_θ for different Z values considered is shown in Figure H.9. ODT results are shown in comparison to a reference LES [64] and the profiles for these quantities are also consistent with earlier results.

H.3 Influence of the LS Mechanism

Large eddy suppression (LS) is important feature introduced for the large eddies to avoid large-scale anomaly, however, the occurrence of these large eddy events is rare which if occurred may dominate the total transport as their turnover time is more than the current run time of the simulations. Hence these eddies should be avoided. There are different ways implemented in the model [89, 98, 100, 92, 85, 28] to restrict such large eddies and also discussed in earlier chapters of the thesis. These eddies can be restricted by ‘frac domain’, ‘elapsed time’, or ‘two-thirds’ LS mechanism and the influence of these suppression mechanism on various statistics and global properties is discussed below for $Re_\theta \approx 2082$ and 2395 in comparison to reference LES data [64] at the same Re_θ .

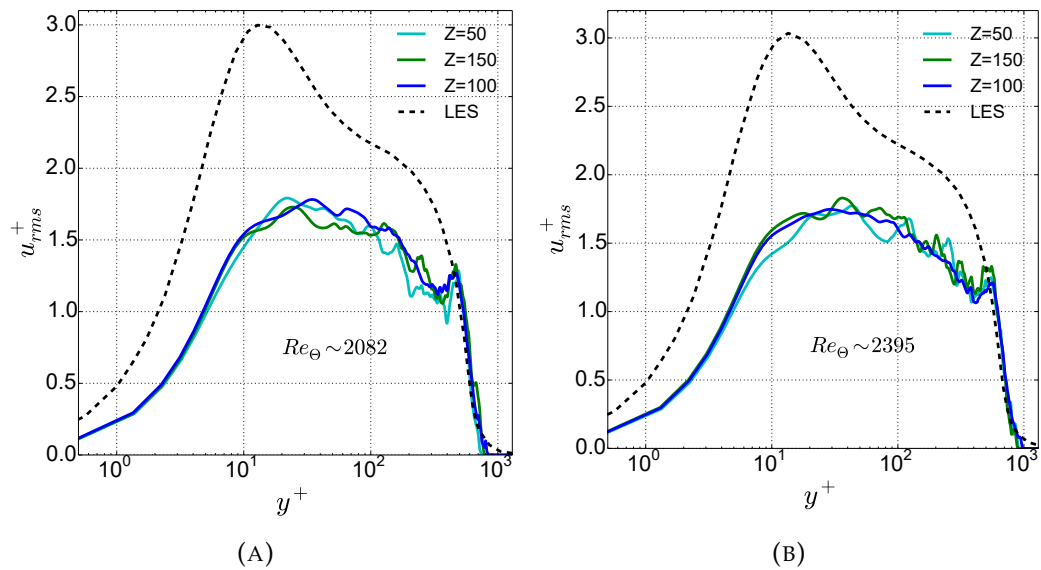


FIGURE H.8: The streamwise root-mean-square velocity profiles versus wall-normal coordinate (in viscous units) for various values of the model parameter Z at (A) $Re_\theta \approx 2082$ and (B) $Re_\theta \approx 2395$. ODT results are shown in comparison to a reference LES [64] at corresponding Re_θ . The other model parameters are fixed.

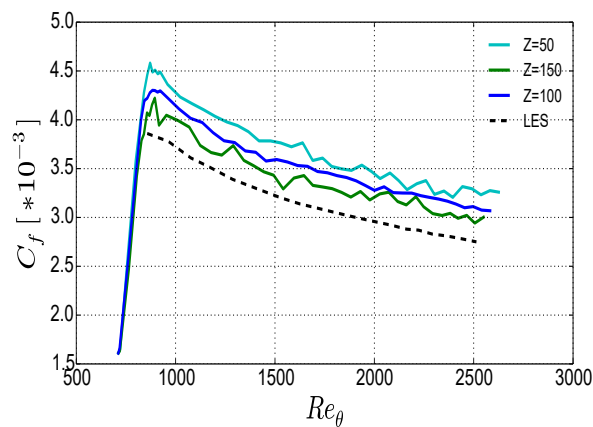


FIGURE H.9: Skin friction coefficient C_f as a function of Re_θ for various values of the model parameter Z . ODT results are shown in comparison to a reference LES [64]. The other model parameters are fixed.

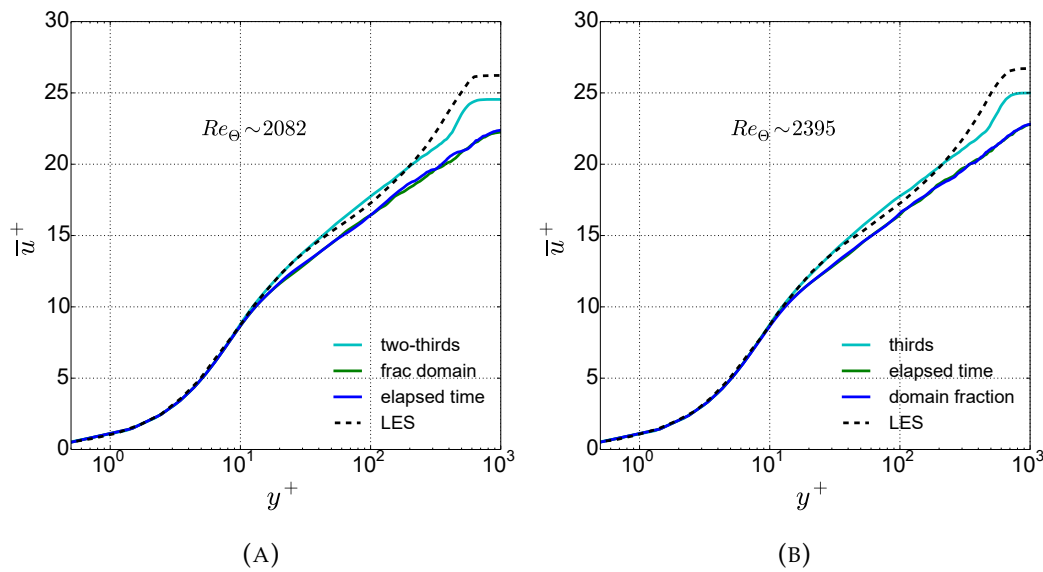


FIGURE H.10: Normalized wall-normal profiles of the mean streamwise velocity \bar{u} for various LS suppression mechanisms at (A) $Re_\theta \approx 2082$ and (B) $Re_\theta \approx 2395$. ODT results are shown in comparison to a reference LES [64] at corresponding Re_θ . The other model parameters are fixed.

The influence of the LS mechanism on the mean streamwise velocity component scaled with inner and outer units have been presented in Figure H.10 and H.11, respectively. The representation of inner and outer units remains same as explained in previous section for the C parameter and also all the other parameters are fixed at their optimal values.

In the viscous sublayer, there is no influence of LS mechanism on mean velocity profile as shown in Figure H.10 at (A) $Re_\theta \approx 2082$ and (B) $Re_\theta \approx 2395$ in comparison with reference data. Hence the near-wall similarity solution is obeyed for all ODT solutions. The influence is observed in the region $y^+ > 10$ and the velocity profile agrees with the LES data for the two-thirds LS mechanism. For the frac domain and elapsed time suppression mechanisms, the profile is under-predicted as compared to the LES data. The profile in the buffer region as well as outer log region is the same for the frac domain and the elapsed time mechanism. As expected and discussed for SBL and TBL cases, the LS suppression mechanism impact the outer region the most and as a result u_τ as well as normalized free-stream velocity, \bar{u}^+ , is changed.

Figure H.11 shows the mean streamwise velocity profile in outer units. This figure explains the shape change by faster boundary layer growth for LS mechanism. A good large- y collapse for elapsed time and frac domain mechanism is obtained. The LS mechanism have more effect than the Z parameter on the occurrence of large eddies that control the boundary layer growth, however, for blowing case, note that C , Z and LS suppression are important unlike SBL and TBL cases. For the blowing configuration, two-thirds mechanism is used for the simulations.

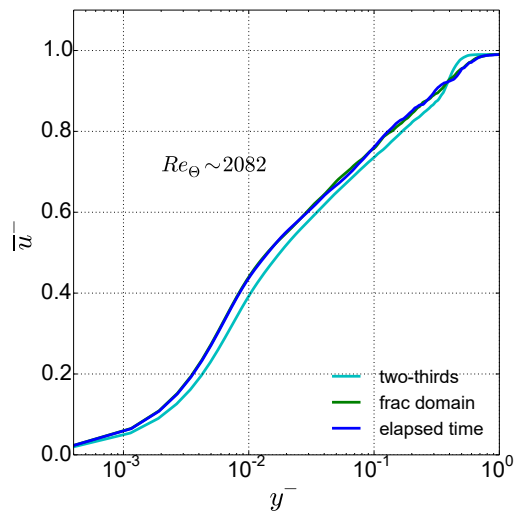


FIGURE H.11: The profiles of the mean streamwise velocity normalized with the outer units for various LS suppression mechanisms at $Re_\theta \approx 2082$. The other model parameters are fixed.

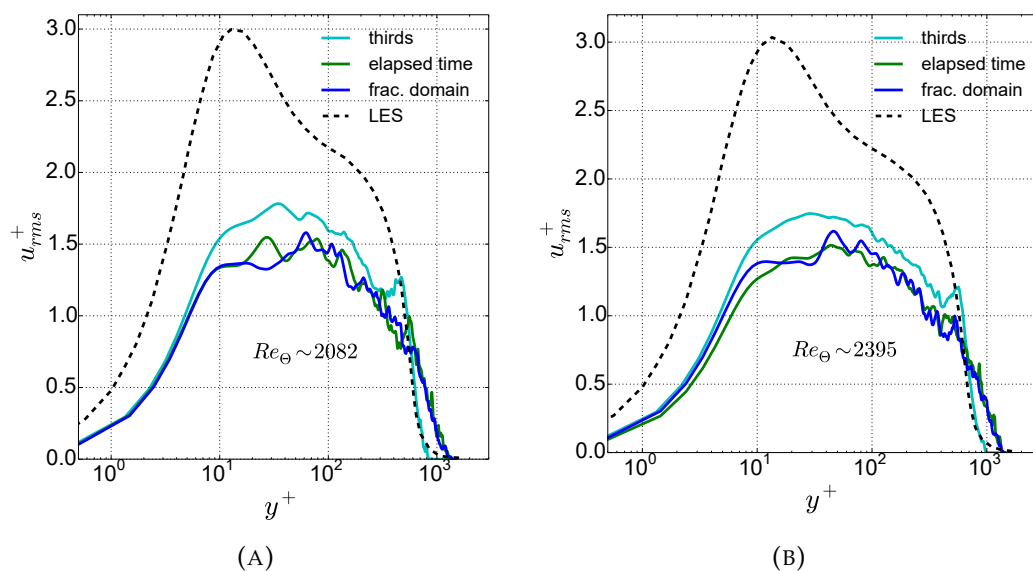


FIGURE H.12: The streamwise root-mean-square velocity profiles versus wall-normal coordinate (in viscous units) for various LS suppression mechanisms at (A) $Re_\theta \approx 2082$ and (B) $Re_\theta \approx 2395$. ODT results are shown in comparison to a reference LES [64] at corresponding Re_θ . The other model parameters are fixed.

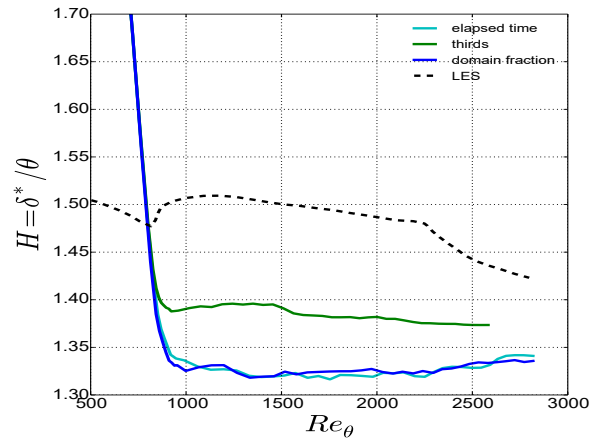


FIGURE H.13: The quantity H as a function of Re_θ for various LS suppression mechanisms. ODT results are shown in comparison to a reference LES [64]. The other model parameters are fixed.

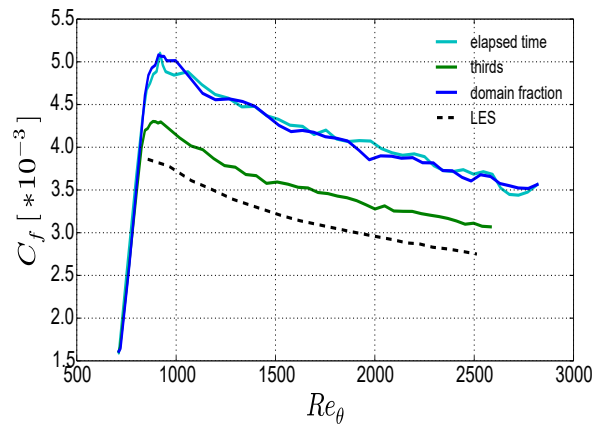


FIGURE H.14: Skin friction coefficient C_f as a function of Re_θ for various LS suppression mechanisms. ODT results are shown in comparison to a reference LES [64]. The other model parameters are fixed.

In Figure H.12, the rms of the streamwise velocity component as a function of wall-normal coordinate is shown. The profiles are shown for both Re_θ considered above at (A) $Re_\theta \approx 2082$ and (B) $Re_\theta \approx 2395$ for different LS suppression mechanisms with reference data for comparison from [64] at corresponding Re_θ . The other model parameters are kept fixed while performing simulations for various LS methods. All the profiles are consistent with the other results discussed.

Variation of global properties, i.e., H and C_f with Re_θ for different LS suppression mechanisms considered is shown in Figure H.13 and Figure H.14, respectively. ODT results are shown in comparison with the reference LES from [64]. The profiles for these quantities are also consistent with earlier results and hence their further discussion is avoided.

H.4 Variation of the Model Parameter α

The pressure fluctuations may not be universal [29] and that the pressure fluctuations do not necessarily imply a maximization of the inter-component kinetic energy transfer. Therefore, the model parameter α was introduced to control the exchange of the turbulent energy between the three velocity components. This parameter takes values in the range $[0, 1]$, with 0 means no and 1 maximal transfer of the kinetic energy and for $\alpha = 2/3$, equipartition of the energies is approximated which can be interpreted as a tendency to small-scale isotropy [29]. The other model parameters are kept fixed here for calibrating the α parameter.

The mean streamwise velocity for variation of the α parameter is shown below in Figure H.15 as a function of wall normal coordinate in viscous units. The profiles are not discussed as they are consistent with other results presented in previous Appendix and in earlier sections of this Appendix. Only difference is that for SBL and TBL, $\alpha = 2/3$ gave good match with reference results whereas, for blowing configuration, all α considered gives same trend and the profiles are independent of the choice of the α parameter.

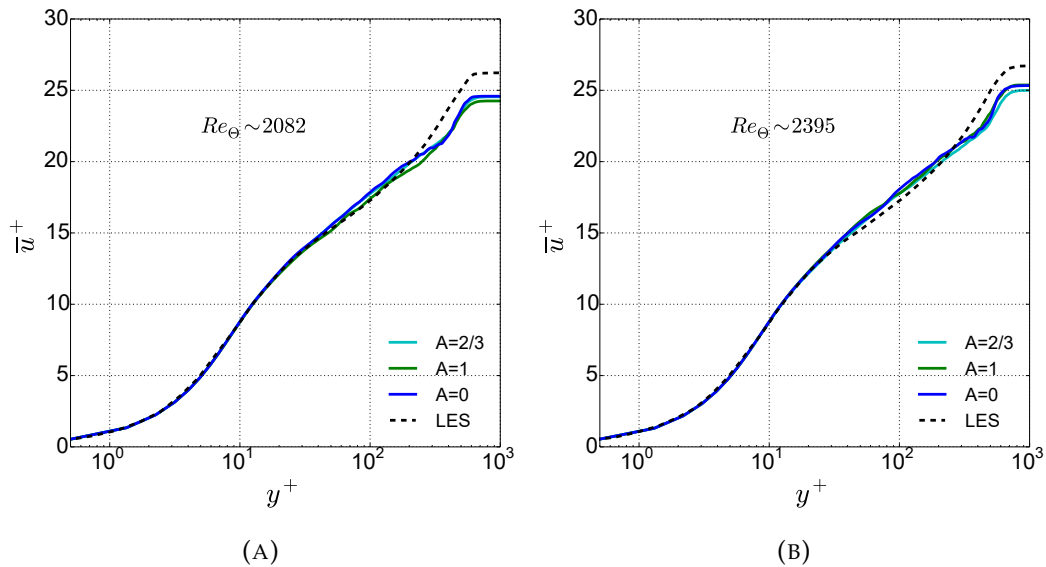


FIGURE H.15: Normalized wall-normal profiles of the mean streamwise velocity \bar{u} for various values of the model parameter α at (A) $Re_\theta \approx 2082$ and (B) $Re_\theta \approx 2395$. ODT results are shown in comparison to a reference LES [64] at corresponding Re_θ . The other model parameters are fixed.

Bibliography

- [1] S. B. Pope. *Turbulent Flows*. Cambridge University Press, University Printing House, Cambridge CB2 8BS, United Kingdom, 2000.
- [2] A. S. Monin and A. M. Yaglom. *Statistical Fluid Mechanics: Mechanics of Turbulence, Volume 1*. MIT Press, Cambridge, MA, 1971.
- [3] A. A. Townsend. *The Structure of Turbulent Shear Flow (2nd ed.)*. Cambridge University Press, Cambridge, 1976.
- [4] J. O. Hinze. *Turbulence (2nd ed.)*. McGraw-Hill, New York, 1975.
- [5] W. J. A. Dahm and P. E. Dimotakis. Mixing at large schmidt number in the self-similar far field of turbulent jets. *Journal of Fluid Mechanics*, 217:299–330, 1990.
- [6] C. Tong and Z. Warhaft. Passive scalar dispersion and mixing in a turbulent jet. *Journal of Fluid Mechanics*, 292:1–38, 1995.
- [7] L. Euler. Principes généraux du mouvement des fluides [The General Principles of the Movement of Fluids]. *Mémoires de l'académie des sciences de Berlin (in French)*, 11:274–315, 1757.
- [8] R. B. Bird, W. E. Stewart, and E. N. Lightfoot. *Transport Phenomena*. John Wiley & Sons, 2nd edition, 2007.
- [9] J. Anderson. *Computational Fluid Dynamics*. McGraw-Hill Education, ISBN 978-0-07-001685-9, 1995.
- [10] E. F. Toro. *Riemann Solvers and Numerical Methods for Fluid Dynamics: A Practical Introduction*. Springer, ISBN 978-3-540-65966-2, 1999.
- [11] J. C. Sutherland, N. Punati, and A. R. Kerstein. A unified Approach to the Various Formulations of the One–Dimensional–Turbulence Model. Technical Report ICSE100101, ICSE Report, 2010.
- [12] J. H. Ferziger and M. Perić. *Computational Methods for Fluid Dynamics*. Springer, ISBN 978-3-540-42074-3, 2002.
- [13] H. Kuerten, B. Geurts, V. Armenio, and J. Fröhlich. *Direct and Large Eddy Simulation VIII*. Springer, ISBN 978-94-007-2481-5, 2011.
- [14] J. Smagorinsky. General Circulation Experiments with the Primitive Equations. *Monthly Weather Review*, 91 (3):99–164, 1963.

- [15] J. Deardorff. A numerical study of three-dimensional turbulent channel flow at large Reynolds numbers. *Journal of Fluid Mechanics*, 41 (2):453–480, 1970.
- [16] H. Pitsch. Large-Eddy Simulation of Turbulent Combustion. *Annual Review of Fluid Mechanics*, 38 (1):453–482, 2006.
- [17] C. Wagner, T. Hüttl, and P. Sagaut. *Large-Eddy Simulation for Acoustics*. Cambridge University Press, ISBN 978-0-521-87144-0, 2007.
- [18] P. P. Sullivan, J. C. McWilliams, and C. Moeng. A subgrid-scale model for large-eddy simulation of planetary boundary-layer flows. *Boundary-Layer Meteorology*, 71 (3):247–276, 1994.
- [19] U. Piomelli and B. Elias. Wall-layer models for large-eddy simulations. *Annual Review of Fluid Mechanics*, 34:349–374, 2002.
- [20] P. R. Spalart. Detached-eddy simulation. *Annual Review of Fluid Mechanics*, 41:181–202, 2009.
- [21] R. O. Fox. Large-eddy-simulation tools for multiphase flows. *Annual Review of Fluid Mechanics*, 44 (1):47–76, 2012.
- [22] P. Sagaut. *Large Eddy Simulation for Incompressible Flows*. Springer, ISBN 978-3-540-26344-9, 2006.
- [23] R. Osborne. On the Dynamical Theory of Incompressible Viscous Fluids and the Determination of the Criterion. *Philosophical Transactions of the Royal Society of London A*, 186:123–164, 1895.
- [24] R. Fransen. . In *3rd INCA colloquium*, ONERA. Toulouse, France, 2011.
- [25] D. C. Wilcox. *Turbulence modeling for CFD*. DCW Industries, ISBN 978-1-928-72908-2, 2006.
- [26] André Bakker. Applied Computational Fluid Dynamics, Lecture 10 - Turbulence Models. <http://www.bakker.org/dartmouth06/engs150/10-rans.pdf>.
- [27] T. Poinsot, D. Veynante, F. Nicoud, B. Cuenot, L. Selle, G. Lartigue, L. Gicquel, V. Moureau, and S. Candel. Simulation tools for 3D reacting flows. <https://docplayer.net/19075274-Simulation-tools-for-3d-reacting-flows.html>.
- [28] A. Kerstein. One-dimensional turbulence: model formulation and application to homogeneous turbulence, shear flows, and buoyant stratified flows. *Journal of Fluid Mechanics*, 392:277–334, 1999.
- [29] A. Kerstein, W. Ashurst, S. Wunsch, and V. Nilsen. One-dimensional turbulence: vector formulation and application to free shear flows. *Journal of Fluid Mechanics*, 447:85–109, 2001.

-
- [30] H. Schlichting. *Boundary-Layer Theory*. New York: McGraw-Hill, 7th ed., 1979.
- [31] T. L. Bergman, A. S. Lavine, F. P. Incropera, and D. P. Dewitt. *Fundamentals of heat and mass transfer*. John Wiley & Sons, ISBN 978-0470-50196-2, 6th edition, 2011.
- [32] L. Prandtl. Über Flüssigkeitsbewegung bei sehr kleiner Reibung. In *Verhandlungen des Dritten Internationalen Mathematiker-Kongresses*. Heidelberg, Germany, 1904.
- [33] National Aeronautics and Space Administration. <https://www.grc.nasa.gov/www/k-12/airplane/boundlay.html>.
- [34] T. von Kármán. Mechanical Similitude and Turbulence. *Tech. Mem.*, 5:58–76, 1930.
- [35] M. Schultz, J. Finlay, M. Callow, and J.A. Callow. Three models to relate detachment of low form fouling at laboratory and ship scale. *Biofouling*, 19 Suppl:17–26, 2003.
- [36] T. von Kármán. Über laminare und turbulente Reibung. *Zeitschrift für Angewandte Mathematik und Mechanik*, 1 (4):233–252, 1921.
- [37] T. L. Bergman, A. S. Lavine, F. P. Incropera, and D. P. Dewitt. *Fundamentals of Heat and Mass Transfer*. John Wiley & Sons, ISBN 13 978-0470-50197-9, 7th edition, 2011.
- [38] P. R. Spalart. Direct simulation of a turbulent boundary layer up to $R_\theta = 1410$. *Journal of Fluid Mechanics*, 187:61–98, 1988.
- [39] X. Wu and P. Moin. Direct numerical simulation of turbulence in a nominally zero-pressure-gradient flat-plate boundary layer. *Journal of Fluid Mechanics*, 630:5–41, 2009.
- [40] P. Schlatter, R. Örlü, Q. Li, G. Brethouwer, J. H. M. Fransson, A. V. Johansson, P. H. Alfredsson, and D. S. Henningson. Turbulent boundary layers up to $R_\theta = 2500$ studied through simulation and experiment. *Physics of Fluids*, 21:051702–1–051702–4, 2009.
- [41] P. Schlatter and R. Örlü. Assessment of direct numerical simulation data of turbulent boundary layers. *Journal of Fluid Mechanics*, 659:116–126, 2010.
- [42] J. Jiménez, S. Hoyas, M. P. Simens, and Y. Mizuno. Turbulent boundary layers and channels at moderate Reynolds numbers. *Journal of Fluid Mechanics*, 657:335–360, 2010.
- [43] T. Sayadi, C. W. Hamman, and P. Moin. Direct numerical simulation of complete H-type and K-type transitions with implications for the dynamics of turbulent boundary layers. *Journal of Fluid Mechanics*, 724:480–509, 2013.

-
- [44] P. Schlatter and R. Örlü. Turbulent boundary layers at moderate Reynolds number: inflow length and tripping effects. *Journal of Fluid Mechanics*, 710:5–34, 2012.
- [45] Q. Li, P. Schlatter, L. Brandt, and D. S. Henningson. DNS of a spatially developing turbulent boundary layer with passive scalar transport. *International Journal of Heat and Fluid Flow*, 30:916–929, 2009.
- [46] A. Ferrante and S. E. Elghobashi. Reynolds number effect on drag reduction in a microbubble-laden spatially developing turbulent boundary layer. *Journal of Fluid Mechanics*, 543:93–106, 2005.
- [47] G. J. Brereton and W. C. Reynolds. Dynamic response of boundary-layer turbulence to oscillatory shear. *Physics of Fluids*, A3:178–187, 1991.
- [48] M.P. Martin. Direct numerical simulation of hypersonic turbulent boundary layers. Part 1. Initialization and comparison with experiments. *Journal of Fluid Mechanics*, 570:347–364, 2007.
- [49] M. Kozul and D. Chung. Direct numerical simulation of the incompressible temporally developing turbulent boundary layer. In H. Chowdhury and F. Alam, editors, *Proceedings of 19th Australasian Fluid Mechanics Conference, 8th-11th December 2014*. Australasian Fluid Mechanics Society, 2014.
- [50] M. Kozul, D. Chung, and J. P. Monty. Direct numerical simulation of the incompressible temporally developing turbulent boundary layer. *Journal of Fluid Mechanics*, 796:437–472, 2016.
- [51] T. S. Lund, X. Wu, and K. D. Squires. Generation of turbulent inflow data for spatially-developing boundary layer simulations. *Journal of Computational Physics*, 140:233–258, 1996.
- [52] A. Ferrante and S. E. Elghobashi. A robust method for generating inflow conditions for direct simulations of spatially-developing turbulent boundary layers. *Journal of Computational Physics*, 198:372–387, 2004.
- [53] J. P. Mellado. Direct numerical simulation of free convection over a heated plate. *Journal of Fluid Mechanics*, 712:418–450, 2012.
- [54] R. J. Adrian, C. D. Meinhart, and C. D. Tomkins. Vortex organization in the outer region of the turbulent boundary layer. *Journal of Fluid Mechanics*, 422:1–54, 2000.
- [55] D. Chung, J. P. Monty, and A. Ooi. An idealised assessment of Townsend’s outer-layer similarity hypothesis for wall turbulence. *Journal of Fluid Mechanics*, 742:R3, 2014.
- [56] J. Kim and P. Moin. Transport of passive scalars in a turbulent channel flow. Technical Report 89463, NASA Tech. Mem., 1987.

-
- [57] M. Lee, N. Malaya, and R. D. Moser. Direct numerical simulation for turbulent channel flow at high reynolds number. *65th Annual Meeting of the APS Division of Fluid Dynamics*, 2012.
- [58] M. Bernardini, S. Pirozzoli, and P. Orlandi. Velocity statistics in turbulent channel flow up to $R_\tau = 4000$. *Journal of Fluid Mechanics*, 742:171–191, 2014.
- [59] D. Feldmann and C. Wagner. Direct numerical simulation of fully developed turbulent and oscillatory pipe flows at $Re_\tau = 1440$. *Journal of Turbulence*, 13:1–28, 2012.
- [60] J. P. Mellado. The evaporatively driven cloud-top mixing layer. *Journal of Fluid Mechanics*, pages 1–32, 2010.
- [61] E. Dietze, H. Schmidt, B. Stevens, and J. P. Mellado. Controlling entrainment in the smoke cloud using level set-based front tracking. *Meteorologische Zeitschrift*, 2014.
- [62] Y. Sumitani and N. Kasagi. Direct numerical-simulation of turbulent transport with uniform wall injection and suction. *AIAA Journal*, 33:1220–1228, 1995.
- [63] Y. Kametani and K. Fukagata. Direct numerical simulation of spatially developing turbulent boundary layers with uniform blowing or suction. *Journal of Fluid Mechanics*, 681:154–172, 2011.
- [64] Y. Kametani, K. Fukagata, R. Örlü, and P. Schlatter. Effect of uniform blowing/ suction in a turbulent boundary layer at moderate Reynolds number. *International Journal of Heat and Fluid Flow*, 55:132–142, 2015.
- [65] K. Fukagata, S. Kern, P. Chatelain, P. Koumoutsakos, and N. Kasagi. Evolutionary optimization of an anisotropic compliant surface for turbulent friction drag reduction. *Journal of Turbulence*, 9:N35, 2008.
- [66] C. White and M. Mungal. Mechanics and prediction of turbulent drag reduction with polymer additives. *Annual Review of Fluid Mechanics*, 40:235–256, 2008.
- [67] R. Garcia-Mayoral and J. Jiménez. Drag reduction by riblets. *Philosophical Transactions of the Royal Society A*, 369:1412–1427, 2011.
- [68] S. Türk, G. Daschiel, A. Stroh, Y. Hasegawa, and B. Frohnäpfel. Turbulent flow over superhydrophobic surfaces with streamwise grooves. *Journal of Fluid Mechanics*, 747:186–217, 2014.
- [69] H. Choi, P. Moin, and J. Kim. Active turbulence control for drag reduction in wall-bounded flows. *Journal of Fluid Mechanics*, 262:75–110, 1994.
- [70] J. Kim. Control of turbulent boundary layers. *Physics of Fluids*, 15:1093–1105, 2003.

-
- [71] J. Kim and T. Bewley. A linear systems approach to flow control. *Annual Review of Fluid Mechanics*, 39:383–417, 2007.
- [72] P. Ricco and M. Quadrio. Wall-oscillation conditions for drag reduction in turbulent channel flow. *International Journal of Heat and Fluid Flow*, 29:601–612, 2008.
- [73] N. Kasagi, Y. Suzuki, and K. Fukagata. Microelectromechanical systems-based feedback control of turbulence for skin friction reduction. *Annual Review of Fluid Mechanics*, 41:231–251, 2009.
- [74] N. Tomiyama and K. Fukagata. Contribution of Reynolds stress distribution to the skin friction in wall-bounded flows. *Physics of Fluids*, 25:105115, 2013.
- [75] J. Kim, K. Kim, and H. Sung. Wall pressure fluctuations in a turbulent boundary layer after blowing or suction. *AIAA Journal*, 41:1697–1704, 2003.
- [76] M. Pamiés, E. Garnier, A. Merlen, and P. Sagaut. Response of a spatially developing turbulent boundary layer to active control strategies in the framework of opposition control. *Physics of Fluids*, 19:108102, 2007.
- [77] V. Kornilov and A. Boiko. Efficiency of air microblowing through microporated wall for flat plate drag reduction. *AIAA Journal*, 50:724–732, 2012.
- [78] K. Fukagata, K. Iwamoto, and N. Kasagi. Contribution of Reynolds stress distribution to the skin friction in wall-bounded flows. *Physics of Fluids*, 14:L73–L76, 2002.
- [79] S. Yoshioka, J. Fransson, and P. H. Alfredsson. Free stream turbulence induced disturbances in boundary layers with wall suction. *Physics of Fluids*, 16:3530–3539, 2004.
- [80] I. Marusic, B. J. McKeon, P. A. Monkewitz, H. M. Nagib, A. J. Smits, and K. R. Sreenivasan. Wall-bounded turbulent flows at high Reynolds numbers: recent advances and key issues. *Physics of Fluid*, 22:065103, 2010.
- [81] J. Wallace. Highlights from 50 years of turbulent boundary layer research. *Journal of Turbulence*, 13:N53, 2012.
- [82] G. Eitel-Amor, R. Örlü, and P. Schlatter. Simulation and validation of a spatially evolving turbulent boundary layer up to $R_\theta = 8300$. *International Journal of Heat and Fluid Flow*, 47:57–69, 2014.
- [83] A. Kerstein. One-Dimensional Turbulence: A new approach to high-fidelity subgrid closure of turbulent flow simulations. *Computer Physics Communications*, 148:1–16, 2002.

-
- [84] R. Schmidt, A. R. Kerstein, S. Wunsch, and V. Nilsen. Near-wall LES closure based on one-dimensional turbulence modeling. *Journal of Computational Physics*, 186:317–355, 2003.
- [85] W. T. Ashurst and A. Kerstein. One-dimensional turbulence: Variable-density formulation and application to mixing layers. *Physics of Fluids*, 17, 2005.
- [86] S. Wunsch and A. R. Kerstein. A stochastic model for high-Rayleigh number convection. *Journal of Fluid Mechanics*, 528:173–205, 2005.
- [87] A. R. Kerstein and S. Wunsch. Simulation of a stably stratified atmospheric boundary layer using one-dimensional turbulence. *Boundary Layer–Meteorology*, 118:325–356, 2006.
- [88] E. Gonzales-Juez, A. R. Kerstein, and D. O. Lignell. Fluxes across double-diffusive interfaces: a one-dimensional-turbulence study. *Journal of Fluid Mechanics*, 677:218–254, 2011.
- [89] D. O. Lignell, A. Kerstein, G. Sun, and E. Monson. Mesh adaption for efficient multiscale implementation of One-Dimensional Turbulence. *Theoretical and Computational Fluid Dynamics*, 27:273–295, 2013.
- [90] F. Schulz, C. Glawe, H. Schmidt, and A. Kerstein. Toward modeling of CO₂ multi-phase flow patterns using a stochastic multi-scale approach. *Environmental Earth Science*, 70:3739–3748, 2013.
- [91] Z. Jozefik, A. Kerstein, H. Schmidt, S. Lyra, H. Kolla, and J. Chen. One-dimensional turbulence modeling of a turbulent counterflow flame with comparison to DNS. *Combustion and Flame*, 162:2999–3015, 2015.
- [92] J. Hewson and A. Kerstein. Stochastic simulation of transport and chemical kinetics in turbulent CO/H₂/N₂ flames. *Combustion Theory and Modelling*, 5:669–697, 2001.
- [93] J. Hewson and A. Kerstein. Local extinction and reignition in non-premixed turbulent CO/H₂/N₂ jet flames. *Combustion Science and Technology*, 174:35–66, 2002.
- [94] H. Schmidt, A. Kerstein, R. Nédélec, S. Wunsch, and B. J. Saylor. Analysis and numerical simulation of a laboratory analog of radiatively induced cloud-top entrainment. *Theoretical and Computational Fluid Dynamics*, 27:377–395, 2013.
- [95] C. Glawe, F. Schulz, E. Gonzales-Juez, H. Schmidt, and A. Kerstein. ODTLES simulations of turbulent flows through heated channels and ducts. In *Proceedings of TSFP-8, 28-30 August 2013*. Poitiers, France, 2013.
- [96] M. M. Fragner and H. Schmidt. Investigating Asymptotic Suction Boundary Layers using a One-Dimensional Stochastic Turbulence Model. *Journal of Turbulence*, 18:899–928, 2017.

-
- [97] M. Klein and H. Schmidt. Stochastic Modeling of Turbulent Scalar Transport at Very High Schmidt Numbers. *Proceedings of Applied Mathematics and Mechanics*, 17:639–640, 2017.
- [98] D. O. Lignell, V. B. Lansinger, J. Medina, M. Klein, A. R. Kerstein, H. Schmidt, M. Fistler, and M. Oevermann. One-dimensional turbulence modeling for cylindrical and spherical flows: model formulation and application. *Theoretical and Computational Fluid Dynamics*, 32:495–520, 2018.
- [99] J. A. Medina M., M. Klein, and H. Schmidt. One-dimensional turbulence investigation of variable density effects due to heat transfer in a low mach number internal air flow. *International Journal of Heat and Fluid Flow*, 80:108481, 2019.
- [100] T. Echekki, A. Kerstein, and T. Dreeben. One-dimensional turbulence simulation of turbulent jet diffusion flames: model formulation and illustrative applications. *Combustion and Flame*, 125:1083–1105, 2001.
- [101] D. O. Lignell and D. S. Rappleye. One-dimensional-turbulence simulation of flame extinction and reignition in planar ethylene jet flames. *Combustion and Flame*, 159:2930–2943, 2012.
- [102] E. I. Monsoon, D. O. Lignell, M. A. Finney, C. Werner, Z. Jozefik, A. R. Kerstein, and R. S. Hintze. Simulation of Ethylene Wall Fires Using the Spatially-Evolving One-Dimensional Turbulence Model. *Fire Technology*, 52:1–30, 2014.
- [103] R. Schmidt, A. Kerstein, and R. McDermott. ODTLES: A multi-scale model for 3D turbulent flow based on one-dimensional turbulence modeling. *Computer Methods in Applied Mechanics and Engineering*, 199:865–880, 2010.
- [104] E. Gonzales-Juez, R. Schmidt, and A. Kerstein. ODTLES simulations of wall-bounded flows. *Physics of Fluids*, 23, 2011.
- [105] M. M. Fragner and H. Schmidt. Investigating Asymptotic Suction Boundary Layers using a One-Dimensional Stochastic Turbulence Model. *Proceedings of Applied Mathematics and Mechanics*, 17:637–638, 2017.
- [106] M. M. Fragner and H. Schmidt. Investigating Asymptotic Suction Boundary Layers using a One-Dimensional Stochastic Turbulence Modelling Approach. In *Proceedings of TSFP-10, 6-9 July 2017*. Chicago, USA, 2017.
- [107] M. M. Fragner and H. Schmidt. Using the one-dimensional turbulence model to study asymptotic suction boundary layers. In *16th European Turbulence Conference, 21-24 August 2016*. Stockholm, Sweden, 2016.

-
- [108] C. Glawe, J. A. Medina M., and H. Schmidt. IMEX based multi-scale time advancement in ODTLES. *Zeitschrift für Angewandte Mathematik und Mechanik*, 98:1907–1923, 2018.
- [109] Rakhi, M. Klein, J. A. Medina M., and H. Schmidt. One-dimensional turbulence modeling of incompressible temporally developing turbulent boundary layers with comparison to DNS. *Journal of Turbulence*, 20:8:506–543, 2019.
- [110] Rakhi and H. Schmidt. A stochastic approach to investigate the incompressible temporally developing turbulent boundary layer. In *Proceedings of CMFF'18, 4-7 September 2018*. Budapest, Hungary, 2018.
- [111] Rakhi and H. Schmidt. Investigating incompressible temporally developing turbulent boundary layers using One-Dimensional Turbulence. *Proceedings of Applied Mathematics and Mechanics*, 18:e201800214, 2018.
- [112] Rakhi and H. Schmidt. Using a Stochastic One-Dimensional Turbulence model to study Incompressible Spatially Developing Turbulent Boundary Layers. In *Proceedings of TSFP-11, 30 July-2 August 2019*. Southampton, UK, 2019.
- [113] G. K. Batchelor. *An Introduction to Fluid Dynamics*. Cambridge University Press, ISBN 978-0-521-66396-0, 1967.
- [114] A. Kerstein. Linear–Eddy modelling of turbulent transport. Part 6. Microstructure of diffusive scalar mixing fields. *Journal of Fluid Mechanics*, 231:361–394, 1991.
- [115] A. R. Kerstein and T. D. Dreeben. Prediction of turbulent free shear flow statistics using a simple stochastic model. *Physics of Fluids*, 12(2):418–424, 2000.
- [116] S. V. Patankar. *Numerical Heat Transfer and Fluid Flow*. Hemisphere Publishing Corporation, McGraw-Hill Book Company, 1221 Avenue of the Americas, New York 10020 ISBN 0-07-048740-5, 1980.
- [117] H. K. Versteeg and W. Malalasekera. *AN INTRODUCTION TO COMPUTATIONAL FLUID DYNAMICS The Finite Volume Method Second Edition*. Pearson Education Limited, Pearson Education Limited, Edinburgh Gate, Harlow, Essex CM20 2JE, England, ISBN: 978-0-13-127498-3, 2007.
- [118] J. D. Hoffman. *Numerical Methods for Engineers and Scientists*. CRC Press, New York, 2001.
- [119] D. Coles. The problem of the turbulent boundary layer. *Zeitschrift für Angewandte Mathematik und Physik*, 5:181–203, 1954.
- [120] D. Coles. The law of the wake in the turbulent boundary layer. *Journal of Fluid Mechanics*, 1:191–226, 1956.

-
- [121] N. Hutchins, T. B. Nickels, I. Marusic, and M. S. Chong. Hot-wire spatial resolution issues in wall-bounded turbulence. *Journal of Fluid Mechanics*, 632:431–42, 2009.
- [122] I. Marusic, R. Mathis, and N. Hutchins. High Reynolds number effects in wall turbulence. *International Journal of Heat and Fluid Flow*, 31:418–28, 2010.
- [123] J. S. Alexander, M. J. Beverley, and I. Marusic. High-Reynolds Number Wall Turbulence. *Annual Review of Fluid Mechanics*, 43:353–75, 2011.
- [124] M. Guala, S. E. Hommema, and R. J. Adrian. Large-scale and very-large-scale motions in turbulent pipe flow. *Journal of Fluid Mechanics*, 554:521–542, 2006.
- [125] H. M. Nagib, K. A. Chauhan, and P. A. Monkewitz. Approach to an asymptotic state for zero pressure gradient turbulent boundary layers. *Philosophical Transactions of the Royal Society A*, 365:755, 2007.
- [126] M. Klein and H. Schmidt. Investigating the Reynolds number dependency of the scalar transfer to a wall using a stochastic turbulence model. *Proceedings of Applied Mathematics and Mechanics*, 18:e201800238, 2018.
- [127] Rakhi and H. Schmidt. One-dimensional turbulence: application to incompressible spatially developing turbulent boundary layers. *International Journal of Heat and Fluid Flow*, 85:108626, 2020.
- [128] P. Schlatter and R. Örlü. Turbulent asymptotic suction boundary layers studied by simulation. In: *13th European Turbulence Conference (ETC13)*, pages 1–10, 2011.
- [129] A. Bobke, R. Örlü, and P. Schlatter. Simulations of turbulent asymptotic suction boundary layers. *Journal of Turbulence*, 17:157–180, 2015.
- [130] C. Glawe, H. Schmidt, A. Kerstein, and R. Klein. XLES Part i: Introduction to Extended Large Eddy Simulation. *Journal of Computational Physics*, 2015.
- [131] C. Glawe, H. Schmidt, A. Kerstein, and R. Klein. XLES Part ii: From Extended Large Eddy Simulation to ODTLES. *Journal of Computational Physics*, 2015.
- [132] C. Glawe. *ODTLES: turbulence modeling using a one-dimensional turbulence closed extended large eddy simulation approach*. PhD thesis, Berlin: Freie Universität Berlin, 2015.
- [133] G. Hasanuzzaman, S. Merbold, C. Cuvier, V. Motuz, J. M. Foucaut, and Ch. Egbers. Experimental investigation of turbulent boundary layers at high Reynolds number with uniform blowing, part I: statistics. *Journal of Turbulence*, 21:3:129–165, 2020.

- [134] J. Jimenez and A. Pinelli. The autonomous cycle of near-wall turbulence. *Journal of Fluid Mechanics*, 389:335–359, 1999.
- [135] J. Kim, P. Moin, and R. Moser. Turbulence statistics in fully developed channel flow at low reynolds number. *Journal of Fluid Mechanics*, 177:133–166, 1987.
- [136] V. Giddey, D. W. Meyer, and P. Jenny. Modeling three-dimensional scalar mixing with forced one-dimensional turbulence. *Physics of Fluids*, 30(12):125103, 2018.
- [137] J. S. Bendat and A. G. Piersol. *Random data: analysis and measurement procedures*, volume 729. John Wiley & Sons, 2011.